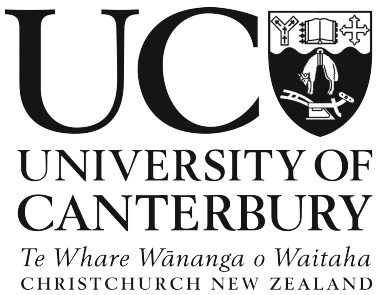

SCHOOL OF PHYSICAL AND CHEMICAL SCIENCES
UNIVERSITY OF CANTERBURY

Large Ring Lasers: Beyond the Macek and Davis Experiment

Author:
Caroline Livan ANYI

Supervisor:
Prof. Jon-Paul R. WELLS

Co-Supervisor:
Prof. Michael F. REID

SUBMITTED IN PARTIAL FULFILMENT OF THE REQUIREMENTS FOR THE DEGREE OF
DOCTOR OF PHILOSOPHY IN PHYSICS

2019

Abstract

Large-scale ring laser gyroscopes are highly sensitive rotation sensors whose operating principle is based upon the Sagnac effect. They are constructed for direct measurement of Earth rotation and offer applications in geodesy, geophysics, seismology and tests of fundamental physics. Motivated by the fact that the scale factor of a ring laser gyroscope is dependent upon the operating wavelength as well as the geometric size; in this thesis, we report on the gyroscopic performance of PR-1, a vertically mounted 2.56 m^2 ring laser gyroscope, operating on different neon transitions other than the standard 632.8 nm ($3s_2 \rightarrow 2p_4$) helium-neon laser wavelength.

State-of-the-art GaAs/AlGaAs crystalline coated, fused silica supermirrors have been employed to operate the laser on the $2s_2 \rightarrow 2p_4$ transition of neon at a wavelength of 1152.3 nm. The gyroscope is readily observed to unlock on Earth rotation, having a Sagnac beat note at approximately 60 Hz and demonstrated comparable performance to that achieved for operation with the industry standard ion beam sputtered (IBS) dielectric multilayer mirrors at 632.8 nm. Our results suggest a high potential for the implementation of crystalline coatings mirrors in the development of large-area ring laser gyroscopes along with other highly sensitive optical interferometric systems.

Earth rotation sensing on the shortest helium-neon laser wavelength at 543.4 nm ($3s_2 \rightarrow 2p_{10}$) was achieved by employing latest generation IBS mirrors that provide an extremely low transmission loss of 0.2 parts per million (ppm) at 543 nm, yielding a stable Sagnac frequency of 132.8 Hz. The gyroscope also exhibits frequency non-degenerate, bi-directional laser operation under the bias provided by Earth rotation while running on the 611.8 nm ($3s_2 \rightarrow 2p_6$) of neon transition, having an operational Sagnac frequency of 117.2 Hz. Our initial assessment of operation at 543.4 nm suggests significant potential in improving the performance of ring laser gyroscopes especially for underground operations where the size of the laser will be limited by the laboratory space.

Finally, we report on preliminary work towards the development of a cavity stabilisation scheme that employs two piezo-actuators acting on two diagonally opposite cavity mirrors to control the laser cavity perimeter. The feedback mechanism was achieved by operating the laser on multiple phase-locked longitudinal modes configuration, yielding a stable Sagnac beat frequency. The frequency difference between adjacent longitudi-

nal modes is heterodyned with a reference frequency generated by a GPS-locked Radio Frequency (RF) generator, and the resulting beat note provides a feedback signal to the piezo-actuator controller. Using this method, the gyroscope achieved a frequency stability of 4.8×10^{-5} relative to Earth rotation, for over 100 s of averaging time.

Acknowledgement

First and foremost, I would like to express my sincere gratitude towards Professor Jon-Paul Wells and Professor Mike Reid, my research supervisors, for the valuable and constructive suggestions during the planning and development of this research work. Their endless encouragement, patient guidance and willingness to give their time so generously are very much appreciated. My genuine appreciation is also extended to Professor Ulrich Schreiber for the opportunity to work with the G ring laser and for the engaging and enthusiastic discussion regarding ring laser research. I would also like to thank Dr Bob Hurst who provided and shared invaluable knowledge related to ring laser physics.

I am particularly grateful for the day to day technical and mechanical assistance given by Mr Rob Thirkettle; in particular for the 'endless runs' of cleaning the intra-cavity mirrors and for the many instrumental queries. My grateful thanks are also extended to Mr Graeme MacDonald who assisted in developing the gain tube's electrode and impedance matching unit and for his many technical advice related to electronics; and Mr Geoff Graham who helped to build the feedback servo system. Also, I would like to offer my special thanks to Dr André Gebauer and Dr Jan Kodet for providing guidance during the experimental works related to the G ring; and to Marinus Mayerbacher for his expertise in operating the Menlo 1500 Frequency Comb.

I am very grateful towards my fellow graduate students of the Department of Physics and Astronomy for the supportive, fun and helpful work environment. I also want to thank Nick, Dian and Jessica for their thorough proof-reading of this thesis.

I wish to thank my family, especially my parents for their love, understanding and encouragement throughout my study, and also my siblings for keeping up with my endless agony and rants. I would not be where I am now without the continuous support from all of you. To my flatmates, Evelyn and Anwar, thank you for providing a lovely and comfortable home atmosphere. To my friends and church family, I am thankful for your thoughtful prayers and for being a part of this research journey.

Finally, I would like to acknowledge the financial support provided by the University of Canterbury in the form of Departmental scholarship; and by the Dodd-Walls Centre in terms of PhD Scholarship.

Contents

List of Figures

List of Tables

1 Introduction

Precise monitoring of the variation of the Earth rotation rate is crucial to establish an accurate geodetic reference system. The angular velocity of the Earth rotation varies due to changes in the mass transport of Earth fluids, wind patterns and the high and low of the ocean tides [1]. Furthermore, the Earth rotation axis varies with respect to a fixed reference frame due to the gravitational influence of the sun and the moon. These small variations of the Earth rotation rate and orientation are represented by the Earth Orientation Parameters (EOPs): precession, nutation, polar motion and variation of the Earth rotation rate. Precession and nutation are the long-term and periodic changes of the direction of the Earth rotation axis with reference to a space-fixed reference system. The 'wobbling' of the Earth's rotation axis with respect to the Earth-fixed reference system is defined as polar motion while the Earth rotation rate, also known as the Length of Day (LoD), is represented by the difference between Universal Time 1 (UT1) and the Uniform Atomic Time (UTC) [2].

EOPs are monitored by space geodetic techniques such as Very Long Baseline Interferometry (VLBI), Satellite Laser Ranging (SLR), Lunar Laser Ranging (LLR), Doppler Orbitography, Radio-positioning Integrated by Satellite (DORIS) and the Global Navigation Satellite Systems (GNSS). The most accurate technique to observe polar motion is GNSS. On the other hand, precession, nutation and LoD are monitored using VLBI [3]. However, none of these geodetic techniques have a direct link to the Earth rotation axis. The network of VLBI observing stations are linked to the Earth rotation axis by a nutation model but the ultimate accuracy of this model is not known. On the other hand, large ring laser gyroscopes (RLGs) are 'strapped down' to the Earth itself [4]. Hence, they are the only space geodetic measurement tool that is referenced to the Earth rotation axis directly. Today, the resolution and stability of large ring laser gyroscopes enable them to measure small perturbations occurring in the Earth rotation axis [4]–[6].

Ring laser gyroscopes are highly sensitive instruments for measuring rotation relative to an inertial frame. The operation of a ring laser gyroscope is based on the Sagnac effect, which was discovered by George Sagnac in 1913 when he tried to detect the relative motion of the ether [7]. The effect can be described as follows: A light beam is split into two so that the two beams propagate around a polygonal-shaped interferometer in opposite directions. If the interferometer is being rotated in clockwise order, the clockwise light beam will take a longer time to arrive at the starting point as compared to the counter-clockwise laser beam. This is because the starting point has moved since

the two beams departed. Hence, the clockwise beam will travel through a longer path than the counter-clockwise beam, giving rise to a phase shift when the two beams are recombined.

Michelson, Pearson and Gale successfully detected the phase shift due to the Earth rotation in their 1925 experiment with a 603 m × 334 m interferometer based on the Sagnac effect [8]. The interferometer was a rectangular arrangement of several air-evacuated 12-inch pipelines laid on the ground in Clearing, Illinois, USA. A coherent light source (generated from a carbon arc) was split into two counter-propagating beams by a thinly coated mirror. The two beams propagate around the interferometer guided by mirrors at each corner and when the light beams were superimposed, the observed fringe shift due to the Earth rotation rate was 0.230 ±0.005. This ultimately led to the working foundation of the passive ring laser gyro we know of today.

An active ring laser gyroscope contains a lasing medium in the laser cavity. The optical frequencies of the counter-propagating beams are determined by the condition that an integer number of wavelengths must be equal to the cavity length. When the laser cavity is stationary, both beams will have the same wavelength, and hence the same optical frequency. For a rotating laser cavity, the path travelled by each beam will be altered due to the Sagnac effect. Therefore, the wavelengths are now unequal and the recombination of the two beams will result in a frequency difference. This frequency is known as the Sagnac frequency. For a large ring laser gyroscope (when it is subjected to the Earth rotation rate), the signal being detected is, δf_s,

$$\delta f_s = \frac{4A}{\lambda P}\vec{n}\cdot\vec{\Omega_E}, \tag{1.1}$$

where P is the laser cavity path length, A is the area travelled by the laser beam, λ is the laser wavelength, and $\vec{n}$ is the normal vector of A and $\Omega_E = 7.3 \times 10^{-5}$ rad/s, is the rotation rate of the Earth.

The first active ring laser gyroscope was demonstrated by Macek and Davis [9] soon after the invention of laser in the early 1960s. Their 1 m^2 ring laser gyroscope was based on a helium-neon gain medium lasing at 1152.3 nm. Four gain tubes with Brewster angle windows and four external corner mirrors defined the laser cavity. Although Macek and Davis postulated the possibilities of measuring the rotation rate of the Earth in their report, the laser did not unlock on the Earth rotation. Nevertheless, their seminal work led to the development of small-sized ring laser gyroscopes (typically 0.02 m^2 in size) that are used in the inertial navigation systems of aeroplanes, rockets and military hardware.

1.1 The Canterbury Ring Laser Project

Laser gyroscopes are commonly operated on a single longitudinal laser mode. For this reason, the effort to build larger ring laser gyroscope (size ≥ 1 m^2) was initially full of uncertainty as single-mode operation was expected to be increasingly difficult to achieve as the frequency spectral range (FSR) decreased in ever larger cavities. Despite that, in 1988, the Canterbury ring laser group constructed Canterbury-I (C-I), a square-shaped ring laser gyroscope with a perimeter of 3.447 m [10], [11]. C-I became the first ring laser gyroscope in the world to unlock on the rotation bias provided by the Earth despite its location in a high rise building[1].

A remarkable technological innovation, C-I was made of four first-generation supermirrors and Pyrex tubes to form the square laser cavity. The stainless steel mirror holders were placed on Zerodur plates and the whole resonator was mounted on a granite block as shown in Figure 1.1 (a). In order to achieve maximum mechanical and thermal stability, C-I was eventually transferred from the sixth-floor laboratory in the Ilam campus to the Cashmere caverns, an old underground war bunker complex at the foot of the Port Hills, in the Christchurch suburb of Cashmere [10].

Following the success of C-I, a second ring laser gyroscope, denoted as C-II, was built through a collaboration with the Technical University of Munich (TUM). The construction of C-II was a test-bed for the plan to build a similar but larger laser structure, G (the Gross-ring), in Germany. C-II is a 1 m^2 ring laser drilled out of a low thermal expansion Zerodur [2] block and the intracavity mirrors are attached to the Zerodur block by molecular adhesion. C-II (as shown in Figure 1.1 (b)) emulates the commercial inertial navigation ring laser design where the entire laser cavity is made out of a Zerodur block to minimise thermal effects. C-II's performance was far superior to C-I due to its monolithic design and the use of next-generation supermirrors [10].

G-0 was another ring laser gyroscope that was built as a prototype for the G ring structure. G-0 has a total perimeter of 14 m, mounted vertically on the wall of the Cashmere caverns [13] as shown in Figure 1.1 (c). It is a heterolithic ring laser where its laser path was enclosed in an Ultra High Vacuum (UHV) cavity by stainless steel pipes. The four mirrors were placed inside stainless steel corner boxes and mounted onto a stable concrete platform, i.e. the walls of the cavern. Although the device was simply built as a prototype to demonstrate that perimeter up-scaling does not hinder the laser to run on a single

[1] At the same time, as C-I was being built, a simultaneous research programme in Germany saw the development of a 1 m^2 triangular ring laser which used argon as the gain medium. However, the argon gain medium introduces axial gas flow within the laser cavity which hindered its potential to measure the rotation of the Earth [12], as this provides a time-varying reciprocal bias.

[2] The Zerodur was produced by the SCHOTT AG Mainz (Germany).

longitudinal mode, G-0 performed surprisingly well as a gyroscope, achieving a sensitivity of 11.6×10^{-12} rad/s/$\sqrt{\text{Hz}}$.

Motivated by the excellent performance of G-0, the Canterbury ring laser group continued to build even larger ring laser gyroscopes. UG-1[3] was constructed in 2000. Its beam paths enclosed a total area of 367.5 m^2, occupying half of the Cashmere cavern floor. It was initially operated with a closed gain tube design. The open-air configuration was eventually replaced by stainless steel pipes [14]. In 2005, UG-2 was constructed as an enlarged version of UG-1 with the total area of 834 m^2 [15] and filled the entire Cashmere cavern floor. Figure 1.1 (d) shows the south-east side of UG-1 and Figure 1.1 (e) is the north-west arm of UG-2.

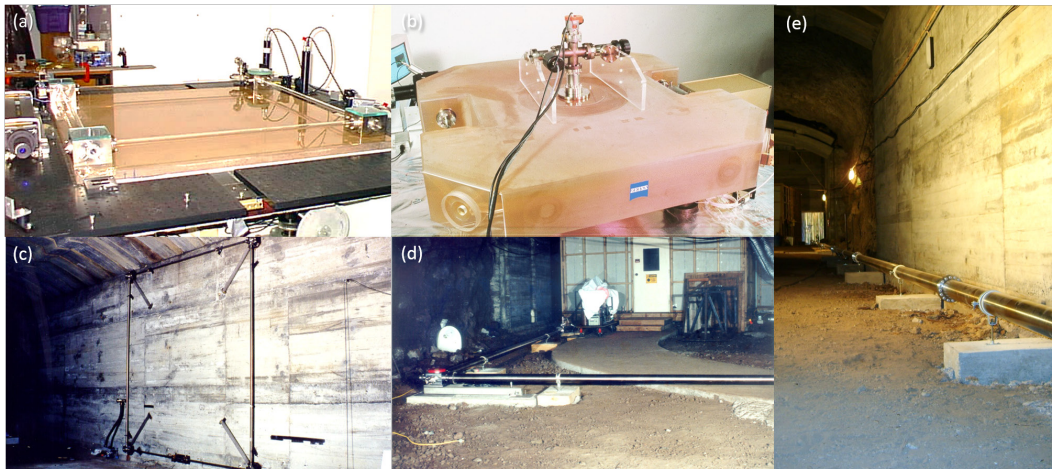

Figure. 1.1.: Canterbury ring laser gyroscopes: (a) C-I; (b) C-II; (c) G-0; (d) UG-1; (e) UG-2.

UG-2 is the most sensitive ring laser gyroscope ever been built, achieving raw sensitivity of 7.8×10^{-12} rad/s/$\sqrt{\text{Hz}}$. However, the stabilities of both the UG-1 and UG-2 lasers were affected by their necessarily heterolithic designs. Furthermore, the Cashmere cavern's floor is subject to thermoelastic strain and atmospheric pressure variations which introduce time-varying beam wander. Moreover, in the case of UG-2, the laser gain was affected by the outgassing of hydrogen gas from the large quantities of stainless steel tubes which prohibited operation for more than two months.

In 2008, UG-2 was dismantled to build UG-3. UG-3 has the same dimension as UG-1 but with several upgrades such as new optical mounting boards at four corners and new supports for the corner boxes. These new upgrades allow for precise four corner phase tracking[4] to provide valuable information about the strain of the cavern's floor. Although the measurement errors (due to the strains) can be corrected, the measured signal from UG-3 was still affected by other noise sources [16].

[3] UG is an abbreviation for 'ultra gross' in German. The UG lasers are categorised as 'ultra-large' ring lasers

[4] The laser beams are combined at all four corners of UG-3 and the detected δf_s at all corners are logged to track the relative phase difference between each measured δf_s.

Note that after the Christchurch earthquake in November 2011, the Cashmere caverns were closed. C-I, C-II, G-0, UG-1 and UG-2 are currently not available for operation.

1.2 The Current State of Large Ring Laser Gyroscope Development and Applications

Over the past 35 years, ring laser gyroscopes have increased in sensitivity by six orders of magnitude. This progress has enabled new applications in the fields of geodesy, geophysics, seismology and potentially tests of fundamental physics [17].

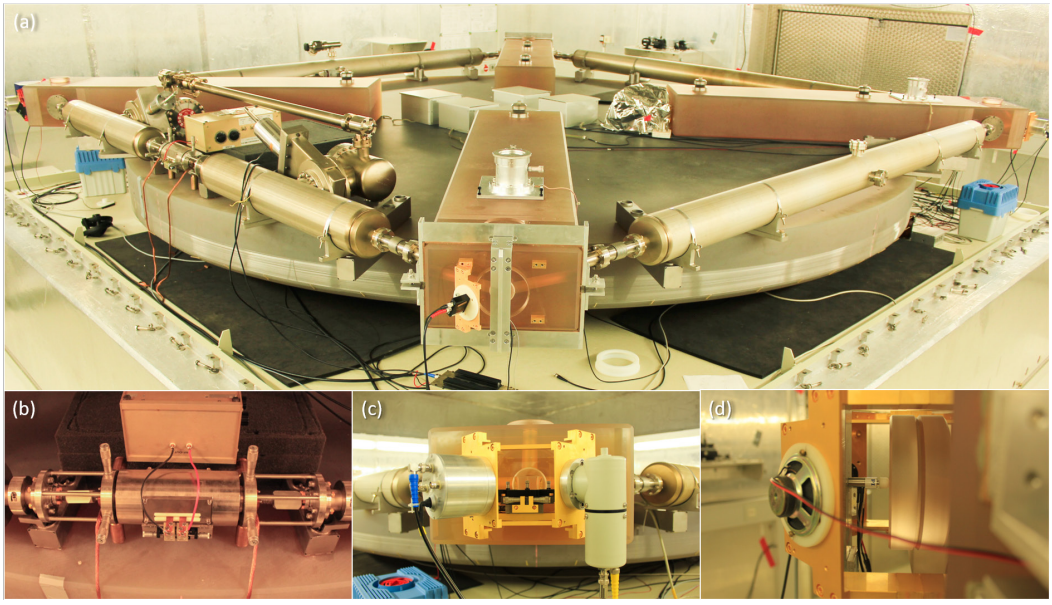

Figure. 1.2.: (a) The semi-monolithic structure of the G-ring laser gyroscope, (b) the laser excitation section, (c) the detection of δf_s by combining the counter-propagating beams through a prism, (d) mirror attached to Zerodur bar by molecular adhesion and the perimeter is actively controlled by means of feedback mechanism pressing on the back of the mirror plate.

As mentioned above, large ring laser gyroscopes are currently the only viable space geodetic measurement tool with a direct link to the Earth rotation axis. In order to achieve the goal of sub-centimetre point positioning, LoD estimations must be accurate to below 100 microseconds and the orientation of the rotational axis with respect to the Earth rotation must be better than an overall residual error of 0.01" in the two orthogonal directions. Today, the G ring laser offers the best overall performance of the large ring laser gyroscopes constructed. G is a semi-monolithic ring laser gyroscope with a total area of 16 m^2. The laser cavity is defined by four mirrors optically contacted to the end of four massive Zerodur bars arranged in a shape of a cross[5] on a 0.25 m thick base plate

[5]The cross-shaped arrangement is the design strategy to maximise the available area provided by the Zerodur base.

as shown in Figure 1.2 (a). G is located in an underground laboratory in Geodetic Observatory Wettzell, Germany. It is enclosed inside an ambient pressure stabilising vessel to counteract any mechanical perturbation to the laser cavity caused by atmospheric pressure and temperature changes [4]. The frequency fluctuations induced by cavity perimeter variation is compensated by locking the ring laser cavity to one spectral line of an optical frequency comb and have achieved an absolute optical frequency stability of 3 $\times 10^{-9}$ relative to Earth rotation [18].

The G ring laser now routinely measures the Chandler (a low frequency (26.6 nHz) free oscillation of the Earth) and annual wobbles (caused by tiny variations of the gravitationally induced torque due to the elliptical Earth orbit (31.7 nHz)) of the Earth [17]. A recent demonstration of the inclusion of single component G ring laser data into the VLBI analysis improved the estimate of the y-direction of the polar motion on average by 16% and the derivation of universal time by 12%, when compared to a VLBI only solution [19]. This demonstrates that high-resolution LoD measurement by large ring laser gyroscopes is achievable. When the long-term stability is further improved, G is at the threshold of meaningful contributions to the VLBI campaigns which precisely monitor LoD variations.

Ring laser gyroscopes have become routine tools in a sub-field of seismology - 'rotational seismology'[6]. The ability of ring laser gyroscopes to detect small rotational motions and their insensitivity to translation yields a new tool for seismologists to study seismic effects that cannot be measured with conventional seismometers. This has paved the way for the development of medium-scale ring lasers dedicated towards seismological studies within the GEO-technology program [20]. GEOsensor was constructed for research in rotational seismology and it is mounted on a rigid concrete slab in an underground laboratory at the Piñon Flat Seismological Observatory in Southern California, USA. The laser cavity is built with four turning mirrors located inside solid corner boxes and linked together by stainless steel tubes. The length of each arm is 1.6 m with a glass capillary of 4 mm inner diameter (located at the mid-section of two mirror corners) for laser gain medium excitation [21]. Another identical design to the GEOsensor, dubbed as PR-1, is currently located in Christchurch, New Zealand.

Furthermore, with regards to research in rotational seismology, the ROMY (ROtational Motions in seismologY) project is the latest ring laser project to have been commissioned. ROMY is the first 3D ring laser gyroscope in the world and it is buried 15 m underground at Fürstenfeldbruck, Munich, Germany [22] as shown in Figure 1.3. ROMY's tetrahedral structure is formed by four triangular ring laser gyroscopes. Three of the ring lasers having a side length of 12 m and one of the ring laser with a side length of 10 m. This 3D ring laser gyroscope has been principally designed to measure seismically induced

[6] Rotational seismology is a field of study that includes all rotational motions induced by seismic events such as earthquakes, explosions and ambient vibration.

rotational ground motion. ROMY was officially inaugurated in August 2017 and the current on-going effort is to develop active cavity stabilisation.

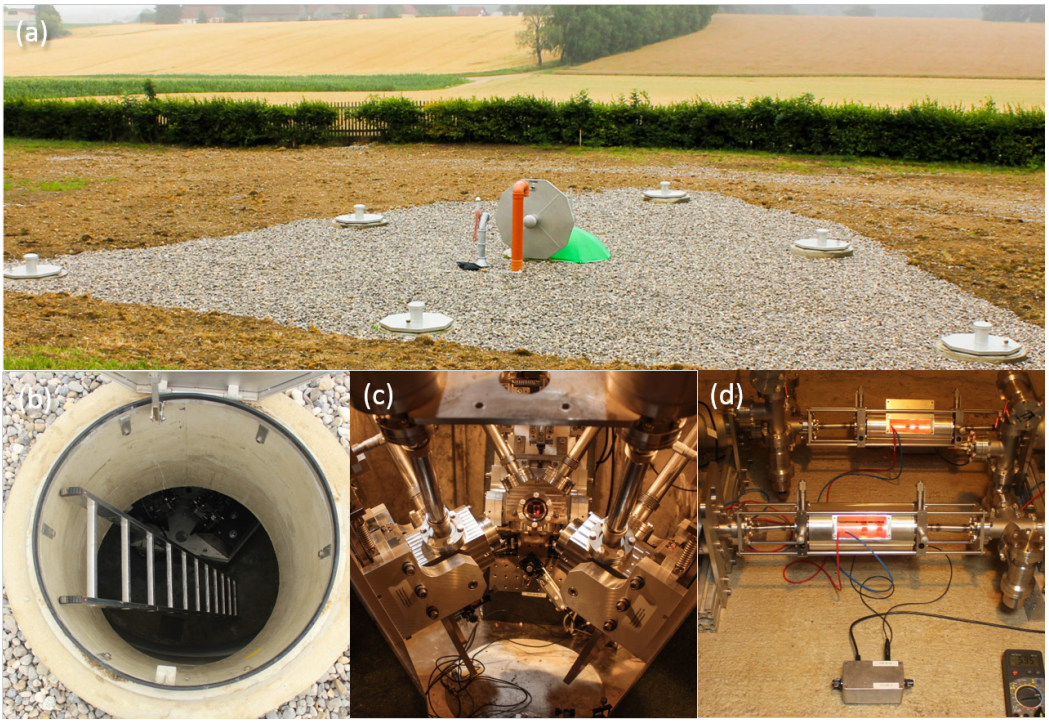

Figure. 1.3.: (a) ROMY is buried 15 m underground; (b) one of the access to the underground laser; (c) the corners of the North, West and East rings of ROMY; (d) laser gain tubes for gain medium excitation.

Further possible applications of ring laser gyroscopes are in tests of fundamental physics, in particular, the detection of general relativistic precessions such as the Lense-Thirring effect ('frame-dragging') [23], [24]. The Lense-Thirring effect was predicted in 1918 based on general relativity where the mass of a rotating object will drag the space-time around it in the same direction [25]. In consequence, any smaller object which is orbiting around the Earth will experience this frame-dragging precession due to the Earth's rotation [26]. VLBI measures the LoD with respect to the fixed stars. Hence, the relativistic precessions are in principle observable by looking for a small difference in the length of day determined by VLBI and an appropriate ring laser gyroscope installation. Therefore, a collaboration for terrestrial detection of the Lense-Thirring effect by ring laser gyroscopes in the Gran-Sasso Laboratories in Italy (denoted as GINGER (Gyroscopes IN GEneral Relativity)) has formed between the University of Pisa (Italy), Technical University of Munich (Germany) and the University of Canterbury (New Zealand) [27], [28].

G-Pisa is the first prototype towards realising GINGER [27]. It has a heterolithic design similar design to GEOsensor with an 'adjustable' dimension of 0.9 m × 0.9 m to 1.4 m × 1.4 m [29], [30]. GINGERino and GP-2 were two other ring laser gyroscopes being built as prototypes for GINGER [31], [32]. GINGERino has a side length of 3.6 m and it is mounted on a granite support. GINGERino is currently located in Laboratori Nazionali del Gran

Sasso (LNGS) to evaluate the environmental noise and stability of the underground laboratory. GP-2, on the other hand, is used as a blueprint for the development of active control strategies to prevent fluctuations of the laser cavity dimensions, which is crucial for GINGER operation in the future [32].

Table 1.1 summarises a number of constructed helium neon large ring lasers over the past 30 years. The gyroscopic characteristics as listed in the table were excerpted from refs. [17], [22], [29], [30], [33]–[38]. Note that the gyroscopic characteristic of the PR-1 ring laser quoted in this table is corresponding to it's initial performance as reported in ref. [33].

RLG	Location	Year Constructed (or of Operation)	δf_s (Hz)	A (m^2)	P (m)	FSR (MHz)	Ω_s (rad/s/$\sqrt{\text{Hz}}$)	Ω/Ω_E
C-I	New Zealand	1989	76.12	0.748	3.84	78.13	7.2×10^{-8}	-
C-II	New Zealand	1997	79.4	1	4	75	1.46×10^{-10}	4×10^{-7}
G-0	New Zealand	1997	288.6	12.25	14	21.43	1.16×10^{-11}	9×10^{-6}
AR-1[7]	USA	1997	511	84.5	40	7.5	-	-
G	Wettzell, Germany	2001	348.5	16	16	18.75	1.2×10^{-11}	3×10^{-9}
UG-1	New Zealand	2000	1512.63	367.5	77	3.896	1.71×10^{-11}	6×10^{-8}
PR-1	New Zealand	2005	113.5	2.56	6.4	46.875	1.5×10^{-9}	8.5×10^{-4}
GEOsensor	USA	2005	102.6	2.56	6.4	46.875	1.08×10^{-10}	-
UG-2	New Zealand	2005	2180	834	121.4	2.48	7.8×10^{-12}	4.5×10^{-8}
UG-3	New Zealand	2008	1512.63	367	77	3.896	-	-
G-Pisa	Italy	2008	111	1.96	5.4	53.57	$\sim10^{-9}$	2×10^{-5}
AR-2[7]	USA	2009	776.3	144.5	51	5.888	-	-
GINGERino	Italy	2014	280.4	12.96	14.4	20.83	1×10^{-10}	$\sim10^{-6}$
GP-2	Italy	2014	184	2.56	6.4	46.875	-	-
ROMY	Germany	2017	555[8]	72	36	8.33	-	-
			309[9]	50	30	10	-	-

Table. 1.1.: A summary of helium-neon based large ring laser gyroscopes constructed since the first demonstration of Earth rotation sensing by C-I large ring laser in 1989. The table lists the location of the ring laser, the year of construction (or of operation), the Sagnac frequency, δ_{fs}, the area (A) and the laser perimeter (P), the free spectral range (FSR), the raw sensitivity (Ω_s) and the relative Allan deviation (Ω/Ω_E, see Section 2.3.4).

1.3 Motivation and Research Objective

Technical advances in ring laser physics at Canterbury have been instrumental in pushing the sensitivity of large-scale ring laser gyroscope towards 10^{-9} of Earth rotation (Ω_E). In order to further improve the resolution of large ring laser gyroscopes, the size of Canterbury's ring laser gyroscopes have evolved from 1 m^2 up to 834 m^2. The reason is, if we refer to Equation 1.1: the beat frequency, δf_s obtained from a ring laser gyroscope is proportional to the scale factor, S = $\frac{4A}{\lambda P}$, the rotational velocity, and the orientation of the laser's normal vector relative to the rotation axis [39]. As the perimeter of the laser structure increases, the area enclosed by the counter-propagating beams will increase

[7] AR-1 and AR-2 are triangular ring lasers having Brewster-angled window gain section.
[8] Three vertically mounted RLGs, denoted as the East, the West, and the North rings.
[9] One of the ring laser is mounted horizontally.

as well. Thus, the scale factor increase leads to an increase in the rotational sensitivity. Although UG-2 achieved the highest raw sensitivity of 7.8×10^{-12} rad/s/$\sqrt{\text{Hz}}$, it was limited by the demanding requirements on the mirror uniformity and the mechanical stability of the device.

An alternative approach is to operate the ring laser gyroscope at different lasing wavelengths because the scale factor of the ring laser depends on the operating wavelength as well. So far, Canterbury's ring laser gyroscopes have operated solely on the 632.8 nm transition of the helium-neon gain medium. Hence, using different laser wavelengths will provide new insight on how to obtain better performance from our laser gyroscopes.

The first successful operation of a continuous wave (CW) laser was achieved with an infrared transition of the helium-neon gain medium. Javan, Benett and Herriot reported their achievement soon after Maiman's first laser action (by using ruby) demonstration [40]. However, helium-neon laser commonly operates at 632.8 nm because it is the highest gain transition available in the visible region of the electromagnetic spectrum. Table 1.2 lists other laser transitions of the helium-neon system. As mentioned earlier, the first ring laser gyroscope in the world was built by Macek and Davis. Their laser gyroscope operated on the 1152.3 nm transition of helium-neon [9]. This wavelength corresponds to the $2s_2 \rightarrow 2p_4$ neon transition. This infrared transition shares the same lower state as that of the 632.8 nm transition. Macek and Davis' gyroscope did not unlock on the bias provided by the Earth rotation. Nowadays, with much improvement in supermirror technology, it is possible to repeat this work with a significantly better result.

There are four other laser transitions that share the same upper state as the 632.8 nm transition [41]. Although the gain[10] at these other transitions is relatively low compared to the 632.8 nm transition, additional total gain may be supplied by lengthening the gain tube or installing multiple gain tubes within the laser cavity. The shortest wavelength is at 543.4 nm which corresponds to the neon $3s_2 \rightarrow 2p_{10}$ transition and was first reported in 1971 [46]. With a ring laser gyroscope operating on the 543.4 nm transition, the scale factor will directly increase by 17%.

All experimental work in this research will be performed on the PR-1 ring laser gyroscope. It is a medium-sized ring laser gyroscope currently mounted vertically on the second floor of the West Rutherford building of University of Canterbury. Since PR-1 is a heterolithic device, its performance is limited by mechanical fluctuations. This perimeter instability is a major drawback for obtaining a highly stable rotation sensing because the laser has a tendency to mode hop. These changes in the cavity perimeter should be compensated

[10] The gain is affected by the laser tube construction, helium to neon gas ratio, total pressure as well as the discharge power. Thus, there are slight variations in relative gain quoted between refs. [42], [43],[44] and [45].

Wavelength λ (nm)	Lasing Transition (Paschen Notation)	Gain (relative to 632.8 nm)
543.4	$3s_2 \rightarrow 2p_{10}$	1/17
593.9	$3s_2 \rightarrow 2p_8$	1/15
604.6	$3s_2 \rightarrow 2p_7$	1/10
611.8	$3s_2 \rightarrow 2p_6$	1/5
632.8	$3s_2 \rightarrow 2p_4$	1
1152.3	$2s_2 \rightarrow 2p_4$	4/5
1152.5	$2s_4 \rightarrow 2p_7$	-
1523.1	$2s_2 \rightarrow 2p_1$	-
3391.2	$3s_2 \rightarrow 3p_4$	44/1

Table. 1.2.: Neon transitions, corresponding energy level notation and gain relative to 632.8 nm [42].

by means of an active control with the use of piezoelectric actuators that move the laser mirrors symmetrically along a diagonal of the ring to stabilise the cavity length [47].

A feedback system will be provided by mixing the single beam output from PR-1 with the output from a linear frequency-stabilised helium-neon laser, taking advantage of the increase in the available power of the 632.8 nm laser output. Other than that, the option of operating the laser on multiple phase-coupled longitudinal modes yielding a stable Sagnac beat frequency will be explored. The frequency difference between adjacent longitudinal modes is heterodyned with a reference frequency generated by a GPS-locked radio frequency (RF) generator and the resulting beat note will provide the error signal to the piezo-actuator controller [48].

1.4 Thesis Structure

Chapter 2

In Chapter 2, we introduce the basic physics of ring laser gyroscopes and various effects that limit the performance of a ring laser. Following this, an overview of the helium-neon laser system in the context of a large ring laser gyroscope is outlined. Then, we describe the operational principles and techniques applied to characterise the gyroscopic performance of a large ring laser.

Chapter 3

This chapter begins with the description of the technical and mechanical designs of a 2.56 m^2 ring laser, denoted as PR-1, which was used as a test cavity in this thesis. As large-sized helium-neon based ring laser gyroscopes typically operate on the $3s_2 \rightarrow 2p_4$ neon transition at the wavelength of 632.8 nm, in the second part of this chapter, we present the experimental works to characterise the gyroscopic performance of PR-1 at this wavelength. This is essential to provide a reference point for comparison with its performance with the other neon transitions.

Chapter 4

We revisit the seminal Macek and Davis experiment in Chapter 4 and operate the PR-1 ring laser at 1152.3 nm (the $2s_2 \rightarrow 2p_4$ neon transition). In this chapter, the gyroscopic performance of a ring laser employing crystalline (GaAs/AlGaAs) coated fused silica supermirrors in the test cavity is investigated.

Chapter 5

Chapter 5 presents a study of frequency up-scaled large gyroscopes. The first part of this chapter mainly outlines the process of modifying the test cavity and designing a new impedance matching unit. Then, the experimental work to demonstrate gyroscopic operation on the 611.8 nm ($2s_2 \rightarrow 2p_6$) and 543.4 nm ($3s_2 \rightarrow 2p_{10}$) neon transitions is presented. The implications and limitations of ring laser operation at shorter wavelengths are discussed in the final section of this chapter.

Chapter 6

In Chapter 6, we describe the preliminary efforts to stabilise the PR-1 optical frequency by actively control the laser perimeter with two piezo-actuators. The first part of this chapter focuses on the experimental details of a cavity stabilisation technique using the beat frequency between adjacent longitudinal modes as the feedback signal. In the second part of this chapter, we outline work towards realising a PR-1 frequency stabilisation scheme which involves a frequency stabilised linear laser as reference.

Chapter 7

Chapter 7 details the key results from this work and discuss the limitations and possible implications arising from this study. This chapter also presents recommendations for future work and concludes the body of this thesis.

2 Helium-Neon Ring Laser Gyroscopes

In this chapter, the essential background material required to understand the operation of a ring laser gyroscope is reviewed. This chapter begins with a brief derivation of Sagnac effect. Readers who are interested in a detailed description of the Sagnac effect can refer to refs. [49], [50], and [10] [51]. The second part of this chapter will focus on the helium-neon laser system which includes the excitation mechanism and a general review on the various neon transitions. Finally, the criteria used to characterise the performance of a large ring laser gyroscope will be explained.

2.1 The Sagnac Effect

The operation of a ring laser gyroscope is based on the Sagnac effect, which was discovered by George Sagnac in 1913 [7]. The Sagnac effect can be illustrated by an idealised circular interferometer with radius, R as shown Figure 2.1.

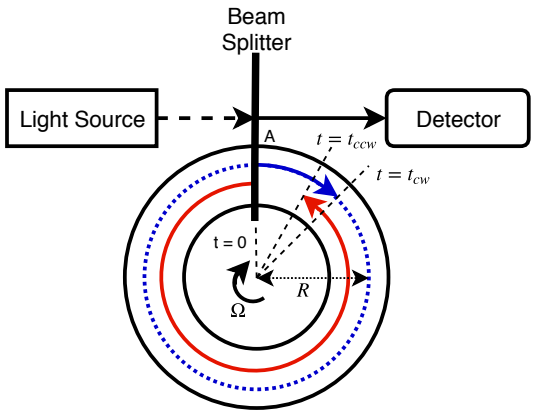

Figure. 2.1.: Simplified Sagnac interferometer diagram.

When light enters the interferometer from point A, it will be split into two oppositely directed beams which propagate around the ring cavity and are denoted as the clockwise beam (CW) and the counter-clockwise beam (CCW). If the interferometer is not rotating, these two beams will be recombined at point A after completing a total path length of $2\pi R$, within a time,

$$t = \frac{2\pi R}{c}, \tag{2.1}$$

where, c is the speed of light. If the interferometer is being rotated clockwise, with angular velocity, Ω, about an axis through the centre and perpendicular to the plane of the interferometer, the CW beam will take a longer time to arrive at the starting point compared to the CCW beam. This phenomenon occurs because the starting point of the two beams has changed after the two beams departed from point A. Therefore, the travel time for the CW beam, t_{cw}, can be represented as,

$$\begin{aligned} t_{cw} &= \frac{2\pi R + R\Omega t_{cw}}{c} \\ &= \frac{2\pi R}{c}\left(1 - \frac{R\Omega}{c}\right)^{-1}, \end{aligned} \tag{2.2}$$

where, $R\Omega t_{cw}$ is the arc length (or the extra path) which the CW beam has to travel before it arrives at point A. On the other hand, the CCW beam will travel a lesser distance than the arc length represented as $R\Omega t_{ccw}$. The CCW beam's travel time is

$$\begin{aligned} t_{ccw} &= \frac{2\pi R - R\Omega t_{ccw}}{c} \\ &= \frac{2\pi R}{c}\left(1 + \frac{R\Omega}{c}\right)^{-1}. \end{aligned} \tag{2.3}$$

The time difference, δt, between the two beams can be represented as

$$\begin{aligned} \delta t &= t_{cw} - t_{ccw} \\ &= \frac{2\pi R}{c}\left[\left(1 - \frac{R\Omega}{c}\right)^{-1} - \left(1 + \frac{R\Omega}{c}\right)^{-1}\right] \\ &= \frac{4\pi R^2\Omega}{c^2 - (R\Omega)^2}. \end{aligned} \tag{2.4}$$

The values of R and the angular velocity, Ω are much smaller than the speed of light, c, ($(R\Omega)^2 \ll c^2$), thus, Equation 2.4 can be simplified to:

$$\delta t \approx \frac{4\pi R^2\Omega}{c^2}. \tag{2.5}$$

Then, Equation 2.5 can be used to calculate the round-trip optical path difference, δP,

$$\delta P = c\delta t = \frac{4\pi R^2\Omega}{c}. \tag{2.6}$$

By referring to the general approach for an arbitrary-shaped interferometer in ref. [39] and the analysis based on Stoke's theorem in ref. [52], Equation 2.6 can be re-written in a general form for any arbitrary shape and configuration as,

$$\delta P = c\delta t = \frac{4A\vec{n}\cdot\vec{\Omega}}{c}, \tag{2.7}$$

where $A = \pi R^2$ is the area enclosed by the two beams and $\vec{n}$ is a unit vector normal to the surface of the interferometer.

For a light source with a wavelength, λ and frequency, $f = c/\lambda$, the phase difference, $\delta\psi$, between the two beams after one round trip can be written as,

$$\delta\psi = 2\pi f \delta t = \frac{8\pi A\vec{n}\cdot\vec{\Omega}}{\lambda c}. \tag{2.8}$$

This simplified version of Sagnac effect analysis is perfectly valid but incomplete. A complete analysis to describe the Sagnac effect is based on general relativity [10], though an approximation by using special relativity would yields the same result as well.

In the context of special relativity, the time difference observed at the beam splitter in Figure 2.1 as observed from a stationary reference frame is represented by Equation 2.4. For a rotating (moving) reference, the time difference as observed by the moving beam splitter (or point A, as it rotates along with the interferometer) is dilated by a factor, γ,

$$\delta t_{BS} = \delta t/\gamma = \frac{4\pi R^2\Omega}{\gamma(c^2 - (R\Omega)^2)}. \tag{2.9}$$

Following the analysis by [53] as described in ref. [50], Equation 2.9 can be evaluated by transforming the line element to a rotating frame of reference. The line element of an inertial frame in cylindrical coordinates is,

$$ds^2 = c^2dt^2 - dr^2 - r^2d\Theta^2. \tag{2.10}$$

For the rotating frame of reference, Equation 2.10 is converted into,

$$ds^2 = \gamma^2c^2dt'^2 - dr'^2 - r^2(d\Theta' + \gamma\Omega dt')^2, \tag{2.11}$$

by the transformation,

$$\begin{aligned} dt &= \gamma dt', \\ dr &= dr', \\ d\Theta &= d\Theta' + \gamma dt'. \end{aligned} \tag{2.12}$$

The line element is cancelled for free space propagation. The spatial trajectory of the counter-propagating beams is circular and occurs at $r' = R$, therefore, $dr' = 0$. Equation 2.11 becomes,

$$ds^2 = \gamma^2c^2dt'^2 - R^2(d\Theta' + \gamma\Omega dt')^2 = 0. \tag{2.13}$$

Equation 2.13 is a quadratic expression in the time element, dt' and has the roots,

$$dt'_{cw,ccw} = \pm Rd\Theta'/\gamma(c \mp \Omega R), \tag{2.14}$$

with respect to the CW and CCW beams. The time taken for the CW and CCW beams to travel in a full circumference of the interferometer can be obtained by integrating Θ' from $0 \rightarrow 2\pi$ and $0 \rightarrow -2\pi$ correspondingly,

$$\begin{aligned} t'_{cw} &= \frac{2\pi R}{\gamma(c-\Omega R)}, \\ t'_{ccw} &= \frac{2\pi R}{\gamma(c+\Omega R)}, \end{aligned} \tag{2.15}$$

by assuming γ is independent of the angle Θ'. As a result, the time difference between the two beams for the rotating frame of reference at the beam splitter is,

$$t'_{cw} - t'_{ccw} = \delta t_{BS} = \frac{4\pi R^2}{\gamma(c^2 - \Omega^2 R^2)}, \tag{2.16}$$

which is identical to Equation 2.9.

Applying the expression for time dilation, $\gamma = \left[1 - \left(\frac{\Omega R}{c}\right)^2\right]^{-1/2}$, into Equation 2.9, one obtained,

$$\begin{aligned} \delta t_{BS} &= \frac{4\pi R^2}{c^2}\left[1 - \left(\frac{\Omega R}{c}\right)^2\right]^{-1/2} \\ &= \frac{4\pi R^2 \Omega}{c\sqrt{c^2 - R^2\Omega^2}}. \end{aligned} \tag{2.17}$$

Then, the Sagnac phase difference detected is,

$$\delta\psi = 2\pi f \delta t_{BS} = \frac{4\pi R^2 \Omega}{c\sqrt{c^2 - R^2\Omega^2}}, \tag{2.18}$$

where, $A = \pi R^2$ is the area travelled by the two light beams, $f = c/\lambda$ is the frequency of the light beams travelling the rotating reference frame and $2\pi f$ is the angular frequency of the light source. Note that, Since $R\Omega \ll c$, thus, Equation 2.18 can be simplified to,

$$\delta\psi = \frac{8\pi A\Omega}{\lambda c^2}, \tag{2.19}$$

where a similar expression to Equation 2.8 is obtained. The author suggests the readers to refer to refs. [50], [54] and [55] for a fuller derivation of the Sagnac effect based on the theory of special relativity and refs. [10], [50] and [54] for excellent reviews on the Sagnac effect from different point of views.

In the case of a rotating active ring laser interferometer, the optical path difference between the two counter-propagating beams from Equation 2.7 translates into a frequency shift rather than a phase shift. The optical frequencies of the CW and CCW beams are nominally independent from each other where their resonance frequencies are deter-

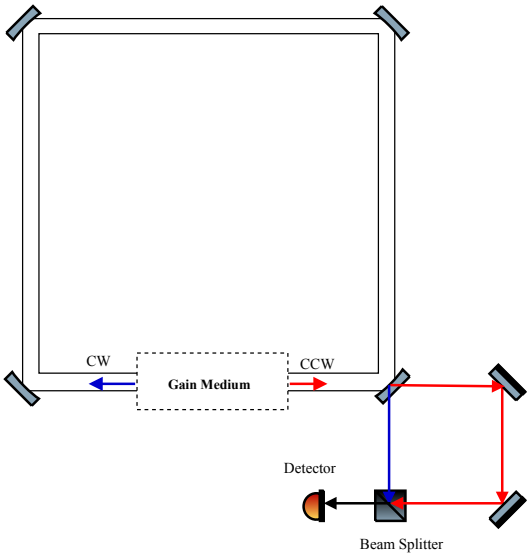

Figure. 2.2.: Schematic representation of a square ring laser configuration.

mined by their optical path lengths. To satisfy the condition of a resonant cavity, a laser cavity will sustain an integer number, m, of wavelengths, λ, to fit in the optical path, P:

$$m\lambda = P. \tag{2.20}$$

The frequency of the CW beam, f_{cw}, and CCW beam, f_{ccw}, can be denoted as

$$f_{cw,ccw} = \frac{mc}{P_{cw,ccw}}, \tag{2.21}$$

where P_{cw} and P_{ccw} are the effective cavity lengths experienced by the CW and CCW beams respectively. Assuming both beams are operating on the same longitudinal mode index, the frequency difference is,

$$\begin{aligned} \delta f = f_{cw} - f_{ccw} &= \frac{mc}{P_{cw}} - \frac{mc}{P_{ccw}} \\ &= \frac{mc\delta P}{P^2} = f\frac{\delta P}{P}, \end{aligned} \tag{2.22}$$

where,

$$\delta P = P_{ccw} - P_{cw} \tag{2.23}$$

and

$$P_{cw} \times P_{ccw} = P^2. \tag{2.24}$$

By substituting Equation 2.7 into Equation 2.22, the Sagnac frequency, δf_s, is obtained as,

$$\delta f_s = \frac{4A}{\lambda P}\vec{n}\cdot\vec{\Omega}. \tag{2.25}$$

The scale factor, S, is determined by the area A traversed by the laser beams, the perimeter P of the cavity and the optical wavelength λ. From Equation 2.25, the beat frequency is proportional to S and to the angular rate of the cavity, Therefore, S determines the resolution of the measured signal.

2.1.1 Non-ideal Ring Laser Gyroscopes

Intra-cavity biases and non-reciprocities in ring laser gyroscopes cause the measured δf_s to differ from the ideal δf_s obtained from Equation 2.25. As such, Equation 2.25 can be written in a more general form as:

$$\delta f_s = S(1 + K_a)\vec{n} \cdot \vec{\Omega_E} + \delta f_0 + \delta f_{bs}, \tag{2.26}$$

where, $S = \frac{4A}{\lambda P}$ is the scale factor, K_a is a constant term that arises from the shifting of the scale factor, δf_0 takes into account a frequency difference for zero rotation rate and giving rise to a null shift error while δf_{bs} represents the backscattering effect [56], [57].

Scale Factor Shift

The term, K_a from Equation 2.26 characterises the contribution of active gain medium to the scale factor. The fluctuations of laser parameters such as gain, gas temperature, pressure, losses and frequency detuning will cause dispersion and introduce a change in the optical frequency of the counter-propagating beams [56]. At the lasing threshold, dispersion varies linearly with the optical frequency of the laser beams. The laser modes will be pulled closer and this effectively will reduce the value of δf_s.

Moreover, scale factor shifts are commonly caused by small changes in the geometry of the laser cavity. The geometry of ring laser gyroscopes mounted on any rigid structure such as a concrete monument vary with the thermal expansion of the base structure. In order to minimise this effect, monolithic ring laser gyroscopes such as C-II and G ring lasers are constructed on low expansion Zerodur blocks in order to maintain the scale factor stability. For heterolithic ring laser gyroscopes, active feedback can be implemented to maintain the laser perimeter. For example, the perimeter of G-Pisa is actively controlled by moving two opposite cavity mirrors symmetrically along the cavity diagonal to increase the gyroscope's long term stability against environmental temperature fluctuations [58].

Null Shift

An example of a null shift effect in ring lasers is Langmuir flow in the discharge tube within which region the gain medium is being excited. Langmuir flow usually occurs in a DC excited plasma where it causes a flow of gas toward the cathode along the centre of the gain-tube and towards the anode along the walls [56], [59]. This net flow of gas will produce a bias in the velocity distribution of the atoms of the gas which leads to a shift in gain and the dispersion curve for the counter-propagating beams [59]. Typically in commercial small ring laser gyroscopes, the null shift is cancelled by introducing two discharge tubes where their individual discharge polarity is opposite to one another. Since Langmuir flow is a prominent error source in DC excited lasers, radio frequency (RF) excitation is employed by most large ring laser gyroscopes to avoid this effect [17].

Null shift errors also arise due to non-reciprocal losses in the active laser medium. Different loss mechanisms lead to different mode pulling coefficients for either beam, which gives rise to a shifted δf_s. Other than that, the intensities of the counter-propagating beams are normally unequal. The frequency pushing effects which arise from different beam intensities will also give rise to a difference in the optical frequency of the laser beams, hence, shifting δf_s.

Backscatter and Frequency Lock-in

In an ideal case, the counter-propagating beams within the cavity are absolutely independent of one another. However, due to cavity mirror imperfections, backscattering may arise and this results in coupling between the two beams. When δf_s falls below a critical value, the ring laser gyroscope becomes insensitive to rotation because the optical frequencies become degenerate. As stated in [56], the Sagnac frequency will vanish if the rotation rate falls below a threshold value of,

$$f_L = \frac{c\lambda^2 r_s}{32\pi A d}, \tag{2.27}$$

where f_L is the lock-in threshold value, c is the speed of light, A is the area enclosed by the cavity, r_s is the total fractional scattered intensity (to indicate the degree of the backscatter contribution from the mirror) and d is the diameter of the laser beam. r_s is approximately:

$$r_s = \sqrt{\frac{z_{1,2}^2 16 d^2}{\lambda^2}}, \tag{2.28}$$

where, $z_{1,2} \approx m_{1,2}\delta f_s \frac{\pi P}{c}$ is the backscatter fractional amplitude coupling and $m_{1,2}$[1] is the fractional amplitude of the laser beam. In order to reduce the lock-in effect, the area enclosed by the ring laser cavity can be increased. Comprehensive backscatter analyses to provide solutions for such errors in ring laser gyroscopes have been performed in refs. [10], [60]. The frequency offset due to backscattering can be expressed as,

$$\delta f_{bs} = \frac{c}{2P}(k_2 \sin(\psi - \epsilon_2) + k_1 \sin(\psi + \epsilon_1)), \tag{2.29}$$

where ψ is the phase of the detected Sagnac signal, $\epsilon_{1,2}$ are the backscatter phase angles and $k_{1,2}$ are the backscatter amplitudes of the respective beam, where,

$$k_{1,2} = \frac{r_s \lambda}{4d}\sqrt{\frac{I_{1,2}}{I_{2,1}}}, \tag{2.30}$$

with $I_{1,2}$ as the intensities of the counter propagating beams.

2.2 Helium-Neon Lasers

Ring laser gyroscopes commonly employ helium-neon gas as the laser medium. The laser cavity is filled with a fixed ratio of helium to neon gas inside an optical cavity and the gain medium is excited to produce laser oscillation at 632.8 nm. Most published reports on the helium-neon system use the Paschen spectroscopic notation to denote atomic energy levels. A schematic energy diagram of the helium-neon system and laser transitions is given in Figure 2.3. Table 2.1 lists the relevant energy levels in electron Volts (eV).

2.2.1 Laser Excitation Mechanism

The helium-neon laser employs a binary gas mix with one component having a metastable state energy near resonance with the excited state of the second gas. This provides a large cross section for inelastic collisions to transfer excitation from the donor atom to the acceptor atom in the excited state. Helium has two metastable energy levels, denoted as 2^1S and 2^3S. These two levels are located approximately 20.61 eV and 19.8 eV above the helium ground level. When an RF electric field (radio frequency discharge typically between 20 - 100 MHz) is applied to the laser gain tube, free electrons accelerate and collide with un-excited helium atoms. This process leads to excitation of the helium atoms up to the requisite metastable levels.

$$\text{He}\,(^1S_0) + \text{e} \rightarrow \text{He}\,(2^1S_0 \text{ or } 2^3S_3)$$

[1] Also known as the monobeam modulation: a single beam amplitude modulation due to the backscattered light from the other beam. $m_{1,2}$ is estimated by dividing the AC signal to the DC signal from a photodetector that measures the single laser beam.

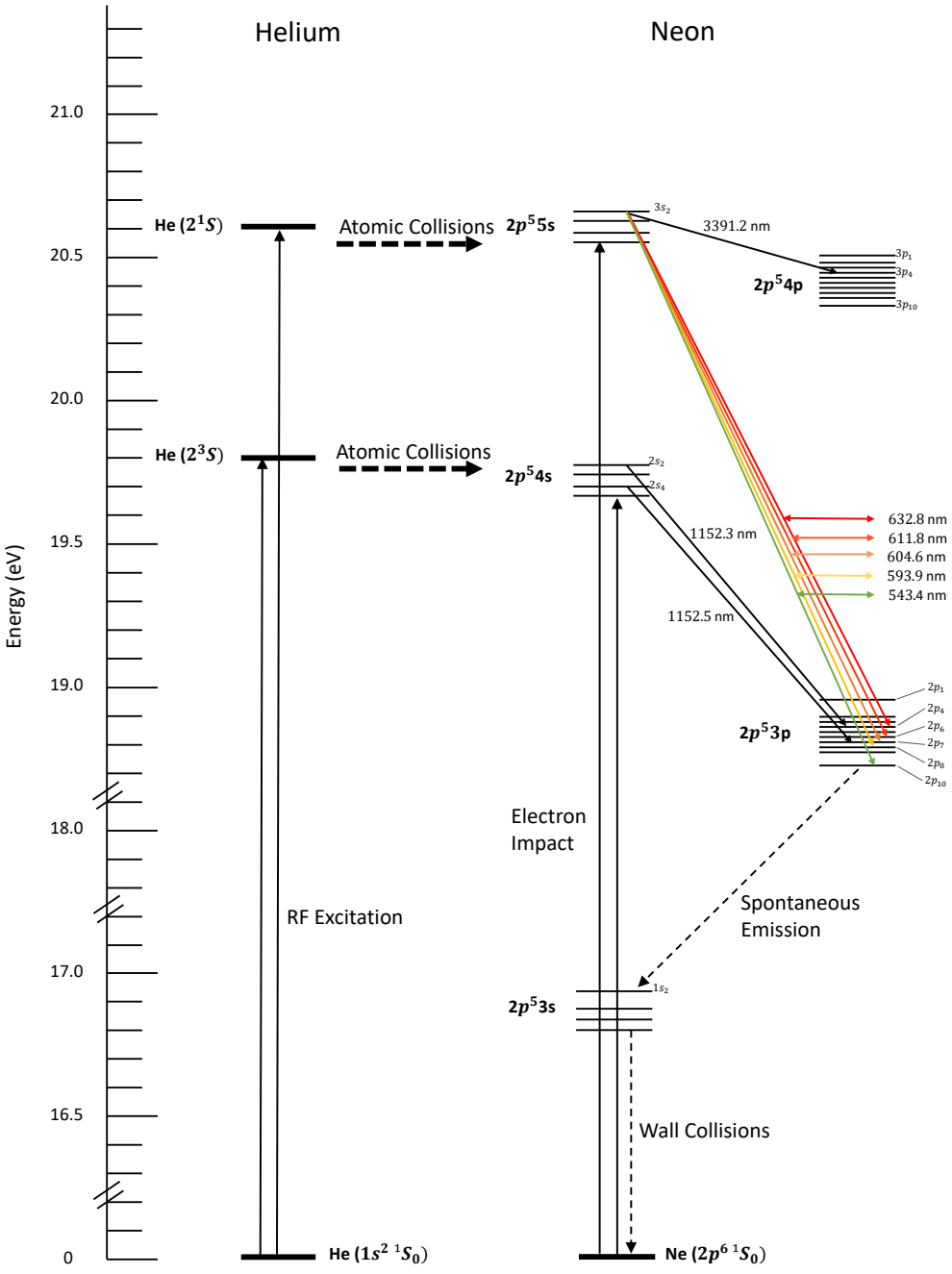

Figure. 2.3.: Schematic energy level diagram of the helium-neon laser system reproduced from [64], [65]

Paschen	Energy Level (eV)	Lifetime (ns)
Ground	0	-
$1s_5$	16.6214312	-
$1s_4$	16.6731888	22
$1s_3$	16.7177544	-
$1s_2$	16.8504468	16
$2p_{10}$	18.3842028	<20
$2p_9$	18.557716	17
$2p_8$	18.5788208	16
$2p_7$	18.6153264	<13
$2p_6$	18.6394072	13
$2p_5$	18.6959884	<11
$2p_4$	18.706702	12
$2p_3$	18.7140056	<13
$2p_2$	18.7290096	<10
$2p_1$	18.9686148	<8
$2s_5$	19.6667844	110
$2s_4$	19.690952	98
$2s_3$	19.7633556	160
$2s_2$	19.7825384	96
$3p_4$	20.3001144	120
$3s_5$	20.5629324	78
$3s_4$	20.5734352	26
$3s_3$	20.6594292	10
$3s_2$	20.665654	55

Table. 2.1.: Energy levels of neon extracted from Moore's atomic energy levels [61] and relevant energy level lifetimes measured by Bennet et al. [62] and Eletskii et al. [63].

Following excitation, excited helium atoms collide with un-excited neon atoms promoting them to the 4s and 5s excited states.

$$\text{He}\,(2^1S_0) + \text{Ne}\,(^1S_0) \rightarrow \text{He}\,(^1S_0) + \text{Ne}\,(2p^5 5s) + \Delta E_1$$
$$\text{He}\,(2^3S_1) + \text{Ne}\,(^1S_0) \rightarrow \text{He}\,(^1S_0) + \text{Ne}\,(2p^5 4s) + \Delta E_2$$

Note that the energy differences, ΔE_1 and ΔE_2 between the helium and neon excited states are necessarily small. By referring to Table 2.1, the lifetimes of $5s$ level ($3s_2$) and $4s$ level ($2s_2$) are 55 ns and 96 ns respectively. The long lifetime of these two energy states allows population inversion to occur. The subsequent decay of neon atoms from the $5s$ and $4s$ levels to the $3p$ states leads to the emission of radiation at various wavelengths. Laser amplification occurs when there is sufficient gain to overcome optical losses in the cavity.

The first gas laser was the helium-neon laser, demonstrated by Javan, Bennet and Herriot in 1961 [40]. They obtained laser action in the near infrared regime. The strongest laser

transition among the observed laser transitions was at 1152.3 nm and this arises from stimulated emission between the $2s_2 \rightarrow 2p_4$ neon levels, whose population inversion is enhanced by energy transfer from the 2^3S_1 helium level. The laser cavity was filled with 0.1 torr of neon and 1 torr of helium inside a 0.8 m quartz tube having a 1.5 mm internal diameter. The discharge was achieved by coupling RF power to the tube by external electrodes. The laser mirrors were planar, fixed at each end of the amplifier tube.

The most recognisable helium-neon laser output wavelength occurs at 632.8 nm. Laser amplification at this wavelength corresponds to the $3s_2 \rightarrow 2p_4$ neon transition. The first report of lasing at this wavelength was obtained by White and Rigdon [66]. They reported laser oscillation with a 10:1 mix ratio of helium to neon gas at a total pressure of 0.7 torr. The discharge was excited by a DC power supply and the laser cavity employed Brewster angled internal windows with external mirrors. In this case, the upper state of the lasing transition ($3s_2$) has about ten times longer lifetime than that of $2p_4$ (see Table 2.1). The neon atom stays in the terminal state of the lasing transition before spontaneously decaying to the 3s level. Note that the $3s$ level is also metastable and loses its energy by colliding with the gain tube walls. Re-population of the 3s level may result from: (1) electron collision excitation of the $3p$ level from the $3s$ level, or (2) re-absorption of a photon emitted by atoms in the lower level due to radiation trapping[2]. Therefore, to increase laser power at 632.8 nm, the diameter of the gain tube is normally small and the gas pressure has to be low so that the frequency of wall collisions is increased.

The $3s_2 \rightarrow 3p_4$ transition at 3391.2 nm shares a common upper level with 632.8 nm. Lasing at this wavelength was first reported by Bloom et al. [67] and it has higher gain due to its longer lifetime and longer wavelength (as laser gain is proportional to λ^2; if Doppler broadening dominates, gain is proportional to λ^3). As a result, the transition at 3391.2 nm has a tendency to dominate and depletes gain at 632.8 nm. To prevent oscillation at 3391.2 nm, a glass window can be added to the laser cavity to introduce more loss at longer wavelengths. Alternatively, lower mirror reflectivity at 3391.2 nm could also be used. In long helium-neon lasers, a methane cell can also be employed to absorb radiation at 3391.2 nm. A further alternative is to induce line-broadening at the transition via the application of a small magnetic field, thereby reducing the peak gain. The effect of a magnetic field on the 632.8 nm transition is small due to its broad Doppler linewidth.

Laser oscillation on other neon transitions that share the same upper state ($3s_2$) with the 3391.2 nm and 632.8 nm transitions can be achieved by introducing additional loss to these higher gain transitions[3]. By incorporating a prism into the laser cavity, Bloom observed laser action at 640.1 nm, 629.3 nm and 611.8 nm which corresponds to transitions from $3s_2$ to the $2p_2$, $2p_5$ and $2p_6$ levels respectively [69]. The total gas pressure

[2] Radiation emitted by one atom is absorbed by another atom in the lower state.

[3] We also employed mirrors that introduces higher losses on wavelengths other than 632.8 nm in our large laser cavities [68].

utilised in this study was 0.5 torr with an 80% helium and 20% neon gas mix. The gain tube was 3 m long with an internal diameter of 4 mm. The incorporation of a prism[4] was used to suppress the 3391.2 nm transition and allow maximum gain at 632.8 nm.

Following Bloom's method to suppress oscillation at 3391.2 nm, White and Ridgen [44] successfully observed lasing at wavelengths of 640.1 nm ($3s_2 \rightarrow 2p_2$), 635.1 nm ($3s_2 \rightarrow 2p_3$), 632.8 nm ($3s_2 \rightarrow 2p_4$), 629.3 nm ($3s_2 \rightarrow 2p_5$) and 611.8 nm ($3s_2 \rightarrow 2p_6$). Moreover, when prisms were added to the cavity as spectrally selective elements, they observed lasing at 604.6 nm ($3s_2 \rightarrow 2p_7$) and 593.9 nm ($3s_2 \rightarrow 2p_8$). The total length of the discharge tube used in their experiment was 2 m long, having a diameter of 3 mm.

Franke et al. [70] also reported simultaneous laser action from $3s_2$, to six different $3p$ levels with a 530 mm long helium-neon discharge. By using a broadband mirrors (610 nm - 650 nm) with 0.5% transmitivity at 632.8 nm, they observed lasing at wavelengths of 611.8 nm, 629.3 nm, 632.8 nm, and 635.1 nm simultaneously. Lasing at wavelengths of 604.1 nm and 593.9 nm was also observed but with a different set of mirrors. Infrared wavelengths were suppressed by means of a Brewster angled window.

The shortest wavelength laser transition available in the helium-neon system is $3s_2 \rightarrow 2p_{10}$ transition at 543.4 nm. Laser action at this wavelength was first reported by Perry [46]. Perry utilised a 0.65 m long, 4 mm diameter tube with a 7:1 helium to neon mixture ratio at a total pressure of 1 torr. The excited discharge was 0.51 m long. The laser cavity was first aligned by getting the laser to oscillate at 611.8 nm. Then, the mirrors were replaced by mirrors coated for high reflectivity at 520 nm and about 18% reflectively at 594 nm to achieve laser action at 543.4 nm. The available gain at this transition is about 30 times smaller than the gain at 632.8 nm [45]. This is due to the higher population density of $2p_{10}$ which results from its higher excitation cross section.

Laser action is also possible for a pure neon discharge without the transfer of energy from excited helium atoms. Enough gain can be obtained by direct electron impact in a gaseous discharge where electric power accelerates the electrons and these fast moving electrons will collide with the neon atoms giving rise to the following transitions:

$$\text{Ne}\ (2p^6\ {}^1S_0) + \text{e} \rightarrow \text{Ne}\ (2p^5 5s) + \text{e}$$
$$\text{Ne}\ (2p^6\ {}^1S_0) + \text{e} \rightarrow \text{Ne}\ (2p^5 4s) + \text{e}$$

The excited neon atom (Ne $(2p^5 4s)$ or Ne $(2p^5 4s)$) can lose energy by stimulated emission due to radiation trapping. By referring to Table 2.1, the lifetimes at $3p$ are shorter than

[4]The dispersion provided by the prism at 632.8 nm transition is about 0.0762 m per 10 nm. Therefore, by carefully re-positioning the mirror with a narrow aperture, the three wavelengths (i.e. 640.1 nm, 629.3 nm and 611.8 nm) were observed.

that of the $5s$ and $4s$ levels, which allows a population inversion to be achieved. Neon lasers typically operate with 0.2 torr of gas pressure or below. For instance, with a 1 m long laser cavity, Patel reported lasing at 1152.3 nm ($2s_2 \rightarrow 2p_4$) at a power of 0.02 mW with a total pressure of 0.08 torr [71].

Bennet and Knutson [72] have reported simultaneous oscillation on the neon doublet having wavelengths of 1152.3 nm ($2s_2 \rightarrow 2p_4$) and 1152.5 nm ($2s_4 \rightarrow 2p_7$). The laser cavity was 3 m long with a 5 mm diameter discharge tube. Excitation was provided by a DC discharge. When helium was added to the system, the oscillation at 1152.5 nm was inhibited. In a pure neon discharge, population inversion at the $2s_2$ level is preferred as this level is optically connected to the ground level. Other than that, the $2p_7$ level maybe populated due to a cascaded transition originating from a helium metastable state.

Heard and Peterson achieved simultaneous oscillation with pure neon in the visible region. These two wavelengths originate from the same upper level, $3s_2$ and terminate at $2p_8$ (593.9 nm) and $2p_6$ (611.8 nm) [73]. The laser cavity had 1 mm diameter of gain-section and was filled with pure neon at 0.2 torr. The discharge was achieved by pulse-current excitation and simultaneous oscillation was observed when dielectric mirrors were incorporated at the end of the discharge tube. The laser action was observed to quench in the presence of helium.

Extensive studies have been performed to determine the optimum design parameters of helium-neon lasers [41], [74]–[76]. In general, the maximum output power of a particular helium-neon transition is a function of helium and neon partial pressure, total pressure, tube diameter and discharge current. The gain per unit length is an inverse function of the diameter of the gain tube. White and Gordon [77] stated that the power output of the visible transitions increase approximately linearly with discharge length so long as it is well above threshold.

Measurement of the optimal pressures for different RF-excited helium-neon gas mixture ratios at different tube diameters, d, between 3 mm to 5 mm have been performed by Mielenz and Nefflen [78]. Their work resulted in an expression relating optimum neon partial pressure as a function of total pressure in p (mbar) and tube diameter, d in mm:

$$p_{ne} = \frac{p}{6.21p + 2.09d - 17.95}. \tag{2.31}$$

This expression is comparable to the optimum gas mixture parameter employed in Canterbury's laser systems [16]. For operation at 632.8 nm, Canterbury's ring lasers historically used a neon partial pressure of 0.2 mbar with an internal gain tube diameter of 4 mm. The total pressures are usually high, between 2 to 12 mbar. Optimum gas mixtures were found experimentally by characterising laser output power as a function

of RF excited power [79], [80]. Wyss et al. quoted the highest efficiency, η (η = laser power output /RF power input) was achieved at a constant, k of 11.5 mm mbar for d = 4 mm and 6 mm, where k is the product of the total gas pressure and the gain tube diameter ($k = pd$).

2.2.2 The Helium-Neon Gain Curve

For a helium-neon based ring laser gyroscope, it is important to consider those process which influence the gain curve and therefore the optical frequency of the laser. The gain curve is strongly influenced by two main line broadening mechanisms; homogeneous broadening due to collisions and inhomogeneous broadening, which predominantly arises from the Doppler effect at lower pressure.

Homogeneous Broadening

Homogeneous line broadening affects all atoms in the gain medium in a uniform way. In the helium-neon laser system, this occurs from both the natural (lifetime broadening), $\Delta\nu_t$ and collision (pressure) broadening, $\Delta\nu_p$.

The most fundamental source of line broadening arises because of the uncertainty in the exact energy of the energy state involved. This gives rise to the natural linewidth in the helium-neon laser system. The uncertainty in the measured energy, $\Delta E = \Delta h\nu$, arises from the finite mean lifetime of the transition involved, Δt. From Heisenberg uncertainty principle,

$$\Delta(h\nu)\Delta t \geq \hbar/2, \tag{2.32}$$

where $\hbar = h/2\pi$. This leads to a Lorentzian spectral lineshape due to the lifetime of the transition. Lifetime broadening linewidth, $\Delta\nu_t$ can be determined by,

$$\Delta\nu_t = \frac{1}{2\pi}\Big[\frac{1}{t_{upper}} + \frac{1}{t_{lower}}\Big], \tag{2.33}$$

where t_{upper} and t_{lower} are the upper and lower state lifetimes [81].

In a gaseous gain medium, the homogeneous linewidth is strongly influenced by pressure broadening. Collisions between atoms causes perturbations of the emission frequency and subsequently broadens the transition. The effect of this collision (pressure) broadening gives rise to a Lorentzian gain curve [82]:

$$\ell(\nu) = \frac{1}{1 + \left(\frac{2(\nu-\nu_0)}{\Delta\nu_\ell}\right)^2}, \tag{2.34}$$

where ν_0 is the optical transition frequency and $\Delta\nu_\ell = \Delta\nu_t + \Delta\nu_p$. Collisional line broadening, $\Delta\nu_p$, depends on the mean time between collisions. The values are usually determined as a function of gas pressure from experimental measurement. Relevant values (from the literature) are listed in Table 2.2.

Wavelength λ (nm)	Ne-Ne MHz/torr	Ne-He MHz/torr
543.4	81 ±13	130
593.9	-	133 ±8
604.6	106 ±10	129 ±7
611.8	78 ±12	134 ±7
632.8	94.5	70.5
1152.3	9.5	28.4

Table. 2.2.: Collision broadening ($\Delta\nu_p$) parameters at different neon transitions reported by [83]–[85]. Ne-Ne: collision between neon and neon atoms; Ne-He: collision between neon and helium atoms.

Inhomogeneous Broadening

Inhomogeneous broadening occurs if different atoms in the neon ensemble have differing resonant frequencies. In helium-neon lasers, Doppler broadening is the dominant broadening contribution due to the Maxwellian distribution of atomic velocities in the gain medium. This yields a Gaussian lineshape, $g(\nu)$ [81]:

$$g(\nu) = \frac{2}{\Delta\nu_D}\sqrt{\frac{\ln 2}{\pi}}e^{-[2(\nu-\nu_0)/\Delta\nu_D]^2\ln 2}, \tag{2.35}$$

where the Doppler linewidth (due to thermal motion), $\Delta\nu_D$, is given by:

$$\Delta\nu_D = 2\nu_0\Big[\frac{2k_BT\ln(2)}{Mc^2}\Big]^{1/2}, \tag{2.36}$$

where T is the temperature in Kelvin, k_B is the Boltzman constant ($1.38^{-23}\mathrm{m^2kgs^{-2}K^{-1}}$) and M is the neon isotope mass (^{20}Ne= 19.9924 AMU; ^{22}Ne= 21.991 AMU; 1 AMU = 1.6605655×10^{-27}kg).

Furthermore, the operating frequency, ν_0 in Equation 2.34 and 2.36 varies according to the different neon isotope ratio because the atomic line centres of ^{20}Ne and ^{22}Ne are separated by an isotopic shift with ^{22}Ne at higher frequency. Table 2.3 lists the isotope shifts corresponding to the laser operating frequency.

Figure 2.4 illustrates the shape of the gain curves for 90% ^{20}Ne and 10% ^{22}Ne and 50% ^{20}Ne and 50% ^{22}Ne at different wavelengths relative to the ^{20}Ne line centre. The gain curves are generated by a using a visual basic code developed by Dr. Bob Hurst. The

Wavelength, λ (nm)	Operating Frequency, ν_o (THz)	Isotope Shift (MHz)
543.4	553	1000
632.8	474	875
1152.3	260	261

Table. 2.3.: Operating frequency and isotope shift at different laser wavelength [86]–[88].

program simulates the expected Voight gain profile (see next section) of ^{20}Ne and ^{22}Ne by taking into account the effects of saturation for the counter-propagating beams to the gain curve in a ring laser. Note that, in this figure, the saturation factor was omitted out to clearly illustrate that the shape of the gain curve is influenced by the ratio of the two neon isotopes. For the rest of the thesis, we will denote a mixture of 90% ^{20}Ne and 10% ^{22}Ne as natural neon while a mixture of 50% ^{20}Ne and 50% ^{22}Ne will be denoted as 50:50 neon.

As shown from Figure 2.4, the centre of the gain curve of each laser wavelength is shifted according the isotope shift value listed in Table 2.3. For 50:50 neon, the peak of the gain curve is essentially at the centre between the ^{20}Ne and ^{22}Ne gain profile. Therefore, the gain profile appears more symmetrical than that of natural neon. If there is only one isotope present, the counter-propagating beams will share the same group of neon atoms. This will result in suppression of one of the laser beams due to mode competition. For this reason, a ring laser gyroscope typically employs a mixture of the ^{20}Ne and ^{22}Ne isotopes to eliminate gain competition between the counter-propagating beams.

The gain curve for 1152.3 nm (Figure 2.4 (c)) is noticeably smaller because the Doppler linewidth at longer wavelength will be narrower (see Equation 2.36).

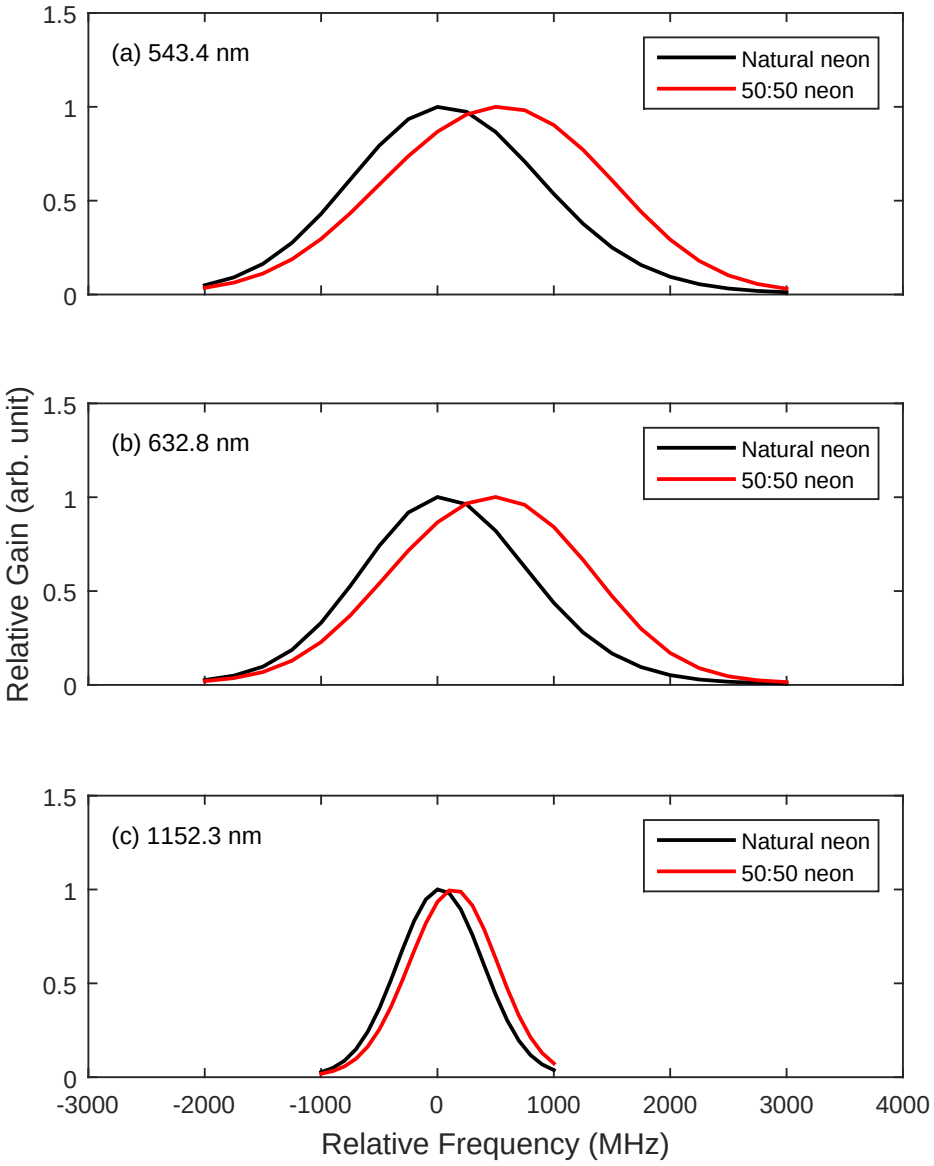

Figure. 2.4.: Gain curve for natural neon and 50:50 neon at: (a) 543.4 nm; (b) 632.8 nm; (c) 1152.3 nm.

The Voight Gain Curve, Gain Saturation and Hole Burning

The gain curve at a given wavelength will be a convolution of the line broadening mechanisms discussed above. This resultant gain curve is known as the Voight gain profile and will be influenced by the fact that in a ring laser, the counter-propagating beams will interact with the gas atoms in the cavity.

When an intense laser beam interacts with an excited atomic ensemble having a homogeneously broadened line, the resulting emission of stimulated radiation depletes the entire atomic group uniformly. This introduces uniform gain saturation and the magnitude of the gain saturation is proportional to the intensity of the laser beam. On the other hand, when the atomic group is Doppler broadened, the intense laser beam will act mainly on the group of atoms with the velocity component in the direction of the wave propagation. The velocities of the atoms are redistributed as a result of these atomic collisions. When a narrow laser beam passes through the gas medium, collisions between atoms are not fast enough to prevent depletion of the atoms within its velocity range. Therefore, a hole forms in the inhomogeneously broadened line.

The overall Voight gain profile will take into account the homogeneous and inhomogeneous broadening mechanism and gain saturation for the counter-propagating beams. The inhomogenoues gain distribution can be modified by introducing saturation, $S(\nu)$,

$$S(\nu) = \frac{1}{1 + F(\nu)}, \tag{2.37}$$

where,

$$F(\nu) = \frac{I}{I_{sat}} \times \frac{1}{1 + \left(\frac{2(\nu - \nu_0)}{\Delta\nu_\ell}\right)^2}, \tag{2.38}$$

with I designated as the intracavity intensity and I_{sat} as the saturation intensity. In order to determine magnitude of the hole burning, the ratio of I to I_{sat} can be calculated. I can be measured with a calibrated power meter, mirror transmission and beam geometry and I_{sat} is the intensity at which the gain drops to exactly half of the small signal gain.

Including the fact that the two counter-propagating beams in the laser will burn their own holes, Equations 2.37 and 2.38 become:

$$S(\nu) = \frac{1}{1 + F(\nu_a, \nu_1, I_1, I_{sat}) + F(\nu_b, \nu_2, I_2, I_{sat})} \tag{2.39}$$

and

$$F(\nu) = \frac{I_1}{I_{sat}} \times \frac{1}{1 + \left(\frac{2(\nu_1 - \nu_a)}{\Delta\nu_{\ell a}}\right)^2} + \frac{I_2}{I_{sat}} \times \frac{1}{1 + \left(\frac{2(\nu_2 - \nu_b)}{\Delta\nu_{\ell b}}\right)^2}, \tag{2.40}$$

where:

$I_{1,2}$: intensity of the saturating signals;

$\nu_{1,2}$: optical frequency of the saturating signals;
$\nu_{a,b}$: optical frequency of the counter-propagating beams;
$\Delta\nu_{\ell(a,b)}$: homogeneous linewidths of the counter-propagating beams.

The Voight gain profile is obtained by integrating the convolution of the Lorentzian gain curve with the saturation parameters and homogeneous gain curve as follow:

$$G(\nu) = \int_{-\infty}^{+\infty} g(\nu)S(\nu)d\nu. \tag{2.41}$$

2.3 Characterisation of Ring Laser Gyroscope Operation

The Canterbury ring laser gyroscopes possess a few similar operating methods; for example, the laser cavities are normally filled with a total gas pressure of 2 to 12 mbar with a helium to neon ratio of 50:1, the laser gain section is narrow (the gain tube typically has a diameter of 4 mm), and the gain medium is excited by capacitively coupled high frequency RF power. Although the laser gyroscopes are normally operated on a single longitudinal mode, the lasers are able to measure a stable rotation signal within a phase-coupled multimode regime as well.

2.3.1 Single-Mode Operation

In general, a ring laser gyroscope operates on a single longitudinal laser mode. A laser will operate in a single longitudinal mode if only one mode lies under that part of the gain curve that is capable of sustaining oscillation. The spacing between longitudinal modes, also known as free spectral range (ν_{fsr}), of a ring laser is defined as,

$$\nu_{fsr} = \frac{c}{nP}, \tag{2.42}$$

where c is the speed of light, P is the perimeter of the laser cavity and n is the refractive index ($n = 1$ in vacuum). As the size of the laser cavity increases, the free spectral range between longitudinal modes decreases. In order to achieve single mode operation with a large ring laser gyroscope, a gain starvation approach is used where servo-control of the RF excitation power maintains the laser power at the lasing threshold [17]. Large ring laser gyroscopes are normally operated with an over-pressured cavity to increase the homogeneous broadening of the laser transition [33]. Homogeneous broadening reduces the curvature of the gain profile at the peak saturation point. This allows weak saturation to persist to higher power than it otherwise would, hence, higher order laser modes do not have enough gain to oscillate [80], [89].

2.3.2 Multi-Mode Operation

Laser gyroscopes can also be operated on multiple longitudinal modes utilising the fact that gas lasers are well known to exhibit phase coupling. This can be desirable because when the laser is running with the gain starvation technique, the laser intracavity power is low. On the other hand, when running on multiple phase-fixed modes, where the laser intensity is raised to allow multiple longitudinal modes to oscillate at the same time, the total intracavity power is usually more than 10 times higher than running the laser in the single longitudinal mode regime.

Phase coupling of longitudinal modes in gas lasers arise due to the intrinsic non-linearity of the gain medium and does not require intra-cavity modulation [90]. The comparison between single mode operation and multi-mode operation has been reported in [91] where the operations of G-0 and UG-2 in 'stable' multimode regime are comparable to their performances in single mode operation. However, running a large ring laser on phase-coupled modes, the laser performance is more susceptible to geometric instability [18], which affects the long-term stability. Nonetheless, for applications where long term stability is not as important (e.g. in seismology), this phase-coupled operating regime is potentially advantageous.

2.3.3 Rotational Sensitivity

In the absence of any external fluctuations and noise sources, the resolution of a ring laser gyroscope is limited by the quantum noise. Quantum noise is a consequence of spontaneous emission which introduces perturbations to the phase and polarisation of the laser beam [92]. This irreducible noise floor gives a limit to the rotational sensitivity of a laser gyroscope [51], [56], [93],

$$\Omega_s = \frac{cP}{4AQ}\sqrt{\frac{h\nu_0}{P_i\, t}}, \tag{2.43}$$

where t is the measurement time and, ν_0 the optical frequency of the laser, P is the laser perimeter, A is the area enclosed by the cavity, Q is the quality factor[5] of the ring cavity, h is the Plank's constant and P_i is the measured laser output power.

From Equation 2.43, one main contributor to the quantum limit is the quality of the mirrors which determines the cavity quality factor. The typical reflectivity of high quality mirrors (often denoted as 'supermirrors') incorporated in large ring lasers is more than 99.99999%. In addition, the main reason that the Canterbury ring laser group were

[5] $Q = 2\pi\nu_0\tau_{decay}$

motivated to up-scale the size of the laser previously was to achieve a higher resolution as the total area of the laser cavity contributes to the sensitivity of the laser gyroscope.

2.3.4 Stability Analysis

All large ring laser gyroscopes in current use do not achieve quantum noise limited rotation sensing because the laser structure is influenced by time varying geometric perturbations[6]. These noises can be identified by analysing the stability of the measured δf_s signal.

Stability is defined as the statistical estimate of the frequency or time fluctuations of a signal over a given time interval. These fluctuations are measured with respect to a mean frequency or time offset. Short-term stability usually refers to signal fluctuations over intervals less than 100 s. Long-term stability on the other hand usually refers to measurement intervals longer than 100 s up to periods longer than 24 hours [94].

The frequency stability of a ring laser gyroscope is assessed by using an Allan variance analysis. The Allan variance is a time domain analysis technique initially developed by David Allan of the National Bureau of Standards to evaluate the cesium beam frequency standards employed as the U.S. frequency standard [95].

The Allan variance analysis of δf_s is done by computing the Allan deviation[7], $\sigma_y(\tau)$ as a function of different averaging times, τ, and then by analysing the log-log scale slopes of the Allan deviation plot against the averaging time to identify the different noise sources [96]. The following steps can be followed to create an Allan deviation plot:

1. Log a set of time series of δf_s over a period of time and let the number of samples (δf_s) to be N and the sample period to be τ_0.
2. Set the averaging time to be $\tau = q\tau_0$, where q is the averaging factor ($q < (N-1)/2$).
3. Divide the time series into clusters, M, corresponding to the chosen averaging time, τ.
4. The Allan deviation of that particular averaging time, τ can be calculated by,

$$\sigma_y(\tau) = \sqrt{\frac{1}{2(M-1)} \sum_{i=1}^{M-1} (y_{i+1} - y_1)^2}, \tag{2.44}$$

where, y_i is the average value of a set of frequency measurements containing $\delta f_{s1}, \delta f_{s2}, \delta f_{s3}$... and so on, in one cluster, M.
5. Calculate the value of $\sigma_y(\tau)$ at different value of τ.
6. Plot $\sigma_y(\tau)$ corresponding to the averaging time, τ on a log-log axis.

[6] We note that currently the G ring laser performs very near to the quantum limit [68].
[7] The Allan deviation is the square root of the Allan variance.

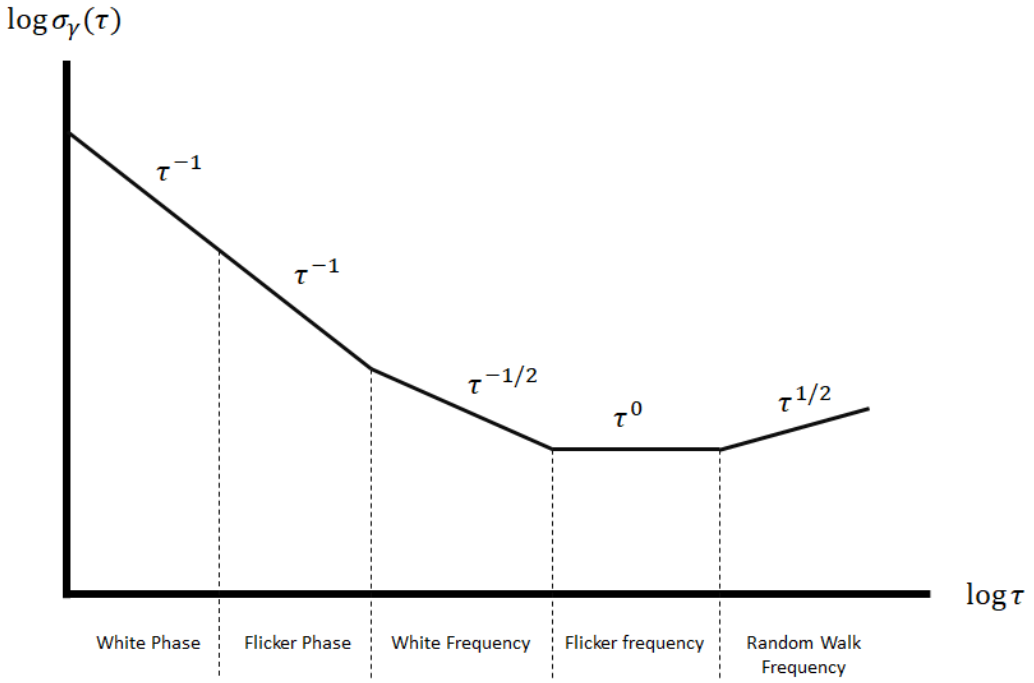

Figure. 2.5.: Noise identification by the slope of an Allan deviation plot

The different types of noise: white phase, flicker phase, white frequency, flicker frequency and random walk frequency, usually appear in different time regions. The noise sources can then be identified according to the slopes, μ, of the plot of $\sigma_y(\tau)$ against τ on a log-log scale as illustrated in Figure 2.5. The calculated $\sigma_y(\tau)$ is usually normalised by the mean value of δf_s to give an absolute stability as a function of τ so that it is easier to compare the absolute stability of different ring laser gyroscopes with different operating frequencies or dimensions. Table 2.4 shows the relationship between the slope, μ and the classification of disturbances that are typically present in a ring laser.

Noise Type	Slope, μ	Noise Source
White phase	-1	Electronic noise such as: intrinsic noises and quantisation noises
Flicker phase	-1	Electronic noise due to thermal effects
White frequency	-1/2	Quantum noise due to spontaneous emission from the gas discharge
Flicker frequency	0	Mechanical shocks
Random walk frequency	1/2	Transient response time

Table. 2.4.: Noise types and their corresponding slopes in a σ_y vs τ plot and the related noises arising in a ring laser gyroscope [96].

3 Technical and Operational Specifications of a 2.56 m^2 Ring Laser Gyroscope

All the experimental work in this research was carried out with a 2.56 m^2 ring laser gyroscope, denoted as PR-1 (Physics Ring 1). PR-1 is currently mounted vertically on the wall of a second-floor laboratory in the West Rutherford Building, at the Ilam campus of the University of Canterbury as presented in Figure 3.1. The design comprises several independent components such as solid corner boxes, mirror chambers and a narrow gain tube. As the components are isolated mechanically, the geometry of the ring cavity can be up-scaled (or down-scaled) conveniently by using different lengths of stainless steel tubes. The goal of this chapter is to establish benchmark performance of the laser gyroscope operating on the standard 632.8 nm laser wavelength. This information is essential in order to compare the operation of PR-1 at 632.8 nm to its performance at different operating wavelengths.

3.1 Technical Details and Optical Design

A schematic diagram of the PR-1 ring laser gyroscope is shown in Figure 3.2. The laser cavity is formed by four very highly reflective mirrors with a reflectivity of more than 99.9999% (supermirrors). These supermirrors are encased firmly in the mirror holders situated inside the stainless steel mirror chambers. Each mirror chamber is connected to a folded lever system which consists of four micrometers to allow precise alignment of each mirror to be within ±10 arc seconds. The mirror chambers and their lever arms are rigidly attached to the solid corner boxes. These corner boxes are made of a granite-epoxy compound for better mechanical stability [35]. The four mirror chambers are connected to the stainless steel tubes by bellows to form a square laser path of 6.4 m in perimeter. Laser excitation is provided by coupling 80 MHz radio frequency (RF) power to the gain medium through a narrow gain tube which is situated midway between two mirror chambers. The gain tube is constructed from fused silica (Pyrex) tube having a diameter of 4 mm and a total length of 100 mm and a stainless steel casing holds the gain tube in place. The alignment of the gain tube can be controlled by two sets of micrometers at each end of the gain tube. The gain tube has a low out-gassing rate and it is able to tolerate the high temperatures needed to generate a helium-neon plasma (see Section

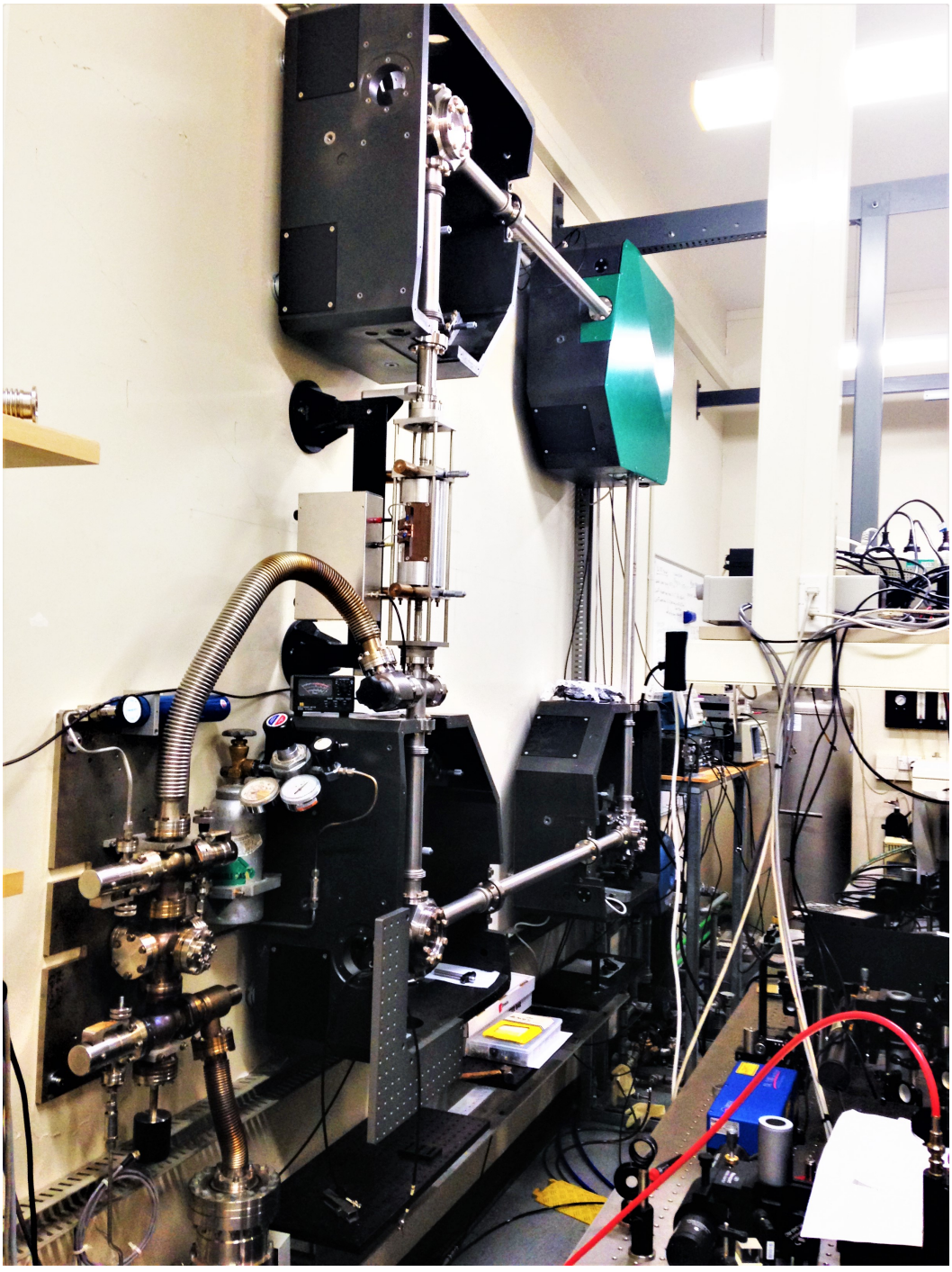

Figure. 3.1.: PR-1 vertically mounted on the wall of the laboratory.

3.1.1). The PR-1 cavity is attached to a vacuum system through an isolation valve. The vacuum system consists of a rotary vane pump and a turbomolecular pump, three gas cylinders: natural neon gas cylinder (90% ^{20}Ne and 10% ^{22}Ne), 50:50 neon gas cylinder (50% ^{20}Ne and 50% ^{22}Ne) and helium (^{4}He) gas cylinder. The vacuum system is isolated from the atmosphere by another isolation valve.

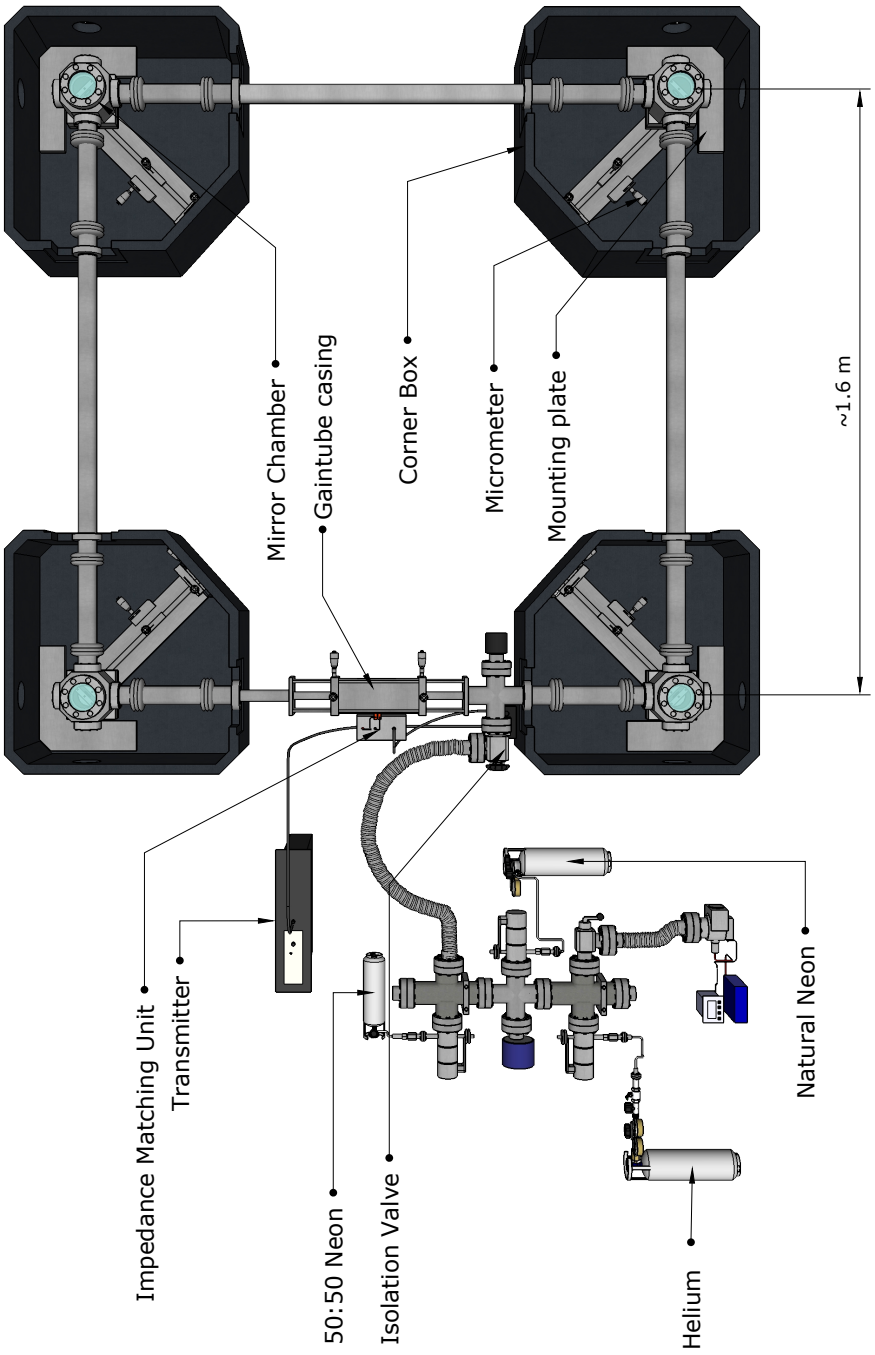

Figure. 3.2.: Schematic diagram of PR-1.

3.1.1 Radio Frequency Excitation

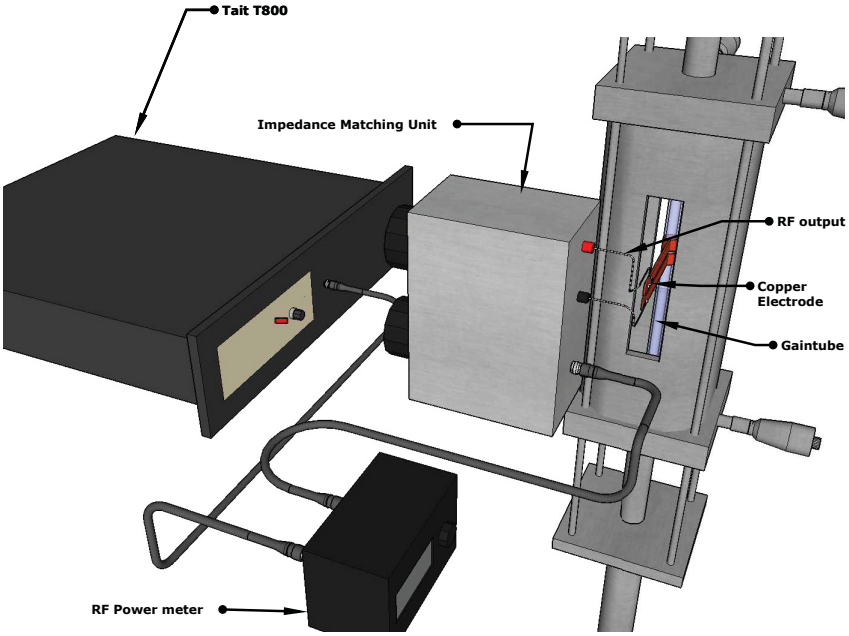

Figure. 3.3.: Illustration of the gain tube and excitation section.

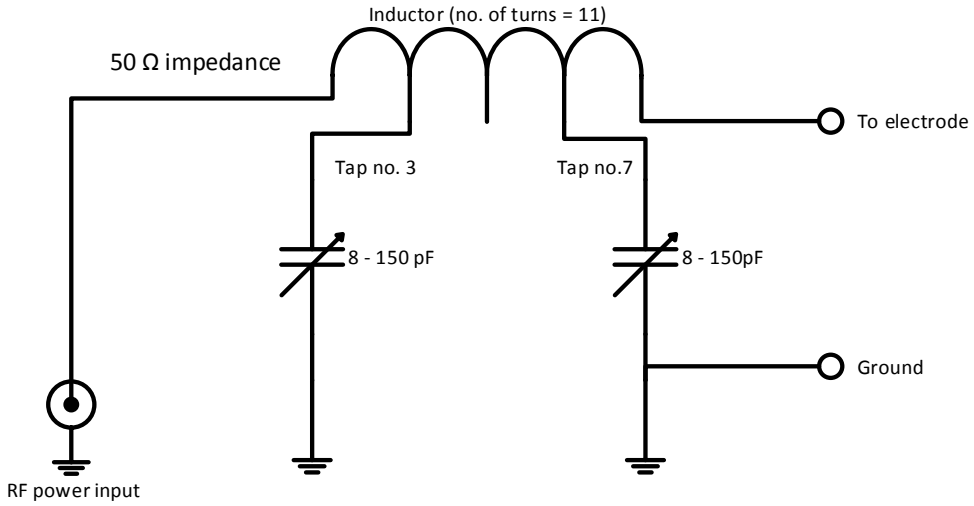

Figure. 3.4.: Schematic circuit diagram of the impedance matching unit.

Radio frequency (RF) excitation is provided by a Tait Radio Communication (Tait T800) transmitter, operating at 80 MHz. The transmitter can provide up to 25 W of RF power. The output of the transmitter is connected to an RF power meter (RS W520). This RF power meter monitors the total transmitted and reflected power between the transmitter and the impedance matching unit. The output from the impedance matching unit is

connected to two copper electrodes that wrap around the gain tube as shown in Figure 3.3. The circuit diagram of the impedance matching unit is shown in Figure 3.4. This unit is a 'pi-network' configuration which consists of two variable capacitors and an air-coil inductor. The two capacitors can be varied between 8 pF to 150 pF. The air-coil conductor is approximately 17 mm in diameter with a total length of 150 mm. The location of the taps on the coil determines the total inductance value. This matching unit will match the 50 Ω impedance from the transmitter to the unknown impedance generated by the helium-neon plasma.

3.1.2 Detection and Data Acquisition System

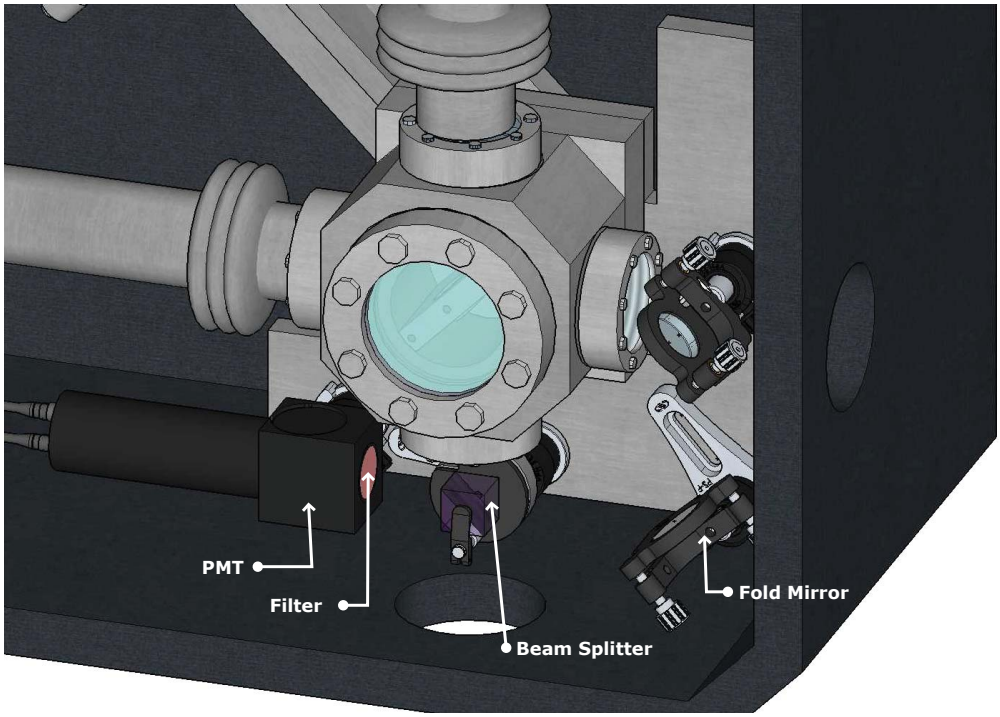

Figure. 3.5.: The CW and CCW beams are superimposed by using a beam splitter and a photomultiplier tube (PMT) which is mounted on the lower right corner box to detect the beat signal (δf_s).

Generally, only about 0.00001% of the counter-propagating laser beam intensities are transmitted through the supermirrors and the mirror chamber's window. The laser intensity is usually measured in the nanoWatt (nW) regime. In order to detect the rotation signal from PR-1, a beam splitter is mounted at the lower corner box to combine the counter-propagating beams as shown in Figure 3.5. This combined beam is detected by a Hamamatsu photomultiplier tube (PMT, R3896). The PMT is powered by a high voltage power supply. There are two high-gain photodiodes (PD) mounted on the top right corner of PR-1 to monitor the clockwise (CW) and counter-clockwise (CCW) beams respectively as shown in Figure 3.6. It is crucial to place a narrow filter in front of all detectors to avoid signal contamination from the plasma light.

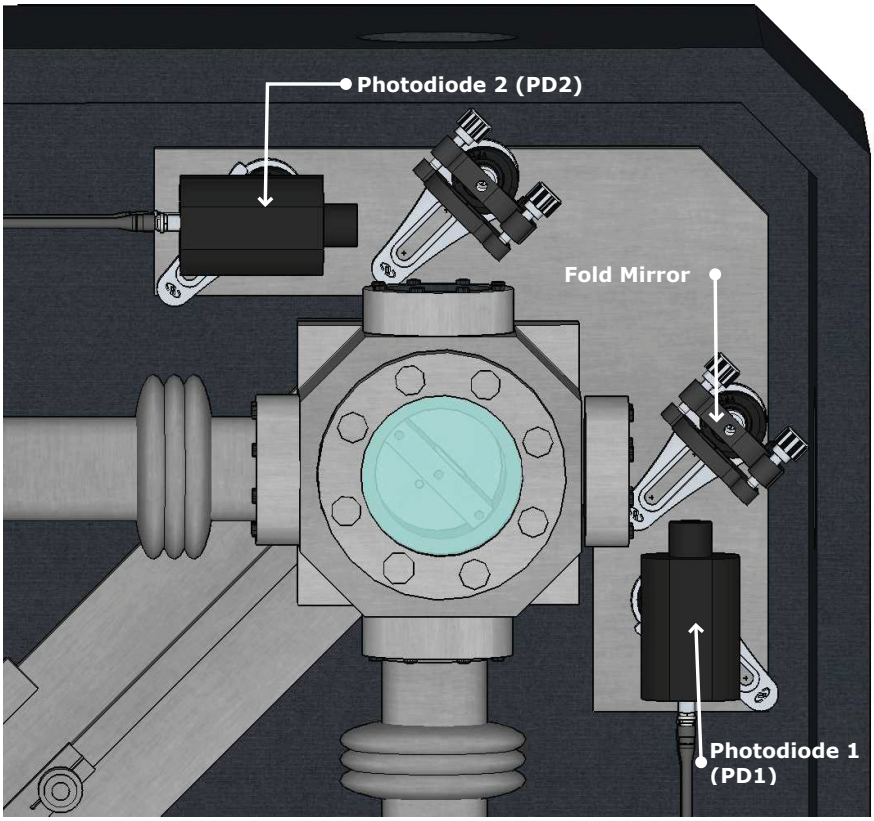

Figure. 3.6.: CW and CCW beams detection via high gain photodiodes (PDs) on the upper right cornerbox.

The signals from the PMT and the two PDs are connected to a National Instrument LabVIEW data acquisition board (USB NI-6216 BNC) and the data acquisition is realised by a LabVIEW logging program. The PMT output signal is an alternating voltage with a carrier frequency which corresponds to the Sagnac frequency, δf_s from Equation 2.25. The frequency is estimated via a Buneman Estimator VI in LabVIEW.

The Buneman Frequency Estimator VI in LabVIEW estimates the frequency of a given sine wave of unknown frequency using the Buneman formula. If an underlying time signal is not precisely periodic with period n, where n denotes the size of the data array, the Buneman algorithm can be used to calculate the unknown frequency of signal X_n. The following formula describes the Buneman algorithm, β:

$$\beta = B + z, \tag{3.1}$$

$$z = \frac{n}{\pi} \arctan \frac{\sin \frac{\pi}{n}}{\cos \frac{\pi}{n} + \frac{|F_b(x)|}{|F_{b+1}(x)|}}, \tag{3.2}$$

where $F_b(x)$ denotes the Fourier transform of the signal input, x_n, and B is the frequency of the input signal.

3.1.3 Control and Feedback System

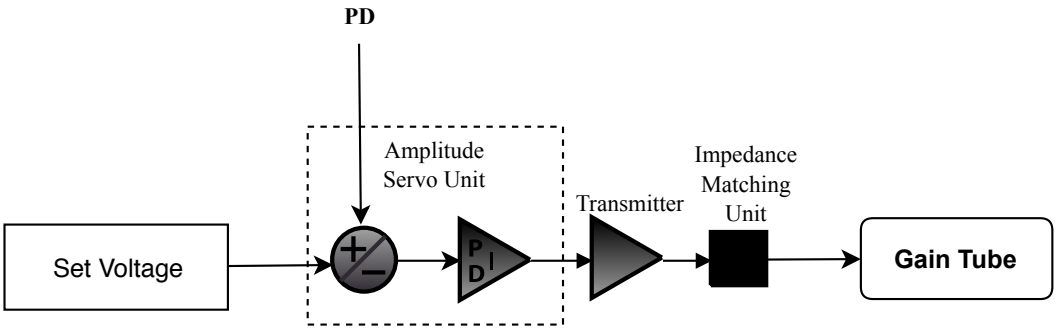

Figure. 3.7.: The block diagram of the laser power feedback system.

The laser intensity tends to fluctuate when the laser is running at the lasing threshold. Therefore, a feedback system is crucial to maintaining a constant laser output power during data logging operation. The laser intensity is maintained by a feedback loop system as shown in Figure 3.7. The feedback system consists of a servo unit which receives the signal from the PD and sends feedback to the RF transmitter driver to fine-tune the RF supply until the laser voltage is equivalent to a set voltage.

The servo unit consists of a simple PID (Proportional, Integral and Derivative) controller circuit. The error signal is generated by subtracting the set voltage (the desired laser intensity in terms of volts) with the PD input (laser intensity is proportional to the DC voltage). The constant (or gain) for the proportional controller is fixed at '1'. It is important to set the gain low to avoid signal overshoot in the system. The integral controller in the servo unit will add a long-term precision to the control loop in conjunction with the proportional controller. The integral constant is set at '0.1' while the derivative constant is set to '0'. The sum of the error signal multiplied by the proportional gain and the integral gain will provide a control output signal to drive the transmitter. The transmitter driver will tune the RF input power being transferred to the gain tube accordingly to control (or to maintain) the laser output power.

3.2 Optical and Gyroscopic Characterisation for Operation at 632.8 nm

As PR-1 is a vertically mounted ring laser located at a latitude of $\phi = -43.52°$ at tilt angle, $\theta_T = 32°$ from north, Equation 2.25 can be re-written as,

$$\delta f_s = \frac{4A}{\lambda P}\Omega_E \cos\phi \cos\theta_T \tag{3.3}$$

Substituting the relevant operational parameters for PR-1, which are, P = 6.4 m, A = 2.56 m^2, λ = 632.8 nm and the Earth rotation rate is $\Omega_E = 7.3 \times 10^{-5}$ rad/s, the anticipated δf_s is 113.5 Hz.

The quality of the supermirrors in a ring laser gyroscope plays a crucial role in determining the performance of the laser. The supermirrors used in the chapter were supplied by Research Electro-Optics, Inc. (REO). The highly reflective coating on these supermirrors was fabricated by the Ion Beam Sputtering (IBS) technique. Two sets of different supermirrors were employed to characterise the performance of PR-1 for operation on the 632.8 nm laser transition. The first set denoted as REO 3 has a lower transmission than the second set, REO 4. The specification of the REO 3 and REO 4 mirror sets provided by REO is summarised in Table 3.1.

	Loss per Mirror (ppm)	Transmission per Mirror (ppm)	Radius of Curvature (ROC) (m)
REO 3	3.7	0.25	4
REO 4	5.1	1.54	4

Table. 3.1.: Specification of the 632.8 nm mirrors as provided by REO.

3.2.1 Measurements of Mirror Loss and Cavity Q

Both sets of mirrors were cleaned before being installed in PR-1. With the REO 3 mirror set, at a gas fill of 0.2 mbar of 50:50 neon and a total gas pressure of 6 mbar, laser operation at 632.8 nm was observed. The laser was running on the lowest order transverse mode, TEM_{00} and the beam spot diameter on the mirrors was measured to be 2.7 mm.

After lasing had been obtained, optimisation of the cavity alignment was performed by fine-tuning the micrometers on the gain tube as well as the micrometers at each lever on the corner box. A power meter (Coherent FieldMaxII-TO) with a silicon sensor (OP-2 VIS) was mounted at the upper left mounting plate to measure the laser power. The optimum alignment is obtained when the laser beam spot is located at the centre of the supermirror and maximum power is measured by the power meter.

A cold cavity ring-down time[1], τ_{decay}, was then measured by mounting a PMT at the lower left corner box to detect the CW beam. The signal from the PMT was connected to an oscilloscope (Tetronix PPO 7104 Digital Phosphor Oscilloscope) via a short coaxial cable. A 1 MΩ resistor was inserted in parallel between the PMT signal and the oscilloscope to further reduce the resistance and the RC time constant to make sure the observed transient was a true reflection of the cavity Q.

[1] To describe the exponential decay of the laser intensity when the gain is removed.

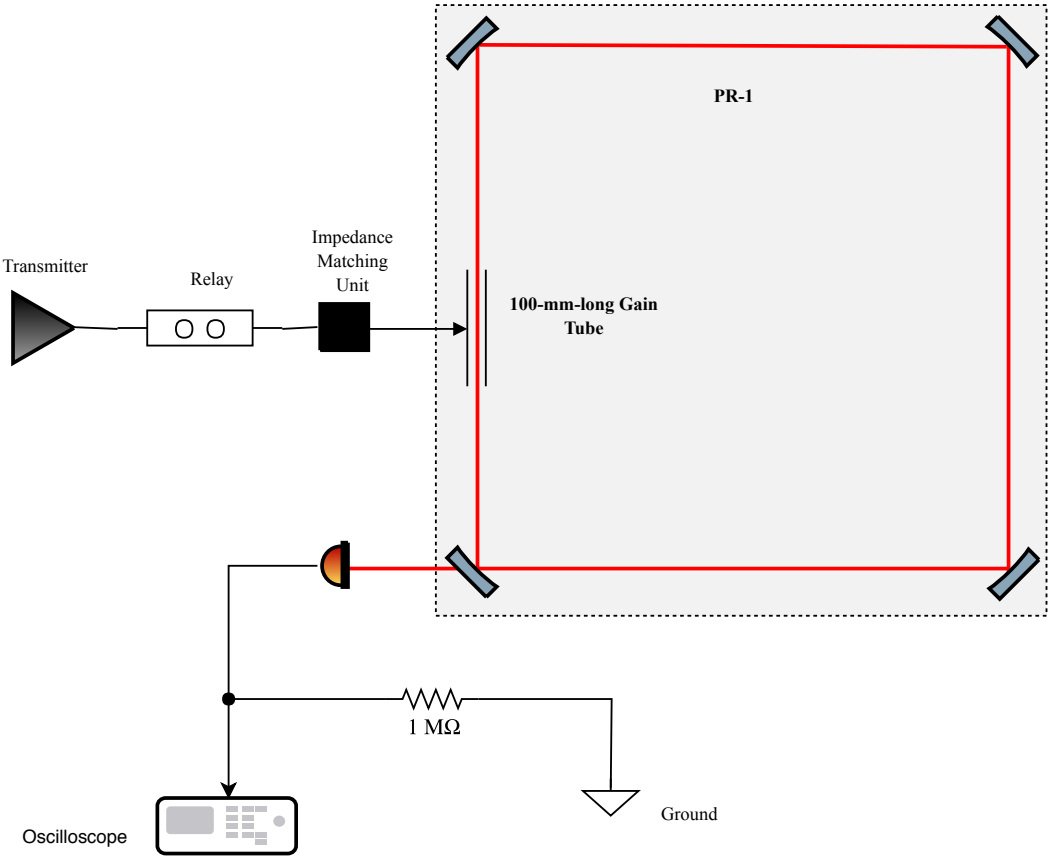

Figure. 3.8.: Experimental setup to measure the cold cavity ring-down, τ_{decay}.

The oscilloscope was set on a manual trigger so that it will only begin taking data when the signal from the PMT reaches the trigger level. A coaxial relay was connected between the RF transmitter and the matching unit to act as a fast switch. Then, the plasma was turned off by pressing the coaxial switch, and the photon decay data was recorded by the oscilloscope. The data taken was fitted to an exponential function of the form,

$$V(t) = V_0 + Ce^{t/\tau_{decay}}, \tag{3.4}$$

where, V_0 is the initial voltage (intensity) and C is the numerical constant.

The τ_{decay} for both sets of supermirrors were measured to be 135 and 120 μs while the calculated total loss were 39.50 and 44.45 ppm per mirror respectively. Table 3.2 summarises the cavity Q factor[2]and finesse[3], F and losses per mirror achieved with the REO 3 and REO 4 supermirrors. Apart from the transmission losses from the mirror, the high losses measured are mainly due to absorption by the mirror substrates and scattering by the mirror surfaces.

[2] see Section 2.3.3
[3] $F = \lambda Q/P$

Parameter	REO 3	REO 4
τ_{decay} (μs)	135	120
Total loss, L (ppm)	158	177.8
Loss per mirror (ppm)	39.5	44.45
Quality factor, Q	4×10^{11}	3.6×10^{11}
Finesse, F	4.0×10^{4}	3.5×10^{4}

Table. 3.2.: Measured τ_{decay} and the corresponding cavity Q factor, finesse, F and loss per mirror achieved with the REO 3 and REO 4 mirror sets.

3.2.2 Maximum Gain

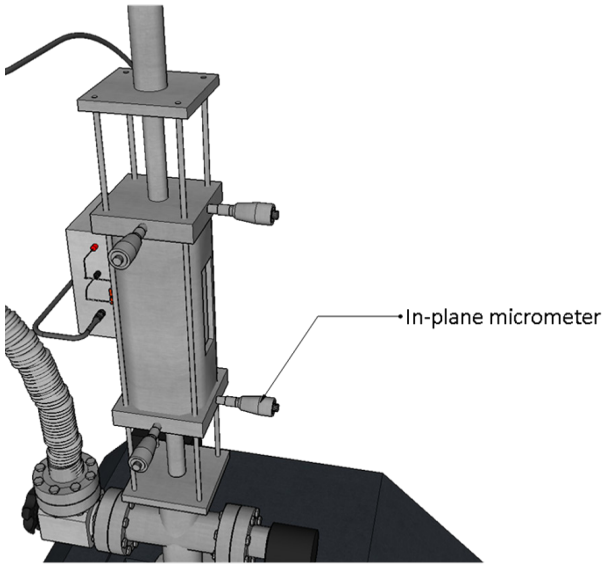

Figure. 3.9.: In-plane micrometer to vary the alignment of the gain tube.

The maximum gain from PR-1's 100 mm-long gain tube was determined by measuring the τ_{decay} at various gain tube alignments. The alignment of the gain tube was altered by varying the lower in-plane micrometer (see Figure 3.9) in the in-plane direction. This is to vary the total fractional loss per circuit. At the same time, for each micrometer setting, the RF power required for the laser to sustain laser output power at 4.5 nW was recorded. The measurement was performed with the REO 3 mirror set and the gas fill was varied at pressures of 2, 4 and 6 mbar with 0.2 mbar of natural neon.

Figure 3.10 displays the gain in parts per million (ppm) measured at total gas pressures of 2, 4 and 6 mbar. At the optimum gain tube alignment, the gain (or total fractional loss per circuit) is the lowest and the RF power required to maintain the laser at 4.5 nW was at 0.6 W. When the gain tube is highly misaligned, the RF power required to maintain laser output power at 4.5 nW will be higher. As seen from the figure, the maximum gain is

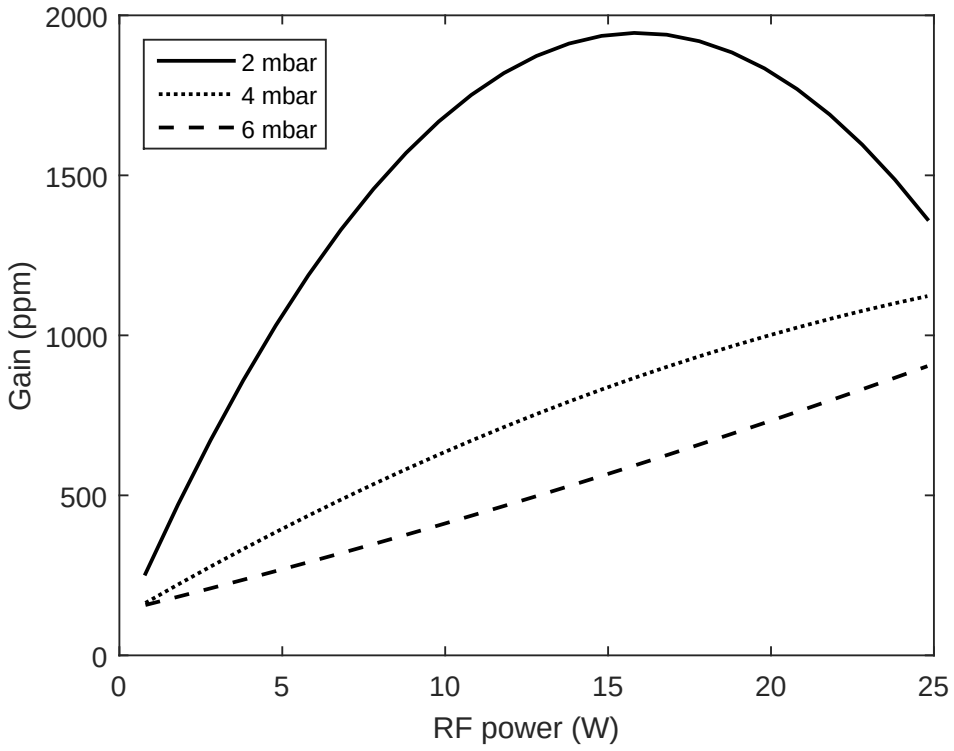

Figure. 3.10.: Variation of gain at total gas pressures of 2, 4 and 6 mbar at various RF input powers.

obtained at 2 mbar of total gas pressure. The maximum gain the existing PR-1 gain tube can provide is 1945 ppm at RF input power of 15 W. The gain decreases for RF powers of more than 15 W at 2 mbar due to gain saturation.

3.2.3 Gyroscopic Performance

The rotation sensing performance of PR-1 (for single-mode operation) was characterised at various helium and neon pressures. The supermirrors employed in this experiment were the REO 3 mirror set. Firstly, the cavity was refilled with 0.2 mbar of 50:50 neon. Then, helium gas was added to achieve a total pressure of 3 mbar. RF excitation was applied, and the laser power was reduced until the laser was oscillating just above the laser threshold. The laser intensity was maintained by the servo system described in Section 3.1.3.

The signals from the PMT and PDs (see Section 3.1.2) were connected to an oscilloscope (Tektronix TDS 220 100 MHz), and the waveforms of the monobeam and combined beam are shown in Figure 3.11. The output signal of the PMT is an AC voltage with a carrier frequency equal to the Sagnac frequency, δf_s whereas the AC modulations on the DC signal of both PD signals are due to backscattering. This arises due to imperfections

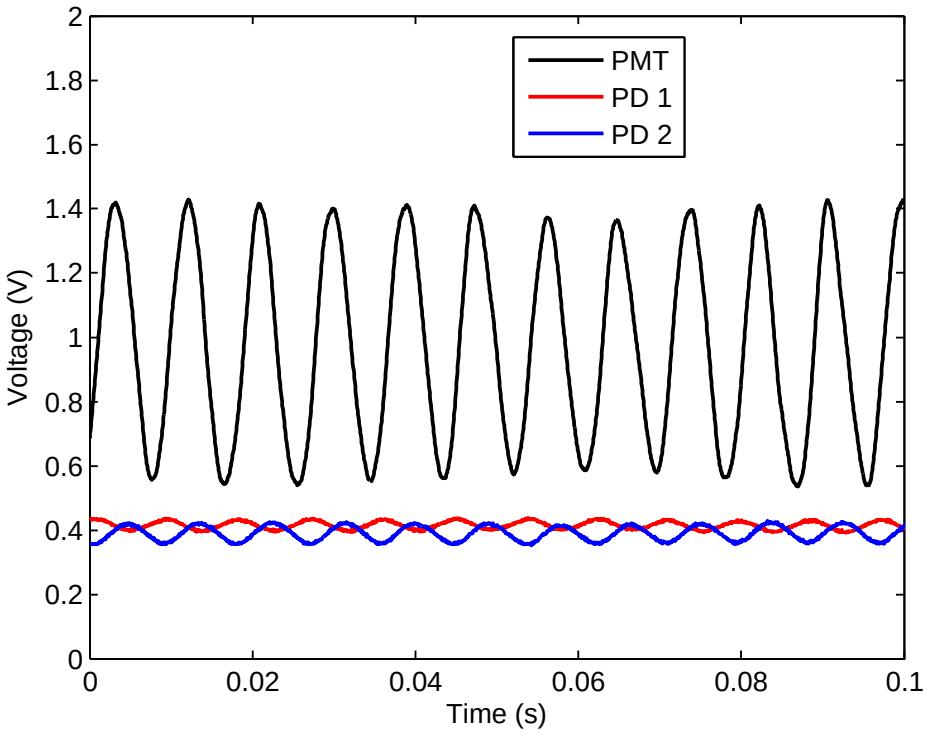

Figure. 3.11.: δf_s and monobeam waveforms detected from the PMT and PDs.

in the dielectric coating or the substrate polish of the supermirrors, as well as due to dust or contamination on the mirrors. These imperfections will cause a portion of the monobeam (a single beam) to be scattered into the beam path of the counter-propagating beam. The amplitude of the monobeam modulation ($m_{1,2}$) is estimated by dividing the AC amplitude with the DC amplitude of the detected monobeam signal [60].

A typical long-term Sagnac time series from PR-1 is shown in Figure 3.12. The time series shows mode hopping and mode splitting as abrupt variations of the detected δf_s. Mode hopping occurs when both beams jump simultaneously to higher or lower longitudinal mode indexes. This is shown as the sudden step up and step down of δf_s in the time series. On the other hand, mode splitting (which is observed as spikes in Figure 3.12) occurs when the CW and CCW beams are operating on different longitudinal modes. This observation is expected from PR-1 output since the laser is a heterolithic wall mounted device. The gyroscopic operation is highly influenced by perimeter instabilities due to temperature variations, mechanical vibrations, electronic jitters and so on. Moreover, PR-1 is mounted on a wall in a high rise building. Hence, the δf_s signal is usually accompanied by frequency modulation side-bands of 2 to 3 Hz as shown in Figure 3.13. This modulation is induced by the natural oscillations of the West Rutherford building, rocking about its long axis.

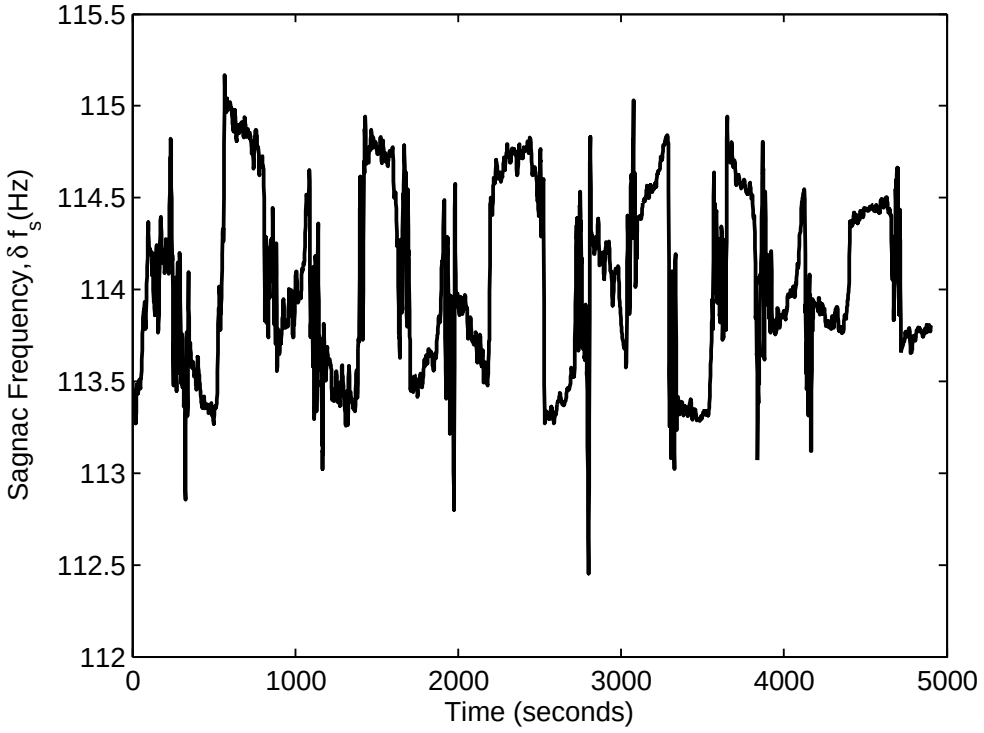

Figure. 3.12.: A typical long term time series which shows mode hopping and mode splitting every 200 to 300 s.

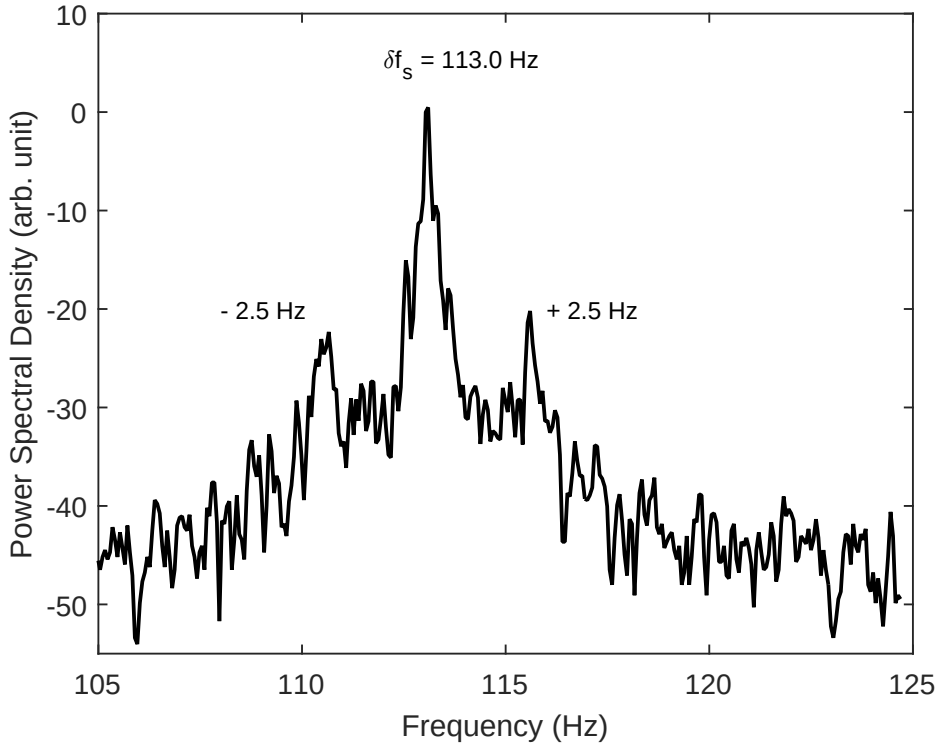

Figure. 3.13.: Typical power spectrum derived from the Sagnac time series.

Figure 3.14 compares the short-term time series of δf_s when PR-1 was operated with a gas fill consisting of 0.2 mbar of 50:50 neon at (a) 3 mbar, (b) 6 mbar and (c) 10 mbar. At 3 mbar, the detected δf_s is approximately 114.1 Hz with excursions between 0.1 to 0.2 Hz. The measured CW and CCW monobeam modulations ($m_{1,2}$) were between 9 - 15%. The backscatter perturbation on the measured δf_s can be estimated by [60], [97],

$$\Delta f_{bs} = m_1 m_2 \frac{\delta f_s}{2}, \tag{3.5}$$

which yields a frequency perturbation of 0.72 Hz. The measured laser power output was 3.5 nW. There was no lock-in effect observed as the lock-in threshold, f_L estimated from Equation 2.27 is 2.4 μHz. At 10 mbar, the δf_s excursion is approximately between 0.01 - 0.02 Hz. The laser output power is 25 nW and the modulation was measured to vary between 3 - 5%. The short-term time series of the δf_s detected when PR-1 was operated on 0.2 mbar of natural neon at various gas pressures is shown in Figure 3.15 while Table 3.3 summarises the operational characteristics correspondingly.

Neon Isotope	Total Pressure (mbar)	Output Power (nW)	m_1	m_2	Δf_{bs} (Hz)	f_L (μHz)
50:50	3	3.5	0.15	0.09	0.72	2.37
	6	15	0.14	0.10	0.74	2.41
	10	25	0.05	0.03	0.08	0.81
Natural	3	2	0.10	0.09	0.51	2.00
	6	7	0.05	0.12	0.34	1.62
	10	20	0.05	0.02	0.06	0.66

Table. 3.3.: Comparison of the fractional monobeam modulation, backscatter perturbation and lock-in threshold at different gas pressures.

Figure 3.16 shows the relative Allan deviation (ADEV) at total gas pressures of 3, 6 and 10 mbar for gas mixtures with both natural neon and 50:50 neon. The corresponding time series are shown in Figure 3.14 and Figure 3.15. Data sets with long-term averaging are not possible with PR-1 as the laser is susceptible to mode hopping and mode splitting. Hence, the data to be analysed is limited to time-periods of less than 200 seconds (the time between mode-hops). The vertical axis of the Allan deviation plot is divided by Ω_E as the scaling factor.

As seen from Figure 3.16, the 'turn around' of the ADEV plots occurs around τ = 2 s. Beyond this 'turn around' point, the measurement is no longer improved by further averaging. The lowest normalised variance (highest stability) $\approx 7 \times 10^{-5}$ at τ = 2 s is achieved at a gas pressure of 10 mbar with 50:50 neon. At a higher operating pressure, the laser runs with higher output power. This translates into improved photon count by the detector.

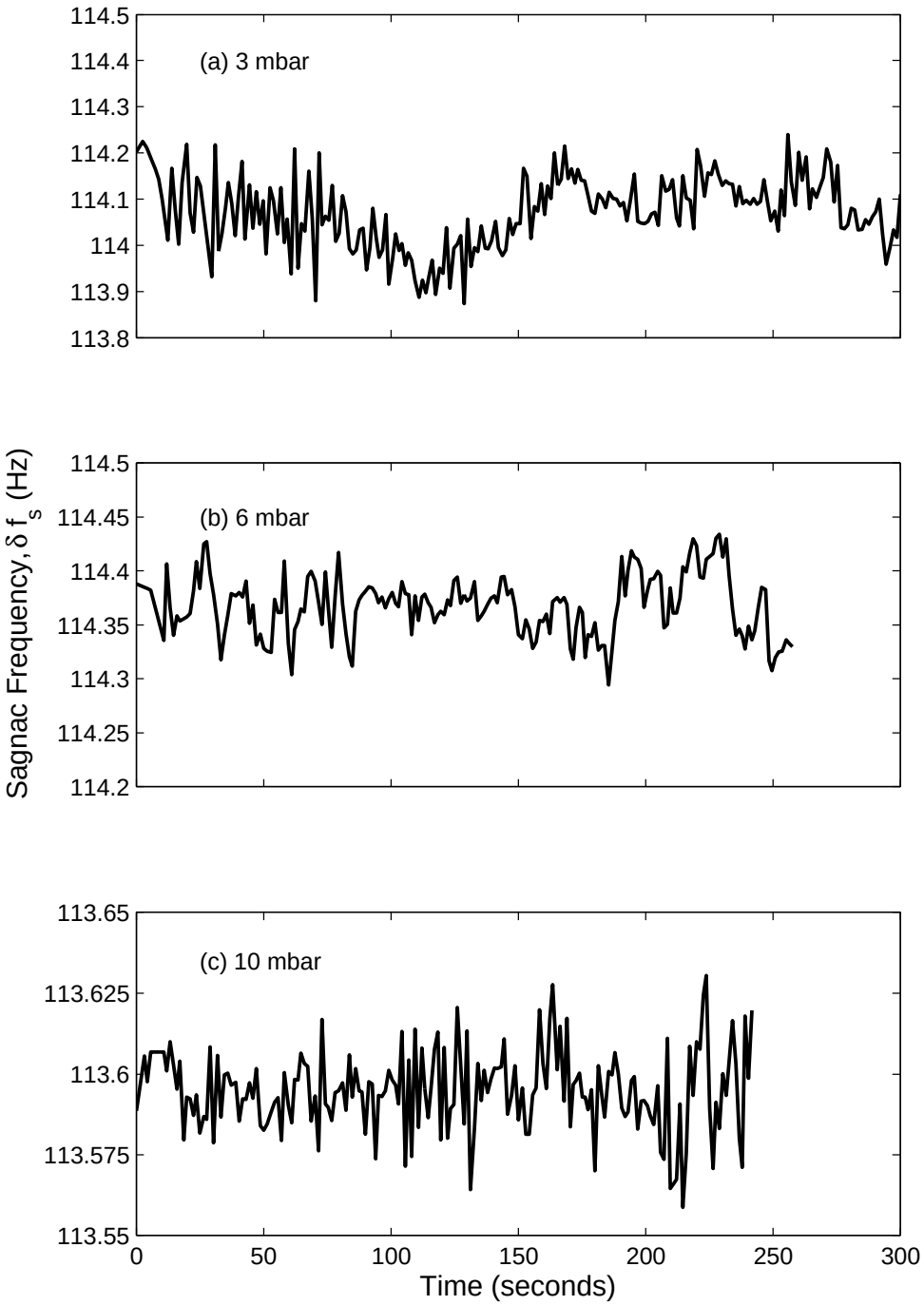

Figure. 3.14.: Short-term time series of δf_s at (a) 3 mbar; (b) 6 mbar; and (c) 10 mbar with a 50:50 neon partial pressure of 0.2 mbar.

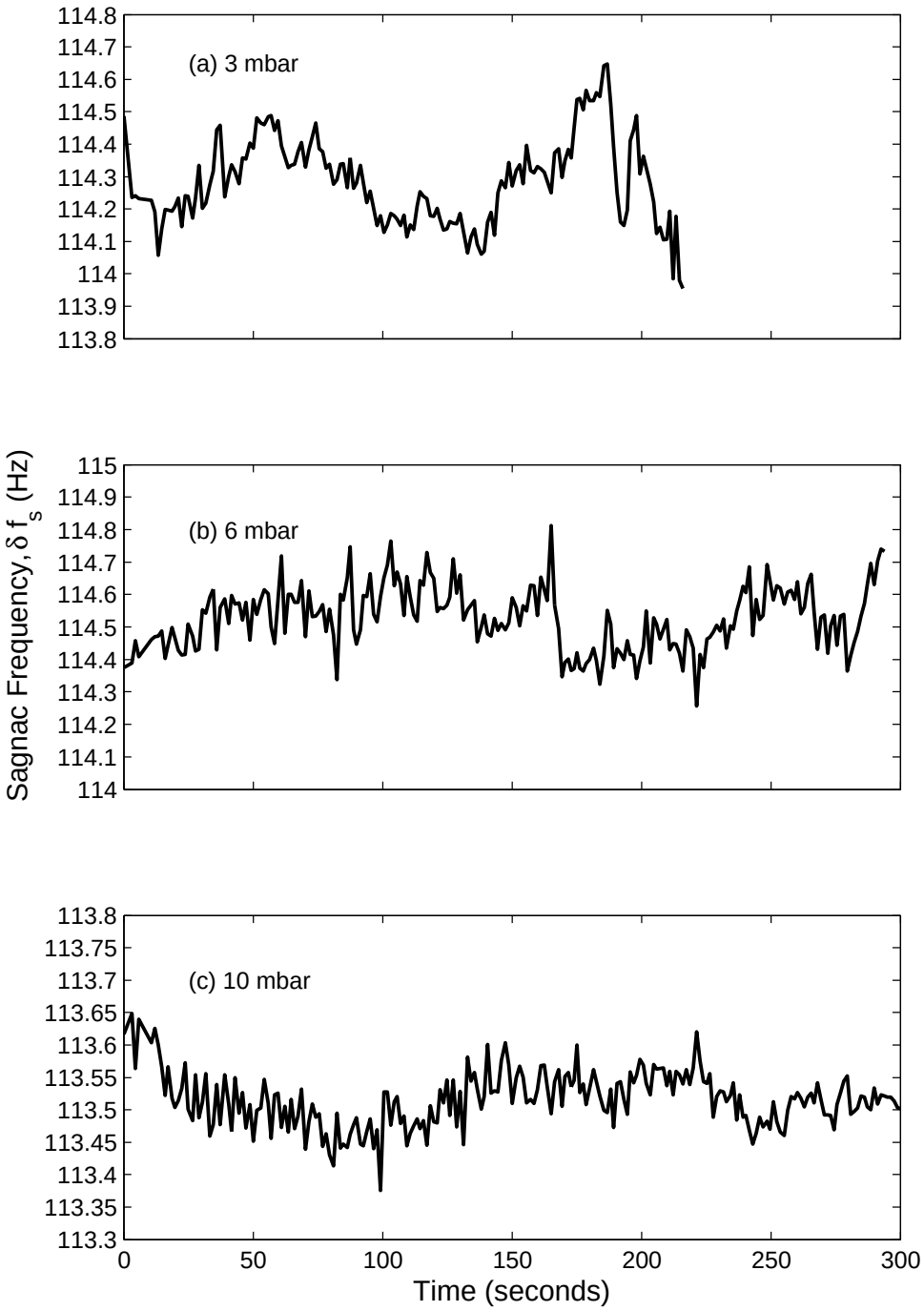

Figure. 3.15.: Short-term time series of δf_s at (a) 3 mbar; (b) 6 mbar; and (c) 10 mbar with a natural neon partial pressure of 0.2 mbar.

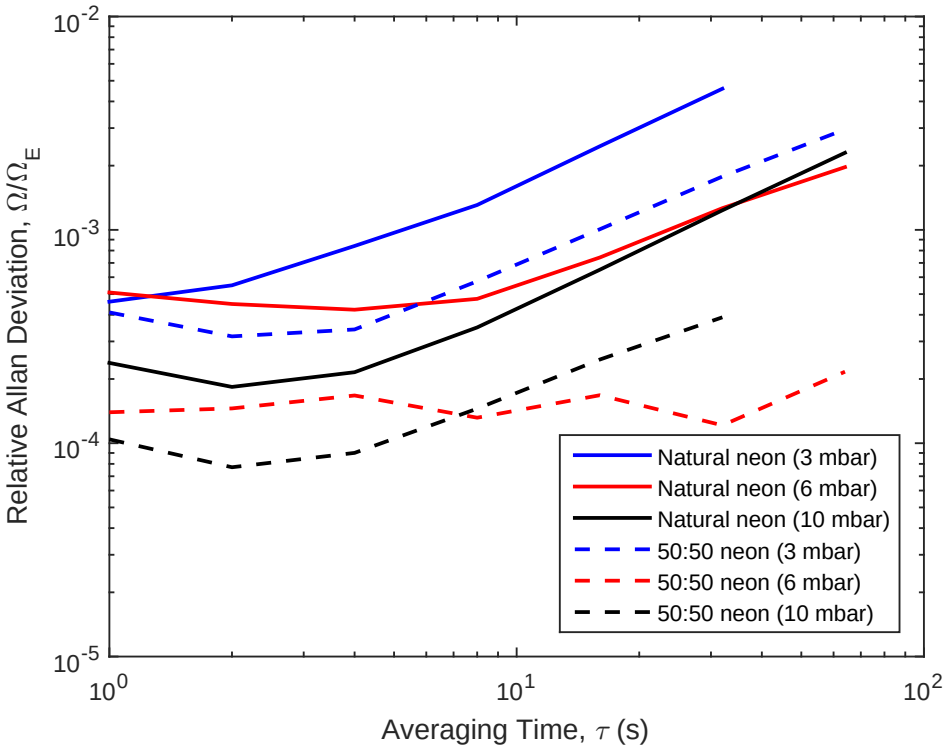

Figure. 3.16.: Allan deviation plots of PR-1 for single-mode operation at different gas mixtures.

3.2.4 Phase-locked Threshold, Multimode Threshold and the Neon Isotope Dependence

A ring laser gyroscope is capable of producing a stable rotation signal when multiple longitudinal modes are oscillating simultaneously (section 2.3.2). This is known as 'stable' multimode operation. When the laser gain is raised to allow multiple laser modes to run under the gain curve[4], the Sagnac signal will fluctuate randomly because the laser modes are essentially free running. However, if these modes are running while having a fixed phase relationship with one another[5], a stable rotation signal can be established.

In order to identify the conditions under which PR-1 operates as a gyroscope on a 'stable' multimode regime, an experiment was performed to measure PR-1 laser's phase-locked threshold and multimode threshold at different gas pressures. The phase-locked threshold in the context of this section is the measured laser output power when PR-1 started to produce a stable δf_s signal while multiple longitudinal modes (besides the main longitudinal mode) are present at the same time. On the other hand, the multimode threshold is where multiple longitudinal modes are oscillating but no stable δf_s signal is observed.

The experimental setup is shown in Figure 3.17. The mirror set employed in this experimental section was the REO 4 mirror set. A Fabry-Pérot interferometer (FP) (Coherent 33-6305-001) was mounted at the lower left corner box to observe the mode spectrum of the CW monobeam. A PMT detected the output of the FP and this signal is observed via the Tektronix PPO 7104 Digital Phosphor Oscilloscope.

As the free spectral range of the FP is 300 MHz, which corresponds to about 6 times the longitudinal mode spacing of PR-1 (ν_{fsr} = 46.875 MHz), an additional observation was performed by monitoring the beat frequency between adjacent modes with another PMT, which was mounted at the lower left corner box to detect the CCW beam. The DC signal from this PMT was coupled out by connecting a capacitor at the PMT output and the remaining AC signal was monitored through an RF spectrum analyser (Hewlett Packard ESA-L1500A).

The combined beam (δf_s) signal was monitored by an FFT network analyser (Model SR770). The Coherent power meter was placed on the top left corner box to measure the laser power. Then, the servo driver was set to the manual mode. This enables the RF power to be controlled by turning the knob manually on the servo driver.

[4] Refer to Figure 2.4 (b).

[5] This is also known as FM mode-locking where the laser is running with similar behaviour to mode-locked laser operation, but without the production of stable pulse trains [98], [99].

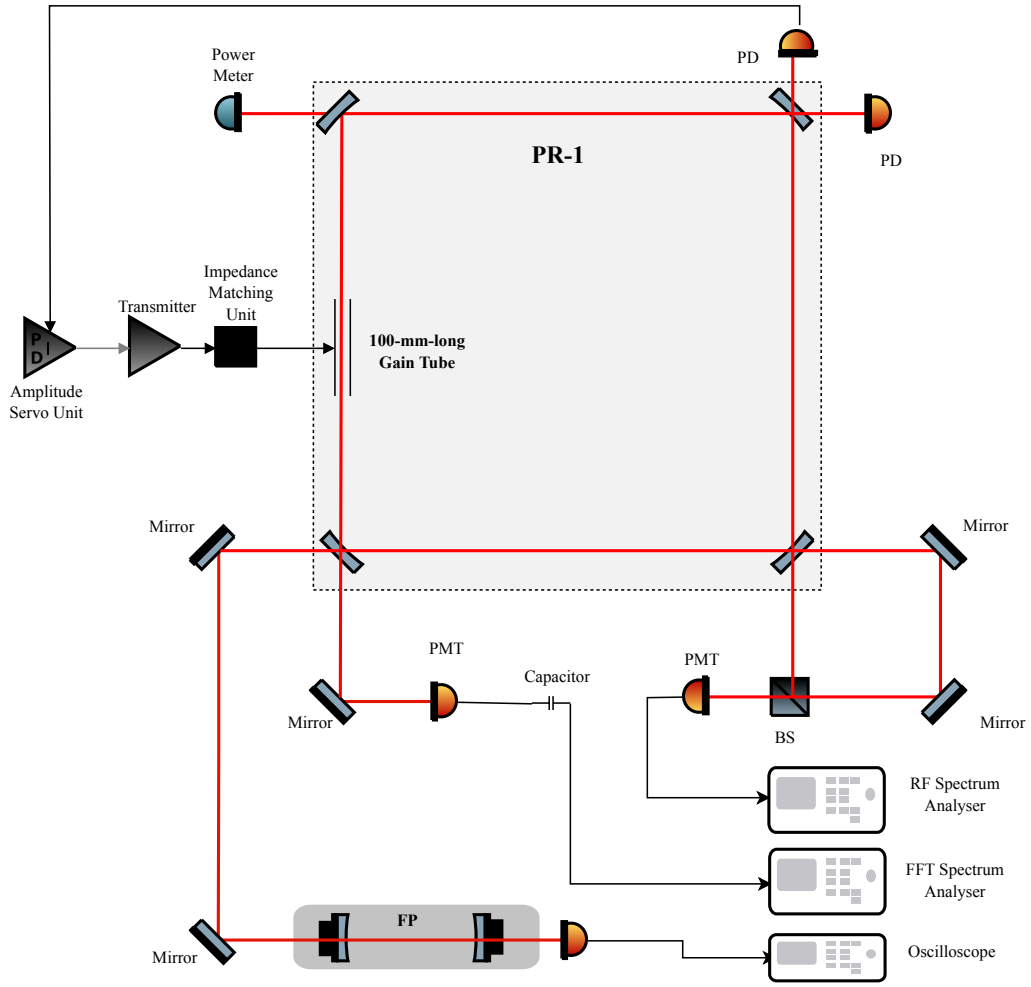

Figure. 3.17.: Experimental setup to measure phase-locked threshold and multimode threshold. BS: beam splitter (prism); FP: Fabry-Pérot interferometer; PD: photodiodes; PMT: photomultiplier tubes.

Initially, the laser cavity was filled with a partial pressure of 0.2 mbar of 50:50 neon and helium gas was added until a total gas pressure of 2 mbar was reached. Then, the RF input was increased slowly from 0 V to a maximum of 4 V (this corresponds to 0 to 25 W of RF power) while observing the laser mode structure scanned by the FP spectrum analyser on the oscilloscope. When multiple longitudinal modes began to appear, the δf_s spectrum on the FFT spectrum analyser is examined. If the observed δf_s spectrum is stable, the laser output power will be noted as the phase-locked threshold. If the observed δf_s spectrum is unstable, the laser output power will be recorded as the multimode threshold. The gas pressure was varied between 2 to 10 mbar and the experiment was repeated with 0.2 mbar of natural neon partial pressure.

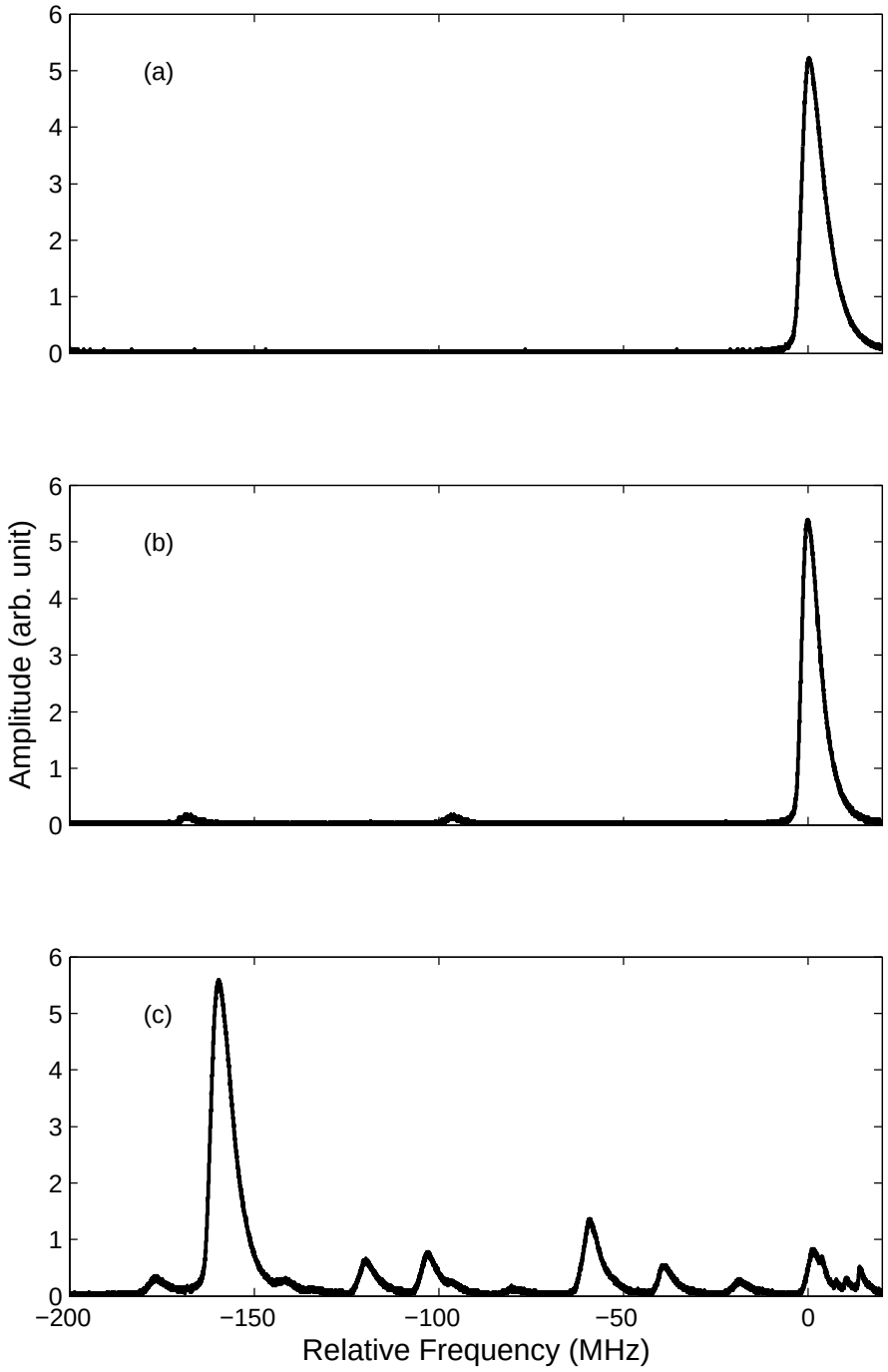

Figure. 3.18.: Laser mode structure observed on the oscilloscope when the laser is running on (a) a single longitudinal mode; (b) 'stable' multiple modes; and (c) 'unstable' multiple longitudinal modes; with gas mixture of 0.2 mbar natural neon and 10 mbar of total pressure.

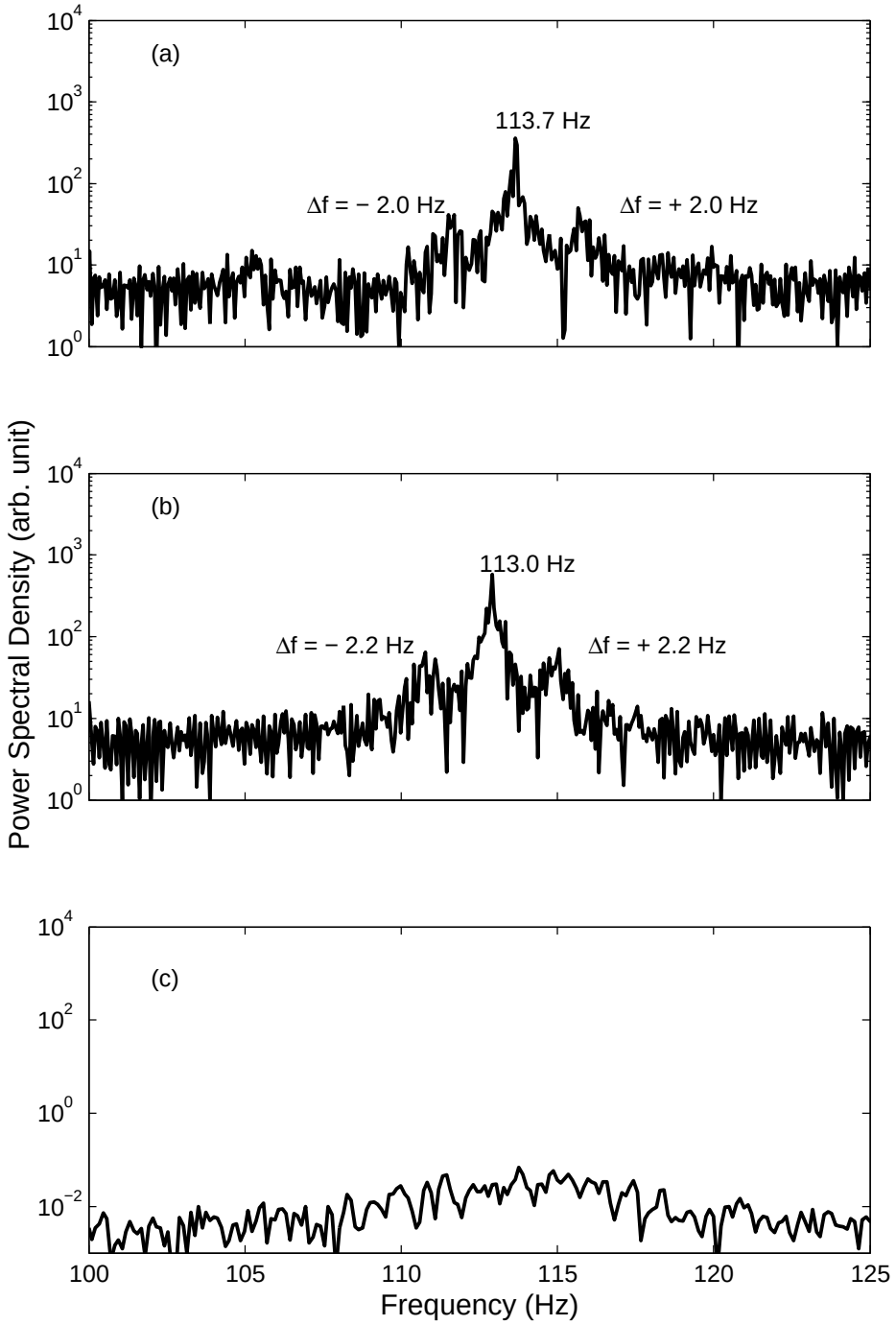

Figure. 3.19.: The power spectrum of δf_s observed for (a) single-mode operation; (b) phase-locked regime; and (c) unstable multimode regime.

An example of a single longitudinal mode spectrum observed on the oscilloscope is given in Figure 3.18 (a) for natural neon at 10 mbar. The corresponding power spectrum of δf_s when the laser is running on a single longitudinal mode is depicted in Figure 3.19 (a). The phase-locked laser mode structure observed is presented in Figure 3.18 (b) and the corresponding δf_s power spectrum observed is shown in Figure 3.19 (b). The free running laser mode structure is shown in Figure 3.18 (c) and there is no δf_s power spectrum observed as shown in Figure 3.19 (c).

Figure 3.20 (a) and (b) are plots of RF input power against the laser output power measured by the power meter at total pressures of 4 mbar and 10 mbar (with 0.2 mbar of 50:50 neon). For a gas pressure at 4 mbar, the laser was running on a single longitudinal mode within the region labelled as (i) in Figure 3.20 (a). Multiple modes began to appear at a laser output power of 24 nW (RF input power = 1.25 W) with a stable δf_s spectrum. This is the phase-locked threshold and phase-locked operation is maintained within the range labelled as region (ii). As the RF input power was increased, the phase-locked regime persisted until the multiple longitudinal laser modes observed on the FP spectrum analyser exhibited chaotic behaviour. The region (iii) in Figure 3.20 (a) is known as the multimode region and the δf_s signal is absent in this operating regime.

Similarly, at 10 mbar of total gas pressure, as the RF input power is increased, the laser reached the phase-locked threshold at a laser output power of 114 nW. However, multimode behaviour was observed between laser powers of 218 nW to 265 nW (region (ii) in Figure 3.20). The laser is essentially free running in this region. Then, as the RF input is increased beyond 14.6 W, the laser began to settle back into phase-locked operation at a laser power of 265 nW. This phase-locked behaviour is observed until the laser power reached 570 nW where the laser began to run in the chaotic multimode regime again.

A gap between the multimode and 'stable' multimode regions was only observed at 6 mbar and 10 mbar of 50:50 neon. There was no gap observed in natural neon or for other gas mixtures. Measurement of 'stable' multimode behaviour in G-0 and UG-2 show gaps at higher pressures [89], [91]. The trend observed for PR-1 was inconsistent with such behaviour probably due to the unstable environment of the PR-1 laser. Therefore, small gaps exhibiting 'unstable' multimode behaviour can be hard to observe.

Figure 3.21 compares the laser power output as a function of total pressure for different neon isotope mixtures: (a) 50:50 neon and (b) natural neon. The gray-shaded region (i) in Figure 3.21 (a) and (b) indicates guaranteed single longitudinal mode operation. The region labelled as (ii) indicates the laser is operating in the 'stable' multimode (phase-locked) regime and region (iii) is indicating the laser is free running where the multiple longitudinal modes are running chaotically and there is no stable δf_s observed.

From Figure 3.21 (a) and (b), the phase-locked and multimode threshold increases as the total gas pressure increases. The phase-locked regime for gas pressures at 2 mbar was not observed for both 50:50 neon and natural neon. The maximum laser power for the laser to run in single-mode operation for 50:50 neon is between 5 nW (at 2 mbar) to 114 nW (at 10 mbar). For natural neon, the maximum laser power for single-mode operation is 10 nW at 2 mbar and single-mode operation can persist until a laser power of 170 nW at 10 mbar. Both the phase-locked threshold and the multimode threshold are higher at higher gas pressure because when the gas pressure is high, pressure broadening dominates. The homogeneous linewidth increases from approximately 120 MHz at 2 mbar to 540 MHz at 10 mbar. Therefore, hole burning at higher pressures will be wider and this allows weak saturation to persist. Hence, the observed higher phase-locked and multimode thresholds.

Single-mode operation with natural neon can be maintained at a higher laser power than 50:50 neon because the Voight gain curve for natural neon is asymmetrical due to the higher ratio of the ^{20}Ne isotope in the gas mixture. As the gas pressure increases, the maximum gain is shifted more towards the ^{20}Ne atomic line centre. Hence, the operating frequency, ν_0 will be pulled toward the ^{20}Ne line centre to obtain the maximum gain. In a non-rotating ring laser gain medium, the CW beam in the laser cavity will saturate the neon atomic group that travels in the same direction. The same situation applies to the CCW beam where this laser beam will saturate the neon atomic group that propagates in the same direction as the CCW beam. As a result, there are two holes on each side of the Doppler-broadened linewidth of ^{20}Ne and ^{22}Ne. Since the Voight gain curve is the convolution of the Doppler broadening of ^{20}Ne and ^{22}Ne and the homogeneous broadening, the resultant gain curve will have three holes close to ν_0 at high total gas pressure for natural neon. Therefore, a single longitudinal mode will prevail.

For 50:50 neon, phase-locked operation is observed for laser output powers between 9 - 19.5 nW at 3 mbar to 114 - 570 nW at 10 mbar. On the other hand, for natural neon gas mixtures, the phased-locked region is observed at laser powers between 38 - 46 nW at 3 mbar and 180 - 220 nW at 10 mbar. The wide range of powers for which phase-locked operation is observed for 50:50 neon is because the Voight gain curve is more symmetric due to the equal ratio of ^{20}Ne to ^{22}Ne. There will be less mode competition between the oscillating laser modes hence the laser modes maintain a fixed phase relationship. As a result, the CW and CCW beams oscillate with greater stability, maintaining a stable δf_s.

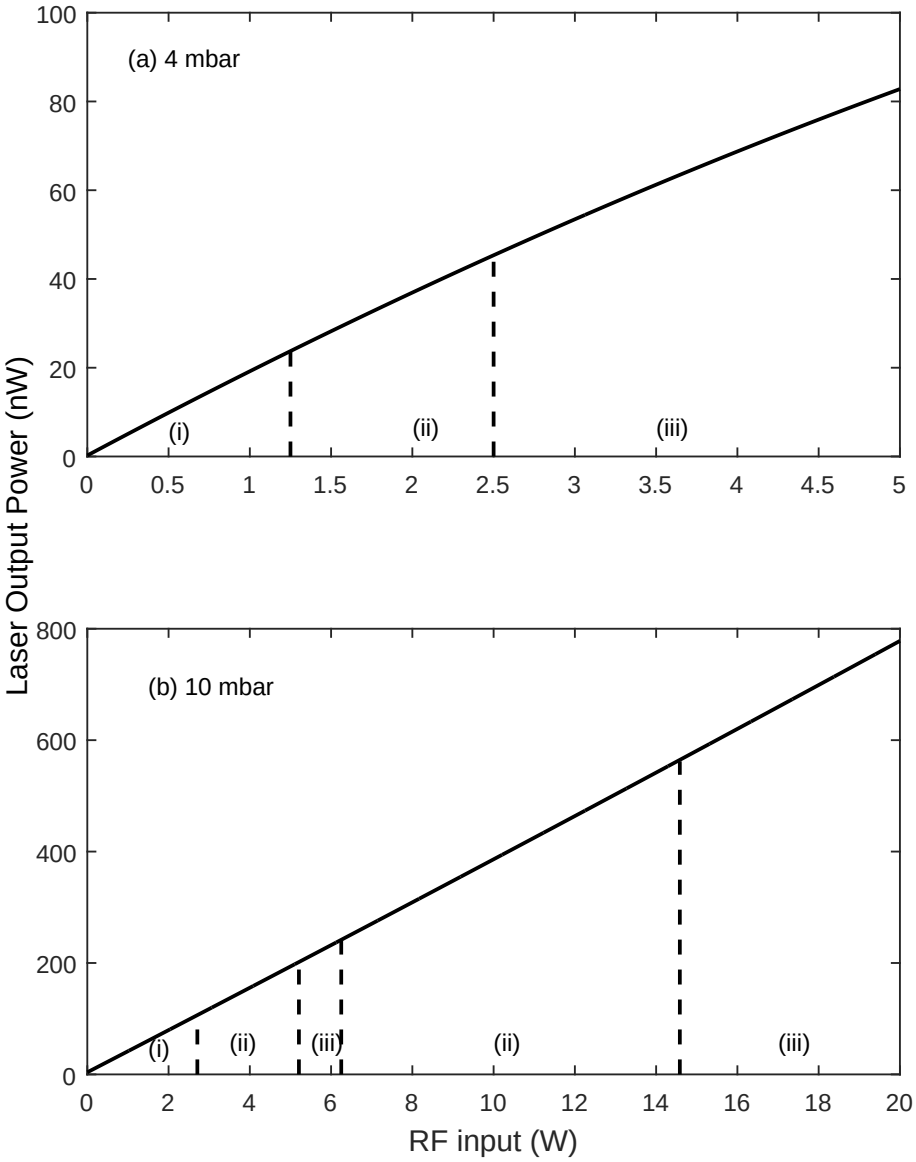

Figure. 3.20.: Laser output power as a function of RF input power with 0.2 mbar of 50:50 neon at total gas pressures of (a) 4 mbar and (b) 10 mbar. Region: (i) indicates the laser is running on a single longitudinal mode; (ii) is where stable multiple longitudinal modes co-exist with the main longitudinal mode and (iii) is where the laser modes is free running (multimode).

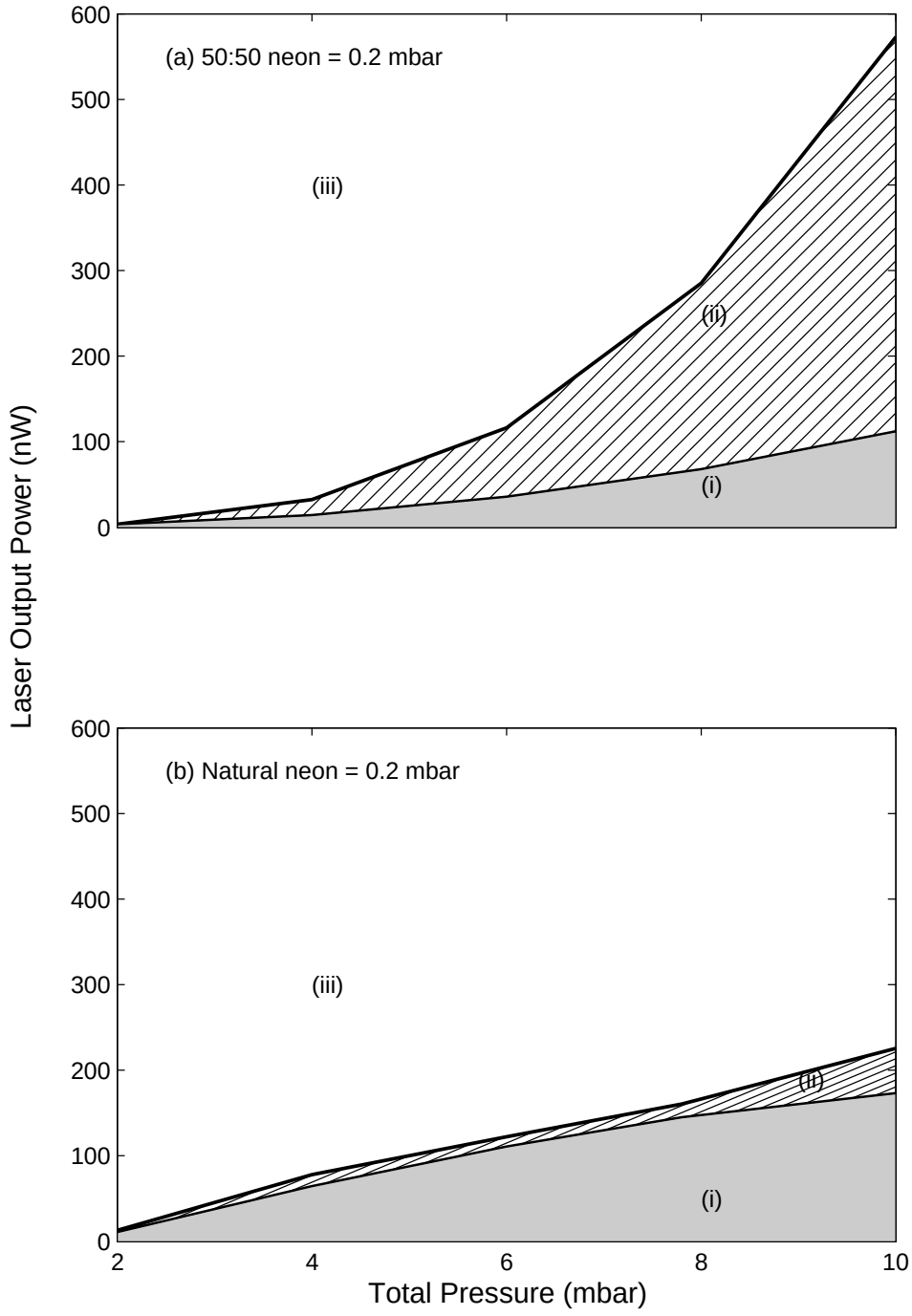

Figure. 3.21.: Laser output power as a function of total gas pressure showing the regions where the laser operates on: (i) a single longitudinal mode; (ii) stable multiple longitudinal modes; and (iii) unstable multiple longitudinal modes; with neon isotopic composition: (a) 50:50 neon; and (b) natural neon.

3.2.5 Comparison between Single-Mode and Phase-Locked Operation

An experiment to characterise the PR-1 performance as a rotation sensor with different laser mode configurations was conducted. With the REO 4 mirror set, the cavity was filled with 10 mbar of total pressure with 0.2 mbar of 50:50 neon. After lasing was established, a laser power was maintained at 75 nW for the laser to run on single-mode operation. The detected δf_s and monobeam signals were logged via Labview for half an hour. Then the laser power was raised to 300 nW where phase-locked configuration was established and the detected δf_s was logged for another half an hour. After that, the experiment was repeated with 0.2 mbar of natural neon and 10 mbar of total gas pressure.

Table 3.4 summarises the parameters recorded to compare the operation of PR-1 on different mode configurations. The Sagnac contrast ratio is the ratio between the AC signal to the DC signal received by the PMT. When PR-1 is operated with a gas fill containing 50:50 neon, the Sagnac contrast ratio was 60% for both operating regimes while the monobeam modulations varied from 1% to 4%. Due to the low backscattering, the estimated backscatter perturbation was small, which is calculated to be between 0.01 to 0.02 Hz.

The contrast ratio of the δf_s detected when PR-1 was operated with natural neon is 28% for single-mode operation and 30% for phase-locked operation. The detected modulation was between 2 to 3%. The backscattering perturbations are still small and comparable to operation with 50:50 neon.

Neon Isotope	Operating Mode	Output Power (nW)	δf_s contrast ratio (%)	m_1	m_2	Δf_{bs} (Hz)	f_L (μHz)
50:50 (10 mbar)	Single-mode	75	60	0.01	0.04	0.02	0.42
	Phase-locked	300	60	0.02	0.03	0.03	0.51
Natural (10 mbar)	Single-mode	80	30	0.03	0.02	0.02	0.51
	Phase-locked	200	28	0.02	0.03	0.03	0.51

Table. 3.4.: Comparison of the gyroscope operational characteristics such as the laser output power, the δf_s contrast ratio, the monobeam modulation, the backscatter perturbations and the lock-in threshold when the PR-1 laser is operated with different laser mode configurations at a total pressure of 10 mbar.

The stability of PR-1 as a rotation sensor for both single-mode operation and phase-locked operation on different neon isotope ratios was characterised by using the relative ADEV plot as shown in Figure 3.22. The performance of PR-1 with natural neon shows a minimum variance at 3×10^{-4} relative to the Earth rotation rate at a measurement time of 10 s. The performance shows geometrical instability after 10 s. The PR-1 performance with 50:50 neon for both single-mode and phase-locked operation shows a comparable

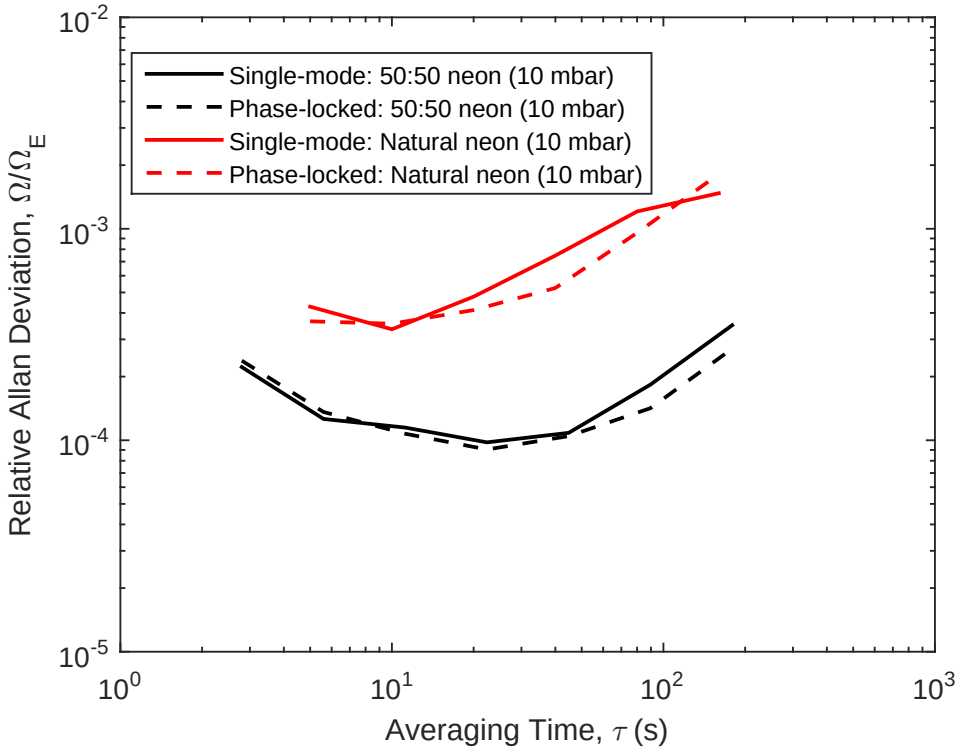

Figure. 3.22.: Comparison of the relative Allan deviation for PR-1 operating in the single-mode and phase-locked regimes.

stability and the minimum variance established was approximately 9×10^{-5} of the Ω_E at $\tau = 20$ s.

Parameter	REO 3	REO 4
Ring-down, τ_{decay} (μs)	135	120
Total loss, L (ppm)	158	177.8
Quality factor, Q	4.0×10^{11}	3.6×10^{11}
Finesse, F	4.0×10^{4}	3.5×10^{4}
Laser power, P_i (nW)	25	75
Resolution, Ω_s (rad/s/$\sqrt{\text{Hz}}$)	1.2×10^{-9}	2.4×10^{-10}
Relative ADEV, Ω/Ω_E	7×10^{-5}	9×10^{-5}
Lock-in threshold, f_L (μHz)	0.42	0.81

Table. 3.5.: Summary of relevant parameters of PR-1 running on 50:50 neon at 10 mbar of total pressure (single-mode regime) at a wavelength of 632.8 nm.

The optimum performance of PR-1 operating at 632.8 nm is summarised in Table 3.5. The table lists the relevant parameters of PR-1 running on a single-mode with the REO 3 and REO 4 mirror sets. The PR-1 laser reached a sensor resolution of 1.2×10^{-9} rad/s/$\sqrt{\text{Hz}}$ and 2.4×10^{-10} rad/s/$\sqrt{\text{Hz}}$ with the REO 3 and REO 4 mirror set respectively. The laser achieved a higher resolution with the REO 4 mirror set because the measured output power was three times higher (due to the higher mirror transmission loss in comparison to

the REO 3 mirror set). The performance of the PR-1 laser is comparable to the GEOsensor laser which achieves a resolution of 1.1×10^{-10} rad/s/$\sqrt{\text{Hz}}$ [17].

3.3 Conclusion

The maximum excess gain from PR-1's 100 mm long gain tube was measured to be less than 2000 ppm. From this measurement, it is concluded that an extra gain tube is needed for laser operation on lower gain neon transitions. PR-1's performance is mostly influenced and limited by environmental factors. As observed from the relative Allan deviation plots in Figure 3.16 and Figure 3.22, operation on gas mixtures of 50:50 neon produces higher stability than gas mixtures with natural neon. This is because the mode competition is much lower with the 50:50 neon gas mixture. Other than that, performance at higher gas pressures is more stable than operation using lower gas pressure. At a higher pressure, the laser output power is higher with a correspondingly higher photon count at the detector.

There is no significant difference between the performance of PR-1 running in the single-mode and phase-locked regimes. The range of laser output powers for operation in the phase-locked regime was larger with an equal ratio of neon isotopes at higher gas pressure. Single-mode operation persists at higher laser powers with natural neon due to the asymmetric gain curve. PR-1 is able to unlock on the Earth rotation at total gas pressures of 2 to 12 mbar and with 0.2 mbar partial pressure of neon gas (for both natural and 50:50 neon).

4

The Macek and Davis Experiment Revisited: A Large Ring Laser Interferometer Operating on the $2s_2 \rightarrow 2p_4$ Transition of Neon

It has recently been demonstrated that a large helium-neon based ring laser gyroscope operating at a wavelength of 1152.3 nm can unlock on the rotation of the Earth [97]. The intra-cavity mirrors employed in the experiment were fabricated via a novel micro-fabrication based substrate-transfer technique with the apparent advantage of minimising thermally induced mechanical fluctuations in the mirror coatings [100]. These mirrors are different from the industry standard ion beam sputtered (IBS) dielectric multilayer mirrors employed previously in our ring laser gyroscopes. The objective of this chapter is to characterise the PR-1 gyroscopic performance on the 1152.3 nm helium-neon transition by incorporating these new state-of-the-art mirrors.

4.1 Near Infrared Ring Laser Gyroscopes

The development of the inertial navigation technology based on ring laser gyroscopes developed rapidly to replace the traditional mechanical gyroscopes[1] after the first demonstration of rotation sensing by a 1 m^2 ring laser in 1963 [9]. In the early implementation of these optical navigation gyros, the operating wavelengths were based on the infrared (1152.3 nm) wavelength before slowly transitioning to the now commonly used 632.8 nm laser wavelength in the late 1970s [101]. Naturally, the sensitivity of navigational ring laser gyroscopes increases tremendously with the implementation of highly reflective mirrors in the cavity. These mirrors (pioneered by Litton Systems Inc for ring laser gyroscopes) have optical scattering and absorption losses at the level of single parts per million (ppm) [102]. Therefore, with the advances in mirror technology available today, it is of interest to reproduce the seminal 1963 Macek and Davis experiment, albeit with a laser system which can detect the rotation of the Earth.

[1] Mechanical gyroscopes use a spinning mass as the sensing element. Therefore, they are subject to many mechanical assemblies, precise machining requirements and rigid manufacturing processes. On the contrary, a ring laser gyroscope has no moving mechanical parts and requires little maintenance. As a result, the performance of the laser gyroscopes supersedes their traditional counterparts.

In addition, backscatter remains as the major source of frequency drift of all ring laser gyroscopes. The backscattering effect leads to mode coupling between the counter-propagating waves. The predominant sources of this coupling are mirror imperfections and contamination since the only intra-cavity elements in our large ring laser gyroscopes are the mirrors which form the cavity itself [17]. One alternative to reduce the systematic error caused by the backscatter is by using a longer operating wavelength. Theoretically, the backscatter amplitude will be reduced dramatically as Rayleigh scattering (assuming we are operating near the Rayleigh limit) is inversely proportional to the fourth power of the laser wavelength [103]. The challenge of operating a large-scale ring laser gyroscope with a longer wavelength is an inevitable reduction in the scale factor of the gyroscope. In principle, however, the reduction in the scale factor should not be a major issue (since the lock-in thresholds are typically in the μHz range) and a net improvement in the performance of ring laser gyroscopes could be anticipated [97].

4.1.1 Ultra Low Loss Crystalline Mirrors

The only optical element inside our ring cavities are the highly reflective mirrors. These high-quality mirrors are usually fabricated via an ion beam sputtering (IBS) technique where highly reflective dielectric multilayers are deposited onto a super-polished substrate (fused silica). The IBS deposition process produces mirror coatings with excellent adhesion, fewer impurities and low absorption loss. For this reason, the IBS technique has become the leading coating method for producing the highly reflective mirrors required by high precision optical measurements [104].

All Canterbury large ring laser gyroscopes incorporate these IBS-mirrors to achieve a high cavity Q for precision sensing. Other than that, the IBS-mirrors are also employed in various highly sensitive optical interferometric systems such as stabilised lasers for optical atomic clocks and gravitational wave detectors [105], [106]. Typically, IBS-mirror coatings consist of alternating layers of silica, SiO_2 films and tantalum pentoxide films, Ta_2O_5. The internal friction in the high index Ta_2O_5 layers causes excess mechanical loss as they are intrinsically amorphous [107]. This excess mechanical loss gives rise to coating thermal noise; where random fluctuations on the mirror surface change the cavity optical path length.

Coating thermal noise limits the performance of precision measurements by highly sensitive optical interferometers [108], [109]. According to the fluctuation-dissipation theorem in optical interferometry, the overall thermal noise floor is determined by the loss angles[2] contributed by the substrate, the spacer and the coatings [110]. The coating mechanical loss is typically several orders of magnitude larger than that of the substrate.

[2]The phase lag between the stress and strain is known as the mechanical loss angle (mechanical dissipation factor). It is defined as a measure of the dissipation of mechanical energy in a material.

Hence, various methods to reduce coating thermal noise have been proposed. These include lowering the coating growth temperature, re-designing the coating thickness, and by doping the tantala layers with other amorphous constituents [104].

Recently, a novel optical coating technology based on direct-bonded monocrystalline multilayers offers a new alternative to compete with the IBS-mirrors. Monocrystalline $Al_xGa_{1-x}As$ heterostructures[3] (AlGaAs) have emerged as a promising candidate for new mirror coatings owing to the material's capability to reduce the loss angles. The mirror is fabricated based on the substrate-transfer coating procedure [100]. These crystalline (GaAs/AlGaAs) coatings achieve a ten-fold reduction in mechanical loss in comparison to the dielectric coating multilayers [100]. Hence, there is a growing interest to implement these new mirrors in precision optical interferometers.

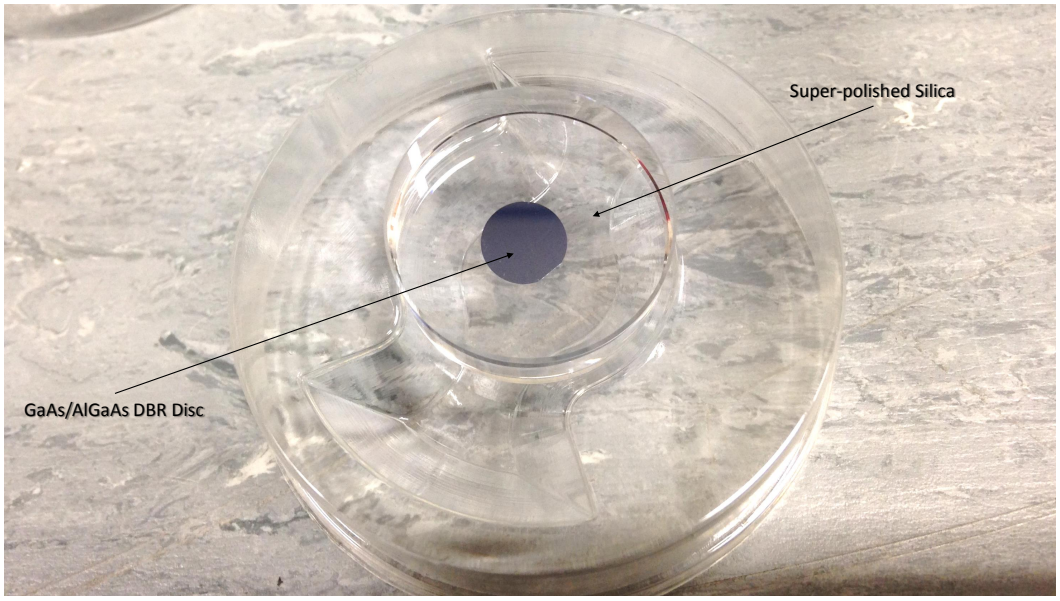

Figure. 4.1.: Crystalline coated mirrors comprising an 8 mm diameter GaAs/AlGaAs mirror pad transferred to a 25 mm diameter fused silica substrate.

In this section, the implementation of the crystalline mirrors in the PR-1 ring laser system will be studied to investigate the effect of these low-thermal-noise mirrors in large-ring laser gyroscopes. The crystalline mirrors were obtained through a collaboration between Crystalline Mirror Solutions (CMS), USA, Technische Universität München (TUM), Germany and University of Canterbury (UoC), New Zealand. Figure 4.1 shows a photograph of a crystalline supermirror. The supermirror structure consists of an 8 mm diameter crystalline (GaAs/AlGaAs disc) coating transferred onto a super-polished fused silica substrate with 4 m radius of curvature (ROC). For a square ring laser configuration, the coating is optimised at a 45° angle of incidence (AOI). Each highly reflective DBR

[3] AlGaAs is widely recognised in quantum optomechanics studies as it offers high optical and mechanical qualities to reach the quantum regime of mechanical motion. The quantum optomechanics field exploits optomechanical interactions within optical cavities to control and study the quantum regime of nano-scale mechanical oscillators [111].

mirror disc consists of 38.5 layer pairs of GaAs and $Al_{0.92}Ga_{0.08}As$. The thickness of each mirror disc is approximately 7.1 μm. The specification of the supermirrors provided by CMS is summarised in Table 4.1 below:

Parameter	Value
Radius of curvature, ROC (m)	4
Transmission (s-polarisation) per mirror at 1152.3 nm (ppm)	1.9
Transmission (p-polarisation) per mirror at 1152.3 nm (ppm)	15.1
Absorption loss per mirror (ppm)	1
Total scatter losses (ppm)	3.4

Table. 4.1.: The crystalline mirror specifications provided by CMS.

4.2 Experimental Details

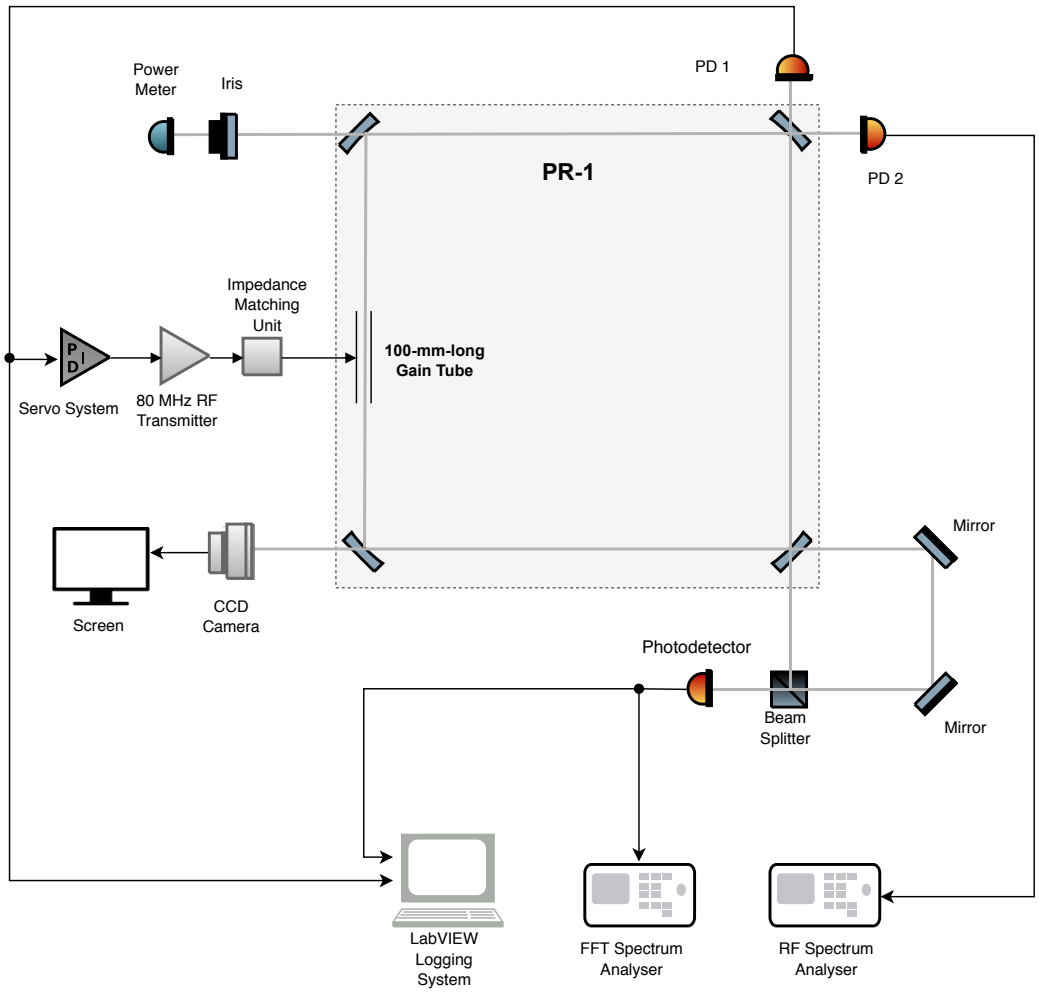

Figure. 4.2.: Schematic diagram of the experimental setup.

Figure 4.2 is a schematic diagram to illustrate the overall experimental setup. After installing the crystalline mirrors, the laser cavity was filled with 0.2 mbar of natural neon followed by excitation via the RF transmitter. A CCD camera (Pacom) was installed at the

lower left corner of PR-1, and the signal from the camera was connected to a small screen to view the infrared laser spot. The bright laser spot from pure neon laser excitation was helpful in terms of aligning the laser cavity, as it is more easily observed by a handheld IR viewer and a ThorLabs NIR detector card (VRC5).

Then, all external fold mirrors were replaced with broadband dielectric mirrors (Thorlabs BB1-EO3) with a coating reflectance of approximately 99.5% at 1.15 μm. A 50:50 non-polarising beam splitter cube (Thorlabs, 1100-1600 nm) was employed to combine the two counter-propagating beams at the lower right corner, and this combined beam was detected by a thermo-electrically cooled type infrared photodetector (Hamamatsu, G6126).

An aperture was placed at one corner of the mirror box, and the power meter sensor (Coherent, OP-2-IR) was fixed after the aperture to measure the laser power. This aperture will prevent light transmitted around the edges of the 8 mm reflective coatings from contaminating the signal detected by the power meter.

Two photodetectors, 10 MHz New Focus Adjustable InGaAs Photoreceiver (PD 1) and 125 MHz New Focus InGaAs Photoreceiver (PD 2) were installed at the top right corner of the laser cavity to detect the monobeams. The output from PD 1 was fed into the servo system while the output from PD 2 was connected to the RF spectrum analyser to monitor the ν_{fsr} beat frequency. The calibration of the detector output to the servo system will be explained in detail in Section 4.2.4.

4.2.1 The Cavity Q-Factor

The laser cavity Q-factor was determined by following the same procedures outlined in Section 3.2.1. The signal from PD 2 was connected to the oscilloscope and the ring-down time was measured to be 33 μs. From the obtained ring-down time, the total loss per mirror is approximately 161.6 ppm which translates to a maximum total fractional loss per circuit of 646.5 ppm. The Q-factor and the cavity finesse are 5.4×10^{10} and 9.7×10^{3} respectively, as shown in Table 4.2 below.

By referring to Table 4.1, the mirror transmission is 1.9 ppm in the s-polarisation, the loss due to absorption is 1 ppm and the loss due to scattering is 3.4 ppm. Therefore, the total loss per mirror should be around 6.3 ppm. The additional loss from the crystalline coated infrared mirrors may be due to extra light being transmitted around the edges of the reflective coatings which only cover a portion of the substrate surface.

After that, the laser power of the counter-rotating laser beams was recorded at every corner of the cavity. With a constant RF input power at 5 W, the output power of the

Parameter	Value
Ring-down time, τ_{decay} (μs)	33
Total loss, L (ppm)	646.5
Loss per mirror (ppm)	161.6
Quality factor, Q	5.4×10^{10}
Finesse, F	9.7×10^{3}

Table. 4.2.: The τ_{decay} measured and the corresponding cavity Q factor, finesse, F and loss per mirror with IR mirrors (ν_0 = 260 THz).

CW beam is approximately 4 to 15% higher than the CCW beam as shown in Table 4.3 below.

Corner	CCW Beam Output Power (nW)	CW Beam Output Power (nW)
Lower right	153.6	-
Lower left	122	145
Upper right	144	163
Upper left	155	162

Table. 4.3.: Power meter reading at each corner of PR-1. The RF power was maintained at 5 W throughout the measurement. Note that the output power of the clockwise beam at the lower right corner was unable to be measured because the beam combining prism was positioned at this corner.

4.2.2 Gas Pressure Optimisation

The laser output power at various helium and neon gas mixtures was measured to investigate the optimum gas fill appropriate to operate the ring laser at 1152.3 nm. The output power in this context is the single beam (CCW laser beam) intensity measured by a power meter located at the upper left side of PR-1 corner box.

Firstly, the laser cavity was filled with 0.1 mbar of neon (either 50:50 neon or natural neon). Then, a constant RF power of 20 W was applied, and the laser output power was recorded. We chose an RF input power of 20 W, which is with the highest available RF power to measure the maximum obtainable laser output power. After that, the RF excitation was turned off, and the cavity pressure was altered by bleeding helium gas slowly into the laser cavity until the desired total gas pressure was obtained. The gas fill was allowed to mix for approximately 10 minutes before the plasma was re-ignited. The reflected power was checked to be a minimum before each laser output measurement to ensure the maximum (20 W) power is transferred to the gain medium. The experiment was repeated with different partial pressures of natural neon and 50:50 neon with total gas pressure variations from 1 mbar to 12 mbar.

During the measurement, the output power of the laser was observed to be changing. Therefore, laser output power measurements were made instantly (at time = 0 s), one

minute (time = 60 s) and two minutes (time = 120 s), after the RF excitation was applied. We did not perform multiple measurements on one specific gas pressure because as the number of gas fill process increases, the risk of dust and impurities from the environment to flow into the PR-1 cavity will be higher.

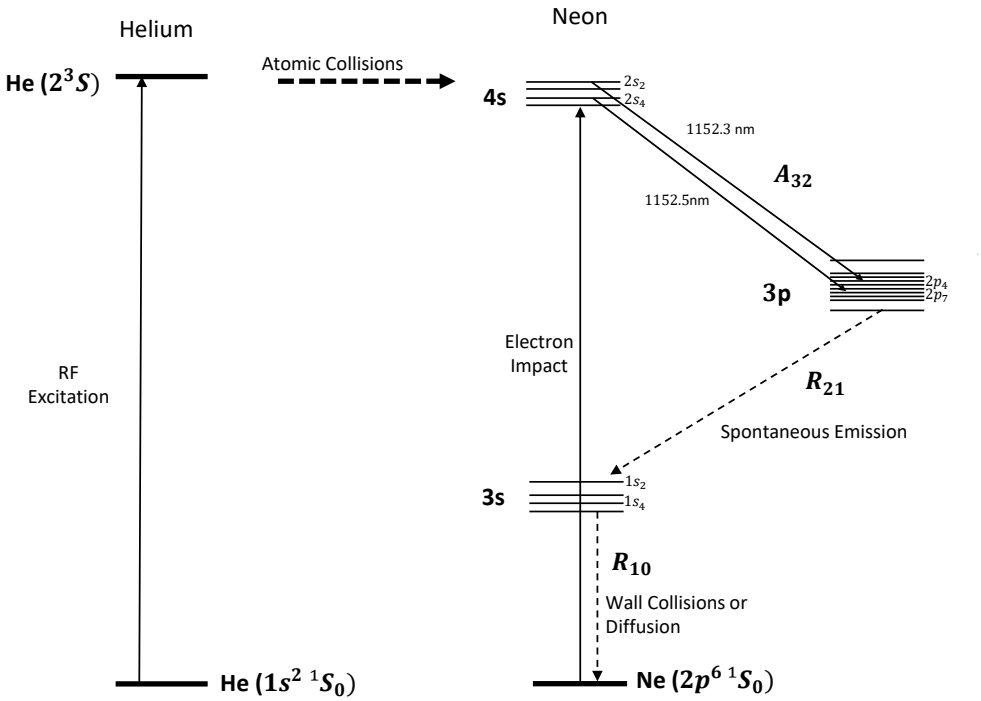

Figure. 4.3.: Schematic diagram representing the helium-neon energy levels involved in the laser action at 1152.3 nm and 1152.5 nm, where A_{32} is the spontaneous decay rate from $4s$ state to $3p$ state; R_{21} is the relaxation rate from $3p$ state to $3s$ state; and R_{10} is the relaxation rate from $3s$ state to the ground state.

Figure 4.3 is a schematic diagram showing the helium-neon energy levels involved in the laser action at 1152.3 nm and 1152.5 nm. As explained earlier in Section 2.2.1, laser action with pure neon can be achieved due to excitation via electron impact. Fast-moving electrons are accelerated via RF excitation and collide with neon atoms. These neon atoms are excited to upper levels ($2s_2$ and $2s_4$) and remain in these upper levels for approximately 96 and 98 ns (Table 2.1). Emission from the neon $4s$ levels are repeatedly reabsorbed by unexcited neon atoms thereby populating the $4s$ metastable level [76]. Population inversion is achieved due to the short lifetime of the terminal $3p$ levels.

Figure 4.4 shows the measured laser output power for gas fills with natural neon and 50:50 neon pressures between 0.1 mbar to 0.6 mbar. It can be observed that the highest gain is achieved at a neon pressure of 0.2 mbar. This is consistent with the measurement reported in ref. [97]. For neon only, this corresponds to simultaneous laser oscillations on the neon doublet split by 51 GHz ($2s_2 \rightarrow 2p_4$ at 1152.3 nm and $2s_2 \rightarrow 2p_7$ at 1152.5 nm) [72]. Note that, the gain at 0.1 mbar declines after two minutes. By contrast, for higher neon pressures, the output power increases after two minutes.

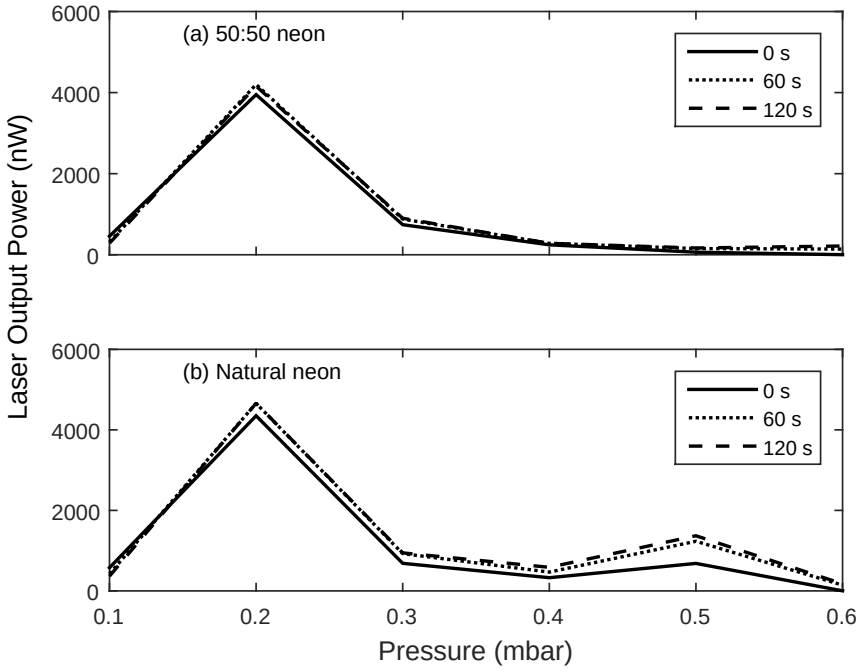

Figure. 4.4.: Laser output power as a function of pressure for (a) 50:50 neon only and (b) natural neon only; at a constant RF input power of 20 W.

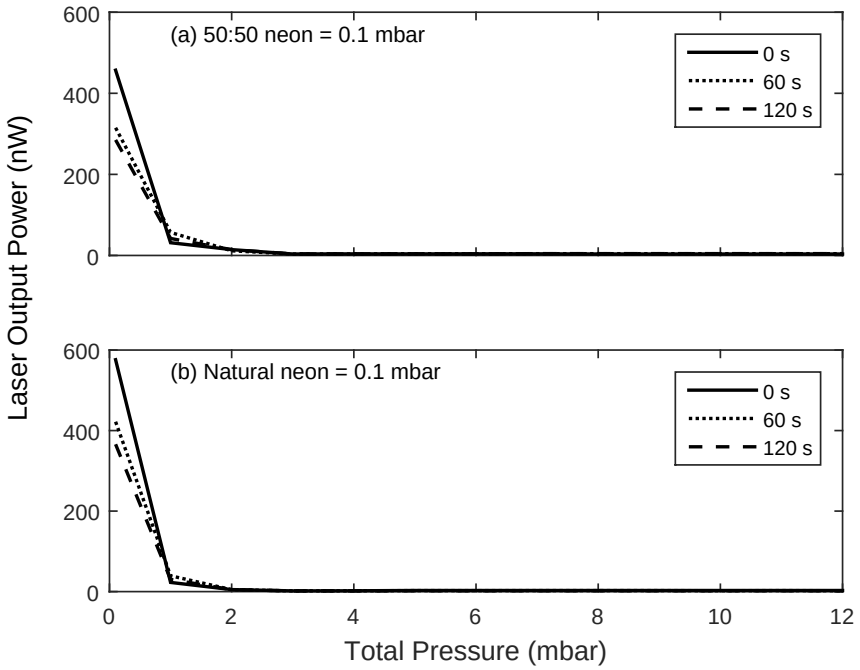

Figure. 4.5.: Laser output power as a function of total helium-neon gas pressure at a constant RF input power of 20 W for: (a) 50:50 neon and (b) natural neon (for a partial neon pressure of 0.1 mbar).

Figure 4.5 shows the laser output power as a function of total pressure with the neon pressure fixed at 0.1 mbar. From the figure, the laser output power for 0.1 mbar 50:50 neon

only was 457 nW (576 nW for natural neon) when the laser power was measured instantly. After two minutes, the power drops to 285 nW (366 nW for natural neon). When helium gas is added into the mixture, the output power begins to decrease to 31 nW at 1 mbar (for 50:50 neon), though, there is a slight increase (to 57 nW) in the laser output power after one minute, then the laser power decreases again (42 nW). The laser extinguishes at 2 mbar of total gas pressure.

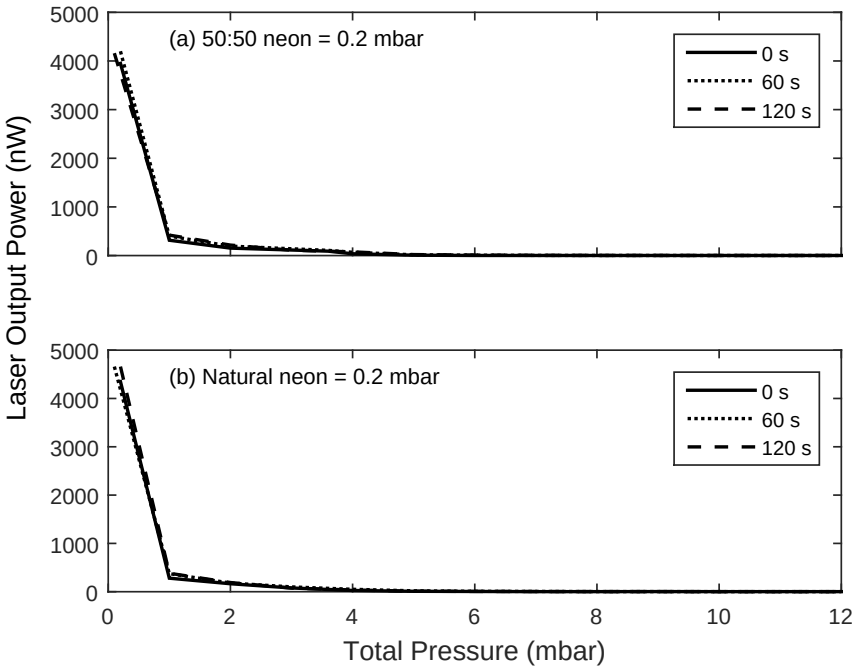

Figure. 4.6.: Laser output power as a function of total helium-neon gas pressure at a constant RF input power of 20 W for: (a) 50:50 neon and (b) natural neon (for a partial neon pressure of 0.2 mbar).

For a neon partial pressure of 0.2 mbar, the addition of helium reduces the laser output power substantially as shown in Figure 4.6 (a) and (b). The laser power is observed to rise slightly after two minutes. Figure 4.6 (b) shows the highest laser output power is 4660 nW with 0.2 mbar of natural neon. The laser power drops to 382 nW at 1 mbar of total gas pressure; and continues to decrease as more helium was bled into the cavity. Finally, the laser ceases at a total pressure of 4 mbar.

In Figure 4.7 (a) and (b), the laser output decreases when helium is added into the laser cavity as observed previously (Figure 4.5 and Figure 4.6). The laser output power is higher after 2 minutes of RF excitation. There is no laser power detected above 7 mbar of total gas pressure. From Figure 4.7, one notable observation is that laser action starts after 1 minute at total pressures of 5 and 6 mbar.

In contrast to the previous observations, for gas mixtures having more than 0.3 mbar of neon gas, the laser output power increases as helium is added into the cavity. For

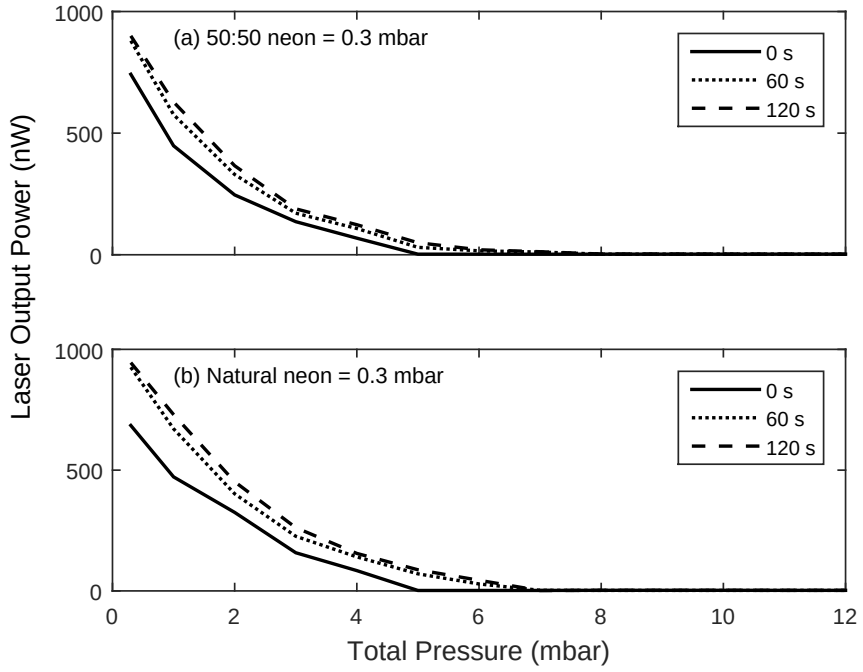

Figure. 4.7.: Laser output power as a function of total helium-neon gas pressure at a constant RF input power of 20 W for: (a) 50:50 neon and (b) natural neon (for a partial neon pressure of 0.3 mbar).

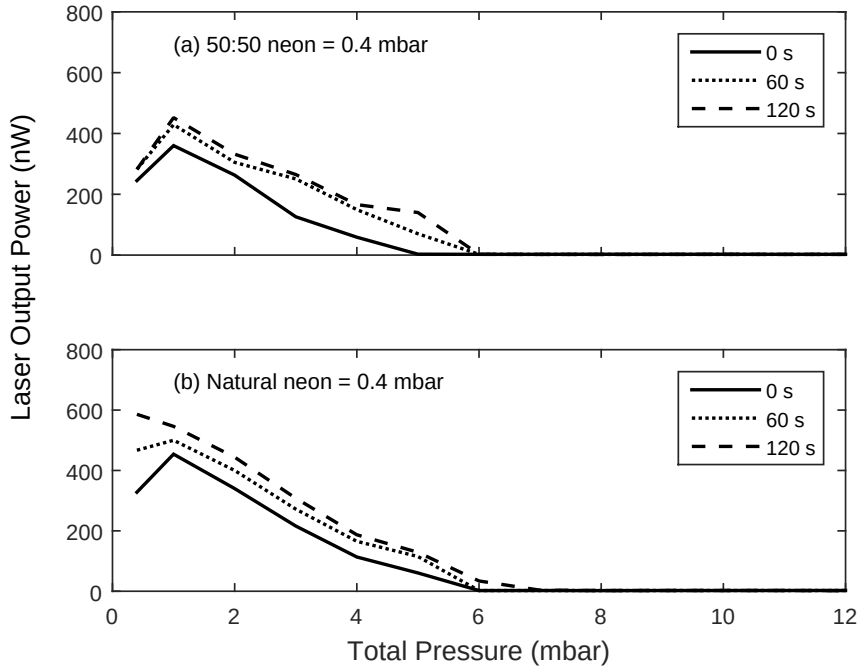

Figure. 4.8.: Laser output power as a function of total helium-neon gas pressure at a constant RF input power of 20 W for: (a) 50:50 neon and (b) natural neon (for a partial neon pressure of 0.4 mbar).

example, at 0.4 mbar of 50:50 neon, the laser power increases from 245 nW (for neon only) to 360 nW when 0.6 mbar of helium is added into the laser cavity. When more helium is added, the output power starts to drop as shown in Figure 4.8 (a) and (b).

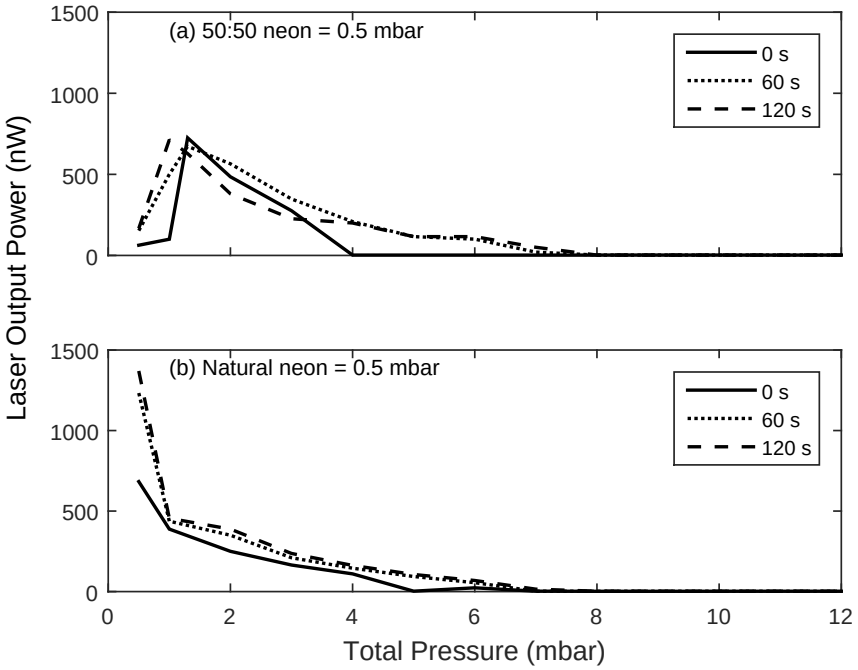

Figure. 4.9.: Laser output power as a function of total helium-neon gas pressure at a constant RF input power of 20 W for: (a) 50:50 neon and (b) natural neon (for a partial neon pressure of 0.5 mbar).

With 0.5 mbar of neon, there is a significant difference between the two neon isotopes. As shown in Figure 4.9 (a), with a 50:50 neon gas fill, the laser output power rises at 1 mbar of total pressure. Then, the power starts to decrease at 2 mbar of total gas pressure. On the other hand, for the natural neon gas fill, the laser output power was the highest with a gas fill of 0.5 mbar of neon-only (Figure 4.9 (b)) and the laser output power drops when helium is introduced into the cavity. Nevertheless, for both neon isotopes, the laser output power decreases above 2 mbar of total helium-neon pressure and the laser action ceases at 7 mbar of total pressure.

At 0.6 mbar of neon, the highest laser power is achieved at 2 mbar of total gas pressure (for both 50:50 neon and natural neon). The laser power starts to drop above 2 mbar of total gas pressure as shown in Figure 4.10 (a) and (b). Also, there is a notable delay in laser action at total gas pressures between 4 mbar to 8 mbar.

Some common observations can be made from the data presented in Figures 4.4 to 4.10. Firstly, the measured laser output power is consistently higher for natural neon than with 50:50 neon because the gain profile for an equal ratio of ^{20}Ne and ^{22}Ne isotopes is symmetrical and the laser operating frequency will be at the centre of the gain curve. On

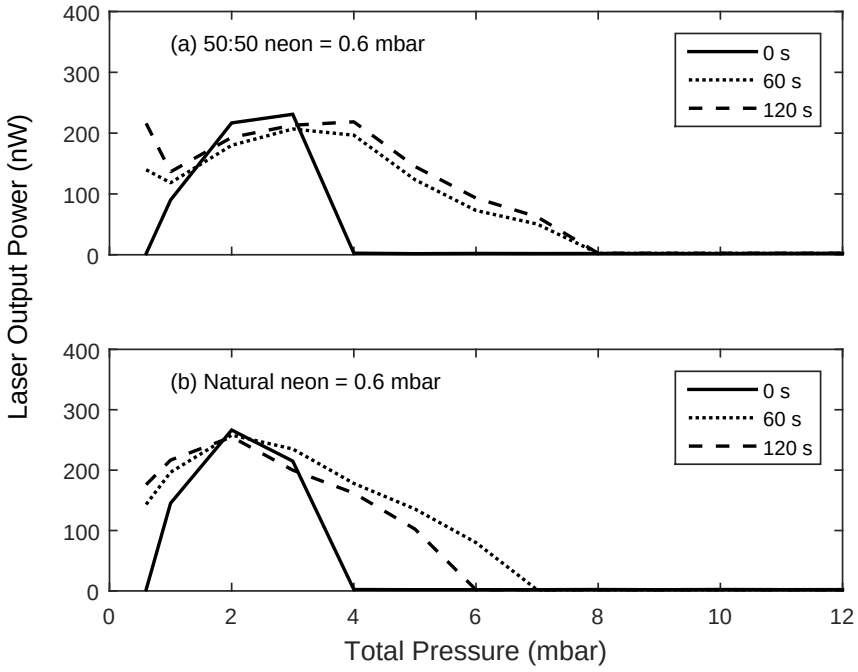

Figure. 4.10.: Laser output power as a function of total helium-neon gas pressure at a constant RF input power of 20 W for: (a) 50:50 neon and (b) natural neon (for a partial neon pressure of 0.6 mbar).

the contrary, the gain profile for natural neon gas is asymmetrical, and the laser operating frequency tends to lie closer to the ^{20}Ne isotope atomic line centre (refer to Figure 2.4 (c)).

Secondly, there is a significant drop in the laser power when helium is added to the gas mixture. This is because the addition of helium causes a rapid increase in the $2p_7$ population. This quenches the 1152.5 nm transition and as a result, only laser oscillation on the 1152.3 nm ($2s_2 \rightarrow 2p_4$) transition remains [72].

Thirdly, the measured laser output power increases for several minutes after igniting the plasma. Moreover, from Figures 4.7 to 4.10, lasing at higher helium and neon content in the cavity happens at a later time (60 to 120 seconds) after the plasma is ignited. The cause of the shift in the laser power over time and the delay in the laser action with higher helium and neon pressures in the cavity is unknown. However, three speculative explanations are offered:

1. The gas temperature affects the gain in the helium-neon laser system [76], [112]. High RF power increases the gas temperature over time. At higher gas temperatures, the rate of excitation transfer from excited helium to unexcited neon atoms will increase. At the same time, the collision rate between electrons with the gain tube

wall will rise. This will prevent population build up on the $3p$ levels[4]. As a result, the population of the upper level ($4s$) will rise, and the laser intensity increases [113].

2. When the plasma is first ignited, though the RF power meter shows maximum RF power has been applied (minimum reflected power), there is a delay in transferring the maximum RF power to the high-density gas mixture. McLeod explained there is a laser 'warm-up' time where the RF power fluctuates for several minutes (up to 10 minutes) before settling into a constant power (refer to Figure 3.29 in ref. [114]).

3. A significant amount of RF power may be dissipated as heat around the gain tube. As a result, the gain tube temperature rises (although the gain tube is never too hot to be touched). This causes variations in the laser path length. Several works have utilised the effect of varying the gain tube temperature to actively-control the laser cavity path length for frequency stabilisation [115], [116]. However, in our case, this should be insignificant due to the massive difference between the gain tube length and the size of the PR-1 cavity.

The change in the laser power (over time) does not affect the final interpretation of the overall trend of the laser output power. Nevertheless, it would be crucial to keep the gain tube and the gas temperature constant in future measurements for a more stable observation.

[4]The lifetimes of the $1s_2$ and $1s_4$ levels are longer than the lifetimes of the $2p_4$ and $2p_7$ levels (refer to Table 2.1).

Laser Efficiency

The influence of different RF input powers on the laser gain was investigated by recording the output power for a variety of gas mixing ratios as a function of RF input power. In this measurement, the RF input power was increased from 0 to 20 W; while the total gas pressure was varied from 1 to 12 mbar at each partial pressure of natural neon (0.1 to 0.6 mbar).

The results are presented in Figures 4.11 to 4.16. From the measurements, the lasing threshold generally occurs between 0.4 W and 0.5 W of RF input and generates a laser power output of between 0.2 and 0.8 nW. As the RF power is increased beyond the lasing threshold, the measured laser output power increases. The efficiency[5] is high between the lasing threshold until 5 W of RF input power for all the measured gas compositions.

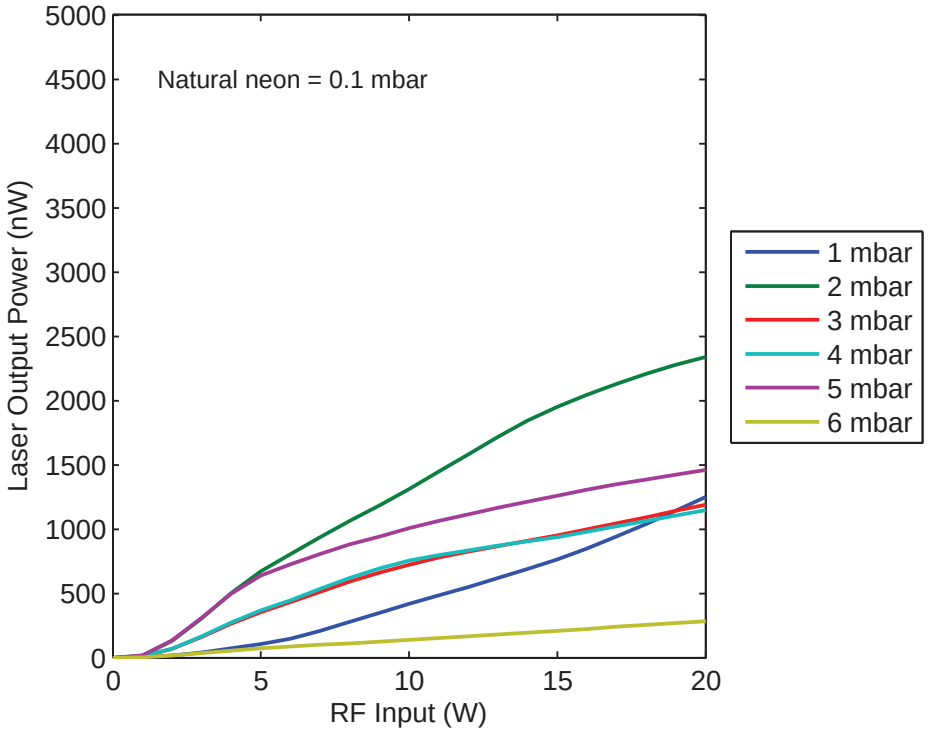

Figure. 4.11.: Laser output power as a function of RF input power at a natural neon partial pressure of 0.1 mbar.

For gas mixtures having a neon content of 0.3 mbar and below (Figures 4.11 to 4.13), the efficiency decreases above 5 W of RF power. Subsequently, the laser output saturates. At 0.4 mbar of neon and above (Figures 4.14 to 4.16), the observed efficiency is negative for high RF input powers.

[5]The slope of the graphs represents the laser input-output efficiency, η, which is denoted by $\eta = \frac{\Delta P_{\text{out}}}{\Delta P_{\text{in}}}$, where ΔP_{out} is the change in the measured laser output power, and ΔP_{in} is the change in RF input power.

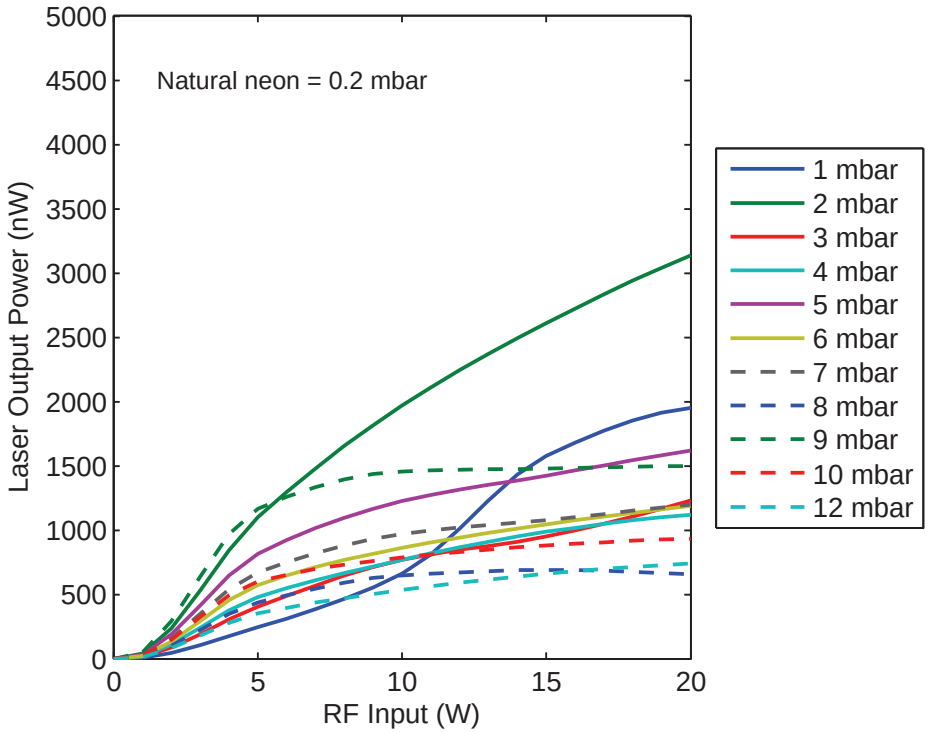

Figure. 4.12.: Laser output power as a function of RF input power at a natural neon partial pressure of 0.2 mbar.

The efficiency of the laser is determined by the rate at which the upper laser state is populated and the rate at which the terminal level is depopulated. By referring back to the schematic diagram in Figure 4.3, in order to achieve a population inversion between the $4s$ and $3p$ levels, the total relaxation rate, R_{21} must be more than the spontaneous decay rate of the laser transition, A_{32}. When the RF excitation power is high, more electrons collide with helium atoms and this produces more excited helium atoms. This increases the number of neon atoms excited to the $2s_2$ level, hence, increasing the population inversion with the $2p_4$ level. Therefore, higher laser output power would be expected and is observed.

With increasing RF input power, the laser output power begins to saturate due to a build-up of population in the $3s$ metastable state. This results from the slow relaxation rate (R_{10}) from the $3s$ level to the ground state relative to R_{21} and A_{32}. Typically, R_{10} can be increased by using a smaller diameter gain tube to increase the gain tube wall collision frequency. Since R_{10} is constant (as the tube diameter is constant), adding more RF power into the system will eventually lead to a higher R_{32} and A_{32} with respect to R_{10}. For this reason, the laser power begins to decrease.

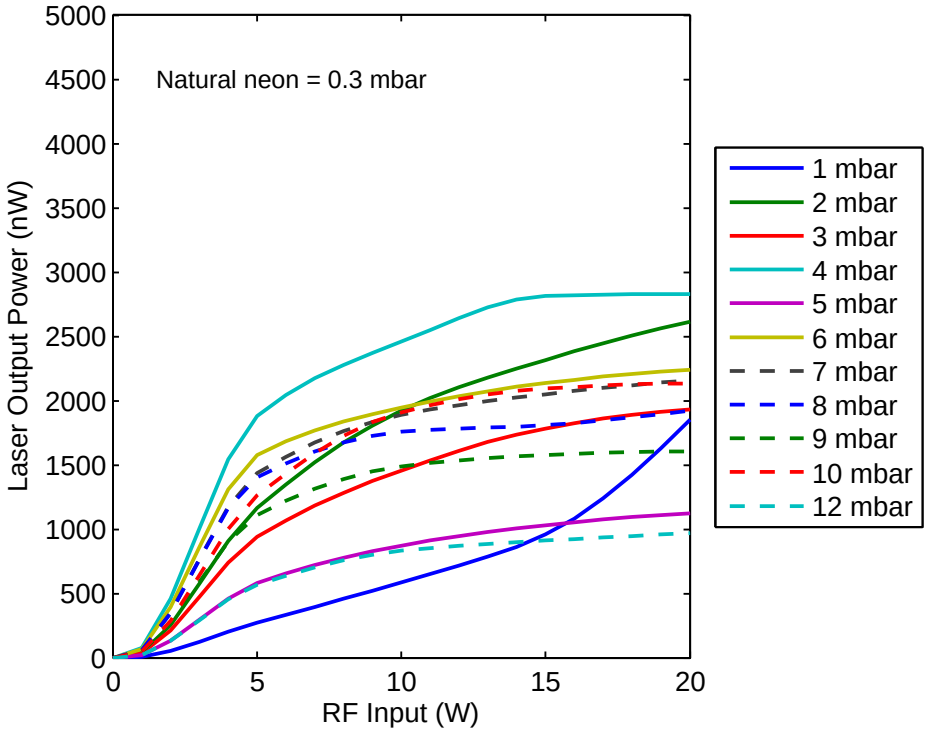

Figure. 4.13.: Laser output power as a function of RF input power at a natural neon partial pressure of 0.3 mbar.

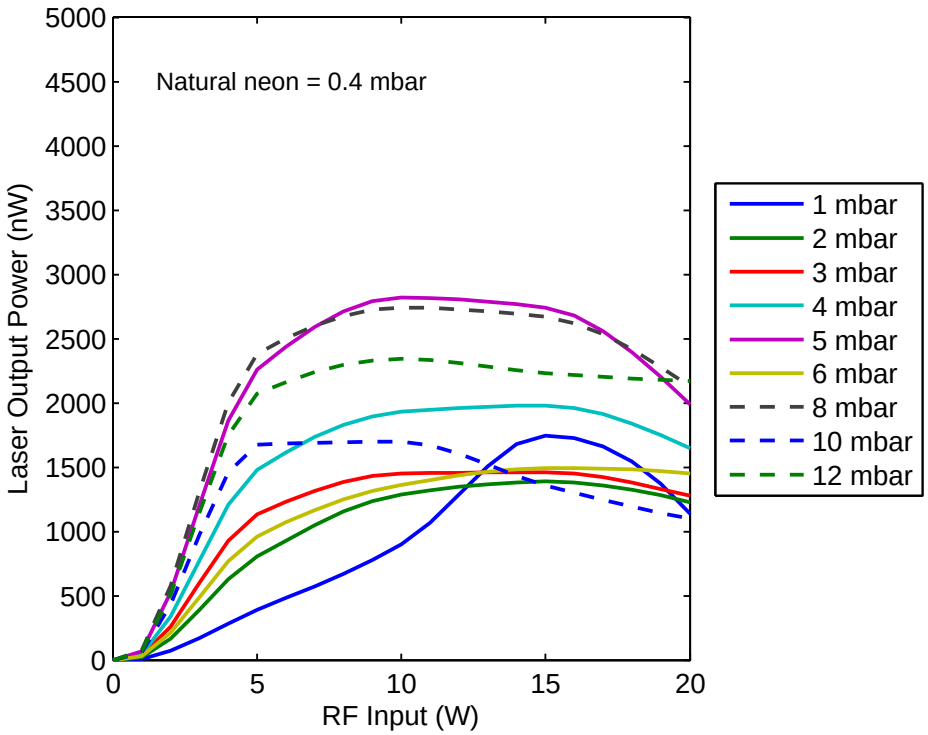

Figure. 4.14.: Laser output power as a function of RF input power at a natural neon partial pressure of 0.4 mbar.

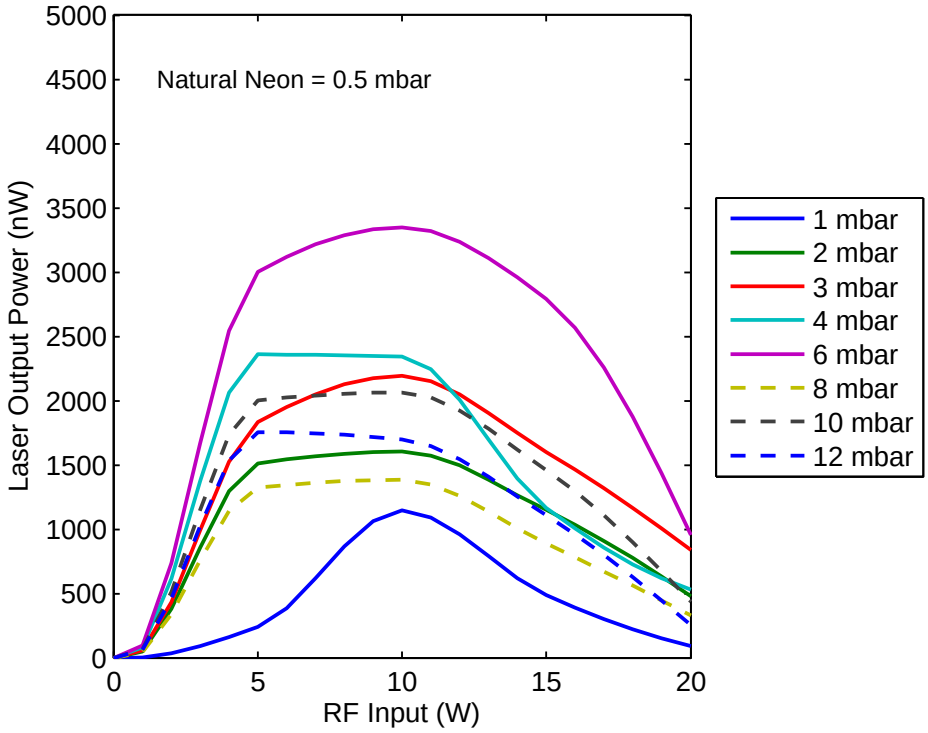

Figure. 4.15.: Laser output power as a function of RF input power at a natural neon partial pressure of 0.5 mbar.

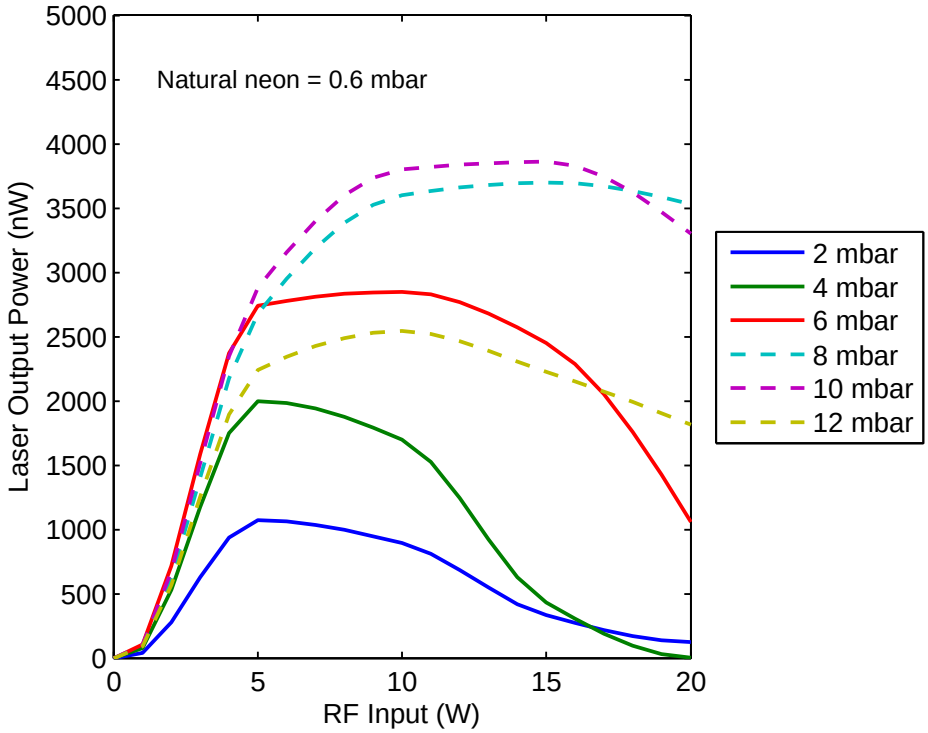

Figure. 4.16.: Laser output power as a function of RF input power at a natural neon partial pressure of 0.6 mbar.

4.2.3 The Single-Mode and Phase-Locked Regimes of Operation

In this section, we aim to determine the single-mode operating regime for operation at 1152.3 nm as a function of various helium-neon gas pressures. The experimental procedure was similar to the procedure described in Section 3.2.4. At the time of the experiment, there was no suitable detector for this wavelength range with sufficient bandwidth available in the laboratory to monitor the very low light intensity signal from the Thorlabs Scanning Fabry Pérot interferometer (SA200-8B). For this reason, to determine whether the laser was operating in the single-mode regime, as the RF input power was increased slowly, an RF spectrum analyser was employed to monitor the absence of a beat signal at the FSR frequency. At the same time, the combined beam power spectrum was observed by using the FFT spectrum analyser.

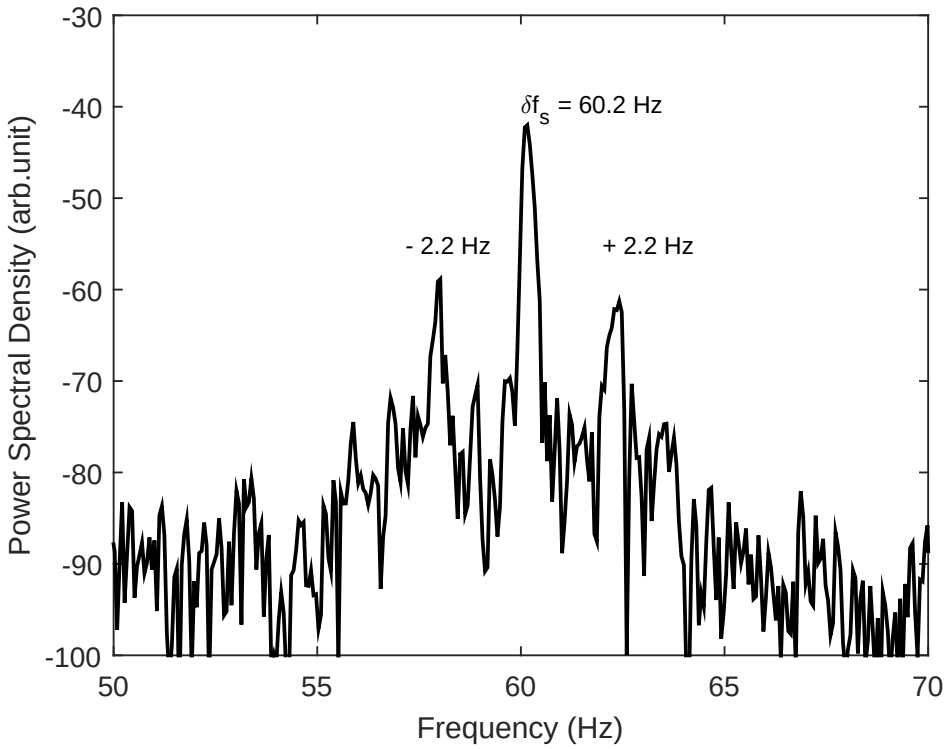

Figure. 4.17.: Sagnac power spectrum as displayed on the FFT spectrum analyser. The peak at 60.2 Hz is due to the rotation of the Earth.

According to Equation 2.25, the Sagnac frequency detected by the PR-1 ring laser gyroscope for operation at 1152.3 nm laser wavelength should be approximately 62 Hz. An example of the power spectrum of the δf_s displayed on the FFT spectrum analyser is shown in Figure 4.17. The combined beam yields a beat signal due to Earth rotation of 60.2 Hz with 2.2 Hz side-bands. The two side-bands are due to the natural oscillations of the West Rutherford building.

Figure 4.18 displays the multimode threshold as a function of total gas pressure at various natural neon partial pressures. The grey-shaded region in the figure indicates the guaranteed single-mode operating regime. Above the grey-shaded area is a regime where more than one longitudinal mode was present in the laser spectrum.

At higher laser powers, a phase-locked threshold is observed (indicated by the 'dashed line' in Figure 4.18 (b) - (f)). The phase-locked threshold was observed when the combined beam signal waveforms on the oscilloscope were no longer fluctuating (and at the same time, the δf_s power spectrum on the FFT spectrum analyser was stable) in the presence of a ν_{fsr} beat on the RF spectrum analyser.

Figure 4.18 (a) shows the multimode threshold for a natural neon partial pressure of 0.1 mbar. In general, there is no stable δf_s signal observed with neon only gas fills due to mode competition. The laser was only observed to unlock on the rotation of the Earth between 1 to 6 mbar of total pressure. In addition, there is no stable δf_s signal observed above the multimode threshold for this gas composition range.

Stable rotation sensing behaviour can be obtained at total gas pressures between 1-12 mbar for natural neon partial pressures of 0.2 mbar and 0.3 mbar (Figure 4.18 (b) and (c)). The single-mode operating range increases as the total gas pressure is increased. The maximum laser output power in the single longitudinal mode regime is approximately 50 nW at a total gas pressure of 12 mbar.

At neon partial pressures of 0.4 mbar and 0.5 mbar (Figure 4.18 (d) and (e)), a stable δf_s signal can be observed above 2 mbar. Figure 4.18 (f) shows for a neon partial pressure of 0.6 mbar, stable rotation sensing is achieved in the pressure region between 3 and 12 mbar. It is notable that the single-mode operating ranges are narrower at higher neon partial pressures.

The single-mode region appears to be much larger when ring lasers are operated at 632.8 nm. This is due to significantly reduced Doppler broadening at this longer wavelength (refer to Figure 2.4). Note that there is no phase-locked region indicated in Figure 4.18. The phase-locked regime is only stable for a small range of laser powers (between 2 to 3 nW). Thus, it was difficult to determine the power range for phase-locked operation.

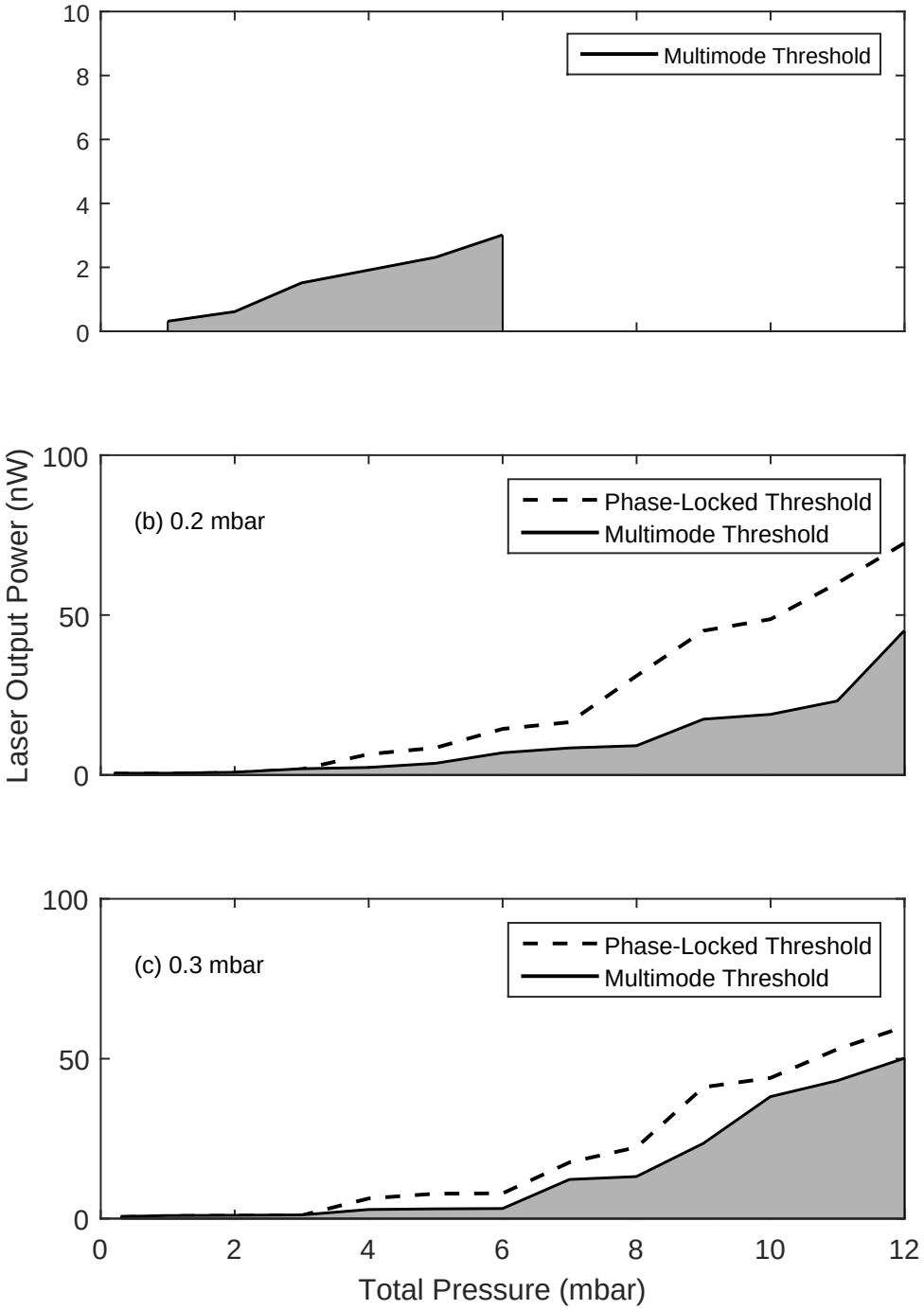

Figure. 4.18.: The laser multimode threshold as a function of total gas pressure for natural neon partial pressures of (a) 0.1 mbar, (b) 0.2 mbar and (c) 0.3 mbar. The grey-shaded area indicates guaranteed single-mode operation.

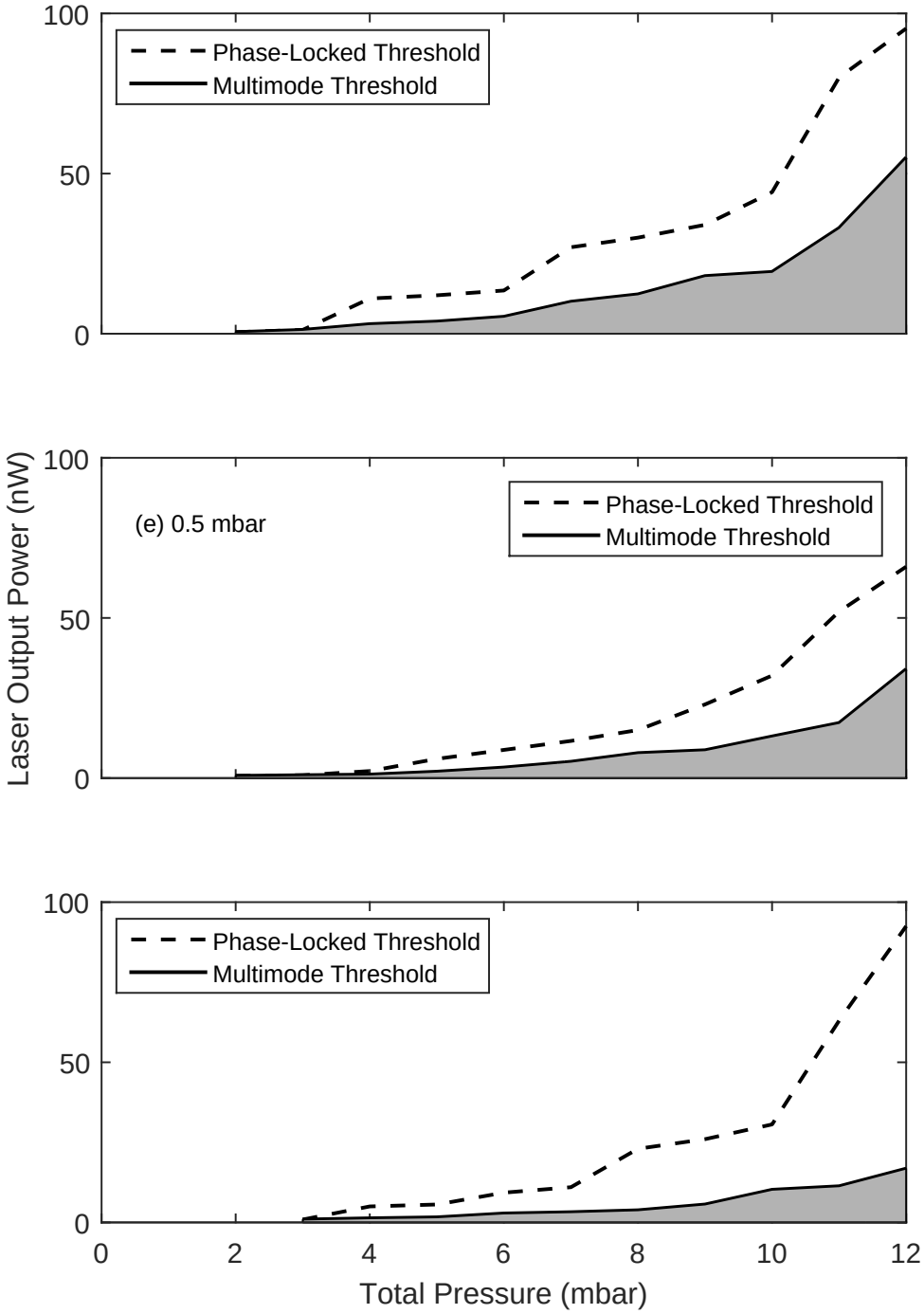

Figure. 4.18. (cont.): The laser multimode threshold as a function of total gas pressure for natural neon partial pressure of (d) 0.4 mbar, (e) 0.5 mbar and (f) 0.6 mbar. The grey-shaded area indicates guaranteed single-mode regime operation.

4.2.4 Gyroscopic Performance

In this section, we characterise the rotation sensing behaviour for a large ring laser operating on the 1152.3 nm infrared laser transition. We focus on gas mixtures containing both helium and neon since stable performance cannot be achieved when both transitions of the neon-doublet are simultaneously active.

The Sagnac frequency and the monobeam signal (PD 1) were recorded over a measurement period via the logging system described in Section 3.1.2. For these studies, the monobeam signal detected by PD 2 was unable to be logged as the DC signal output was too low. The output from PD 1 was connected to the servo system to maintain the laser intensity over the signal logging duration. The New Focus Adjustable Photoreceiver (model 2053) has an active area of 0.08 mm^2 with a range of gain settings as listed in Table 4.4.

Gain Setting	Typical Performance (MHz)
1×1	12
3×1	6
1×10	12
3×10	6
1×10^2	8
3×10^2	6
1×10^3	0.7
3×10^3	0.7
1×10^4	0.25
3×10^4	0.25

Table. 4.4.: Frequency-response details for each gain setting for the New Focus 10 MHz Adjustable Photoreceivers Model 2053.

For rotation sensing operation using a total gas pressure of below 6 mbar, the single-mode operating regime is below 10 nW of laser output power (Figure 4.18). For higher gas pressures (between 6 to 12 mbar), the single-mode operating regime is below 60 nW. This operating regime corresponds to an RF input power of between 0.4 W to 0.5 W as shown in Figure 4.19. Figure 4.20 shows the DC voltage output from PD 1 as a function of laser output power between 0 to 50 nW. From the plotted graph, the highest available gain setting was chosen for PD 1 to provide a suitable voltage range to control the RF excitation power via the servo system.

Figure 4.21 (a) shows a plot of Sagnac frequency, δf_s over time while Figure 4.21 (b) displays the corresponding δf_s contrast ratio[6]. The detected Sagnac signal shows both mode-hopping and mode-splitting because the gyroscope is wall-mounted and therefore

[6] δf_s contrast ratio is the ratio between the AC signal to the DC signal received by the PMT which detects the combined beam (refer to page 52).

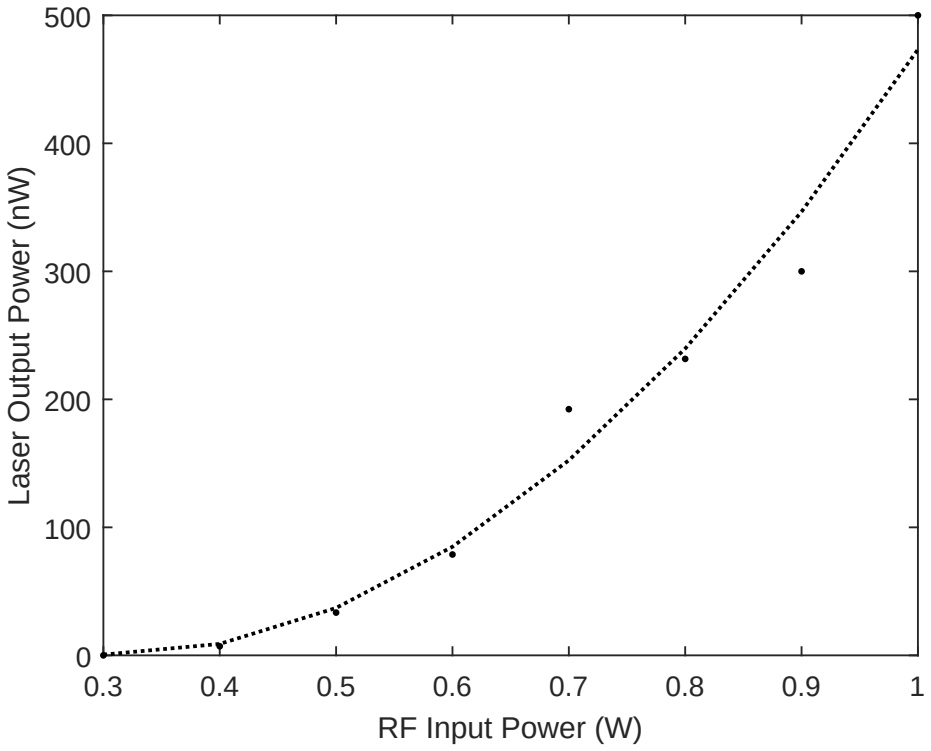

Figure. 4.19.: Measured laser output power as a function of RF input power between 0 W and 1 W.

subject to environmental perturbations. Mode-splitting is clearly indicated when the contrast ratio drops to zero in Figure 4.21 (b).

An example of the short-term δf_s signal over time is shown in Figure 4.22 (a) and (b) at total gas pressures of 2 and 6 mbar (50:50 neon = 0.2 mbar). The operating power at 2 mbar was 1 nW and the monobeam modulation, m, was measured to be 8.7%. At 6 mbar, the laser operating power was 4 nW while the monobeam modulation was 4.5%.

The excursion at 2 mbar of total pressure is about 0.25 Hz whereas, at 6 mbar, the detected δf_s excursion is approximately 0.05 Hz. The frequency excursions in the recorded rotation signals are mainly due to frequency pulling and pushing caused by the backscatter perturbations. From Equation 3.5, the expected backscatter induced perturbations on the detected rotation signal (Δf_{bs}) are 0.23 Hz and 0.06 Hz for operation with 2 mbar and 6 mbar respectively (by assuming $m_1 \approx m_2$).

Figure 4.23 shows Allan deviation (ADEV) plots normalised to Earth rotation (Ω_E). This is used to evaluate the overall rotation sensing performance of the laser operating at this wavelength. The plots correspond to the short-term δf_s depicted in Figure 4.22. The minimum variance achieved is $1\times10^{-4}\Omega_E$ at $\tau = 2$ s with a gas fill of 6 mbar. This is comparable to operation at 632.8 nm. With the same gas fill (0.2 mbar of 50:50 neon and

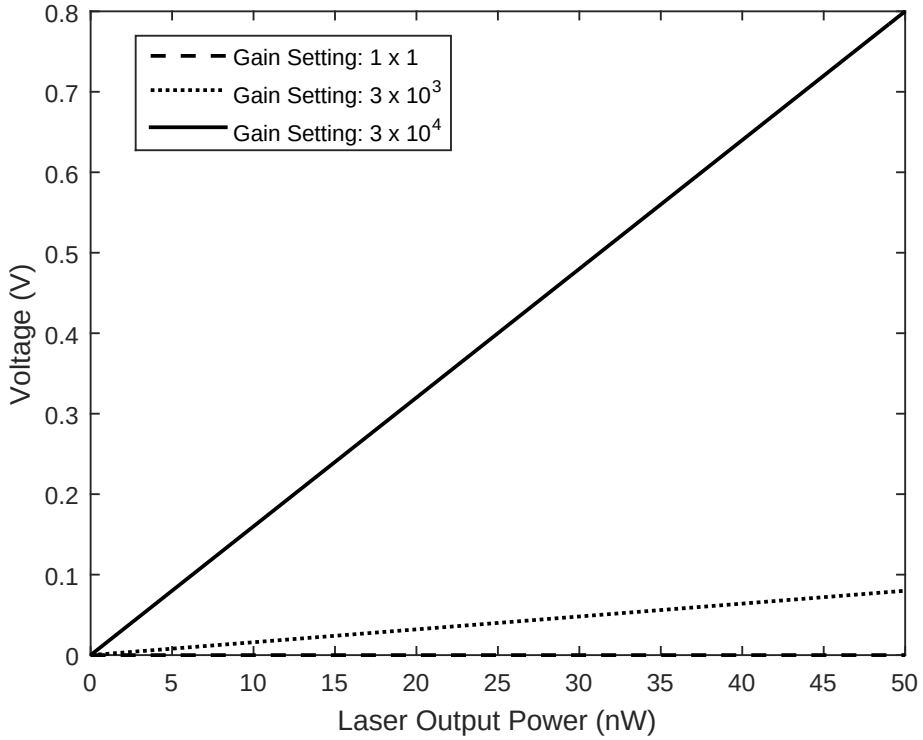

Figure. 4.20.: PD 1 output voltage corresponding to different laser output powers at three different gain settings.

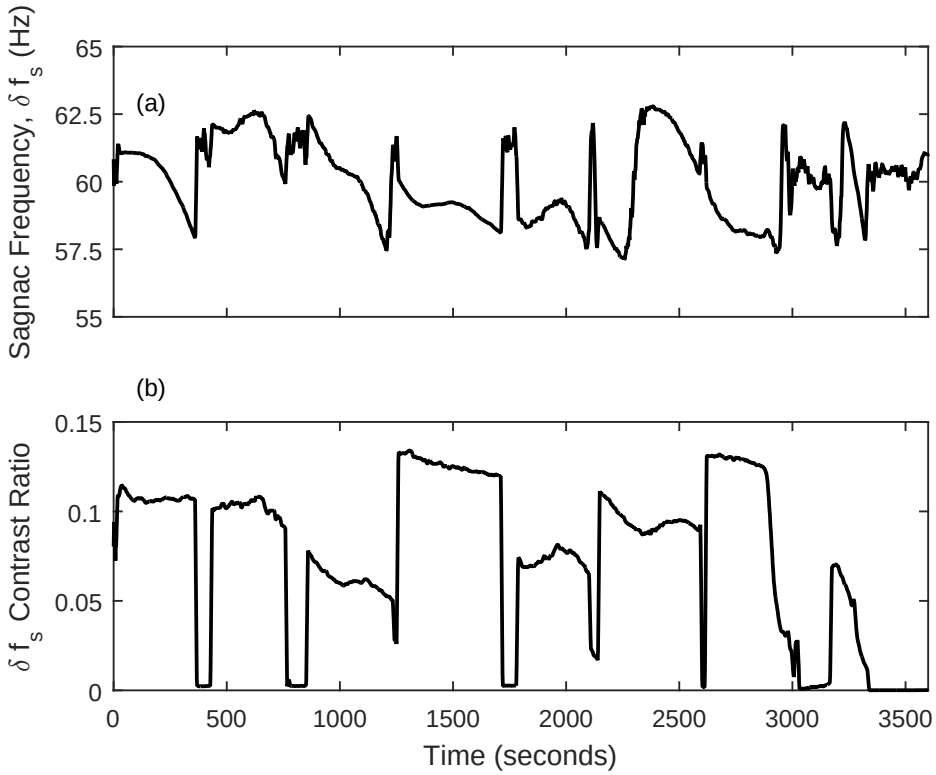

Figure. 4.21.: (a) Typical long term δf_s signal; (b) the corresponding δf_s contrast ratio.

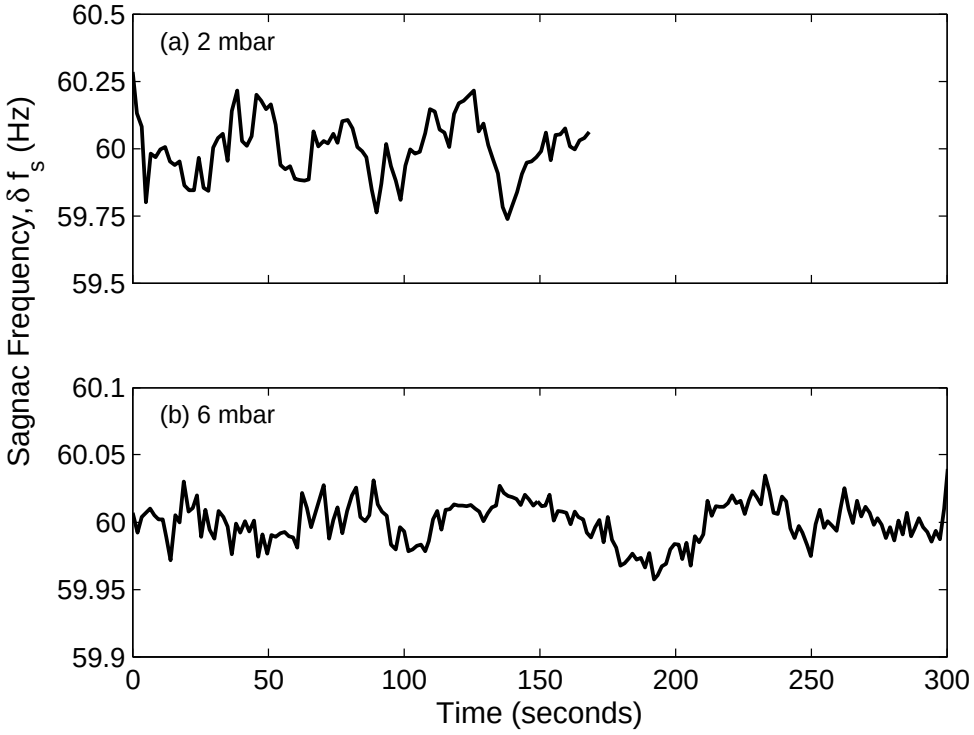

Figure. 4.22.: Short term δf_s as a function of time with a 50:50 neon partial pressure of 0.2 mbar at total gas pressures of: (a) 2 mbar, (b) 6 mbar.

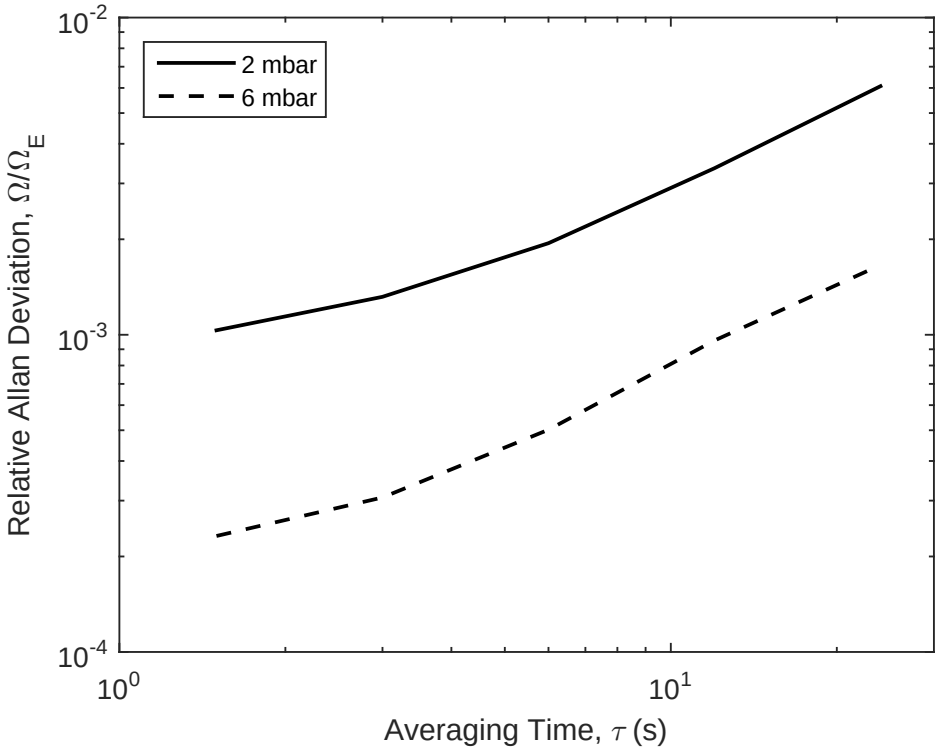

Figure. 4.23.: Plots of relative Allan deviation (ADEV) at 2 mbar and 6 mbar total pressures.

6 mbar of total gas pressure), the minimum variance achieved by the laser at 632.8 nm was $1.3 \times 10^{-4}\Omega_E$ (Figure 3.16).

Table 4.5 summarises the relevant gyroscopic performance of PR-1 ring laser while operating with a gas fill of 0.2 mbar of 50:50 neon a total pressure of 6 mbar. The operating power was maintained at 4 nW for a stable single-mode operation and this corresponds to a resolution of 1.6×10^{-8} rad/s/$\sqrt{\text{Hz}}$. In comparison, the Ω_s for gyroscopic operation at 632.8 nm is 2.4×10^{-10}rad/s/$\sqrt{\text{Hz}}$. The sensor resolution is higher at 632.8 nm because the laser cavity Q is higher at this wavelength (Table 3.2). Moreover, despite operating with the same gas fill, the laser power is three times lower when the ring laser is operated at 1152.3 nm. In comparison to the sensor resolution achieved by another similar size ring laser gyroscope, GEOsensor, it appears that the sensor resolution achieved by PR-1 at 1152.3 nm is inferior to the GEOsensor performance ($\Omega_s = 1.1 \times 10^{-10}$ rad/s/$\sqrt{\text{Hz}}$), also mainly due to the lower laser cavity Q achieved by PR-1 at this wavelength [17].

Parameter	Value
Ring-down, τ_{decay} (μs)	33
Total loss, L (ppm)	646.5
Quality factor, Q	5.4×10^{10}
Finesse, F	9.7×10^{3}
Laser power, P_i (nW)	4
Resolution, Ω_s (rad/s/$\sqrt{\text{Hz}}$)	1.6×10^{-8}
Relative ADEV, Ω/Ω_E	1×10^{-4}
Lock-in threshold, f_L (μHz)	0.94

Table. 4.5.: Summary of relevant parameters of PR-1 running in the single-mode regime on the neon transition at 1152.3 nm (gas fill: 0.2 mbar of 50:50 neon with a total pressure of 6 mbar).

4.3 Discussion

Generally, in a helium-neon laser system, the optimum gas pressure is the gas mixing ratio which provides the highest gain. This is where the laser is operating at the peak of the gain curve. The highest gain at 1152.3 nm is achieved with a gas fill of 0.2 mbar of natural neon only. However, and as discussed earlier, this is not useful for gyroscopic operation.

The second factor which is crucial for optimum laser gyroscope performance is the input-output efficiency characteristic. The highest efficiency is achieved at the lowest RF input power needed to sustain laser action. Other than that, negative efficiency should be avoided as this causes the laser intensity servo control system to fluctuate between positive and negative feedback. For a helium and neon gas mix, the highest gain is achieved at 0.5 mbar of natural neon with a total gas pressure of 6 mbar at an RF input power of 5 W. Despite having the highest gain at this mixing ratio; the laser is not

optimally efficient. The efficiency of the laser at this mixing ratio drops after an RF input of 5 W. The best efficiency is at a gas mixing ratio of 0.2 mbar of natural neon with 2 mbar of total pressure where the laser power is increasing almost linearly as the pump power is increased. This mixing ratio is also the gas composition which yields the maximum gain when PR-1 is running on the 632.8 nm laser wavelength.

The third factor to determine the optimum operating pressure is the gas mixture which provides the highest gain while maintaining a single longitudinal mode operation. Single-mode operation is important to avoid mode competition between several longitudinal modes. In this context, a higher total gas pressure is desired for a wider power range for single-mode operation. Furthermore, a higher operating laser power is preferred because the resolution of a ring laser gyroscope is inversely proportional to the square root of the laser output power (refer to Equation 2.43).

By considering all the three factors mentioned above, the ideal gas composition for PR-1 operating on the 1152.3 nm wavelength is a 50:50 neon isotope mix at either 0.2 mbar or 0.3 mbar and with a total pressure of 6 mbar and above.

Characterisation of the ring laser gyroscope operating at 1152.3 nm was slightly limited by the detectors available during the experiments. Simultaneous logging of the counter-propagating beams was not possible as only PD 1 has enough gain to detect the low laser output power. Estimation of the degree of backscatter perturbations during data logging over time was solely based on one laser beam. Other than that, the laser longitudinal mode spectrum was unable to be observed. Information about the mode behaviour would be useful in terms of determining the phase-coupled behaviour at this wavelength.

Overall, it is unclear whether an improved performance of a large ring laser gyroscope is achieved by employing these low-thermal-noise mirrors. The main factor that influences the performance of PR-1 is backscatter. For these early prototype mirrors, the top surface of the DBR disc was subject to defects during the DBR growth process. For this reason, the measured modulation on a single beam is large compared to the value measured in Section 3.2.3 (refer to Table 3.3). In addition, the small coating diameter allows extra light to be transmitted around the edges of the coating. The coating diameter was limited by the available GaAs wafer size [100].

As a consequence, an effort to improve the optical performance of the crystalline coated mirrors has been undertaken recently [117]. The primary improvement has been achieved using a modified micro-fabrication technique. With the revised fabrication procedure, the DBR disc is turned over before being pressed into contact on to the silica substrate. The back surface of the epitaxial layers shows minimal defects from the buffer and etch stop deposition process. The surface defects on the top surface of the DBR disc are then

buried at the bond interface. This new generation of crystalline mirror demonstrates a lower optical scattering loss with 30 times improvement in thermal conductivity relative to the IBS-mirror. Moreover, the fabrication of a large diameter DBR disc, which will be more suitable for a large-area laser cavity, can be realised through hetero-epitaxial growth on silicon (Si) via relaxed silicon germanium (SiGe) buffer layers [117]. For this reason, the prospect of employing these crystalline mirrors in large ring laser gyroscopes remains extremely promising.

4.4 Conclusion

The performance of the PR-1 ring laser gyroscope operating on the helium-neon transition at 1152.3 nm has been assessed. The supermirrors employed in the laser cavity in this work were supplied by Crystalline Mirror Solutions (CMS). These mirrors are different from the typical IBS-supermirrors which have been used in previous work in our group.

The highest gain is achieved with a gas fill of neon at 0.2 mbar. However, this is not ideal for rotation sensing purposes due to the presence of neon doublet transitions at 1152.3 nm and 1152.5 nm. The optimum gas composition for gyroscopic operation is determined at 0.2 and 0.3 mbar of 50:50 neon with total pressures above 6 mbar. A ring-down time of 33 μs was measured, yielding a cavity Q of 5.4×10^{10}. PR-1 succesfully resolves a Sagnac frequency of 60.2 Hz due to Earth rotation. Also, the operation of PR-1 at 1152.3 nm typically yields output power of between 1 to 10 nW. The estimated lock-in thresholds are within the micro-Hertz range which are comparable with those observed for operation at 632.8 nm.

These observations are encouraging considering that this is the first implementation of crystalline coatings in an active large ring laser cavity. With a new generation of low scatter optical coatings as well as a larger size of crystalline coating area on the mirror substrate, the ultimate optical and thermo-mechanical performance of crystalline mirrors and their impact on large-area, and high-sensitivity ring laser gyroscopes will be more apparent.

5

A Ring Laser Gyroscope Operating on the $3s_2 \rightarrow 2p_6$ and $3s_2 \rightarrow 2p_{10}$ Transitions of Neon

The long-established approach of improving the performance of Canterbury's ring laser gyroscopes by geometric up-scaling has reached a point where no improvement can be observed. Enlarging the size of the gyroscope has eventually resulted in more demanding requirements on the mirror alignment and the mechanical stability of the device [15]. In this chapter, we outline our initial endeavour to operate a 'frequency up-scaled' large ring laser gyroscope by utilising the shortest neon transition at 543.4 nm ($3s_2 \rightarrow 2p_{10}$) as the operating wavelength. We begin this chapter by introducing a long discharge tube to the 2.56 m^2 test cavity to compensate for the low gain available at this wavelength. Then, by employing the latest generation ion beam sputtered (IBS) supermirrors; providing extremely low transmission loss of 0.2 ppm per mirror, we demonstrate, for the first time, a large ring laser which unlocks on the rotation of the Earth while running on the 543.4 nm wavelength. Simultaneously, we report a preliminary result on the first ring laser gyroscope to operate on the $3s_2 \rightarrow 2p_6$ (611.8 nm) neon transition.

5.1 A Frequency Up-Scaled Large Ring Laser Gyroscope

The scale factor of a ring laser is proportional to the area enclosed by the counter-propagating laser beams over the product of the perimeter of the laser and the operating wavelength ($S = \frac{4A}{\lambda P}$). Therefore, over the last three decades, the sensitivity of large ring laser gyroscopes have increased tremendously by increasing the size of the laser cavity. In principle, running a ring laser on a shorter operating wavelength will result in an increase in the scale factor as well. Apart from our recent work as reported in the previous chapter along with ref. [97], large ring laser gyroscopes have only operated on the 632.8 nm of neon transition. Thus, running a large ring laser with a different wavelength will establish a novel approach towards improving the gyroscopic performance of our lasers.

The shortest wavelength in the helium-neon laser system originates from the $3s_2 \rightarrow 2p_{10}$ neon transition that gives rise to laser radiation at 543.4 nm as illustrated in Figure 2.3.

Operating a large ring laser on this transition will instantly increase its scale factor by approximately 17%. Note that there are other wavelengths (which are shorter than 632.8 nm) that share the same $3s_2$ upper level as well, i.e. 611.8 nm ($3s_2 \rightarrow 2p_6$), 604.6 nm ($3s_2 \rightarrow 2p_7$) and 593.9 nm ($3s_2 \rightarrow 2p_8$). Table 5.1 lists the increment (or decline) in the scale factor corresponding to different wavelengths (normalised to 632.8 nm).

Wavelength (nm)	Scale Factor Variation
543.4	1.1647
593.9	1.0655
604.6	1.0432
611.8	1.0343
632.8	1
1152.3	0.5488

Table. 5.1.: The scale factor variation at different operating wavelengths relative to the common 632.8 nm transition.

Even so, running a ring laser on a shorter wavelength may give rise to higher backscatter amplitude as Rayleigh scattering is inversely proportional to the fourth power of the laser wavelength [103]. Furthermore, the gain at the shorter laser wavelengths is significantly lower. For instance, the gain available at the shortest helium-neon transition of 543.4 nm is 30 times smaller in comparison to the well-known 632.8 nm transition [45]. Nonetheless, the gain section of our test cavity can be modified by installing multiple (or longer) gas discharge tubes to provide extra gain to enable these lower gain helium-neon transitions to lase. Moreover, by operating on a shorter wavelength, the laser spot size is expected to be smaller. The optical loss in our ring lasers is proportional to the size of the laser spot on the mirror due to the high order abbreviations arising from the mirror surface [15]. Hence, a smaller spot size may decrease the total optical loss in our ring cavities.

5.2 Capacitively Coupled Radio Frequency Gas Discharges for Exciting Helium-Neon Gas Lasers

The gain medium in all Canterbury ring laser gyroscopes is excited via an RF discharge. An RF discharge is preferred to avoid Langmuir flow (which usually occurs in a DC discharge) which introduces a bias on the true rotation signal [17]. The RF power is capacitively coupled into the gain medium through external electrodes that are wrapped around a narrow gain tube.

In an RF discharge, each electrode behaves as cathode and anode alternatively. As a time-varying potential difference is applied, electrons accelerate and oscillate between

the electrodes and collide with helium and neon atoms, giving rise to two types of collisions, i.e. elastic and inelastic collisions. There is no energy transfer between the accelerated electrons and the heavier gas atoms during elastic collisions [118]. By contrast, inelastic collisions between these particles resulting in energy transfer from the electrons to the neutral helium and neon atoms. In gas lasers, the most crucial collision event is the inelastic collision which leads to helium-neon laser excitation (Section 2.2.1). Also, the inelastic collisions between the electrons and the gas atoms lead to ionisation collisions, where new electrons and ions are produced via a process known as ion-induced secondary electron emission [119]. These secondary electrons will induce new ionisation collisions and produce new electrons and ions. The continuous process of electron and ion production is responsible for sustaining the helium-neon gas discharge [120].

5.2.1 Designing A New Impedance Matching Unit and Electrode Configuration

The gain provided by the 100-mm-long gain tube is insufficient for the low-gain helium-neon transitions to lase (Section 3.2.2). For this reason, we modified the test cavity by installing an extra (and longer) discharge tube. Figure 5.1 (a) shows the schematic drawing of the new gain tube. It is supported by a holder, which also houses two sets of micrometers situated on each end of a Pyrex tube. The gain tube was fabricated by using a good quality fused silica (Pyrex) with an internal diameter of 4 mm as shown in Figure 5.1 (b). The total length of this gain tube is 580 mm with an estimated total active area of 400 mm.

The RF power source is similar to the RF transmitter unit for the 100-mm gain tube. It is an 80 MHz transmitter (Tait T800) which delivers up to 30 W of forward power. Similar to all commercial RF power transmitters, this RF transmitter is standardised to transfer power into a 50 Ω load. For example, if we represent the load impedance, Z_D as,

$$Z_D = R_D + jX_D, \tag{5.1}$$

where R_D is the load resistance and X_D is the load reactant; for a maximum power transfer from the RF source to the discharge, R_D has to be 50 Ω and X_D must equal to zero.

However, the load reactance X_D does not equal to zero. The load impedance varies because the gain tube has capacitive and inductive properties. For instance, close proximity between the gain tube wall with a grounding surface will resemble two plates of a capacitor separated by a distance. Other than that, stray inductive, capacitive and resistive components are essentially present in any electrical and electronic devices. Moreover,

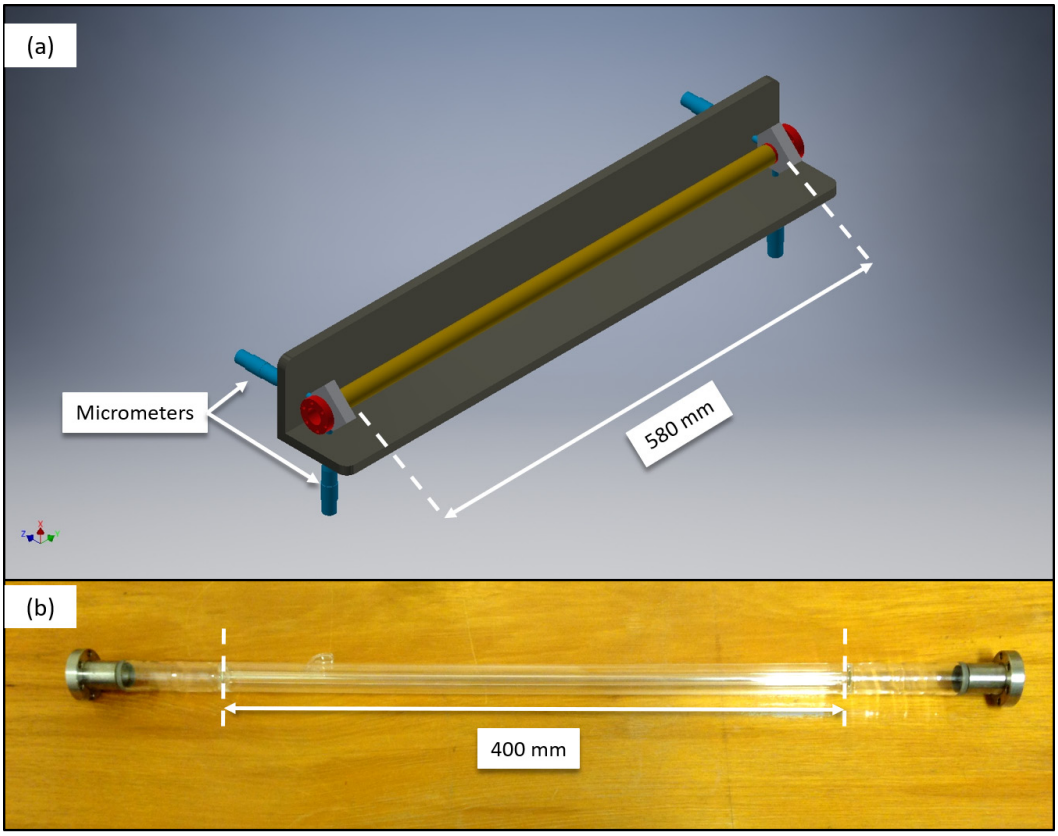

Figure. 5.1.: (a) Schematic drawing of the 580 mm long gain tube (courtesy from R. J. Thirkettle from the School of Physical and Chemical Sciences, University of Canterbury); (b) photo of the 580 mm long gain tube.

the gas discharge creates an unknown impedance which is represented by a complicated function involving plasma density distribution[1] [30], [120], [122].

Therefore, an impedance matching unit is necessary to serve as an adjustable 'transformer' to match the load impedance created by the helium-neon plasma and the 580-mm long Pyrex tube to the required 50 Ω transmitter impedance as seen from the RF source. The output impedance of this matching unit has to be adjustable over a wide range to cancel out the unknown plasma impedance that varies over different gas pressures. Furthermore, a matching unit is essential to protect the RF transmitter. If the source impedance does not match with the load impedance, the forward power will be reflected back to the source and potentially damaging the power source [123].

Thevenin's Theorem states that it is possible to simplify any complex circuit to an equivalent circuit consists of a single voltage source and a series resistance connected to a load. Besides, for any circuit consisting of a resistance (R_s) and a reactance (X_s) in series, there will be a circuit made up of resistance (R_p) and reactance (X_p) in parallel with an equivalent total impedance with the former series circuit configuration. The real values

[1] A simplified model of RF discharge is described in detail in ref. [121]. The plasma 'impedance' is governed by Equation 1.51 in Chapter 1.

of resistance and reactance in an equivalent circuit can be determined by introducing the component quality factor Q, where Q is simply the ratio of the impedances to be matched. For a series circuit, $Q = \frac{X_s}{R_s}$; while for a parallel circuit, $Q = \frac{R_p}{X_p}$. If both the series and parallel circuits are equivalent, the value for Q for both circuits is the same [124].

In basic circuit theory [123], a parallel circuit is equivalent to a given series circuit when,

$$R_p = R_s(Q^2 + 1) \tag{5.2}$$

and

$$X_p = \frac{R_p}{Q}. \tag{5.3}$$

On the other hand, for a given parallel circuit, the equivalent series circuit is,

$$R_s = \frac{R_p}{Q^2 + 1} \tag{5.4}$$

and

$$X_s = QR_s. \tag{5.5}$$

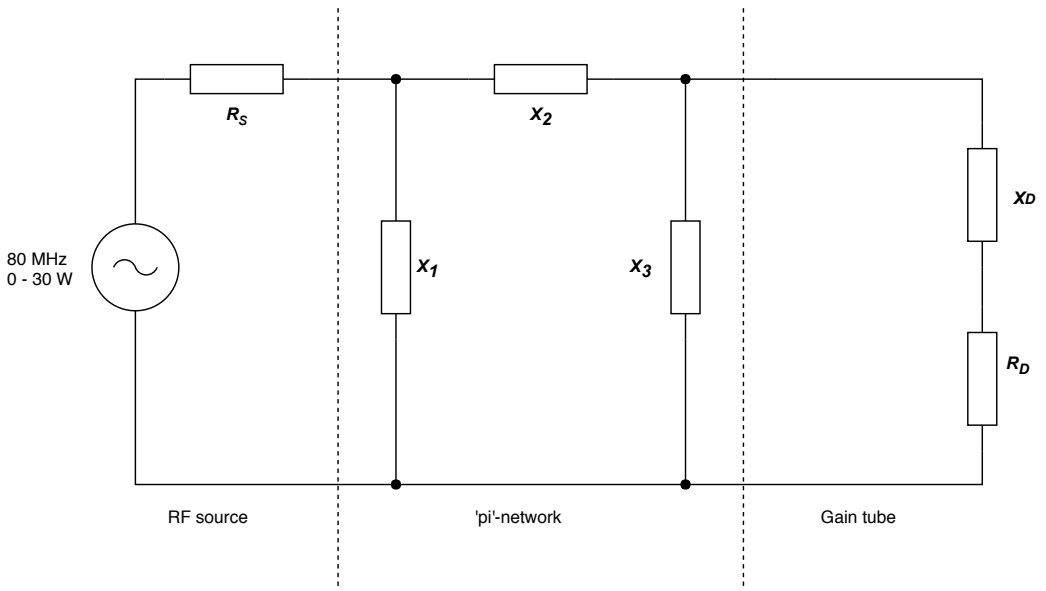

Figure. 5.2.: Equivalent circuit for matching the RF power source to the He-Ne discharge using a 'pi'-network.

There are three basic impedance matching networks used in RF designs which are the L-, 'pi'-, and T-networks. In ring lasers, the most common matching configuration is the 'pi'-network because it allows a gradual impedance change and can handle a larger impedance ratio. An equivalent circuit to illustrate the RF source, the matching network and the gain tube can be represented by Figure 5.2. On the right hand side of the figure is the RF source, which has a 50 Ω impedance, and is denoted as a parallel resistance, R_S in

the figure. On the right-hand side is the load impedance where R_D is the resistance, and X_D is the reactance representing the gain tube and the discharge plasma respectively.

The 'pi'-matching network is inserted in between the source and the load. The circuit consists of two parallel reactances (X_1 and X_3) and one series reactance (X_2). Note that the reactance, X can be either an inductance, L or a capacitance, C and their values can be determined by:

$$L = \frac{X}{2\pi f_r} \tag{5.6}$$

and

$$C = 2\pi f_r X, \tag{5.7}$$

where f_r is the resonance frequency.

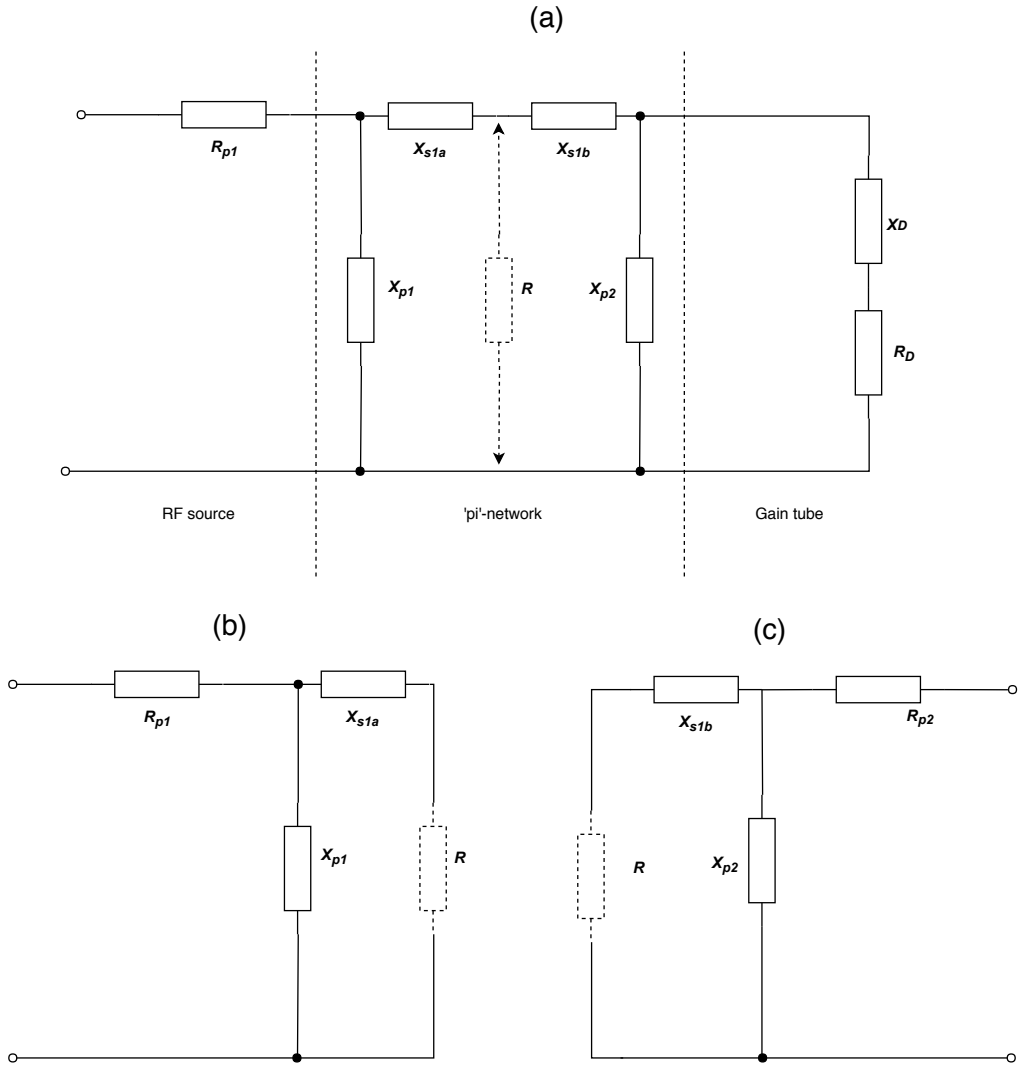

Figure. 5.3.: Analysis of the equivalent circuit for matching the RF power source to the He-Ne discharge using a 'pi'-network.

In principle, to determine X_1, X_2 and X_3, the 'pi'-network circuit in Figure 5.2 can be simplified by converting the 'pi'-network into two equivalent back-to-back L-network circuits as illustrated in 5.3 (a). A virtual load denoted as R can be inserted in the middle so that we can calculate each L-section separately. In the figure, the total impedance from the RF source is represented by a resistance connected in parallel denoted as R_{p1}, the two parallel reactance (X_1 and X_3) are represented by X_{p1} and X_{p2}, while the series reactance (X_2) is divided into X_{s1a} and X_{s1b} respectively.

To solve the first network illustrated in Figure 5.3 (b), from Equation 5.2.1, Q for the first circuit is calculated by,

$$Q_1 = \sqrt{\left(\frac{R_{p1}}{R}\right) - 1}. \tag{5.8}$$

Then, X_{p1} and X_{s1a} are determined by using Equation 5.2.1 and Equation 5.2.1 respectivity:

$$X_{p1} = \frac{R_{p1}}{Q_1}, \tag{5.9}$$

$$X_{s1a} = Q_1 R. \tag{5.10}$$

In Figure 5.3 (c), the total series load impedance can be transformed into a parallel total load impedance, R_{p2}, where,

$$Q_2 = \frac{X_D}{R_D}, \tag{5.11}$$

$$R_{p2} = R_D(Q_2^2 + 1). \tag{5.12}$$

Finally, the values of X_{p2} and X_{p2} can be determined as follows:

$$Q_3 = \sqrt{\left(\frac{R_{p2}}{R}\right) - 1}, \tag{5.13}$$

$$X_{p2} = \frac{R_p}{Q_3}, \tag{5.14}$$

and,

$$X_{s1b} = Q_3 R. \tag{5.15}$$

To design a matching network via the analytical method as above yields precise results which are suitable for computer simulation (if a more complex circuit is involved). Other

than that, we can rely on the Smith Chart[2] to verify the value of the elements graphically [123], [126]. The latter method is usually more intuitive and faster than the former method. However, to design a matching network both analytically and graphically, we have to know the exact value of X_D. The value of X_D is contributed by the gain tube, the gas discharge as well as all electrical and electronic connections between the transmitter and the load. Thus, X_D is impossible to be measured.

5.2.2 Experimental Details

Since the actual value of the total impedance is unable to be determined, the design of the impedance matching unit, as well as the electrode geometry was performed by a trial-and-error method until the best matching was obtained. Ideally, when full RF excitation of 30 W is applied, an excited discharge along the whole gain tube ($\approx$ 400 mm of plasma length) is desired. The goal of this experiment is to achieve a maximum RF power transfer along the new gain tube at the highest possible gas pressure. In other words, the new impedance matching unit has to be able to match the 50 Ω impedance from the transmitter to the highest impedance generated by the gas fill in the gain tube.

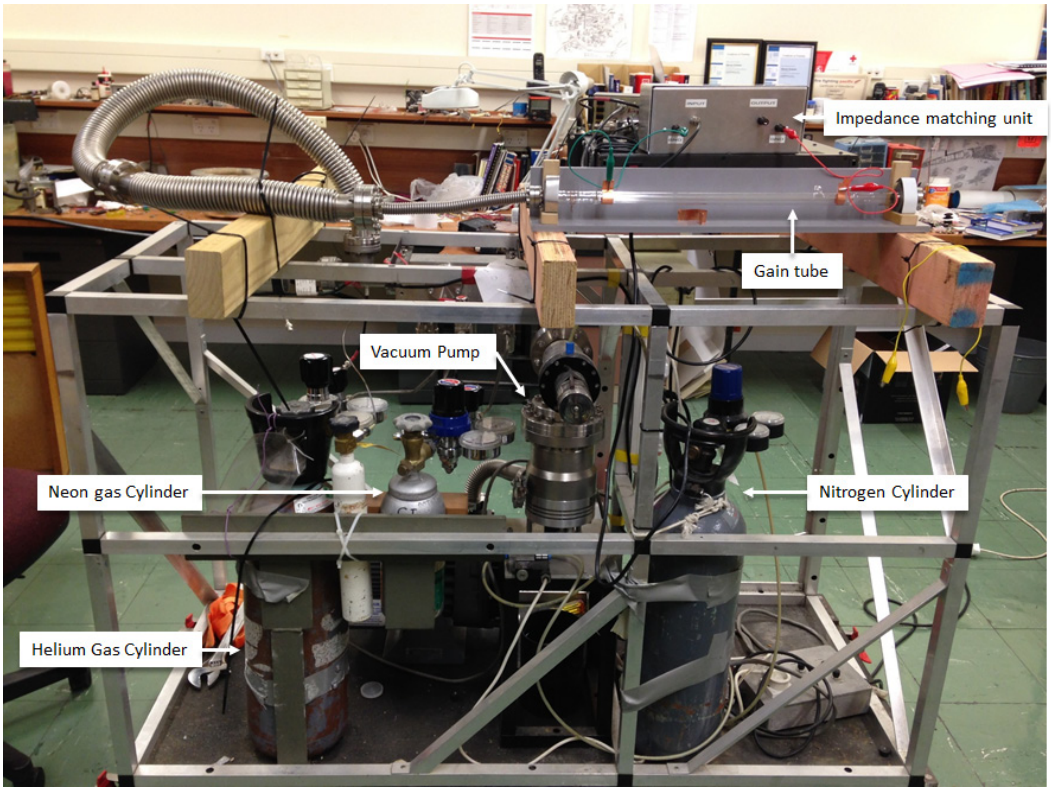

Figure. 5.4.: Experimental setup to establish the ideal impedance matching unit with an optimum arrangement of electrodes for the 580-mm-long gain tube.

[2]The Smith Chart was developed by P.H. Smith in the 1930s to solve the transmission line and impedance matching problems where the values of impedance, admittance and reflection coefficient can be determined based on a graphical method [125].

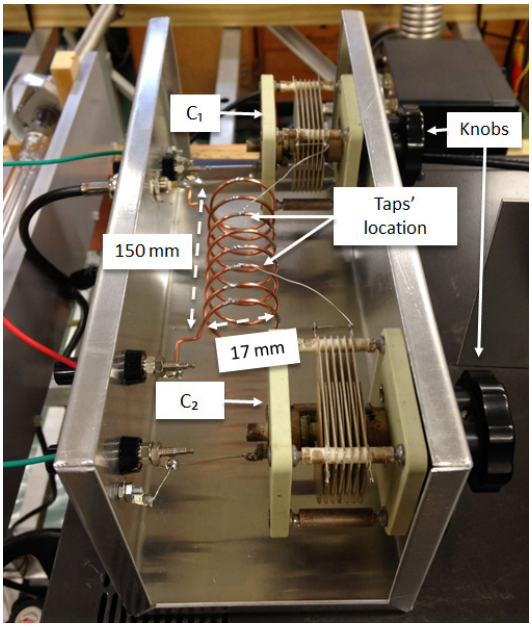

Figure. 5.5.: Initial design of the impedance matching unit

A photo of the experimental setup is shown in Figure 5.4. A directional RF power meter (RS W520) was placed between a transmitter (Tait T800) and an impedance matching unit to measure the total transmitted and total reflected power. Figure 5.5 shows the initial design of the impedance matching unit circuit. This initial design is based on the impedance matching unit for the 100-mm-long gain tube (see Section 3.1.1). The 'pi-network' configuration consists of two variable capacitors and an air-coil inductor. The air-coil inductor is approximately 17 mm in diameter with a total length of 150 mm which yields approximately 0.3 μH of inductance[3]. The location of the taps[4] on the coil enable the total inductance to be varied.

In contrast to the matching unit discussed in Section 3.1.1, the two adjustable capacitors, C_1 and C_2 can be varied from 2 pF to 100 pF instead of 8 pF to 150 pF (refer to Figure 3.4). The output from the matching unit was fed to the gain tube by a wire with crocodile clip to a thin strip of copper sheet with a 15 mm width that wrapped around the gain tube. This initial electrode design was also based on the 100 mm-gain tube's electrode design.

The 580-mm long gain tube was attached to a portable vacuum system via flexible bellows for gas filling and gas evacuation processes. The portable vacuum system consists of a turbo-molecular pump which is coupled through a normally closed pneumatic valve, a nitrogen gas cylinder (for the pneumatic valve), and three different noble gas (helium,

[3]An approximation of an air coil inductance can be calculated by: L (in μH) $= \frac{a^2 n^2}{9a+10b}$; where a is the coil radius in inches, d is the coil length in inches and n is the number of turns [127].

[4]When a coil tap is connected to one end of the coil (or the end disconnected and reconnected to the tap), the section of coil between the tap and its connected end is bypassed and reducing the number of turns in the coil [127].

natural neon, and 50:50 neon) cylinders. Each gas cylinder (except for the nitrogen cylinder) is connected to the system through a pressure regulator and isolated from the system by means of variable leak valves. A pressure gauge is attached between the flexible bellow (which is connected to the gain tube) and the vacuum system to monitor the gas pressure.

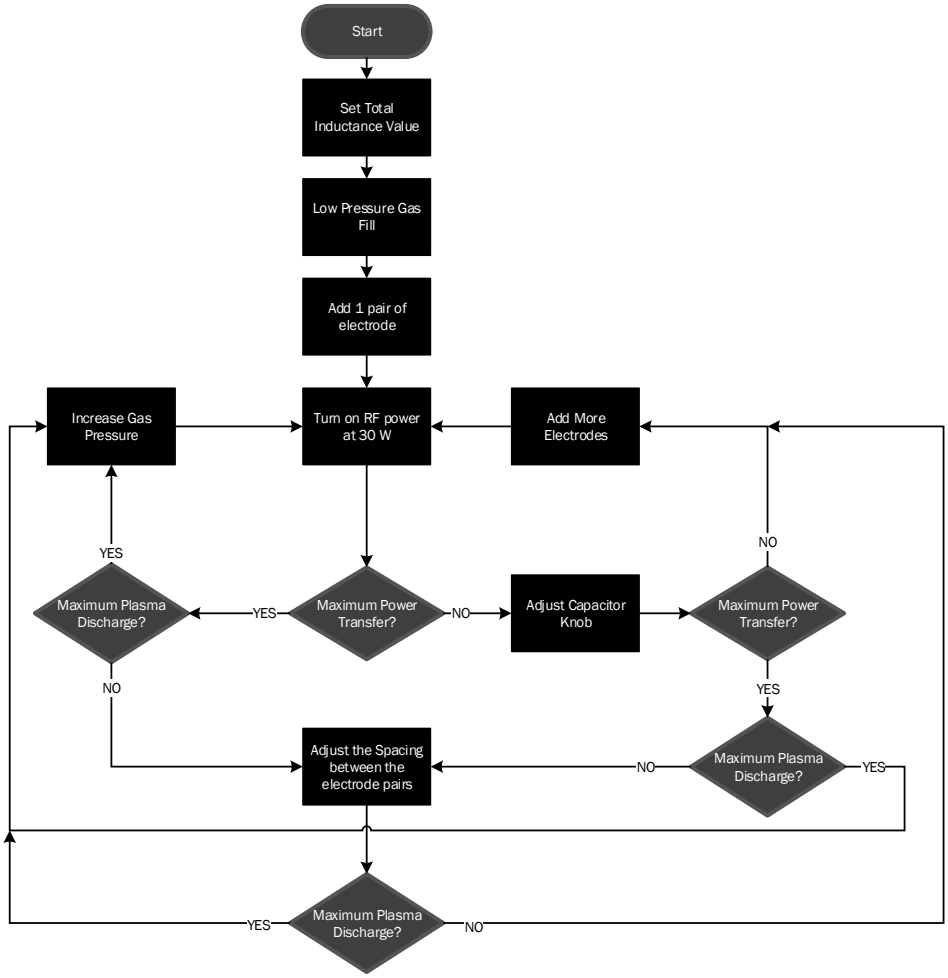

Figure. 5.6.: A flow chart to represent the procedure for designing the impedance matching unit and electrode configuration. For each iteration, the value of inductance (number of coil's turn) and the electrode width were set as a constant.

The experimental procedure is represented by the flowchart illustrated in Figure 5.6. Firstly, the initial inductance value was set to a constant by fixing the location of the taps to the third and the sixth coil on the air-coil inductor. This is to limit the number of variables which influence the load impedance. Also, in order to start from a low impedance value, the gain tube was initially filled with low total gas pressure. Then, the RF transmitter was turned on with a total power of 30 W. After that, the adjustable capacitor knobs on both sides of the matching unit were turned slowly until the reflected power reading was minimised (between 0 to 1 W) while forward power was maximised

(30 W). The tuning of the capacitive knobs was alternated with either varying the spacing between the electrodes or increasing the number of electrodes until a long gas discharge (bright pinkish plasma) was observed inside the gain tube. Afterwards, we gradually raised the pressure inside the gain tube and repeated the preceding steps. Alternatively, the set value of the total inductance should be reset if neither varying the capacitive knobs nor changing the number of electrodes improves the impedance matching.

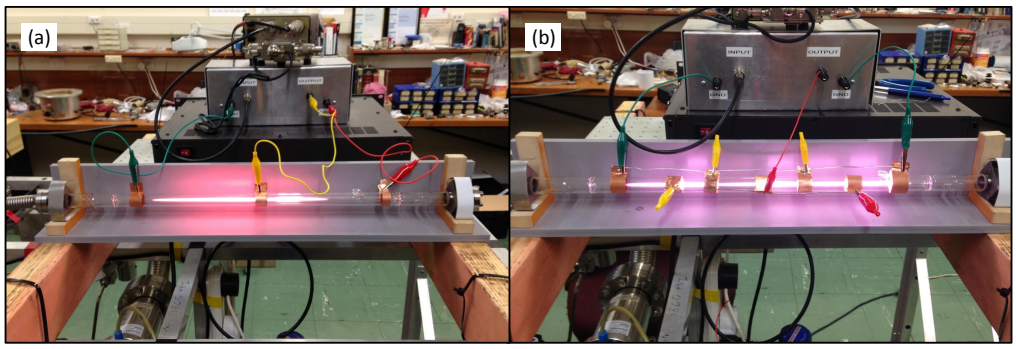

Figure. 5.7.: The longest achievable plasma discharge with (a) one live electrode and two ground electrodes configuration and (b) 3 live electrodes and 4 ground electrodes; for a total gas pressure of 2 torr. Each electrode width was 15 mm.

Initially, with 2 torr of total gas pressure, the longest plasma length achieved at approximately 1 W of reflective power with the electrode configuration shown in Figure 5.7 (a) was only half of the total length of the gain tube. As further adjustments on the capacitive knob and varying the distance between the electrodes did not improve our observation, more electrodes were gradually added along the gain tube while maintaining the same electrode width. A longer plasma along the gain tube was successfully obtained with 3 pairs of electrodes. The spacing between each electrode was about 30 mm apart, and an extra ground electrode was placed at the end of the tube for an additional capacitive grounding as shown in Figure 5.7 (b). However, at higher gas pressure (3.5 torr), the impedance was unable to be matched by the matching unit because a much higher impedance had been introduced (the capacitance along the gain tube was too high due to the increasing number of electrodes as well as the higher gas pressure). At this point in the experiment, we decided to reduce the capacitance value along the gain tube by using thinner copper strips[5].

[5]Larger conductive (plate) area results in more electric field flux (charge collected on the plates) for a given field force (voltage across the plates). Hence, less plate area gives less capacitance.

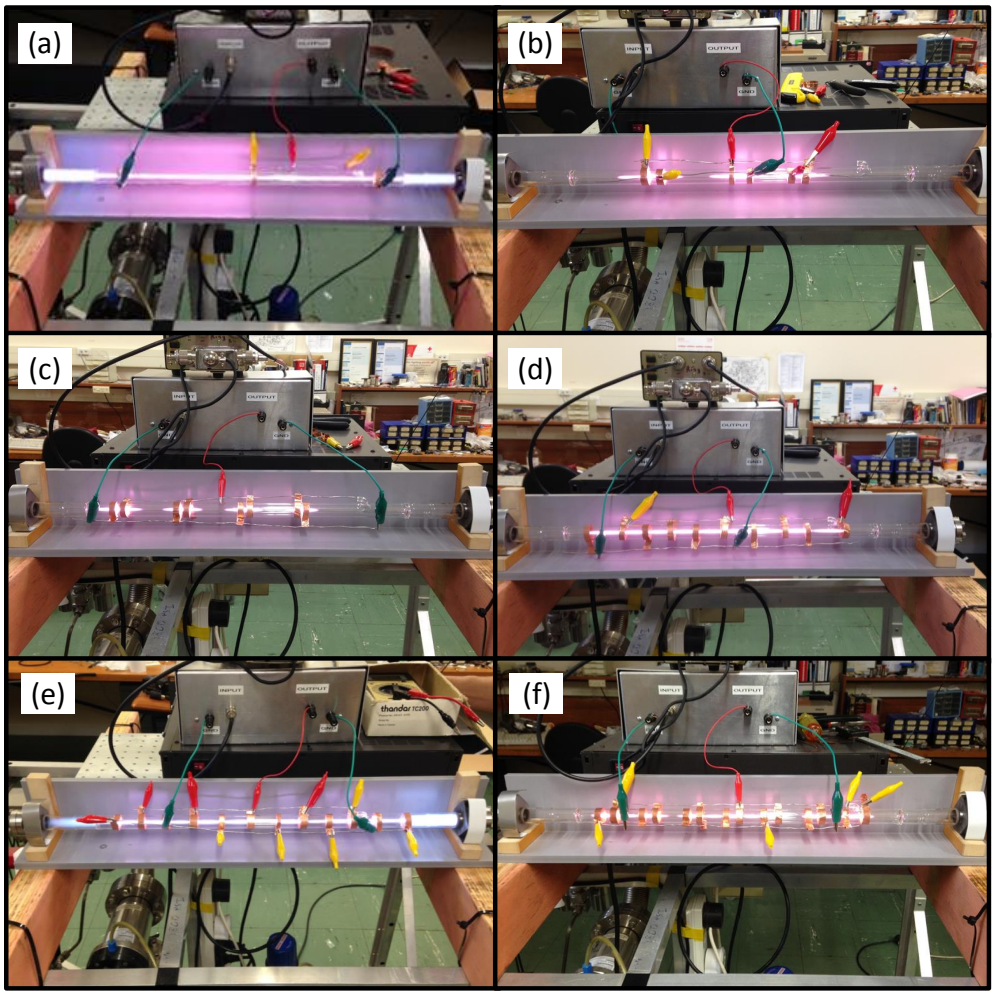

Figure. 5.8.: Gas discharges with 8-mm-width copper electrodes. (a) one live electrode and 2 ground electrodes configuration at a total gas pressure of 2 torr; (b) 3 electrode pairs configuration at a total gas pressure of 3.5 torr; (c) 4 electrode pairs configuration at a total gas pressure of 4 torr; (d) 5 electrode pairs configuration at a total gas pressure of 4 torr; (e) 6 electrode pairs configuration at a total gas pressure of 4 torr; and (f) 7 electrode pairs configuration at a total gas pressure of 6 torr.

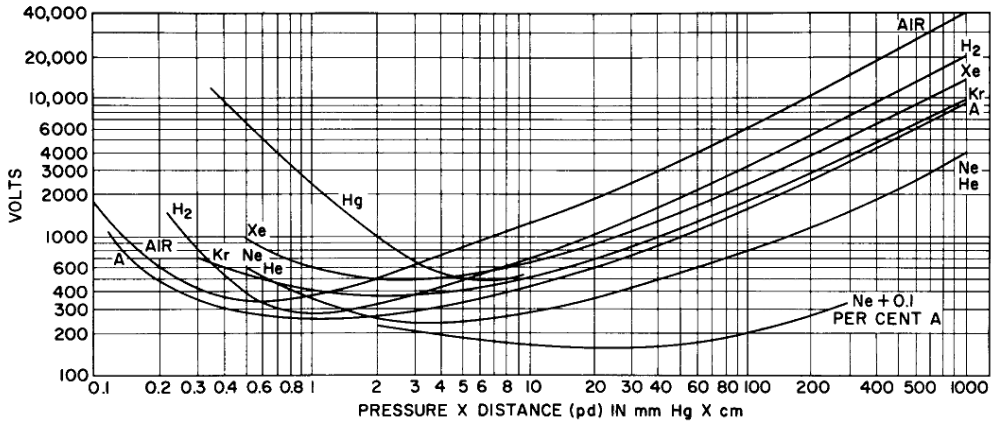

Figure. 5.9.: Paschen's curve for a variety of gases reproduced from Figure 9 in ref. [128].

The electrode width was reduced to 8 mm, which is approximately half of the initial electrode width. With the new electrode size, at 2 torr of total gas pressure, the impedance was easier to match. At the same time, a discharge along the entire gain tube was successfully established with 3 electrodes (one live and 2 ground electrodes) as depicted in Figure 5.8 (a). When the total gas pressure was increased beyond 2 torr, a uniform plasma discharge was not observed. Therefore, more electrodes were gradually added. At the same time, the distance between each electrode and the gap between each electrode pair were varied. This was done to distribute the plasma more uniformly along the gain tube.

A few examples of the plasma discharge at various electrode configurations and total gas pressures are displayed in Figure 5.8 (b)-(f). At higher gas pressures, more electrodes were added to the gain tube. Also, the plasma distribution was more uniform when the distance between each electrode was equal (Figures 5.8 (d) and (e)). These observations can be explained as follows: Paschen's law relates the breakdown voltage, V_B (the voltage required to initiate a gas discharge along the discharge tube) to the product of the gas pressure, p and the distance between electrodes, d_e by,

$$V_B = \frac{\mathrm{B}pd_e}{\ln(\mathrm{A}pd_e) - \ln[\ln(1+\gamma^{-1})]}, \tag{5.16}$$

where A is a constant governed by the saturation ionisation of the gas as a function of the ratio of electric field to the gas pressure, B is the excitation and ionisation energies, and γ is the secondary-electron-ionisation coefficient. A and B are determined experimentally [129].

The breakdown voltage for a gas discharge depends on the probability of collisions between the electrons and gas atoms. When the pressure inside the gain tube is high, the probability of an electron to collide with an atom is higher, which results in a high pd_e product. Electrons lose more energy as a result of colliding with the gas atoms, hence,

the high breakdown voltage. However, the breakdown voltage does not increase linearly with pd_e. Instead, as shown in Figure 5.9, there is a regime where a low pd_e requires high breakdown voltage to initiate the gas discharge. This may arise due to either a close distance between the electrodes, resulting in a low collision probability between electron and gas atom; or in the context of low pressure, fewer gas atoms are available for gas ionisation to occur. For this reason, high V_B is needed to initiate the gas discharge.

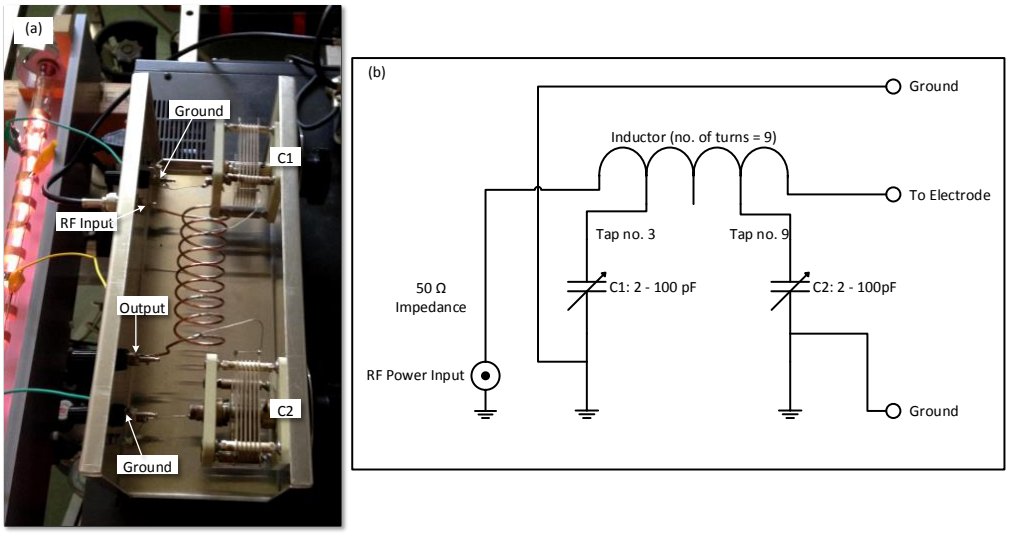

Figure. 5.10.: (a) Final design of the impedance matching unit; and (b) the schematic circuit diagram of the impedance matching unit.

The optimum impedance matching unit design is shown in Figure 5.10. The inductor's coil has 9 turns, and the tap locations are fixed at tap number '3' and number '9'. This is corresponding to an inductance, $L \approx 0.08\ \mu$H.

The total number of electrode pairs which are sufficient to generate a maximum plasma length (approximately 400 mm) for a range of total pressures from 2 torr until 13 torr are 8 pairs. The total capacitance across the electrodes is 20 pF (measured by a capacitance meter). Figures 5.11 (a) to (c) show the plasma discharge along the gain tube with a total pressure of 2 torr, 8 torr and 13 torr respectively at RF power of 30 W. Each electrode is separated by an equal distance of 20 mm.

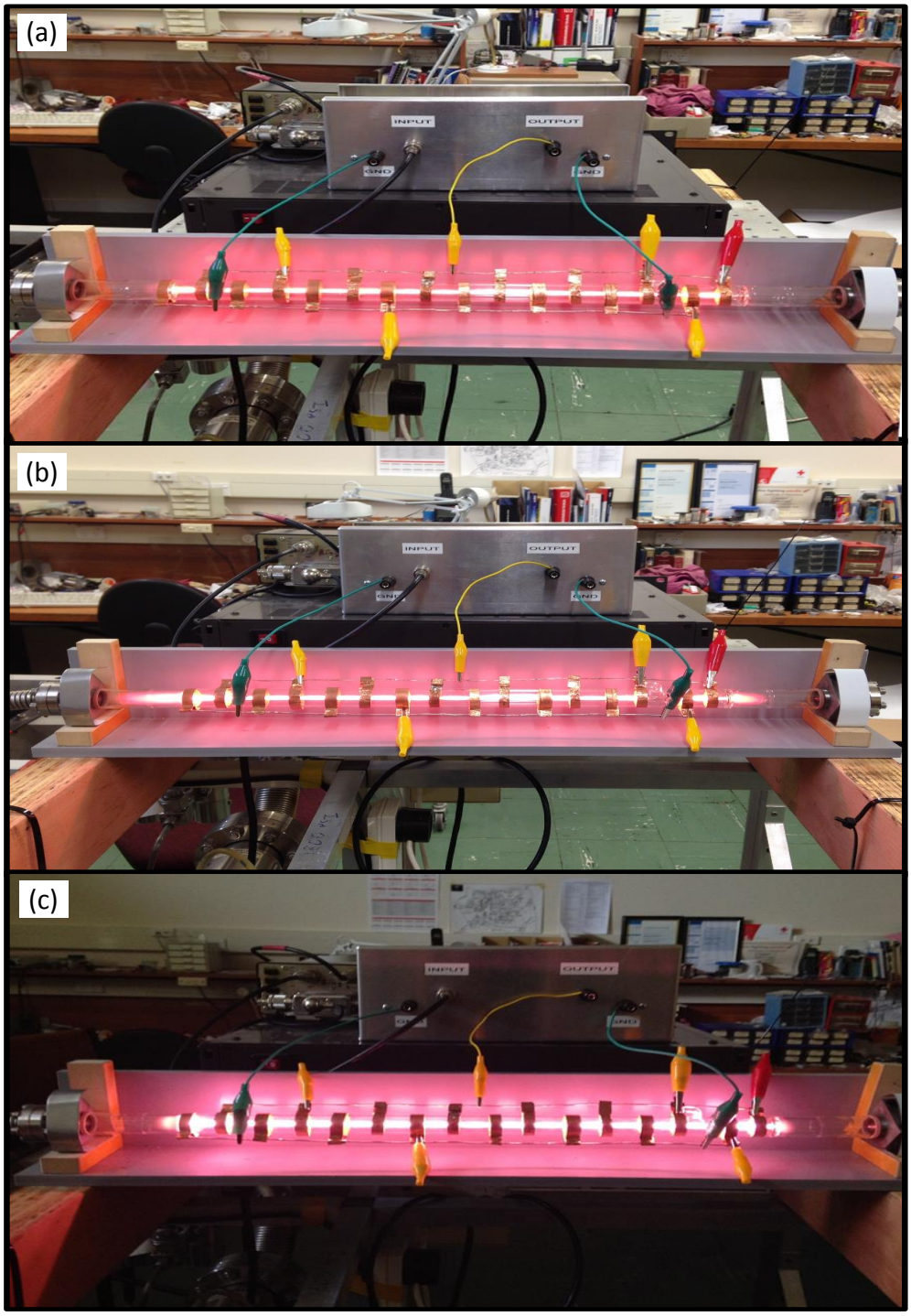

Figure. 5.11.: Plasma discharge along the discharge tube with a total of 8 pairs of 8-mm-width copper electrodes at: (a) 2 torr; (b) 8 torr; and (c) 13 torr.

5.2.3 Reconfiguration of the 2.56 m^2 Test Cavity: Part 1

The modification to the configuration of PR-1 was performed by replacing the ring cavity's right stainless-steel-arm with the 580-mm-long gain tube. Before removing the right arm, the 'red' supermirrors (REO 4 mirror set) were installed into the PR-1 cavity. To imitate the counter-propagating beam path, two 543.4 nm linear He-Ne lasers were injected through the centre of both bottom mirrors in the opposite directions. Then, the laser cavity was aligned by directing the green laser beam path such that both laser beams will pass through the centre of the gain tube and all four mirrors. The green laser beams will be our reference for the position of the new discharge tube.

After that, the stainless steel tube was carefully removed. As displayed in Figure 5.12 (a), a stainless steel mounting plate was fixed on the wall to serve as a base plate to mount the new matching unit and the micrometer holder. Next, the long gain tube was connected to the top and bottom bellows as shown in Figure 5.12 (b). Subsequently, the electrodes were wrapped around the Pyrex tube before fixing the micrometer holder around the gain tube (see Figure 5.12 (c)). The position (the top and bottom end) of the gain tube was aligned by the two sets of micrometers in the in-plane and out-of-plane positions respectively. Finally, the new matching unit was mounted on the wall, next to the new gain tube as pictured in Figure 5.12 (d). The directional RF power meter was connected between the mounted matching unit and the 80 MHz RF transmitter.

After the new gain tube was installed, we filled the PR-1 cavity with 0.2 mbar of natural neon and 2 mbar of total pressure. The first transmitter was turned on (at 20 W) to excite the gas mix with the 100-mm gain tube. When lasing at 632.8 nm was successfully obtained, the second transmitter was turned on. A full discharge along the 580 mm long gain tube was observed as shown in Figure 5.12 (d).

The optimisation of the new gain tube's position was performed by measuring the laser power while carefully varying the tube in the in-plane and out-of-plane directions. The RF power to the shorter gain tube was turned off to let PR-1 operate solely on the new gain tube. The top and bottom micrometers were adjusted carefully until a maximum power was measured to indicate that the new gain tube is at the optimum position. At the optimum alignment, the output power was measured to be 5600 nW at 25 W of RF input power.

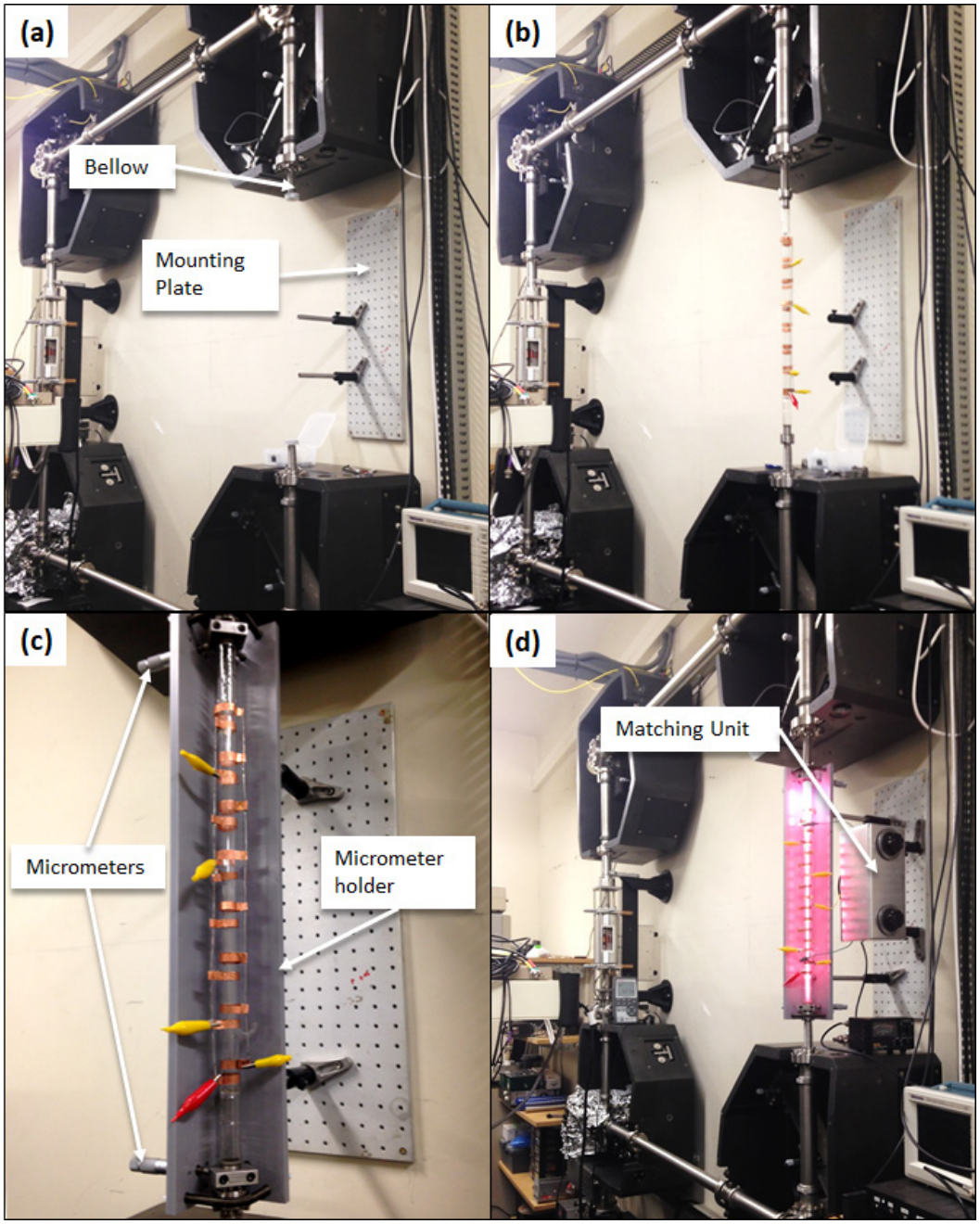

Figure. 5.12.: (a) Two flexible bellows were connected to the top and bottom bellows of the two mirror chambers, and a stainless steel mounting plate was fixed on the wall; (b) the new gain tube was installed by connecting each tube's end to bellows; (c) the electrodes were wrapped around the new gain tube and a holder with two sets of micrometers was mounted to hold the discharge tube; (d) the matching unit was mounted beside the new gain tubes.

5.2.4 A Multi-Wavelength Ring Laser Gyroscope

Subsequently, the REO 4 mirrors in the cavity were replaced with a new set of supermirrors. These new supermirrors were also provided by REO and were fabricated by means of the IBS technique similar to the supermirrors discussed previously in Chapter 3. The only difference between this new set of supermirrors from all the previous IBS-supermirrors is they are polished as planar surfaces as opposed to using the 'spindle-polishing' technique. These mirrors were subsequently 'stretched' to provide the desired radius of curvature [130]. The substrate surface modulations arising from the spindle-polishing technique yield increases in the total loss in the laser cavity [15]. As the new approach to mirror surface preparation avoids the spindle polishing technique, it is expected to provide a significant improvement in the quality of the substrate in comparison to the previous REO-mirrors. These new supermirrors have transmission values at 45° angle of incidence (AOI) in the s-polarisation direction as listed in Table 5.2.

Wavelength (nm)	Transmission (ppm)	Absorption + Scatter (ppm)	Total Loss (ppm)
543.4	0.18	7.6	7.7
593.9	6	-	-
604.6	32	-	-
611.8	158	-	-

Table. 5.2.: The specifications of the new IBS-supermirror provided by REO Inc (ROC = 2.5 m).

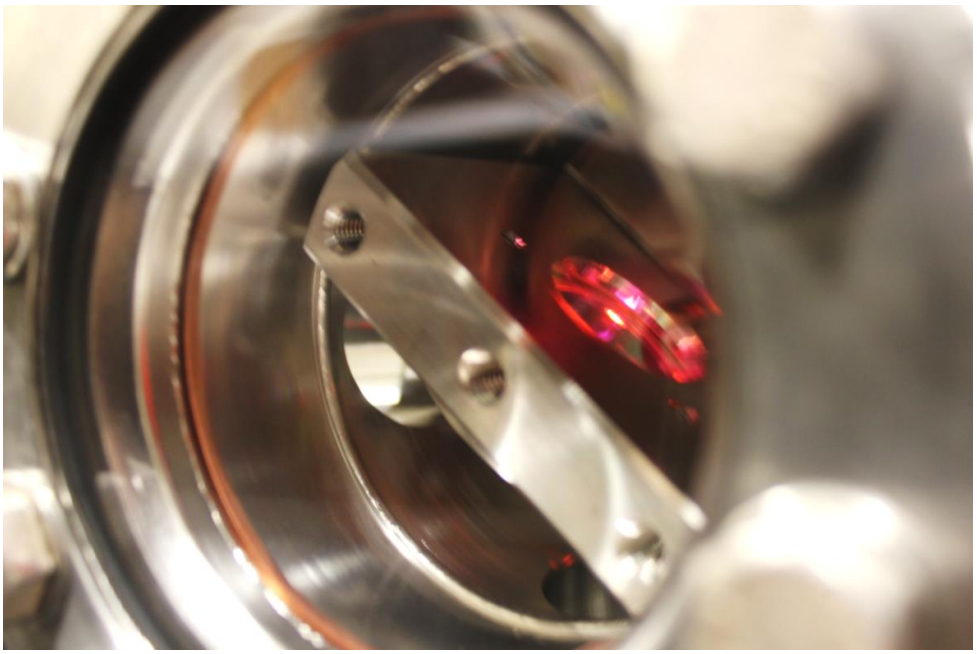

Figure. 5.13.: 'Red-orange' laser beam spot on the mirror surface.

After the mirror change procedure, the laser cavity was refilled with 0.2 mbar of natural neon and 2 mbar of total pressure. When maximum RF power was applied to both of the PR-1 gain tubes, the beam spot observed on the supermirrors was bright 'red-orange' as depicted in Figure 5.13.

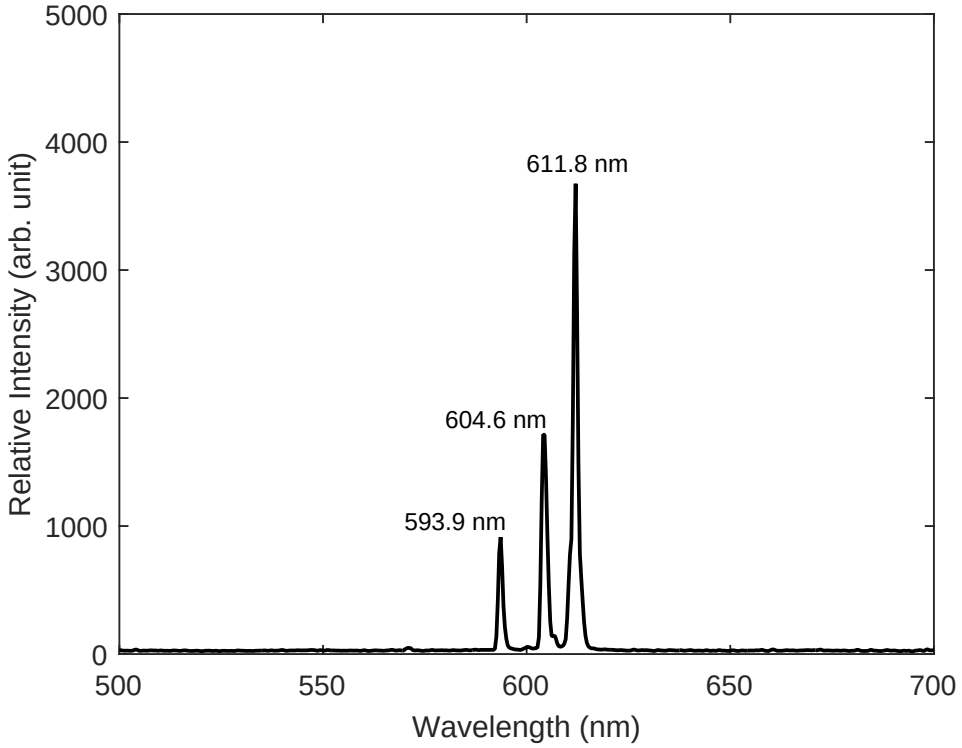

Figure. 5.14.: Laser transitions at 611.8 nm, 604.6 nm and 593.9 nm detected by an Ocean Optics spectrometer.

As the laser beam was fed into a spectrometer (Ocean Optics USB2000+ UV-Vis-NIR) via a fibre optic cable, lasing at three different wavelengths was observed. Figure 5.14 shows laser transitions at 611.8 nm, 604.6 nm and 593.9 nm. By referring to Table 5.2, the mirror transmission at 611.8 nm is the highest (158 ppm). Also, the gain at 611.8 nm is much higher than that of 604.6 nm and 593.9 nm transitions (Table 1.2). Therefore the laser spot observed was dominated by the orange (611.8 nm) colour.

The transmission spectrum of the supermirrors was measured by using a spectrometer and a Quartz Tungsten-Halogen Lamp as the broadband source. The broadband source provides emission of 400 - 2200 nm. The experimental setup is shown in Figure 5.15. An iris was mounted in between the broadband source and the IBS-supermirror so that the light source can be focused onto the centre of the supermirror. The transmitted light after the supermirror was fed by a fibre optic cable into the spectrometer via an SMA connector. Then, the signal from the spectrometer was connected to a laptop to observe the spectrum.

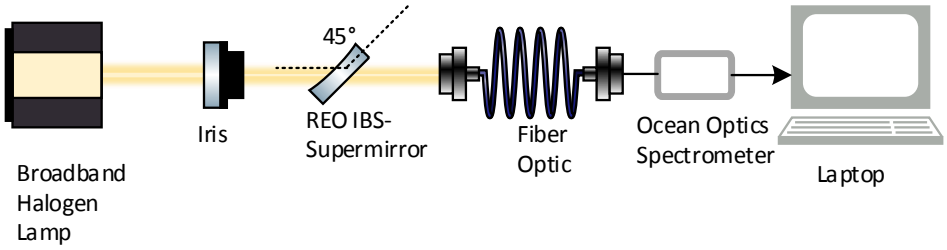

Figure. 5.15.: Experimental setup to characterise the transmission of the supermirrors.

Figure 5.16 (a) shows the broadband spectrum detected by the spectrometer and the supermirror transmission at normal incidence and at 45° angle of incidence is shown in Figure 5.16 (b) and (c). The broadband spectrum was observed to fall in the 400 nm to 1000 nm range as shown in Figure 5.16 (a). This is consistent with the specifications of the spectral range of the Ocean Optics spectrometer. As seen from Figure 5.16 (c), the lowest transmission loss is centred at a wavelength of 543.4 nm. Although the peak reflectivity for this mirror is centred at a wavelength of 543.4 nm, it still has relatively low transmission loss at 611.8 nm, 604.6 nm and 593.9 nm. In order to achieve lasing at 543.4 nm, the mirror should be designed either by shifting the maximum mirror reflectivity towards a wavelength shorter than 543.4 nm or by introducing much higher transmission loss at the longer wavelengths [46].

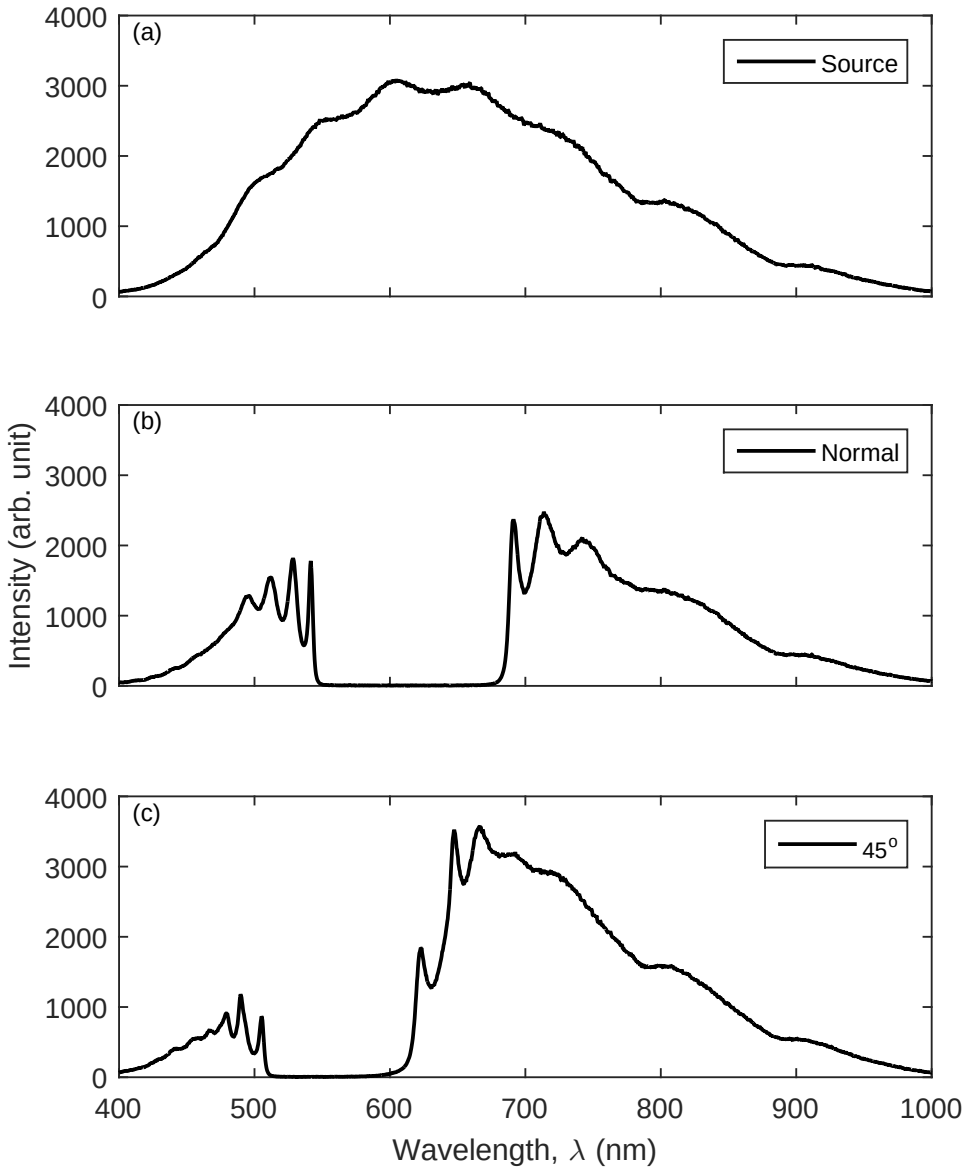

Figure. 5.16.: The spectrum of the (a) broadband light source; (b) supermirror transmission at normal incidence and at (c) 45° transmission of the supermirror.

5.2.5 The Cavity Q Factor and Gain Measurement at 611.8 nm, 604.6 nm and 593.9 nm

The quality factor of the PR-1 laser cavity with the new IBS-supermirrors was determined by connecting a coaxial relay to the RF transmitter which is coupled to the 580 mm long gain tube. The RF transmitter that is connected to the 100 mm long gain tube was switched off so that the laser gain was sustained solely by the longer gain tube.

A cold cavity ring-down time measurement yielded τ_{decay} = 70 μs. Therefore, the loss on each mirror can be calculated to be 76.2 ppm (by assuming ν_0= 490 THz) and the cavity Q factor with these supermirrors is inferred to be 2.2 $\times 10^{11}$.

Parameter	Value
Ring-down time,τ_{decay} (μs)	70
Total loss, L (ppm)	304.76
Loss per mirror (ppm)	76.2
Quality factor, Q	2.2 $\times 10^{11}$
Finesse, F	2.1 $\times 10^{4}$

Table. 5.3.: Measured τ_{decay} and the corresponding cavity Q factor, finesse, F and loss per mirror achieved with the new REO mirror sets.

Afterwards, an experiment to measure the gain at 611.8 nm, 604.6 nm and 593.9 nm at a fixed RF input power was conducted. The objective of this experiment was to investigate whether there is an optimum helium to neon gas mixing ratio which will encourage the laser transition at 543.4 nm; and at the same time, quenching laser action at 611.8 nm.

Figure 5.17 shows the experimental setup. A grating was employed to separate the CW laser beam into the three laser wavelengths. Note that, during this experiment, the laser beam was running on a high order transverse mode (TEM_{13}). The output power at each wavelength was measured by the OP-2-VIS silicon sensor which was connected to the Coherent power meter. An aperture was placed in front of the power sensor to avoid multiple laser beams being detected by the silicon sensor.

After refilling the cavity with a certain gas mixture, the gas was allowed to mix for half an hour before applying the RF excitation. The gas inside the cavity took a longer time to mix due to the extra long narrow path introduced by the 580 mm long gain tube. The total RF input power to excite the gain medium was maintained at 50 W (a total of 20 W RF power was supplied to the 100 mm gain tube while 30 W of RF power was applied to the 580 mm gain tube). The laser spectrum was observed simultaneously by feeding the CCW beam into the fibre optic cable and sending the signal to the spectrometer.

Figure 5.18 shows the laser transition at 611.8 nm can be obtained with natural neon partial pressures of 0.1 mbar to 0.5 mbar and at total gas pressures of 0.5 to 4 mbar. The

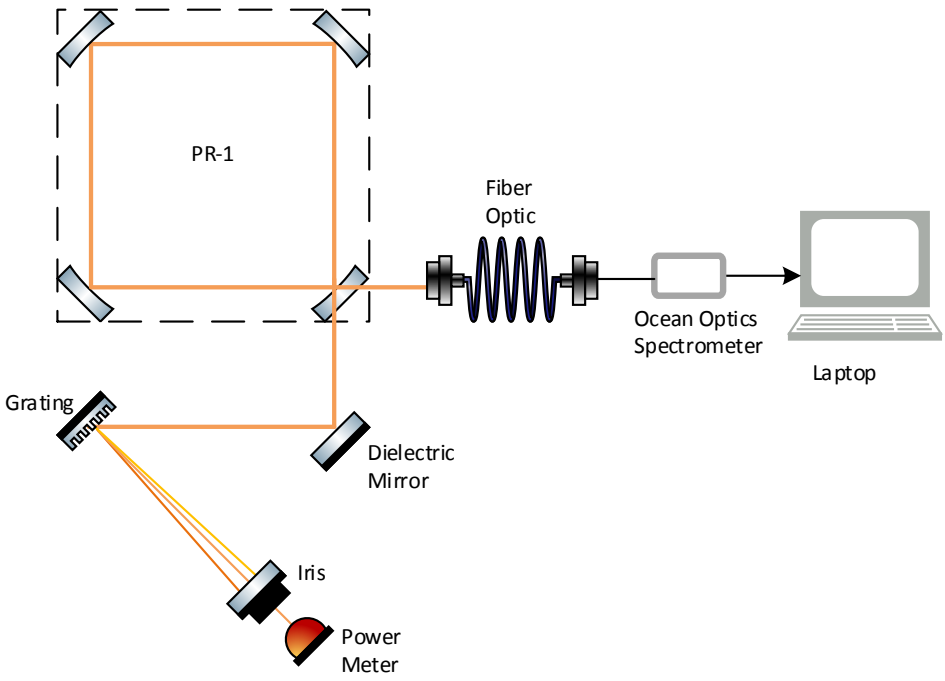

Figure. 5.17.: Experimental setup to measure the laser power at 611.8 nm, 604.6 nm and 593.9 nm

highest intracavity power achieved at this wavelength was 20 μW with a helium to neon ratio of 3 : 17 (0.375 mbar of neon and 2.5 mbar of total gas pressure).

The laser transition at 604.6 nm was observed at natural neon pressures from 0.1 to 0.5 mbar and total pressures of 0.5 to 3 mbar. The highest laser gain was achieved at 18 μW with a helium to neon ratio of 3 : 13 (0.375 mbar of neon and 2 mbar of total gas pressure). Finally, the laser transition at 593.9 nm can be achieved at a natural neon pressure of 0.2 to 0.375 mbar and total pressures between 1 to 3 mbar. The highest intracavity laser power at this wavelength was 10 μW at 1.8 mbar of total gas pressure with a natural neon partial pressure of 0.2 mbar.

Laser action was not possible with more than 4 mbar of total pressure. There was no hint of lasing at 543.4 nm. It is concluded that the mirror design will not allow laser action at 543.4 nm because the 611.8 nm transition will always dominate the gain.

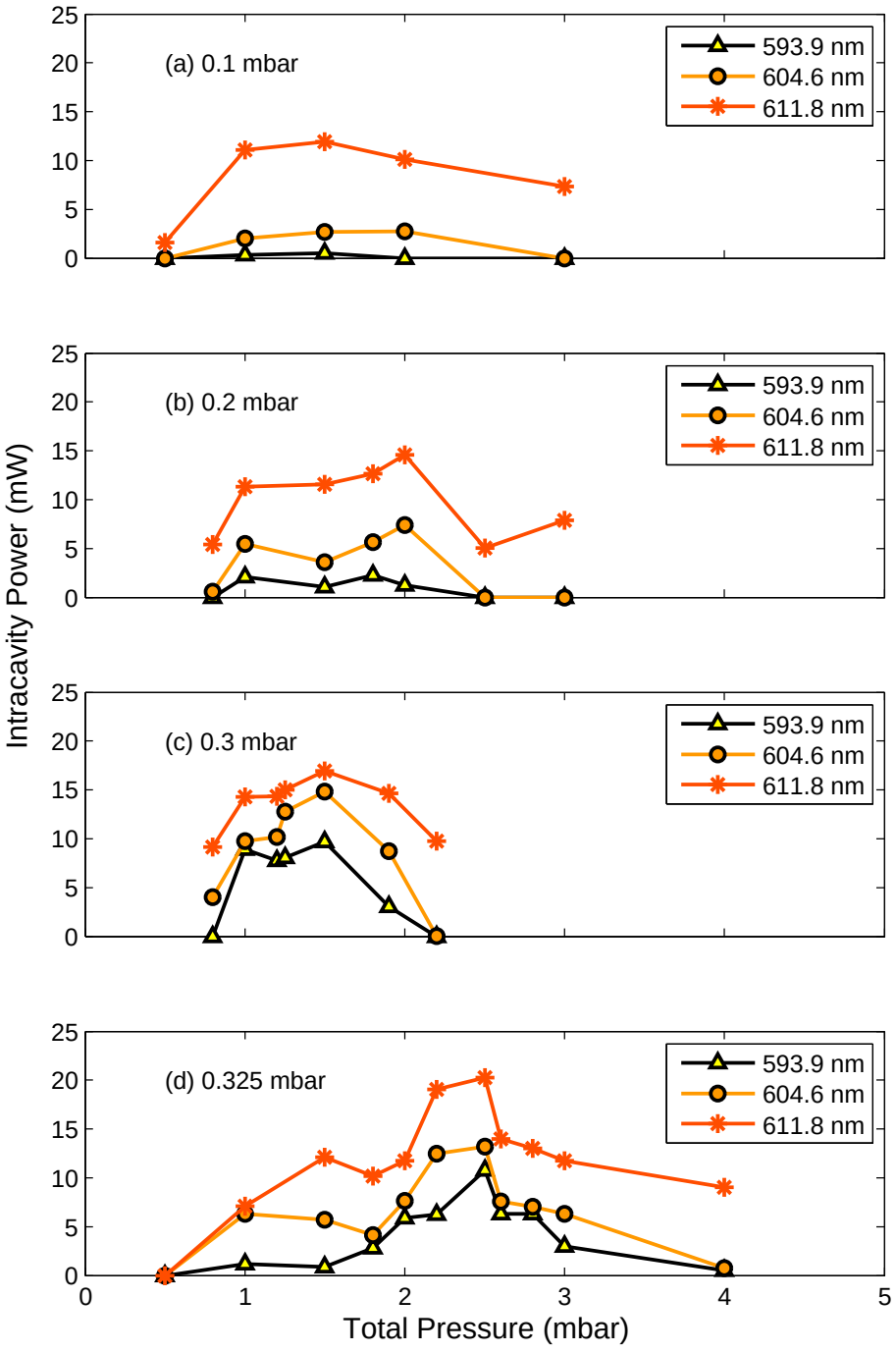

Figure. 5.18.: Intracavity laser power for laser transitions at 611.8 nm, 604.6 nm and 593.9 nm with the natural neon partial pressure fixed at: (a) 0.1 mbar; (b) 0.2 mbar; (c) 0.3 mbar; and (d) 0.325 mbar; as a function of total gas pressure when a constant 50 W of RF input power is applied to the gain medium.

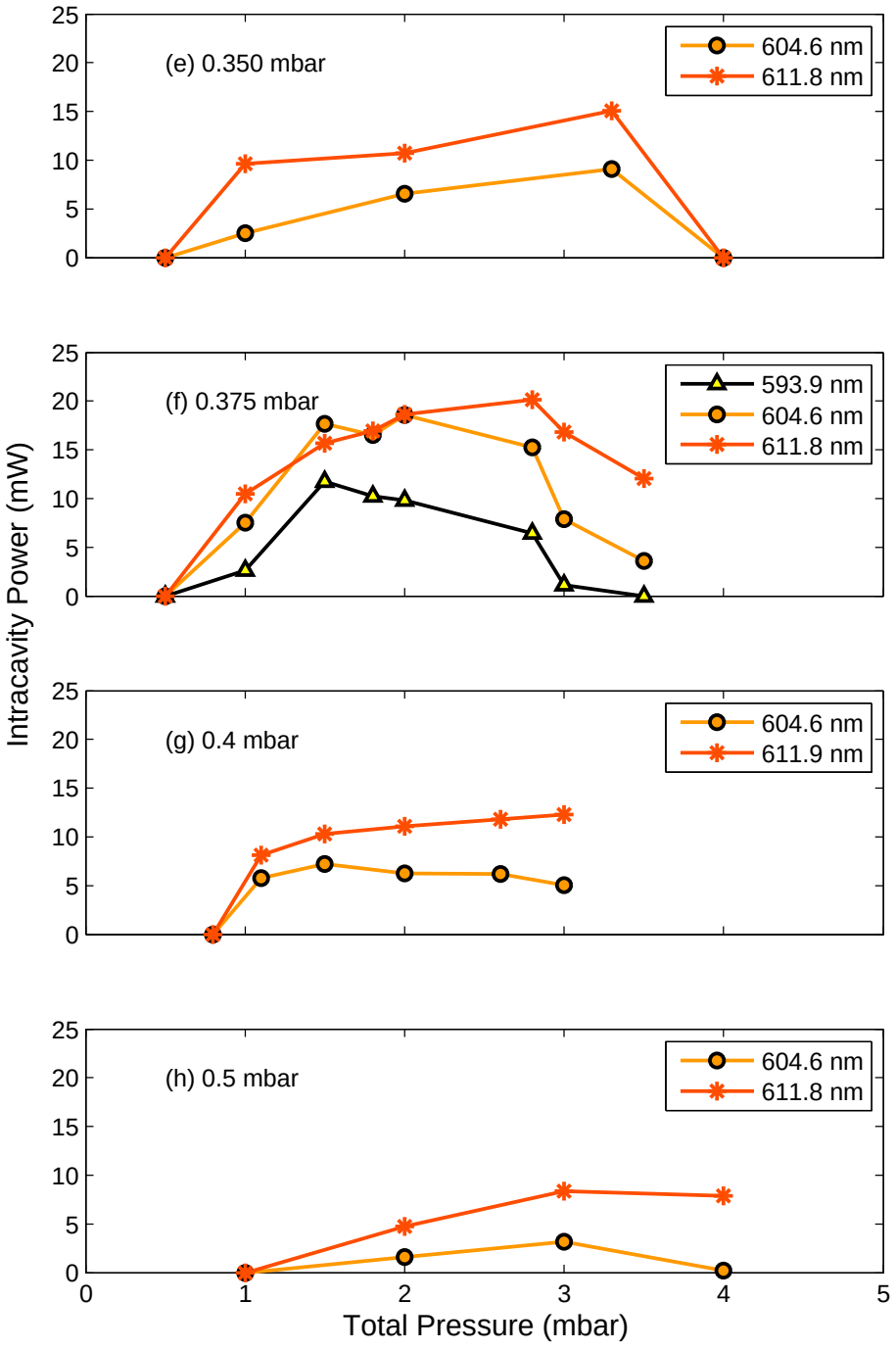

Figure. 5.18. (cont.): Intracavity laser power for laser transitions at 611.8 nm, 604.6 nm and 593.9 nm with the natural neon partial pressure fixed at: (e) 0.350 mbar; (f) 0.375 mbar; (g) 0.4 mbar; and (h) 0.5 mbar; as a function of total gas pressure when a constant 50 W of RF input power is applied to the gain medium.

5.3 Rotation Sensing with a Large He-Ne Ring Cavity Operating at 611.8 nm

Although lasing on the 543.4 nm ($3s_2 \rightarrow 2p_{10}$) transition was not achievable with the current IBS-supermirrors, we took this opportunity to study the optical and gyroscopic performance of a ring laser operating on the 611.8 nm ($3s_2 \rightarrow 2p_6$) neon transition. Due to time limitations, we did not investigate gyroscopic operation at 604.6 nm and 593.9 nm.

5.3.1 Gas Pressure Optimisation

The optimum gas mixing ratio at 611.8 nm was investigated by repeating the laser output power measurement in the previous section by using an equal mixture of ^{20}Ne and ^{20}Ne isotopes in the helium-neon gas mix. Before experimenting, the laser cavity was re-aligned[6] to achieve the lowest order transverse mode (TEM_{00}) as operation on the lowest order mode is desirable. Afterwards, the RF power was reduced until only the laser transition at 611.8 nm was observed. Fortunately, the 580-mm-long gain tube was sufficient to sustain the laser oscillation at 611.8 nm. Therefore, in this section, the 100 mm-long gain tube was not utilised.

After realigning the laser cavity, a cold cavity ring-down time of 40 μs was measured. This resulted in a cavity Q of 1.2 $\times 10^{11}$ and a total loss of 533 ppm. Note that these values differed from the measurement values quoted in Table 5.3 because the ring-down measurement in Section 5.2.5 was performed without separating the three laser wavelengths.

The mirror specification as listed in Table 5.2 indicates that the transmission loss at 611.8 nm is 158 ppm per mirror. So, the expected total loss at 611.8 nm should be more than 600 ppm. As the measured total loss was lower than expected; this suggests that the mirror transmission loss at this wavelength is lower than the specified value. The cavity finesse is 1.2 $\times 10^4$ as listed in Table 5.4, which is about 70% lower in comparison to the cavity finesse when the laser is running on the 632.8 nm wavelength. The lower cavity finesse achieved is due to the high mirror transmission loss at 611.8 nm.

The laser spot size on the mirror was measured to be approximately 2.7 mm in diameter. There was no reduction in the beam spot size in comparison to that 632.8 nm laser beam diameter measured in Chapter 3. We also note that there was approximately 5% discrepancy between the CW and the CCW beam powers. The variation in the power between the counter-propagating beams is commonly observed in large ring lasers [17].

[6] This was achieved by adjusting the micrometers on both of the gain tubes by careful iterations.

Parameter	Value
Ring-down time, τ_{decay} (μs)	40
Total loss, L (ppm)	533
Loss per mirror (ppm)	133.25
Quality factor, Q	1.2×10^{11}
Finesse, F	1.2×10^{4}

Table. 5.4.: The measured τ_{decay} and the corresponding laser cavity Q factor, finesse, F and loss per mirror at 611.8 nm helium neon transition. ν_0 = 490 THz.

From there on, the laser cavity was filled with a fixed partial pressure of 50:50 neon followed by the application of a constant 30 W of RF power to the 580 mm long gain tube for laser excitation. The laser output powers at 611.8 nm, 604.6 nm and 593.9 nm were measured by detecting the third order of diffraction of the laser beam after the diffraction grating. As the beam intensity at higher order diffraction is low, it is crucial to monitor the laser spectrum via the spectrometer simultaneously for validation.

From Figures 5.19 (a) to (f), lasing at 611.8 nm and 604.6 nm can be obtained for various (0.1 mbar to 0.6 mbar) 50:50 neon partial pressures with total pressures between 1 mbar to 6 mbar. On the other hand, lasing at 593.9 nm was only observed with 0.2 mbar of 50:50 neon at total pressures of 1 and 2 mbar, which is contrary to our previous observation in Figure 5.18. The laser transition at 593.9 nm was readily observed between 0.1 to 0.375 mbar of natural neon, for total gas pressures up to 4 mbar because the measurement was done by using two gain tubes (with a total RF input power of 50 W). Thus, with higher RF input powers, lasing at 593.9 nm with a higher neon content can be achieved.

The highest laser power was obtained with 0.2 mbar of 50:50 neon partial pressure at a total pressure of 2 mbar as shown in Figure 5.19 (b). This agrees with the optimum neon partial pressure for the 632.8 nm wavelength in Chapter 3. The optimum neon partial pressure (at 632.8 nm) is commonly 0.2 mbar in any large ring laser we operate because of the use of gain tubes of the same diameter (4 mm).

Conversely, for 0.5 mbar and 0.6 mbar of 50:50 neon partial pressure, the maximum laser power at 611.8 nm was measured at a higher total gas pressure, i.e. between 3 mbar and 4 mbar as depicted in Figures 5.19 (e) and (f). With higher neon content, more helium atoms are needed to excite the neon atoms up to the $3s_2$ state. Therefore, the maximum output power for a higher neon partial pressure was observed at a higher helium content.

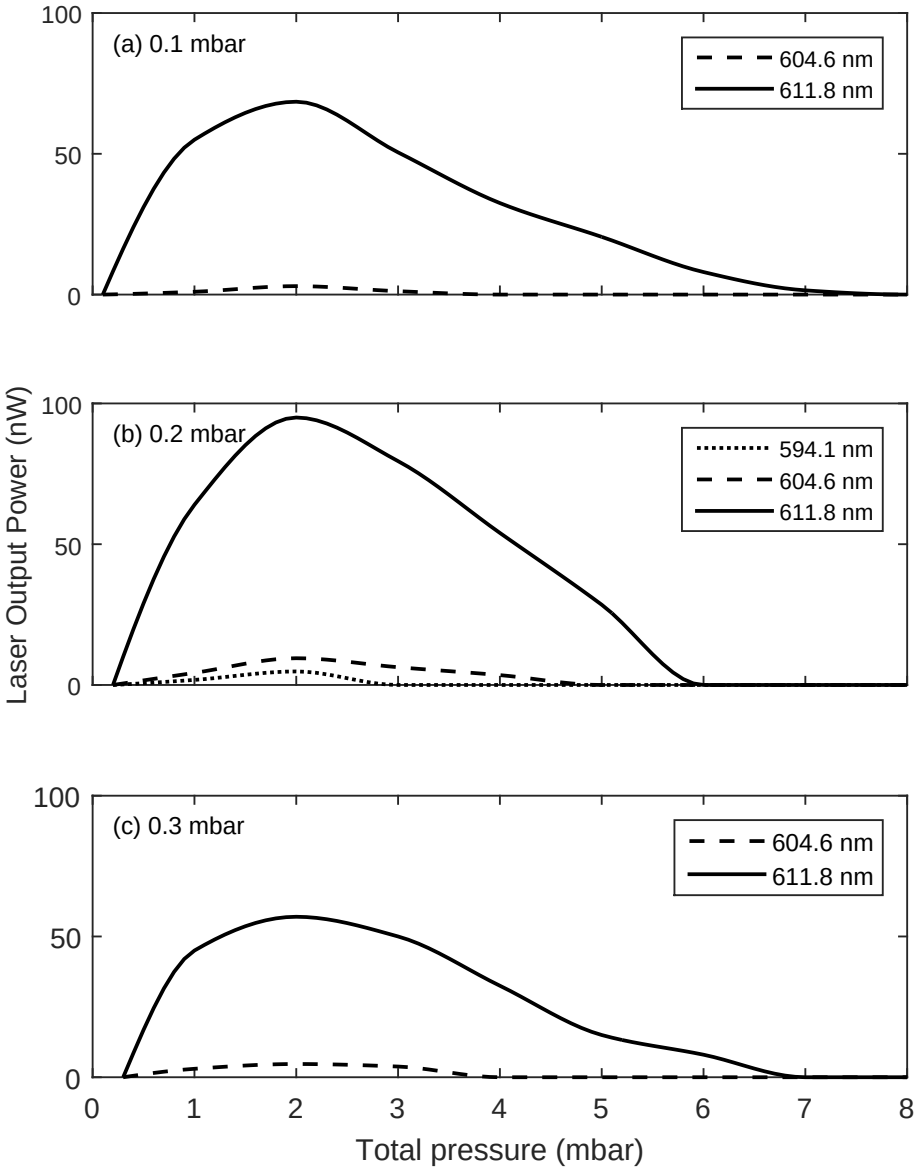

Figure. 5.19.: Laser output power measured at various total gas pressures with the 50:50 neon partial pressure fixed at: (a) 0.1 mbar; (b) 0.2 mbar; and (c) 0.3 mbar. The RF input power was fixed at 30 W.

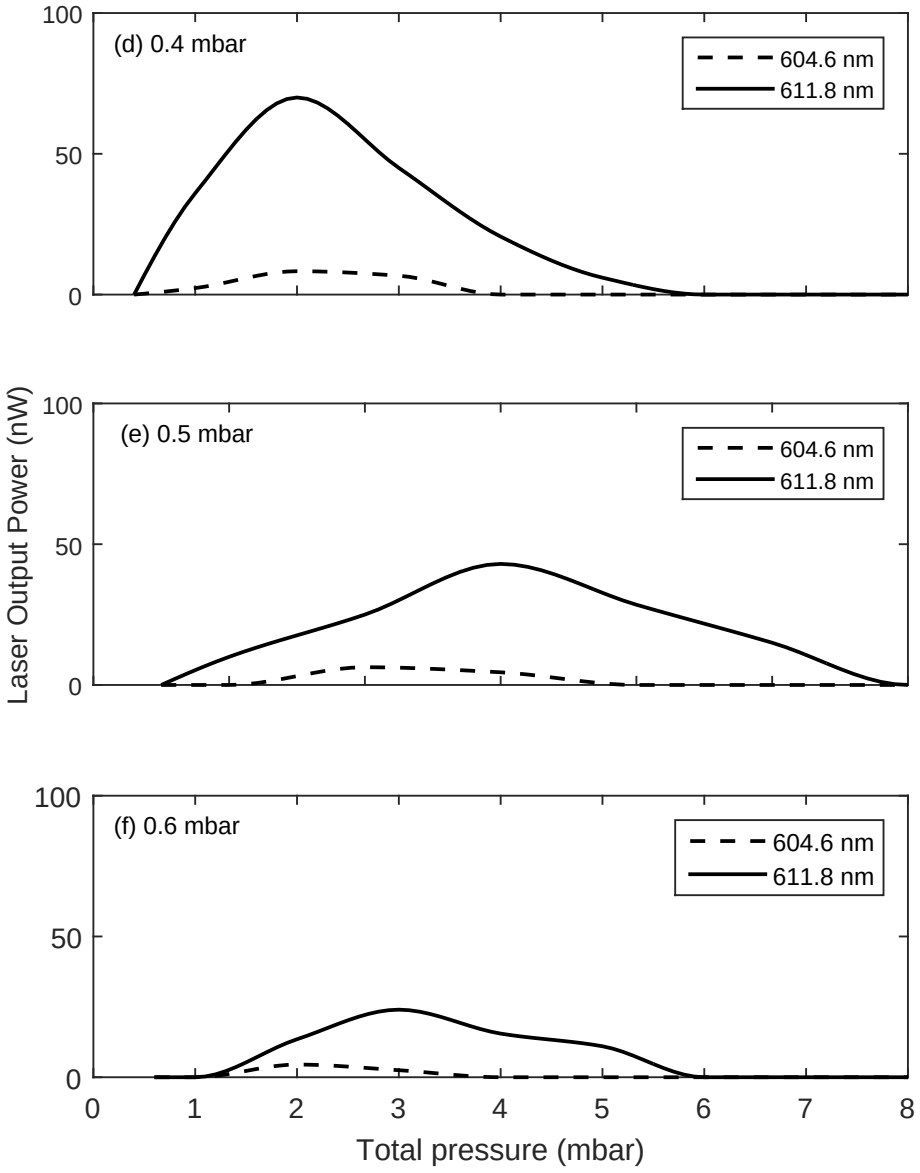

Figure. 5.19. (cont.): Laser output power measured at various total gas pressures with the 50:50 neon partial pressure fixed at: (d) 0.4 mbar; (e) 0.5 mbar; and (f) 0.6 mbar. The RF input power was fixed at 30 W.

5.3.2 Gyroscopic Performance

From Equation 2.25, the expected Sagnac frequency, δf_s (arising from the bias provided by Earth rotation) detected with a 2.56 m^2 ring laser with an operating wavelength at 611.8 nm, is 117 Hz. As we combined the CW and CCW laser beam at the lower right corner box (see Figure 3.5) and employed a PMT to detect the combined signal, a beat signal at 117.2 Hz was detected and an example of the δf_s power spectrum observed on the FFT spectrum analyser is shown in Figure 5.20. The detected δf_s is accompanied by two side-bands (2 to 3 Hz away from the beat signal) which were induced by the natural oscillation of the Rutherford building.

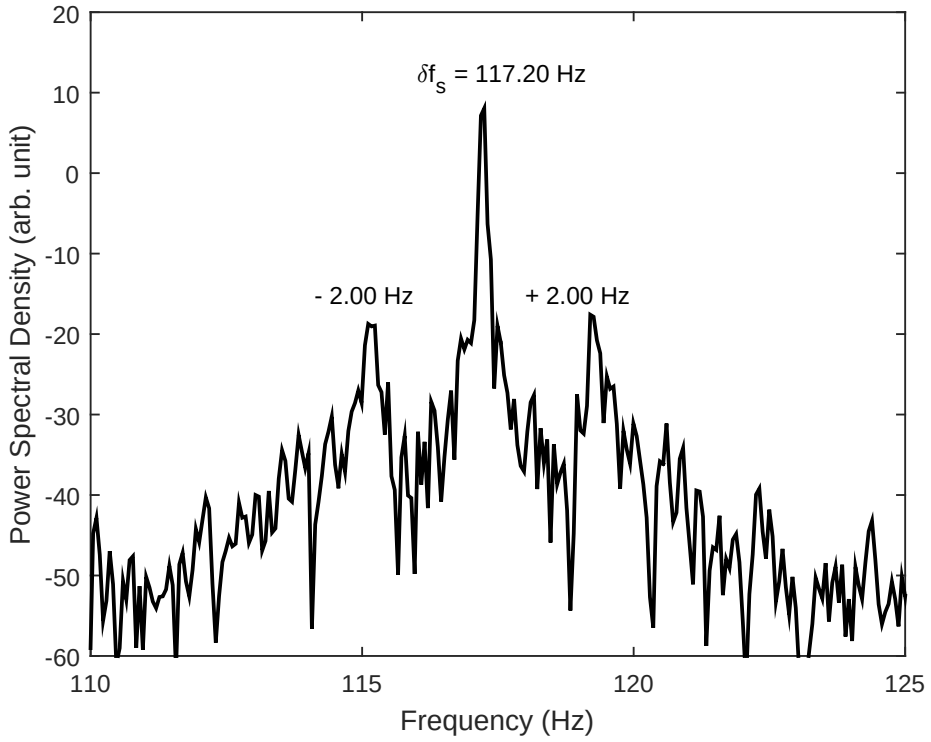

Figure. 5.20.: Power spectrum observed at a cavity gas mix of 0.2 mbar of 50:50 neon and 3.5 mbar of total pressure.

The continuous data acquisition system for PR-1 operation as a gyroscope at 611.8 nm was more or less identical to the system discussed in Section 3.1.2. The laser line filters in front of the PMT and the two high gain PDs (refer to Figure 3.6) were replaced with narrow band-pass filters having a centre wavelength at 610 nm (Thorlabs FB610-10, FWHM = 10 ±2 nm) to minimise plasma light contamination in the detected signal. The peak transmission of these filters is 50%. Since the gain from the 580 mm long gain tube was enough to sustain the laser operation at 611.8 nm, the output signal from the servo unit was connected to the second transmitter driver for the laser intensity feedback system; to maintain the laser output power.

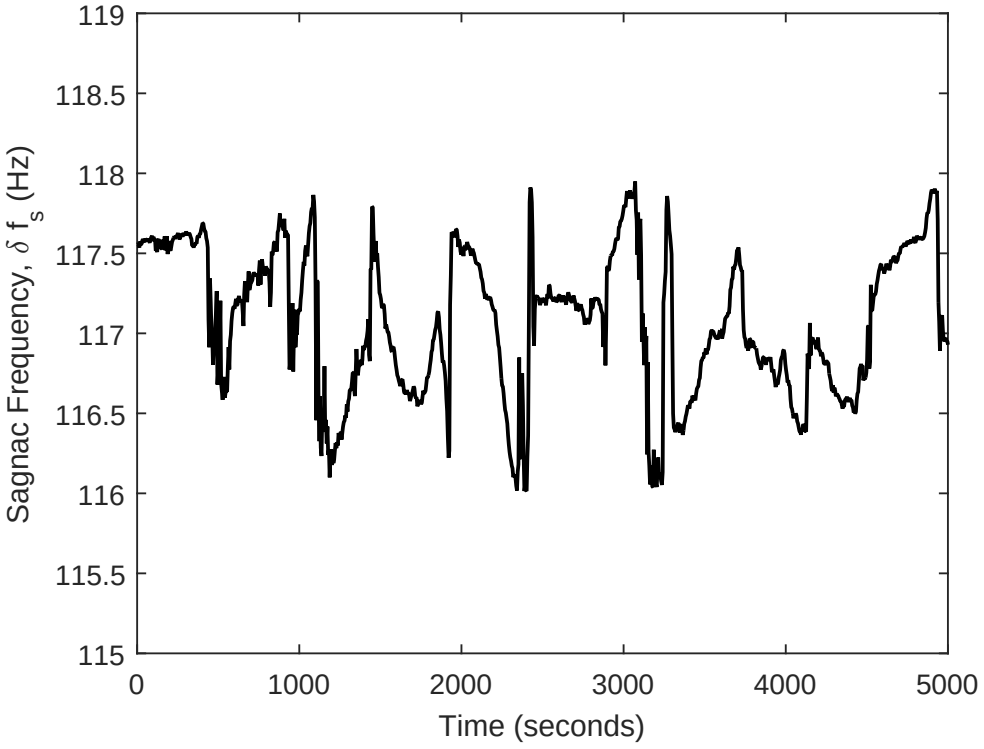

Figure. 5.21.: Raw Sagnac frequency detected with a gas fill of 0.2 mbar 50:50 neon and 3.50 mbar total pressure over 5000 seconds.

A plot of the logged Sagnac frequency from PR-1 over an hour is given in Figure 5.21. As explained previously, the PR-1 cavity is subject to geometric expansion (or compression) due to wall temperature variations. As can be observed from Figure 5.21, the data shows a sudden change in δf_s between 200 to 300 seconds of logging time due to the changes in the longitudinal mode index as a result of changes in the laser perimeter.

Backscatter perturbations will also give rise to a time-varying bias in the detected rotational signal. For instance, we compare the short-term δf_s signal data series (logged over 300 seconds between mode jump and mode split) between PR-1 gas compositions of (a) 3 mbar and (b) 3.5 mbar total pressures with a fixed 0.2 mbar 50:50 neon. The δf_s excursion observed in Figure 5.22 (a) is approximately 0.5 Hz. The monobeam modulations were measured to be between 5 to 16%, which resulted in estimated Sagnac frequency (see Equation 3.5) perturbations of 0.47 Hz, consistent with the data excursion observed in Figure 5.22 (a). The laser was operating at 500 nW to maintain single mode operation. By contrast, for gyroscopic operation with a total pressure of 3.5 mbar, the laser power was maintained at 1000 nW. For this operation, the modulations on the monobeams were between 4 to 5%. As a result, the estimated Δf_{bs} is 0.12 Hz.

The relative Allan deviation (ADEV) plots in Figure 5.23 evaluate the stability of the data presented in Figure 5.22 (a) and (b). The laser stability with gas pressure at 3.5 mbar is

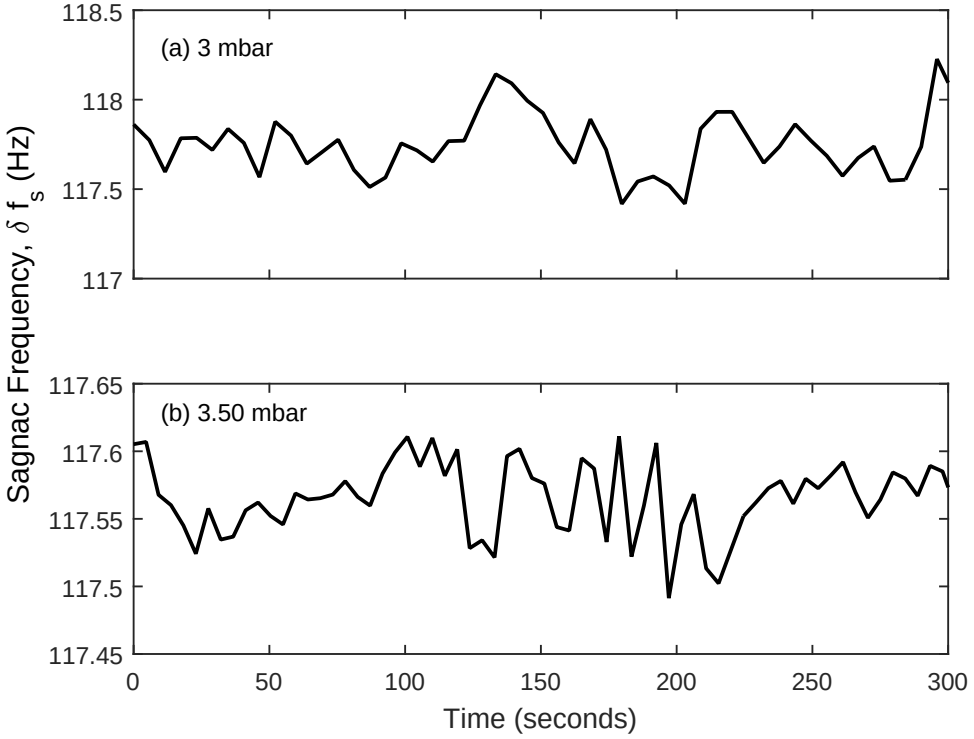

Figure. 5.22.: The short-term Sagnac frequency detected over 300 s with gas fills with 0.2 mbar of 50:50 neon partial pressure and at total pressures of: (a) 3 mbar and (b) 3.5 mbar.

higher due to its higher operating power in contrast to operation at 3 mbar. The lowest variance was measured to be at 1.6×10^{-4} relative to the rotation of the Earth, Ω_E at an averaging time, τ of 10 s at 3.5 mbar. The laser was operating at 1000 nW and the corresponding gyroscopic resolution is 2.7×10^{-10} rad/s/$\sqrt{\text{Hz}}$.

Table 5.5 summarises the relevant gyroscopic parameters of the PR-1 ring laser gyroscope operating on the 611.8 nm neon transition with a total gas fill of 3.5 mbar (50:50 neon partial pressure = 0.2 mbar). From the table, we note that the lowest variance (for an optimum operation) was achieved at 1.6×10^{-4} relative to the rotation of the Earth, which means that the gyroscopic performance at 611.8 nm is still inferior to the best gyroscopic performance at 632.8 nm; where the lowest variance was achieved at $9 \times 10^{-5} \Omega_E$. This is because the cavity mirror was not optimised for the laser transition at 611.8 nm.

Even so, the best sensor resolution achieved at 632.8 nm was 2.4×10^{-10} rad/s$\sqrt{\text{Hz}}$, which is almost equal to the Ω_s achieved with 611.8 nm system which suggests that the ring laser operates well. As the mirror transmission loss is high at this wavelength, the cavity Q was low, which contributed to the higher Ω_s value. However, this set back was compensated by the higher laser operating power (between 800 to 1000 nW for a

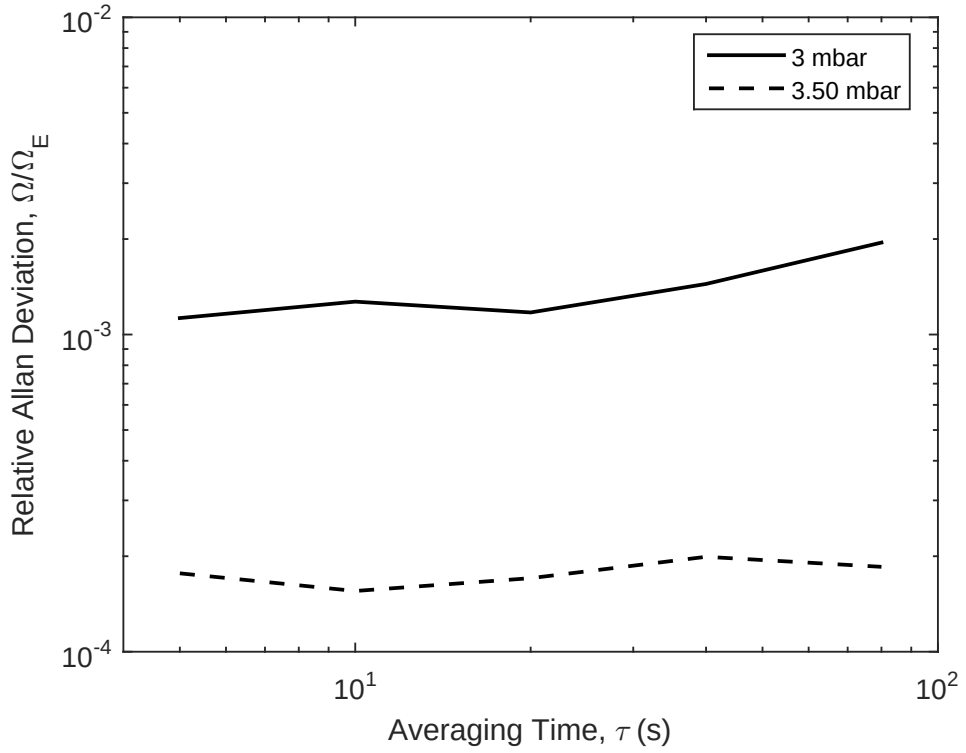

Figure. 5.23.: The plots of ADEV plot with respect to the rotation of the Earth, Ω_E corresponding to the short-term data in Figure 5.22 (a) and (b).

single-mode operation) in comparison to the same system when the laser was running on 632.8 nm laser wavelength.

It is also notable that the optimum operating pressure at 611.8 nm is lower than that of 632.8 nm (Chapter 3) and 1152.3 nm (Chapter 4). By referring to Figure 5.19 (b), lasing at 611.8 nm was only observed between 1 to 5 mbar (with the optimum neon partial pressure of 0.2 mbar) whereas lasing at 632.8 nm and 1152.3 nm were achievable up to 12 mbar of total gas pressure. In this regard, we aim to achieve a higher operating pressure for ring laser operation on the 611.8 nm helium-neon transition by providing more gain to the laser cavity; which we discuss in the next section.

5.3.3 Reconfiguration of the 2.56 m^2 Test Cavity: Part 2

From Table 1.2, we note that the gain generated at 593.9 nm neon transition is about the same as the gain at 543.4 nm. Although the mirror transmission loss at this wavelength is relatively low (6 ppm, see Table 5.2), the total gain provided by both 100 mm and 580 mm long gain tubes were barely sufficient for the laser transition at 593.9 nm to run. Apart from that, laser operation at 611.8 nm could not be achieved with gas pressures above 6 mbar. This suggests that it is necessary to improve the current PR-1 gain section

Parameter	Value
Ring-down, τ_{decay} (μs)	40
Total loss, L (ppm)	533
Quality factor, Q	1.2×10^{11}
Finesse, F	1.2×10^{4}
Laser power, P_i (nW)	1000
Resolution, Ω_s (rad/s/$\sqrt{\text{Hz}}$)	2.7×10^{-10}
Relative ADEV, Ω/Ω_E	1.6×10^{-4}
Monobeam modulations, $m_{1,2}$ (%)	4 to 5
Lock-in threshold, f_L (μHz)	0.94

Table. 5.5.: The best PR-1 gyroscopic parameters at 611.8 nm with 0.2 mbar of 50:50 neon and 3.5 mbar of total pressure.

to accommodate lasing at 543.4 nm. For this reason, we replaced the 580-mm-long tube with a 3-mm-diameter, 400-mm-long discharge tube because laser gain is inversely proportional to the gain tube diameter. This is attributed to the higher collision frequency between the $1s$ level to the wall of the gain tube [112].

The gain tube replacement was performed following the same procedures in Section 5.2.3. The supermirrors installed in the PR-1 cavity were the same IBS-supermirrors used in the previous section because the high mirror transmission (and high gain) at 611.8 nm wavelength was helpful to align the new and narrower gain tube. Before changing the gain tube, the two 543.4 nm He-Ne linear lasers employed in the previous experimental setup (see Section 5.2.3) were substituted by two 632.8 nm He-Ne linear lasers to imitate the counter-propagating laser beams inside the ring cavity.

After that, the pressure inside the laser cavity was brought up to atmospheric pressure by bleeding helium gas slowly into the cavity. Then, the 580-mm-long capillary tube was removed carefully from the PR-1 cavity. We mounted the new capillary tube using the red laser beam as a guide[7]. The length of this narrower gain section is 180 mm shorter than the previous long gain tube. Therefore, the total number of electrode pair was reduced to 6 pairs with an equal distance of 15 mm between each electrode. The width of each copper electrode is 8 mm. This new gain section was connected to the impedance matching unit which was described in Section 5.2.1 (see Figure 5.10). Figure 5.3.3 shows the photo of the 3-mm-diameter gain tube installed on the right arm of the PR-1 ring cavity.

As soon as the 3-mm-diameter gain tube was mounted securely, helium gas in the laser cavity was evacuated for several hours to achieve vacuum before re-filling the laser cavity with a new gas fill. Soon after the cavity reached vacuum, we fill the laser cavity with 0.3 mbar of 50:50 neon and 5 mbar of total pressure. A total of 50 W of RF forward power

[7] The position of the gain tube was approximated by making sure the red laser beams to pass through the centre of the gain tube.

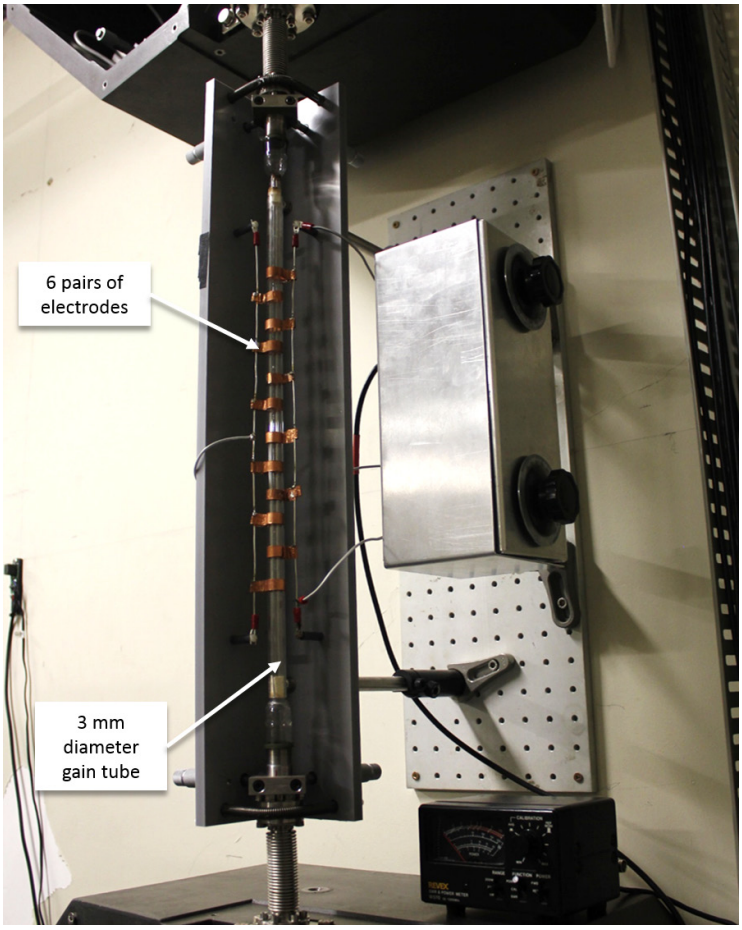

Figure. 5.24.: Photo of the 3-mm-diameter gain tube mounted on the right arm of the PR-1 laser cavity.

(20 W to the 100-mm-long gain tube and 30 W to the longer gain tube) was applied to excite the gas. Fortunately, the matching unit was able to match the impedance between the new gain tube with the 50 Ω impedance from the transmitter. As anticipated, a 'red-orange' laser beam was observed. The CCW laser beam on the lower left corner box was directed into a fibre optic cable to be fed into a spectrometer (Ocean Optics USB2000+ VIS-NIR), and laser transitions at 611.8 nm, 604.6 nm and 593.9 nm were observed. Afterwards, a power meter (Coherent, OP-2-VIS) was installed on the top left corner box of the PR-1 cavity to measure the CCW beam laser power. The new gain tube alignment was optimised by following the same procedure described in Section 5.2.3.

After obtaining the optimum alignment, the PR-1 laser cavity Q was measured. A ring-down time of 33.5 μs was achieved and this corresponds to a Q-factor of 1×10^{11}. The loss per mirror is 160 ppm (by assuming $\nu_0 = 490$ THz). The slightly low ring-down time is most likely due to higher scattering losses on the surface of these mirrors. The mirrors have been subject to particle and dust contamination after numerous gas exchanges conducted in the experimental work in the previous section.

Subsequently, the maximum output power achievable with PR-1's new gain section was investigated. For this measurement, the RF input power was fixed at 50 W and the laser output power was measured at different helium and 50:50 neon gas compositions. Note that the total laser power measured by the power meter during this measurement was the total power of the 3 laser transitions because they were not separated as in Figure 5.18. An iris was mounted in front of the power sensor to avoid extra plasma light contaminating the power measurement.

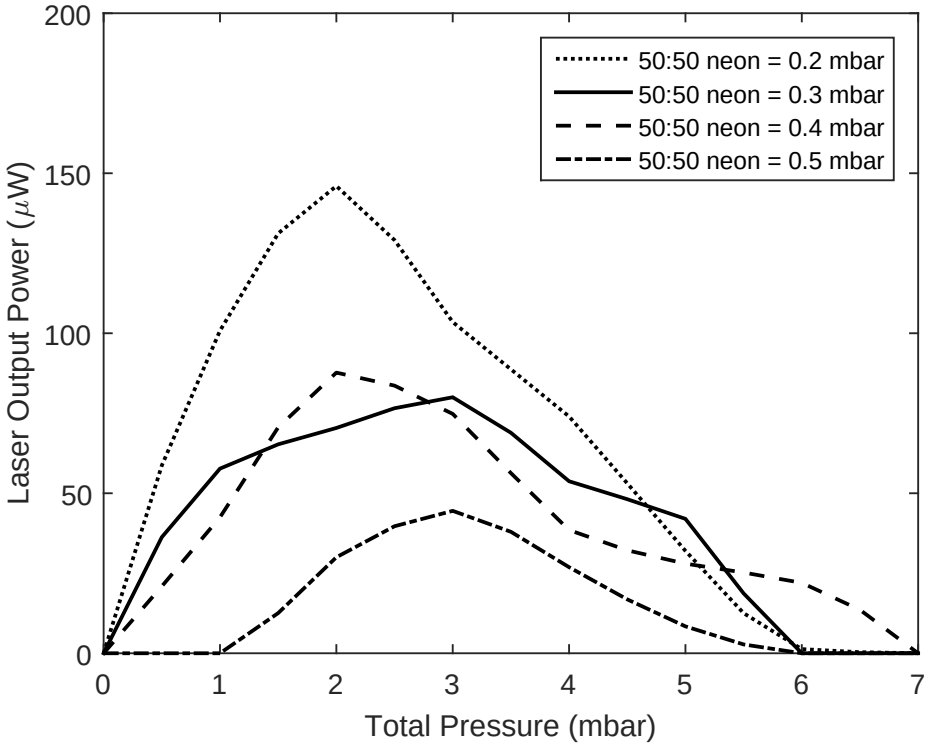

Figure. 5.25.: The laser output power measured at a constant RF input power of 50 W for various gas mixing ratios. The measured laser power is the total output power of laser transitions at 611.8 nm, 604.6 nm and 593.9 nm.

By referring to Figure 5.25, the highest output power was achieved at a gas composition of 0.2 mbar of 50:50 neon and 2 mbar at 146 μW. This is 40 times larger compared to the maximum total output power measured previously in Section 5.2.4 (refer to Figure 5.18). The laser power began to decrease as the total pressure was increased. Eventually, lasing ceased at 6 mbar. A similar trend was observed in Figure 5.19 (b) where for a gas fill with a constant 0.2 mbar of 50:50 neon partial pressure, lasing terminated at 6 mbar of total gas pressure.

For gas fills with 0.3 mbar of 50:50 neon partial pressure, the highest laser power was achieved at 80 μW at a total gas pressure of 3 mbar. The laser was terminated at 6 mbar as well. With a higher neon content, i.e. at 0.4 mbar, lasing was observed between 1 mbar to 6 mbar of total pressures with the highest laser power was noted at 2 mbar. On the other

hand, for 0.5 mbar of 50:50 neon partial pressure, lasing does not occur below 1 mbar of total gas pressure. The highest laser power was 44.5 μW at a total gas pressure of 3 mbar. There is no lasing observed above 6 mbar.

In a helium-neon laser system, the laser gain per unit length is inversely proportional to the diameter of the gain tube [131]; which is evidenced by the significantly higher laser power reported here. Therefore, we conclude that the gain provided by the 3-mm gain tube should be sufficient for laser operation at 543.4 nm.

5.3.4 Single-Mode and Phase-Locked Regime of Operation

The characteristic of the single-mode and phase-locked regime of operation for ring laser operation at 611.8 nm was explored. The experimental setup was according to the setup shown in Figure 3.17; except for the servo system, which in this experiment, was connected to the second transmitter. The servo system was set to manual mode so that we can control the RF input power (to the new gain tube) by turning the knob on the servo driver. The RF supply to the 100-mm gain tube was switched off for this measurement. As the RF power was increased, the CW laser beam was scanned via the Coherent 33-6305-001 FP interferometer while the mode structure was observed via an oscilloscope. At the same time, the CCW laser beam power was measured by a power meter located at the top right corner box.

Figure 5.26 (a) to (c) are examples of the 611.8 nm laser mode structures observed with the FP spectrogram at a gas mixture of 0.2 mbar 50:50 neon and 6 mbar of total pressure. The laser was running on a single-mode at a laser power of 57.2 nW and the laser spectrum as seen on the FP spectrogram is shown in Figure 5.26 (a). As the laser power was increased; two longitudinal modes (denoted as 'b') began to appear on each side of the main longitudinal mode 'a' as shown in Figure 5.26 (b). The laser mode labelled as 'b' is about 2 free spectral range (FSR) away from the main mode (from Equation 2.42, ν_{fsr} = 46.875 MHz). At 248 nW, the laser mode, denoted as 'c' in Figure 5.26 (c) began to emerge. From the figure, the location of 'c' appears to be at 112 MHz away from the centre mode 'a'. In reality, 'c' was actually located at approximately 4 times FSR apart from mode 'a'. This was confirmed by observing the ν_{fsr} beat at 93.6 MHz and 187 MHz on the RF spectrum analyser.

Figure 5.27 depicts the single-mode and multimode operating regimes for the 611.8 nm operating wavelength for various gas compositions with a constant 0.2 mbar of 50:50 neon partial pressure. The single-mode operating regime is represented by the grey-shaded region labelled as (i). From the figure, the phase-locked threshold is increased as the total pressure is increased from 1 mbar to 3 mbar. The widest regime for single-mode operation is at a total gas pressure of 3 mbar, where the laser maintained single-mode

operation until 800 nW of laser output power. We note that the single-mode operating regime started to decline at 4 mbar.

In Figure 5.27, the laser is running in phase-locked regime in the region labelled as (ii) while the laser is running chaotically (free-running regime) in the region labelled as (iii). As before, the 'unstable' multimode threshold is rising as the total gas pressure is increased. From the figure, the broadest phase-locked regime is observed at a total gas pressure of 4 mbar where it can be maintained between 600 nW to 1800 nW of laser output power. Then again, the phase-locked regime drops dramatically above 5 mbar of total gas pressure.

The decrease in the single-longitudinal mode, as well as 'stable' multimode regimes at higher gas contents for PR-1 operation at 611.8 nm, is inconsistent with our observation with the 632.8 nm and 1152.3 nm systems in Chapter 3 and 4. The latter two operating wavelengths demonstrate the regime of single-mode operation and phase-locked operation rises as the total gas pressure is increased. At this stage, the reason for the phenomena observed in Figure 5.27 remained unclear. Due to time limitations, further investigation on the PR-1 gyroscopic performance on the phase-locked regime while running on the 611.8 nm wavelength was not performed.

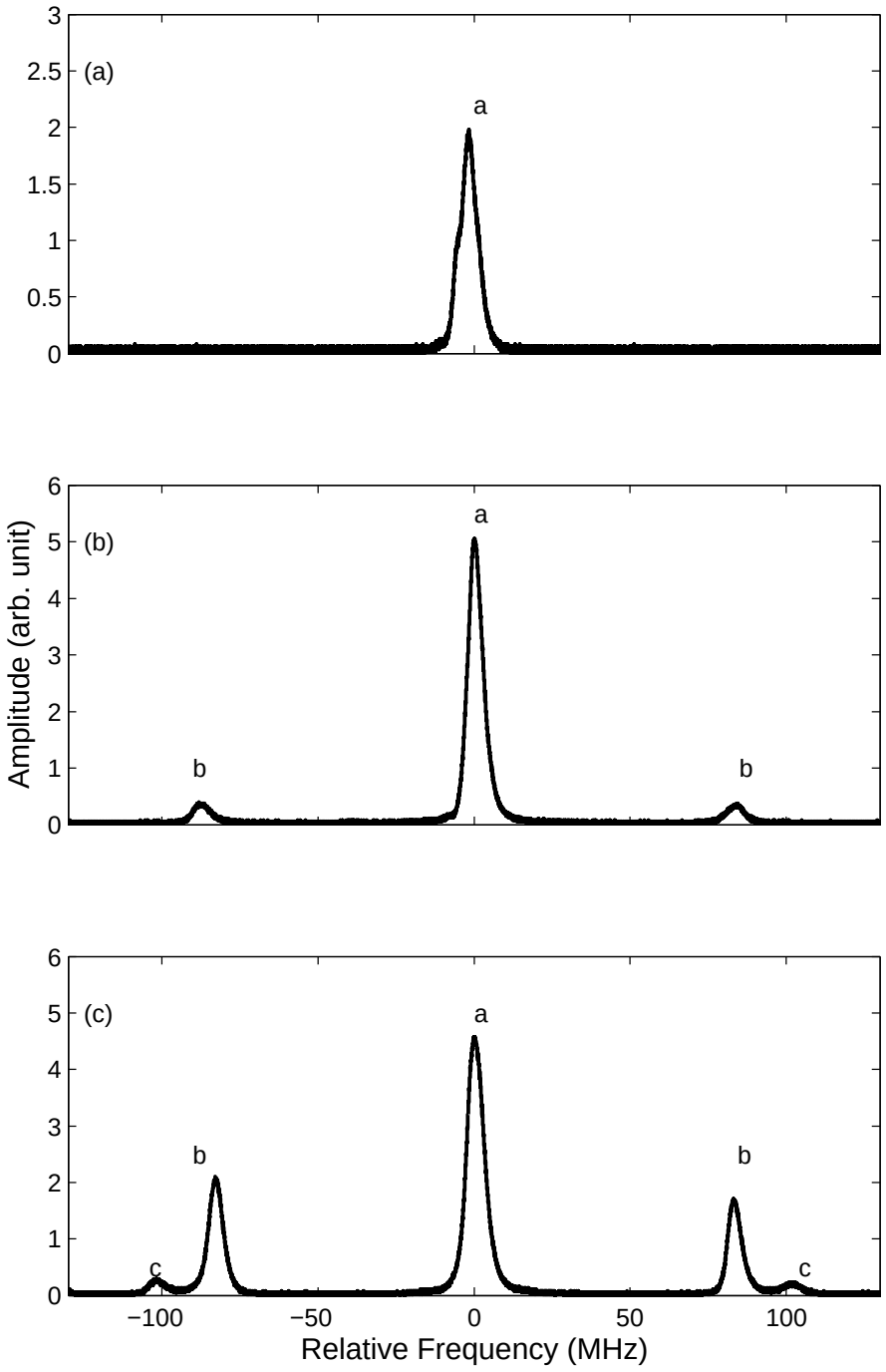

Figure. 5.26.: Laser mode structure observed with FP spectrogram at gas mixtures of 0.2 mbar 50:50 neon and 6 mbar of total pressure where: a is the main longitudinal mode; b is a mode oscillating 2 FSR away from the main mode; c is the longitudinal mode at 4 FSR away from the main mode. (a) single longitudinal at laser power of 57.2 nW; (b) phase-locked regime at laser power = 200 nW; and (c) phase-locked regime at laser power = 248 nW.

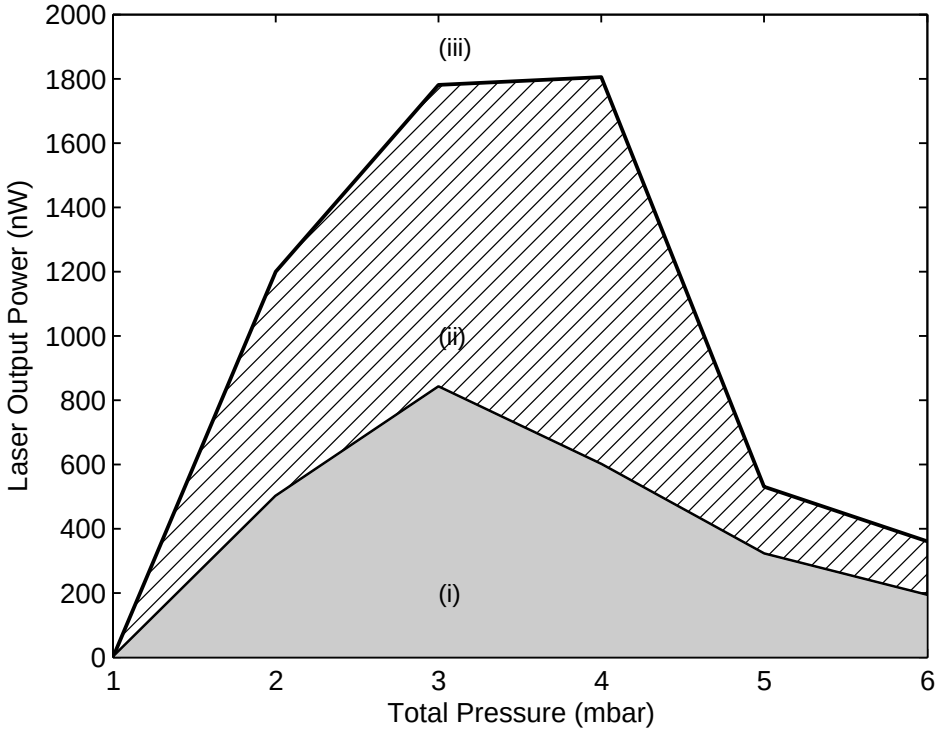

Figure. 5.27.: Phase-locked and multimode threshold as a function of total gas pressure (with a fixed 50:50 neon partial pressure of 0.2 mbar) at 611.8 nm with the 3 mm diameter gain tube. (i) Single-mode regime; (ii) phase-locked regime; (iii) multimode regime (free-running laser).

5.4 Rotation Sensing with a Large He-Ne Ring Cavity Operating at 543.4 nm

In this section, we report preliminary work to operate the ring laser on the 543.4 nm laser wavelength by employing a new set of IBS-supermirrors. These new mirrors were provided by FiveNine Optics (in partnership with REO) and the mirror specifications are listed in Table 5.6. As specified in the table, the mirror transmission loss at 543.4 nm wavelength is extremely low, between 0.05 ppm to 3 ppm, while the mirror transmissions at 593.3 nm, 604.6 nm and 611.8 nm are very high, i.e. more than 10000 ppm.

Wavelength (nm)	Transmission (ppm)	Absorption and Scatter (ppm)	Total Loss (ppm)
543.4	0.05 to 0.3	-	< 12
593.9	> 10000	-	-
604.6	> 10000	-	-
611.8	> 10000	-	-

Table. 5.6.: The specifications of the new 543.4 nm IBS-supermirror transmissions at 45° angle of incidence (AOI) in the s-polarisation direction provided by FiveNine Optics (ROC = 2.5 m).

Before installing these mirrors into the ring cavity, we conducted a measurement to characterise the transmission losses. The experimental setup was mainly the same as the setup illustrated in Figure 5.15; where a broadband source (Thorlab, Quartz-Tungsten-Halogen lamp) was directed at normal and 45° angles of incidence to the centre of the supermirror. Then, the transmitted light was detected by a fibre optic, and the signal was transferred to the spectrometer (Ocean Optics USB2000+ VIS-NIR) to be analysed via a personal laptop.

The transmitted spectrum is presented in Figure 5.28. As depicted in Figure 5.28 (b), for a light source directed at a normal angle of incidence to the centre of the supermirror, the lowest transmission is observed between 500 nm to 610 nm. At 45° angle of incidence, the centre peak reflectivity is at 520 nm as seen in Figure 5.28 (c). The mirror transmission loss is clearly higher at 611.8 nm, 604.6 nm and 593.9 nm, consistent with the specification listed in Table 5.6. We note that in the first report of helium neon lasing at 543.4 nm, the experiment was carried out by using mirrors with peak reflectivity centred at 520 nm as well [46].

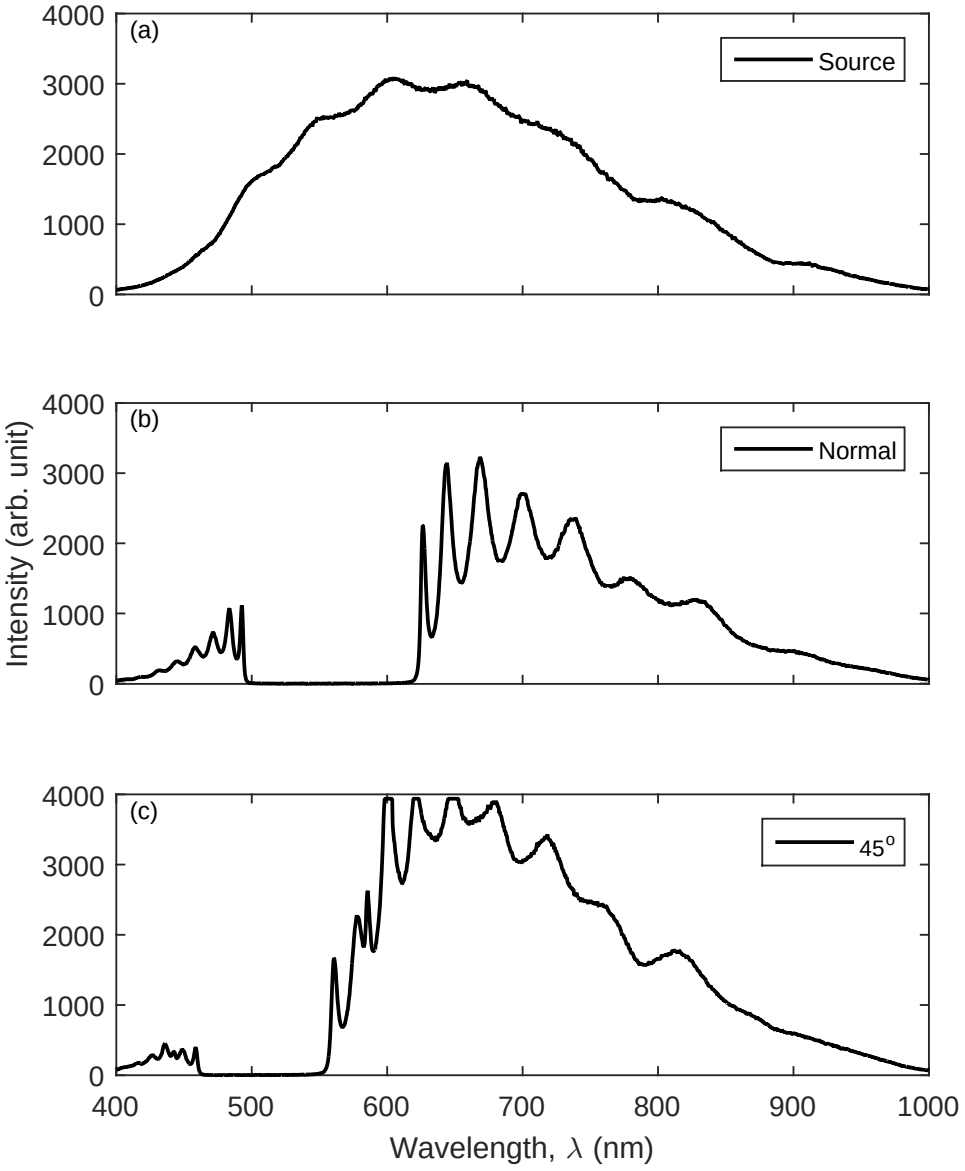

Figure. 5.28.: The spectrum of the (a) broadband light source; (b) supermirror transmission at normal incident and at (c) 45° transmission of the supermirror.

The mirrors employed in the PR-1 cavity for laser operation at 611.8 nm provide low transmission loss at 543.4 nm. For this reason, we only replaced one mirror located in the PR-1 lower right corner box with the new IBS-mirror. After replacing the mirror, the laser cavity was filled with 0.2 mbar of 50:50 neon and 1 mbar of total pressure. By applying a maximum RF power of 50 W to excite the gas, laser transition at 543.4 nm was achieved as shown in the photo in Figure 5.29. The laser beam spot on the mirror was measured to be 2.5 mm. This is about a 10% reduction in beam spot relative to the 'red' beam diameter reported in Chapter 3.

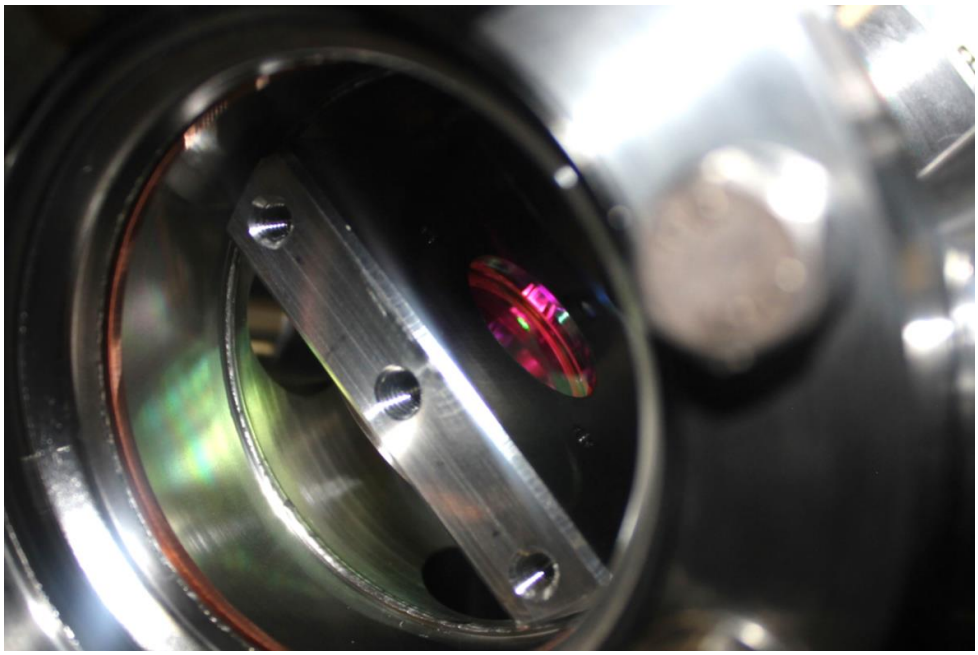

Figure. 5.29.: A photograph of the green laser spot at the centre of the supermirror. The laser beam diameter is 2.5 mm.

Right after lasing at 543.4 nm was achieved, the power meter was mounted at the lower left corner to detect the CW laser beam. The lasing threshold occurs at an RF power of 6.5 W and approximately 7 nW of laser output was detected.

5.4.1 The Cavity Q Factor

A cold cavity ring-down time of 112 μs was measured and Table 5.7 summarises the calculated cavity Q, cavity finesse, F and the total cavity loss. From the table, the total loss measured from the ring-down time is 4 times higher than the total loss stated in Table 5.6. Although we expect that the total optical loss will decrease as a result from the reduction in the beam size, the higher than expected loss is presumably due to the other three supermirrors which have been subject to particle contamination during gas exchange procedures.

Parameter	Value
Ring-down time, τ_{decay} (μs)	112
Total loss, L (ppm)	190.5
Loss per mirror (ppm)	47.63
Quality factor, Q	3.9×10^{11}
Finesse, F	3.3×10^{4}

Table. 5.7.: Measured τ_{decay} and the corresponding cavity Q factor, finesse, F and loss per mirror achieved at 543.4 nm. ν_0= 552 THz.

5.4.2 Gas Pressure Optimisation

To find the optimal gas composition and pressure for gyroscopic operation at 543.4 nm, the output powers for various helium to neon gas fills were measured at a constant RF excitation power of 30 W. The RF supply to the 100-mm-long gain tube was turned off for this measurement because the gain provided by the 3-mm-diameter discharge tube was enough to sustain laser action.

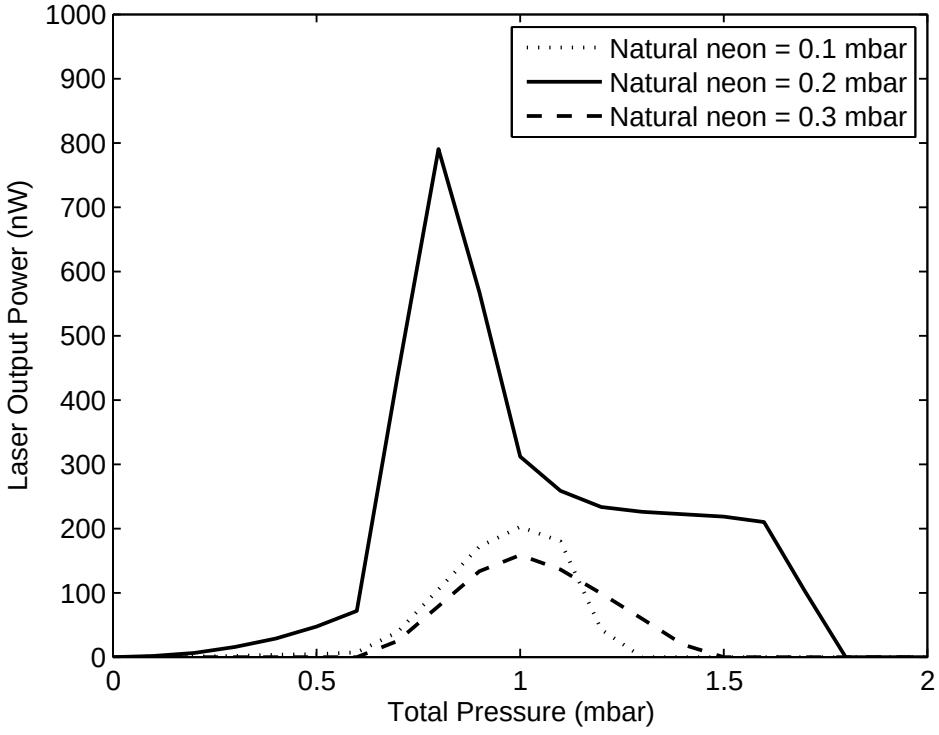

Figure. 5.30.: Laser output power measured when a total RF input power of 30 W was applied to the 3-mm-diameter gain tube at various helium neon gas mixtures.

For laser operation at 543.4 nm, gas compositions with 0.2 mbar of natural neon partial pressure achieved higher output power than gas fills with 0.1 mbar and 0.3 mbar neon partial pressures as shown in Figure 5.30. At neon partial pressure of 0.2 mbar, the highest power was observed at 800 nW with a total gas pressure of 0.8 mbar. The laser output

declines as the total gas pressure rises and eventually lasing is quenched at pressures above 1.6 mbar.

The highest gain was also achieved at 0.2 mbar of neon partial pressure with the 4-mm-diameter gain tube (length = 100 mm) when the ring laser was operating at 632.8 nm [33] and 1152.3 nm (Section 4.2.2). Similarly, at 611.8 nm, the optimum neon partial pressure was determined at 0.2 mbar with both 4 mm (length = 580 mm) and 3 mm (length = 400 mm) diameter discharge tubes (refer to Section 5.3).

In comparison to 632.8 nm and 611.8 nm operation with the same cavity, it appears that at 543.4 nm, the optimum gas composition occurs at a lower total pressure (0.8 mbar) while the two longer wavelengths achieved maximum power at a total gas pressure of 2 mbar. This is because the gain at 543.4 nm is low relative to the available gain at 632.8 nm and 611.8 nm. Furthermore, according to ref. [45], the lower optimum pressure for 543.4 nm (despite sharing the same upper level with the 632.8 nm transition) is because of the higher excitation cross section at $2p_{10}$ state. The neon excitation process from the ground-level and $1s$ level to the $2p_{10}$ level via electron impact occurs more rapidly in comparison to the neon excitation process from the ground and $1s$ levels to the $2p_4$ and $2p_6$ states. As a result, the $2p_{10}$ level is populated at a faster rate.

Laser Efficiency

In order to investigate the correlation between the RF input to the laser output power, the CW beam power was recorded as the RF excitation power to the 400-mm-long gain tube was increased from 0 to 30 W.

Figure 5.31 (a) to (c) are the recorded laser output powers for different helium and neon gas compositions at RF input power of 0 to 30 W. From the measurement, it is notable that laser operation with gas compositions consisting of neon partial pressures at 0.1 mbar and 0.3 mbar are inefficient in comparison to gas fills with 0.2 mbar of neon. As can be observed from Figure 5.31 (a), the highest efficiency[8] is at 1.1 mbar of total pressure. The laser power output rises after the lasing threshold (at 8 W of RF power) and reaches the highest output power of 200 nW at an RF input power of 20 W. The power began to saturate beyond 20 W and eventually, the power drops to 180 nW at RF power of 30 W. Meanwhile, for a higher neon content (i.e. natural neon = 0.3 mbar), the highest laser efficiency was observed at 1.5 mbar of total pressure, where the lasing threshold occurs at an RF input power of 5 W. However, as shown in Figure 5.31 (c), the efficiency is negative beyond an RF input power of 10 W. The highest laser power was noted at 219 nW with 1 mbar of total gas pressure at an RF power input of 20 W. In contrast, with 0.2 mbar

[8] See note. [5] in Chapter 4.

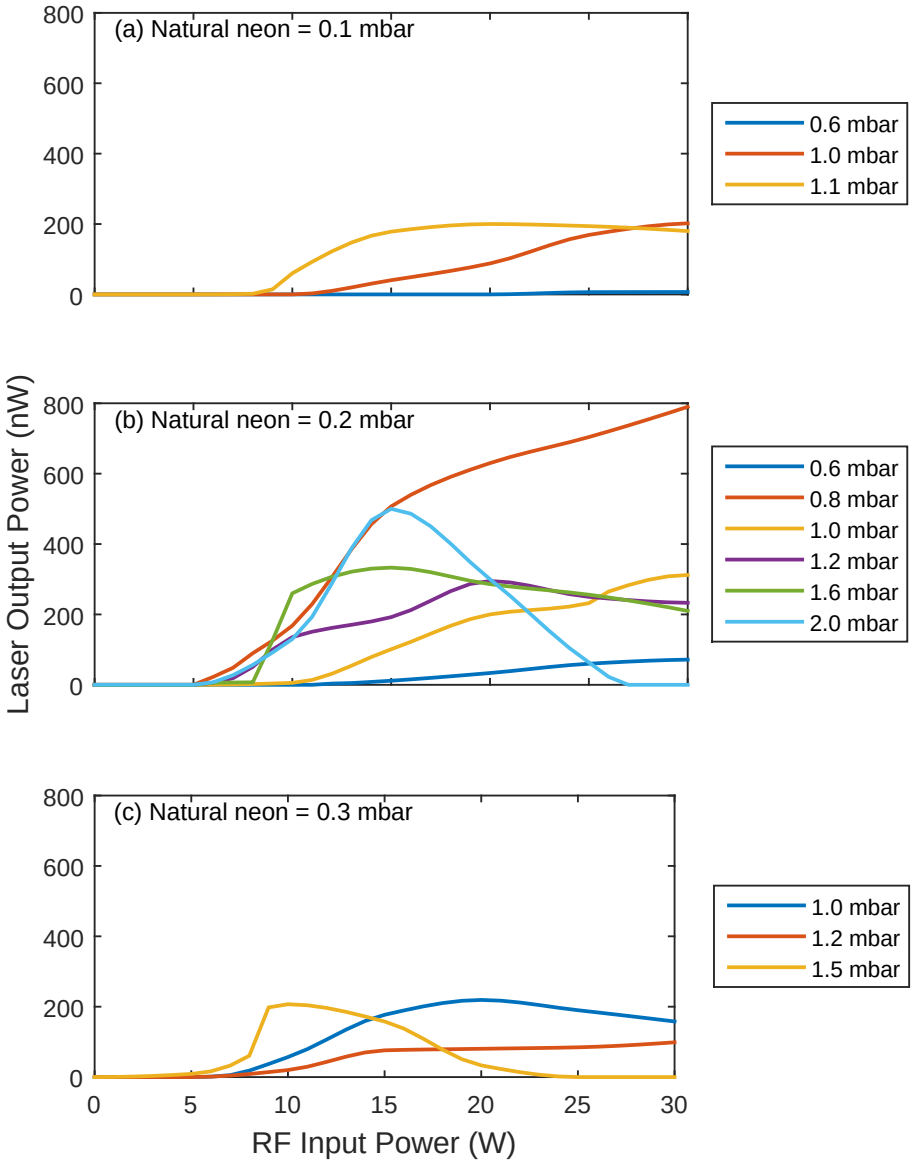

Figure. 5.31.: Laser output power as a function of the RF input power at various total gas pressures with a natural neon partial pressure of (a) 0.1 mbar; (b) 0.2 mbar; and (c) 0.3 mbar. The RF power which was applied to the 400 mm-long gain tube was increased from 0 to 30 W of total power.

of neon partial pressure, the highest efficiency was noted at 0.8 mbar of total pressure; where, with an RF input power of 15 W, the laser generated an output power of 500 nW.

Figure 5.31 (b) shows that for a constant neon partial pressure of 0.2 mbar, lasing at 543.4 nm can be observed between 0.6 mbar to 2 mbar of total gas pressures. For total gas pressures above 0.6 mbar, the lasing threshold occurs at an RF input power between 5.5 to 7 W. The best input-output efficiency is observed with a total gas pressure of 0.8 mbar between 5 W and 15 W of RF input power. Although the input-output efficiency decreases between 15 W to 30 W, the laser reached maximum output power at 30 W of RF power. For a higher total gas pressure (2 mbar), we observed high input-output efficiency between the lasing threshold (5 W) to 15 W of RF input power as well. However, the output power decreases dramatically beyond 10 W of RF input power, and lasing stops above 25 W of RF input power.

As the laser efficiency is determined by the correlation between the rate of populating the upper laser state and de-populating the lower state. With a higher helium concentration in the cavity, more helium atoms are available to be excited to higher energy level and transfer their energy to neon atoms. As a consequence, the $3s_2$ level is populated and the laser output power increases. However, as higher excitation energy is applied, the electron concentration in the plasma increases. De-excited neon atoms that decayed from the $2p$ state to the $1s$ state will collide with these electrons. These atoms are excited back to the $2p$ level instead of colliding with the gain-tube wall and return to the ground state. The population in the $2p$ level begins to increase, which in turn, depletes the population inversion between $3s_2$ and $2p_{10}$. Hence, the laser power decreases.

5.4.3 Single-Mode and Phase-Locked Regime of Operation

The goal of this experiment is to determine the single-mode and phase-locked operating regime for PR-1 ring laser gyroscope while operating at a wavelength of 543.4 nm. The experimental setup was similar to the configuration illustrated in Figure 3.17, where the CCW laser beam transmitted from the lower left corner was directed into the FP interferometer (Coherent, 33-6305-001) to monitor the laser mode structure. As the RF input power was raised slowly, the laser mode structure was scanned by the FP and the laser mode spectrum was observed on the spectrum analyser. Note that the mirror set for the FP interferometer is optimised for the wavelength range between 550 - 650 nm. Therefore, as the laser mode was scanned by the FP, the ν_{FSR} beat on RF spectrum analyser was monitored at the same time. Simultaneously, the combined beam power spectrum was observed via the FFT spectrum analyser.

For the PR-1 ring laser operating at 543.4 nm, the Sagnac frequency induced by the rotation of the Earth is 132.8 Hz as shown in Figure 5.32. This is within 1 Hz of the

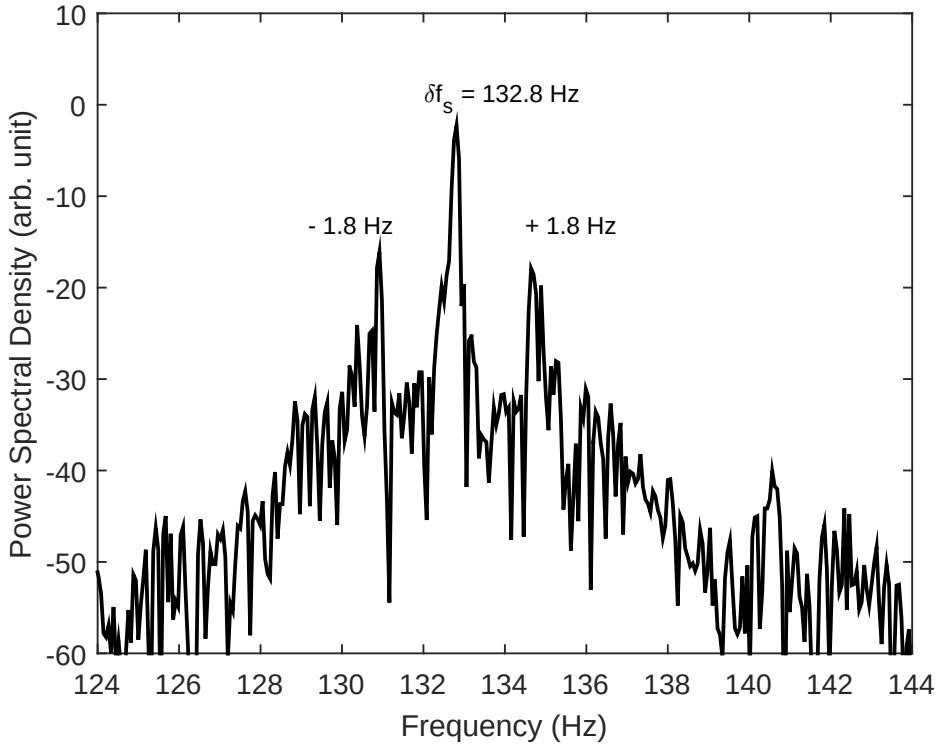

Figure. 5.32.: The power spectrum detected shows the Earth rotation bias at 132.8 Hz with 1.8 Hz side-bands generated by the building motion.

expected value from Equation 2.25 (from Equation 2.25, δf_s = 131.7 Hz). Cavity perimeter changes (due to wall contraction or expansion) cause the variation in the detected Sagnac frequency while the rocking of the Rutherford building generates the two side-bands.

Figure 5.33 depicts the laser mode structure scanned by the FP at 0.2 mbar of natural neon and 0.8 mbar of total pressure. At the lasing threshold (3.5 nW), two laser modes approximately equal in intensity were observed as shown in Figure 5.33 (a). In the figure, the two modes appear to be about 40 MHz apart from each other. However, there was no ν_{fsr} beat observed on the RF spectrum analyser to verify whether these mode were 1 FSR apart from each other. When the laser power was raised beyond the lasing threshold, one laser mode began to dominate. The single longitudinal mode spectrum is shown in Figure 5.33 (b).

At a higher laser power, laser operation at 543.4 nm began to demonstrate phase-locked operation with a second longitudinal mode approximately, 2 FSR away from the centre mode as observed in Figure 5.33 (c). At the same time, a stable δf_s power spectrum was displayed on the FFT spectrum analyser. The location of the second longitudinal mode was confirmed by the ν_{fsr} beat at 93.6 MHz, as observed on the RF spectrum analyser.

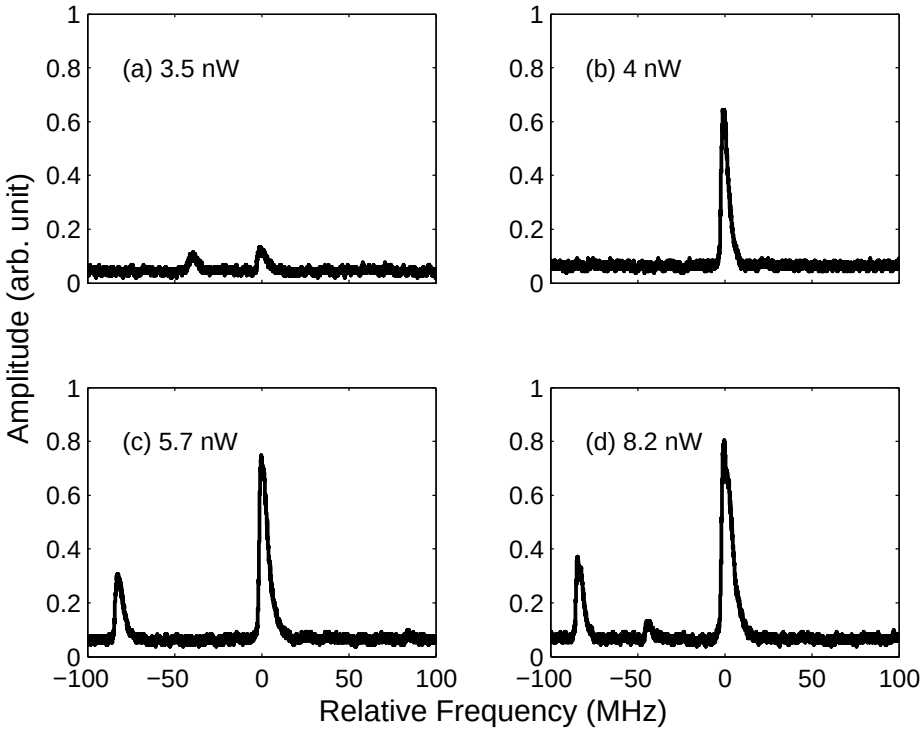

Figure. 5.33.: Fabry Perot spectrogram of the laser mode structure with a gas composition of 0.2 mbar of natural neon and 0.8 mbar of total gas pressure at the laser output powers of (a) 3.5 nW; (b) 4 nW; (c) 5.7 nW and (d) 8.2 nW.

As the laser power was raised further, a third mode began to emerge, as observed in Figure 5.33 (d). In this instance, the δf_s spectrum was still stable. However, only ν_{fsr} = 93.6 MHz was seen on the RF spectrum analyser. Therefore, the third mode (which appeared between the main mode and the mode at one FSR away from the main mode) was not able to be identified.

Figure 5.34 shows the single-mode and phase-locked operating regimes for gas compositions with a natural neon partial pressure of 0.2 mbar at total pressures between 0.6 mbar to 1.6 mbar. The grey-shaded region labelled as (i) indicates that the laser is running on a single-mode. The area labelled as (ii) indicates the laser is operating in the phase-locked regime while the region marked as (iii) is where the laser is free running.

There is no phase-locked operating regime for a total gas pressure of 0.6 mbar. As expected, the multimode threshold increases as the total pressure is increased. The widest regime for single-mode operation is at a total pressure of 1.2 mbar where the phase-locked threshold is noted at 14 nW of laser output power. Meanwhile, the widest regime for the laser to operate in a stable multimode regime is at 1.6 mbar of total gas pressure.

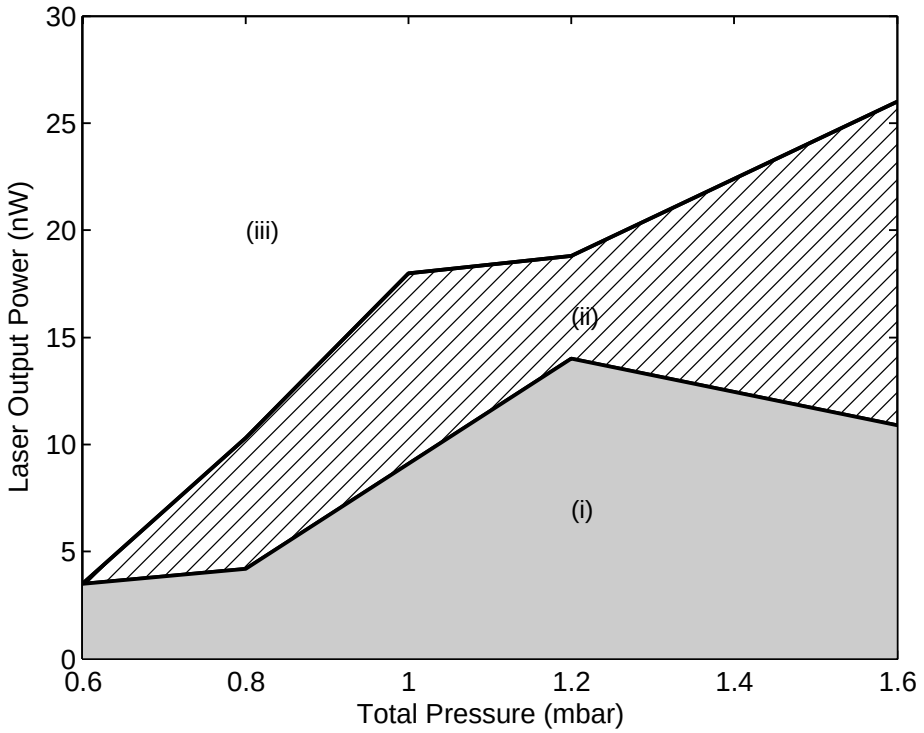

Figure. 5.34.: The laser output power as a function of total gas pressure (for 0.2 mbar of natural neon partial pressure) to show the regions where the laser is operating on: (i) a single longitudinal mode; (ii) 'stable' multiple longitudinal modes; and (iii) 'unstable' multiple longitudinal modes.

Unlike operation with the 632.8 nm transition, the single-mode and phase-locked operating regime are narrow for operation at 543.4 nm because lasing is not observed for total pressures above 2 mbar. Typically, we operate ring lasers with higher gas pressure to maintain the suppression of adjacent longitudinal modes, which allows single mode operation for larger laser cavities to run at a higher laser power [4]. Nonetheless, despite the narrow single-mode and phase-locked regime demonstrated by the laser operation at 543.4 nm, the laser operates well as a rotation sensor (comparable to the low pressure operation at 611.8, 632.8 nm and 1152.3 nm) and this will be discussed further in the following section.

5.4.4 Gyroscopic Performance

In this section, an experiment was performed to characterise the gyroscopic behaviour while running on the $3s_2 \rightarrow 2p_{10}$ neon transition, and to compare the gyroscopic performance between the single-mode and stable multimode regime of operations.

Although lasing at 543.4 nm can be sustained solely by excitation on the longer (and narrower) discharge tube, in this experiment, the PR-1 ring laser utilised both gain tubes

to run as a rotation sensor. The reason is that the servo system did not perform optimally when the servo unit was connected to the driver of the second transmitter (the RF transmitter for the longer discharge tube). Therefore, the laser power was maintained by implementing the laser power feedback control which comprises the first RF transmitter driver as shown in Figure 3.7. The plasma discharge on the 400-mm-long gain tube was very unstable as well. To counteract this, we employed 6 permanent magnets along the gain tube to stabilise the plasma discharge (refer to Section 5.5 for further discussion on this approach).

Both photo-detectors which detect the CW and CCW beams as illustrated in Figure 3.6 were replaced by two R3896 Hamamatsu photomultiplier tubes (PMT). The reason we replaced the photo-detectors with the PMTs was that for this laser transition, the output power (to obtain a stable Sagnac signal) was low, typically below 30 nW, as illustrated in Figure 5.34. Moreover, we placed a 543.4 nm line filter (Thorlab, FL543.5-10) in front of each PMT to avoid measurement contamination by other light sources such as the room light and the plasma light; which reduces the detected laser intensity by 30%. Meanwhile, the detection of the combined beam remained at the lower right corner (Figure 3.5). The detected δf_s and monobeam signals were logged via the data logging system described in Section 3.1.2.

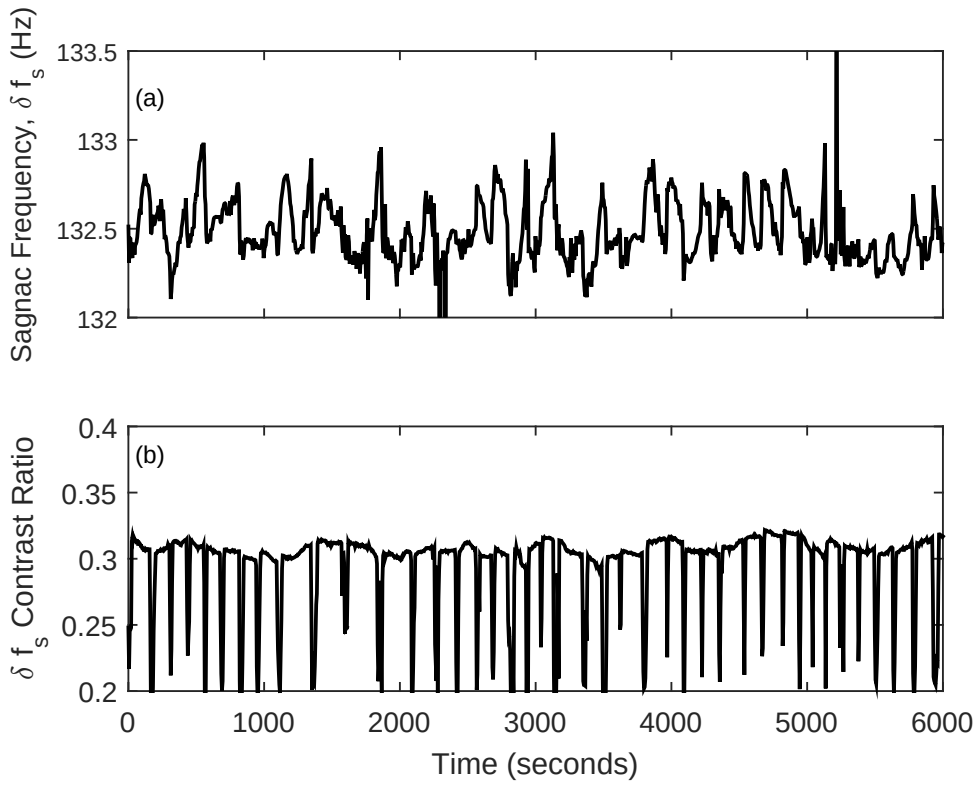

Figure. 5.35.: (a) The detected Sagnac beat frequency over 6000 s (raw signal) and (b) is the corresponding Sagnac contrast ratio. The plasma discharge was stabilised by employing six magnets along the 400 mm gain tube (Gas fill: 0.2 mbar natural neon, total pressure = 1.2 mbar).

For a gas fill with 0.2 mbar of natural neon and 1.2 mbar of total gas pressure, the laser power was maintained at 6 nW for single-longitudinal mode operation. The observed Sagnac frequency raw signal for a period of over an hour is shown in Figure 5.35 (a). The corresponding Sagnac signal contrast ratio (the ratio between the AC voltage to the DC voltage from the PMT) is shown in Figure 5.35 (b). As can be seen from the figure, the detected δf_s signal suffers from mode hopping and and mode-splitting (indicated by the sudden jump and sudden drop in the Sagnac signal contrast ratio) due to the laser geometrical instability. The δf_s contrast ratio was 31%; which is comparable to the detected δf_s contrast ratio when the laser cavity was running at 632.8 nm, as tabulated in Table 3.4.

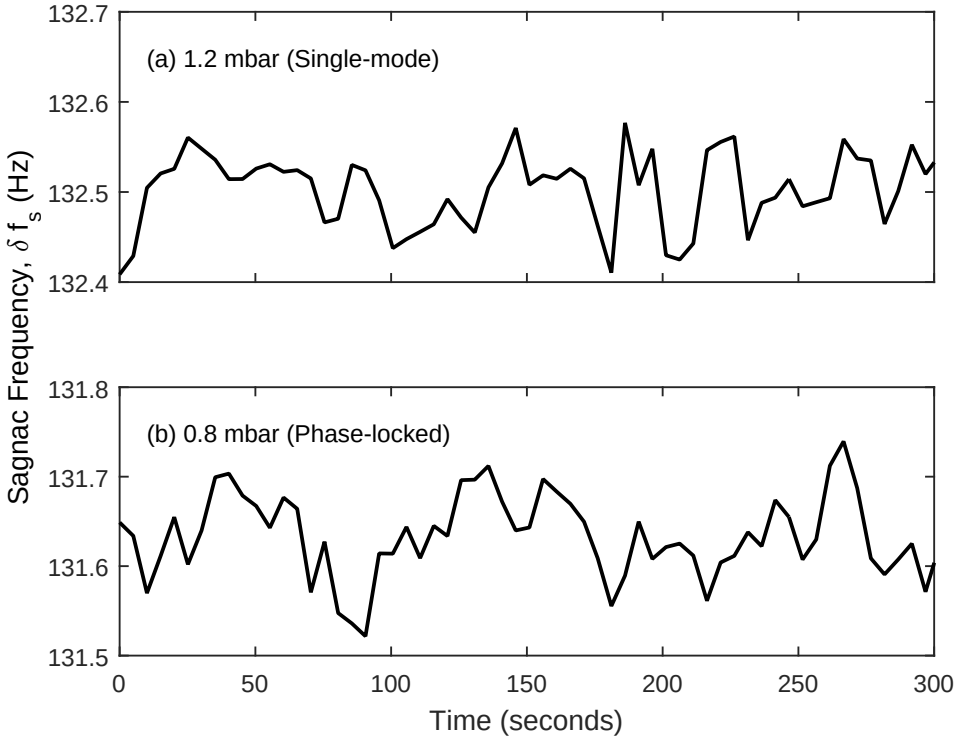

Figure. 5.36.: The short-term (between mode-hop) rotational signal detected when the laser operates on (a) single-mode with a gas mix of 0.2 mbar natural neon and 1.2 mbar of total gas pressure and (b) phase-locked with a gas mix of 0.2 mbar of natural neon and 0.8 mbar of total gas pressure.

Figure 5.36 compares the Sagnac signal logged over a short time (between mode hopping and mode splitting) when the laser was running on a single-mode regime and the phase-locked regime. The short-term rotational signal in Figure 5.36 (a) is extracted from the long-term data series in Figure 5.35, while the short-term δf_s in Figure 5.36 (b) corresponds to a cavity gas fill of 0.2 mbar of natural neon partial pressure and 0.8 mbar of total pressure where the laser power was maintained at 13 nW for PR-1 operation in the phase-locked regime.

In Figure 5.36 (a), the δf_s excursion is approximately 0.2 Hz. The monobeam modulations, m_1 and m_2 were measured to be between 4 to 8%. From Equation 3.5, the backscatter perturbation is estimated to be 0.21 Hz, which is close to the observed excursion in 5.36 (a). For phase-locked operation, Figure 5.36 (b) shows the δf_s excursion is also approximately 0.2 Hz. However, the detected monobeam modulations were lower, between 2 to 3%. We also note that the Sagnac contrast ratio measured was 21%, which is lower than the δf_s contrast ratio for single-mode operation.

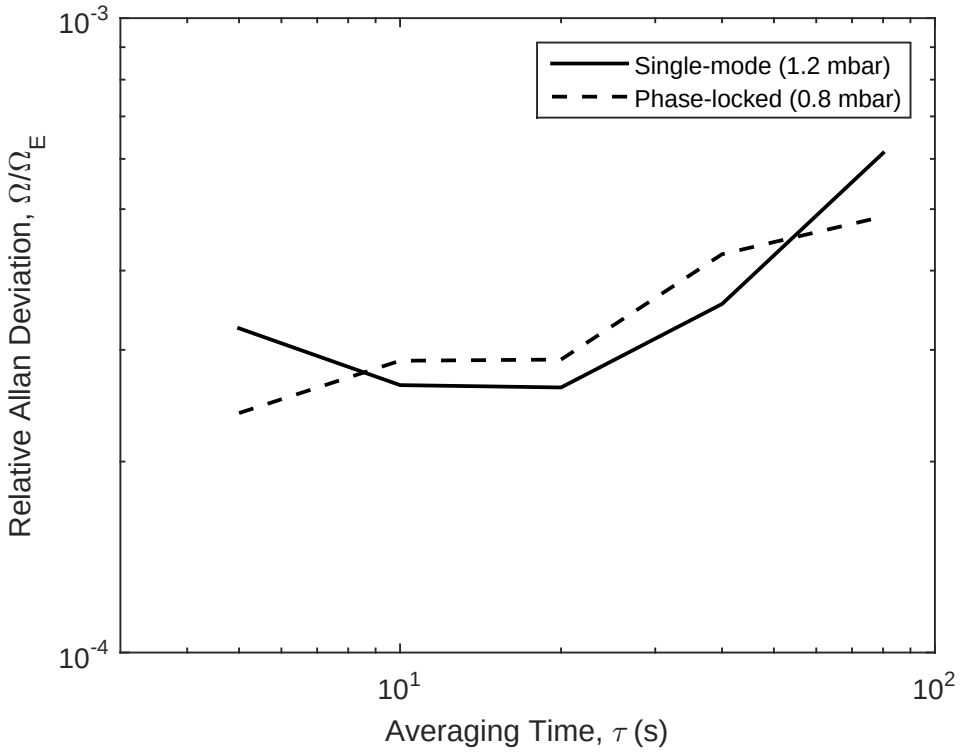

Figure. 5.37.: Relative Allan deviation (ADEV) plots correspond to the short-term data series in Figure 5.36 (a) and (b). For the single-mode operation, the minimum Ω/Ω_E is 2.6×10^{-4} at $\tau = 20$ s. On the other hand, the minimum Ω/Ω_E is 2.9×10^{-4} at $\tau = 20$ s for the phase-locked operation.

Figure 5.37 shows the calculated Allan deviation (ADEV) plots, normalised to Ω_E, for the δf_s data in Figure 5.36 (a) and (b); to evaluate the short-term stability of the rotation signal as a function of averaging time, τ. The minimum variance achieved when PR-1 was operating in the single-mode regime is 2.6×10^{-4} relative to Ω_E at $\tau = 20$ s, while the stability of the rotation signal when the laser is operating in the phase-locked regime is 2.9×10^{-4} Ω_E at $\tau = 20$ s. The performance of both the single-mode and stable multimode operating regimes are comparable, which is consistent with operation on the 632.8 nm wavelength in Figure 3.22. In terms of the laser stability, the minimum variance achieved with 632.8 nm in Chapter 3 is significantly lower, $7 \times 10^{-5} \Omega_E$. We attribute this to the higher operating powers available.

The relevant gyroscopic parameters for operation on the 543.4 nm transition are listed in Table 5.8. From the table, for single-mode operation, we note that the calculated sensor resolution (Equation 2.43) is 8.4×10^{-10} rad/s/$\sqrt{\text{Hz}}$. The sensor sensitivity for PR-1 operating on the 632.8 nm transition is 2.4×10^{-10} rad/s/$\sqrt{\text{Hz}}$ (refer to Table 3.5). The higher sensor resolution achieved with the operating wavelength of 632.8 nm is mostly due to the significantly higher operating power, 75 nW while the operating power at 543.4 nm is only 6 nW.

Operating Mode	Single-mode	Phase-locked
Laser power, P_i (nW)	6	13
Resolution, Ω_s (rad/s/$\sqrt{\text{Hz}}$)	8.4×10^{-10}	5.7×10^{-10}
Relative ADEV, Ω/Ω_E	2.6×10^{-4}	2.9×10^{-4}
Monobeam modulations, $m_{1,2}$ (%)	4 to 8	2 to 3
δf_s contrast ratio (%)	31	21
Backscatter induced perturbations, Δf_s (Hz)	0.21	0.03
Lock-in threshold, f_L (μHz)	1.2	0.4

Table. 5.8.: Summary of the relevant gyroscopic parameters for PR-1 running on the 543.4 nm neon transition.

5.5 Discussion

The optimum neon partial pressure for the PR-1 ring cavity with a 3 mm-diameter gain tube running on the 543.4 nm neon transition is 0.2 mbar. The maximum output power is obtained at 0.8 mbar of total pressure which leads to an optimum helium to neon gas ratio at 3:1. The best pressure mixture for gyroscopic operation is at 1.2 mbar of total pressure as this pressure provides a wide power range for the laser to run in the single-mode operating regime. This resulted in an optimum ratio of 5:1 which agrees with the optimum (maximum gain) ratio reported in ref. [45] (the optimum ratio was quoted as 5:1 at a total gas pressure of 2.1 mbar). In contrast, refs. [46] and [88] both quoted a 7:1 optimum helium to neon ratio. The variations in the quoted optimum ratio are mostly attributed to the difference in the diameter of the laser tubes.

The optimum gas mixture for our laser gyroscopes often differs from the literature. This is because the optimum gas ratio for an ideal gyroscopic operation depends on several factors such as the best RF excited power input to laser output efficiency and the highest laser output while maintaining single-longitudinal mode operation. In this study, the optimum gas mixtures for the 2.56 m^2 test cavity were found experimentally by: (i) characterising laser output power as a function of gas pressures at a fixed RF excited power; and (ii) characterising the single-mode operating regime as a function of total gas pressure.

d (mm)	ℓ (mm)	λ (nm)	p_{ne} (mbar)	p (mbar)	k (mm-mbar)	p_{opt} (mbar)	Optimum Ratio
3	400	543.4	0.2	0.8	2.4	0.8 to 1.2	3:1 to 5:1
		611.8	0.2	2	6	2 to 4	9:1 to 19:1
		632.8	-	-	-	-	-
		1152.3	-	-	-	-	-
4	100	543.4	-	-	-	-	-
		611.8	-	-	-	-	-
		632.8	0.2	2	8	4 to 10	19:1 to 49:1
		1152.3	0.2	0.2	0.8	6 to 12	29:1 to 59:1
4	580	543.4	-	-	-	-	-
		611.8	0.2	2	8	2 to 4	9:1 to 19:1
		632.8	-	-	-	-	-
		1152.3	-	-	-	-	-

Table. 5.9.: The optimum helium to neon ratio corresponding to three different gain tubes to obtain maximum power and ideal gyroscopic operation at different operating wavelengths. Parameters: d: gain tube diameter; ℓ: gain tube length; λ: operating wavelength; p_{ne}: neon partial pressure; p: total pressure; k = pd; p_{opt}: optimum pressure.

Table 5.9 summarises the optimum gas pressure for different operating parameters such as the gain tube length and diameter at different operating wavelengths for the PR-1 ring laser system. Note that the optimum pressure, p_{opt} listed in this table is the pressure range with the highest gain while maintaining single-mode operation; while k is the pd product which produces the highest laser power (the laser is free running)[9]. From the table, we can infer that for gain tube diameters of 3 mm and 4 mm, the optimum neon partial pressure is 0.2 mbar. This agrees with the neon partial pressure generally employed for the 632.8 nm transition, where the neon pressure is usually fixed at 0.2 mbar and independent from the total gas pressure [17]. The optimum pressure for operation at 543.4 nm is clearly lower than the other three operating wavelengths due to the low available gain. A common strategy applied to increase the laser gain is by using a narrower diameter laser tube since the laser gain varies inversely to gain tube diameter [112], [131]. In ref. [45], the highest optimum pressure is achieved at 2.1 mbar by using a 60 mm long gain tube with a diameter of 1 mm. However, for PR-1, the minimum gain tube diameter should not be less than 2.5 mm because the beam waist diameter is calculated[10] to be 2.33 mm. We note that the first He-Ne laser operation at 543.4 nm was utilising a 4 mm diameter gain tube with a total discharge length of 510 mm (gain tube length = 650 mm) [46]. In future work, it will be interesting to investigate 543.4 nm laser operation using the 580-mm long gain tube.

[9] As mentioned in Section 2.2, the maximum laser power for different gain tube diameters can be found empirically by fulfilling the following equation: pd = k, which relates the total pressure (p) to the gain tube diameter (d) [75], [131], where k is a constant.

[10] The calculation was done by a program originally developed by Dr. Bob Dunn and Prof. Geoff Stedman to do cavity stability calculations for planar rectangular cavities.

Further characterisation of the performance of PR-1 rotation sensing on the 611.8 nm and 543.4 nm neon transitions was hampered by gas impurities. The laser lifetime was remarkably short, approximately 13 hours. We found traces of air in the cavity after spectrally evaluating the plasma. A leak test was conducted and the new gain tube fitting was found to be leaking. Other than that, we noticed the supermirror situated at the bottom of the 400-mm-long gain tube was contaminated by dust falling from the gain tube. Due to low gain available, a slight increase in cavity loss will terminate the laser action at these wavelengths. Hence, in future works, it is advised that the new gain tube should be cleaned thoroughly before mounting the tube to the laser cavity.

When the ring laser was operating near the lasing threshold (RF = 6 to 7 W) at 543.4 nm, the plasma discharge was very unstable and inhomogeneous over the length of the tube. We speculate that the reasons behind the unstable and inhomogenous plasma distribution are due to fewer gas atoms available for electron-atom collisions in the plasma tube (p_{opt} = 1.2 mbar) and the RF power transfer from the transmitter to the plasma discharge was inefficient as the RF matching unit was optimised for the 580-mm-long gain tube. We also observed pulsing and flickering of the long plasma discharge. The pulsing in the plasma may be due to the reflections of acoustic waves travelling in the gain tube while the flickering may be caused by the "stuttering" of the servo loop that controls the transmitter.

The plasma discharge was stabilised when 6 magnets were employed along the gain tube. The 'brightness' of the plasma was increased and the plasma distribution became more homogeneous. Furthermore, the plasma no longer pulsed and flickered. A magnetic field has been known to increase the efficiency of power transfer from the RF source to the plasma. When a magnetic field is present in an electric field, the collision probability between the electron and atom is increased which leads to a higher ionisation rate. Other than that, the strong magnetic field confines the secondary-electrons close to the electrodes. This ensures a higher rate of secondary electron and ion production and thus, sustains the plasma discharge [118], [120]. In addition, a magnetic field is commonly used in a helium-neon laser system for frequency stabilisation as well to optimise the laser output power. With a strong magnetic field, the highest gain transition at 3391.2 nm will be suppressed due to the Zeeman effect. As a consequence, laser gain at the shorter wavelengths (lower gain transitions) will be improved [132]–[135].

The effect of magnetic fields to the gyroscopic operation remains to be explored. Despite the fact that the plasma can be stabilised with the installation of magnets along the plasma tube, a new matching unit is still needed for the 3-mm-diameter long gain tube for a more efficient gas excitation mechanism in future measurement.

5.6 Conclusion

Due to unforeseen design errors in the cavity mirrors, we had an opportunity to operate the first large ring laser gyroscope on the 611.8 nm ($3s_2 \rightarrow 2p_6$) neon transition where the laser generates a Sagnac beat frequency, induced by the rotation of the Earth, at approximately 117.2 Hz. As the mirror transmission is high at this wavelength, the output power for rotation sensing on a single longitudinal mode operation was high, at 1000 nW. This resulted in a comparable sensor performance with the 632.8 nm system despite having a low cavity Q. The best gyroscopic operation on this wavelength was observed with a gas fill of 0.2 mbar of neon and a total pressure of 3.5 mbar, achieving a resolution of 2.7×10^{-10} rad/s/$\sqrt{\text{Hz}}$.

We also present the first implementation of a large ring cavity to operate as a rotation sensor while running on the shortest helium-neon laser wavelength, at 543.4 nm. The $3s_2 \rightarrow 2p_{10}$ transition has a factor of 30 less gain than the traditional $3s_2 \rightarrow 2p_4$ transition. For this reason, the gain tube of the test cavity was replaced with a 400 mm-long gain tube with an inner diameter of 3 mm to provide excess gain. The laser successfully unlocked on the bias provided by the Earth rotation by generating a Sagnac frequency of 132.8 Hz. The highest output power of 800 nW was achieved at a partial pressure of 0.2 mbar of natural neon for a total gas pressure of 0.8 mbar. The range of total pressures for the laser operation was very narrow, in contrast to the operation at 632.8 nm, 611.8 nm and 1152.3 nm. Stable gyroscopic operation was readily observed in both the single-mode and stable multimode operating regimes. By operating on a higher optical frequency (ν_0 = 552 THz), a sensor resolution of 8.4×10^{-10} rad/s/$\sqrt{\text{Hz}}$ was achieved, which is reasonably good in comparison to the same system running on the high gain 632.8 nm transition ($\Omega_s = 2.4 \times 10^{-10}$ rad/s/$\sqrt{\text{Hz}}$) due to the lower laser output power.

The gyroscopic performance of the ring laser for either the 611.8 nm or 543.4 nm operating wavelength was limited by laser perimeter instability. More work is still needed to explore the best operating conditions for these 'frequency up-scaled' ring laser gyroscopes to unleash their full potential as highly sensitive ring laser interferometers.

6 Optical Frequency Stabilisation of a 2.56 m^2 Ring Laser Gyroscope

Laser frequency fluctuations due to perimeter variations limit the performance of a wall-mounted laser gyroscope. In this chapter, we report an actively-stabilised ring laser gyroscope by using the beat frequency between adjacent longitudinal modes as the feedback signal. We also report on preliminary work on the development of a frequency stabilisation scheme based on the optical heterodyned RF beat frequency between the single beam output from PR-1 with a stabilised helium-neon laser.

6.1 Heterolithic Ring Laser Gyroscopes

Constructing a large laser gyroscope based on a heterolithic design is a good compromise between achieving high sensor sensitivity and stability. Moreover, a heterolithic ring structure offers more flexibility as the laser is easy to assemble and transport. Typically, a heterolithic ring structure is constructed from stainless steel tubes and is mounted on a rigid base such as a granite slab or a thick concrete structure. The stability of the laser, to a high degree, depends on the stability of the mounting structure. Other than that, other sources which disrupt the stability of the laser frequency are the expansion of the stainless steel tubes, atmospheric pressure variations, mechanical disturbances, random noise due to spontaneous emissions, and stray magnetic fields from nearby electronics devices [17], [136].

The PR-1 ring laser is mounted on a wall of a high-rise building. Naturally, the laser cavity dimensions vary according to the wall temperature variations. As the concrete wall is expanding or shrinking, the laser cavity changes by several wavelengths correspondingly; causing perturbations in the rotational signal due to longitudinal mode index changes. This effect is known as mode hopping. Another effect arises from the laser perimeter fluctuations is denoted as mode splitting where the counter-propagating beams are running with different longitudinal mode indices. In this case, no beat frequency can readily be observed. These effects are prominent in PR-1 gyroscopic operation; and are typical for all heterolithic ring laser gyroscopes [21], [30].

Ideally, to compensate for thermal variations, passive frequency stabilisation such as mounting the laser in a temperature controlled environment can be applied. Also, the

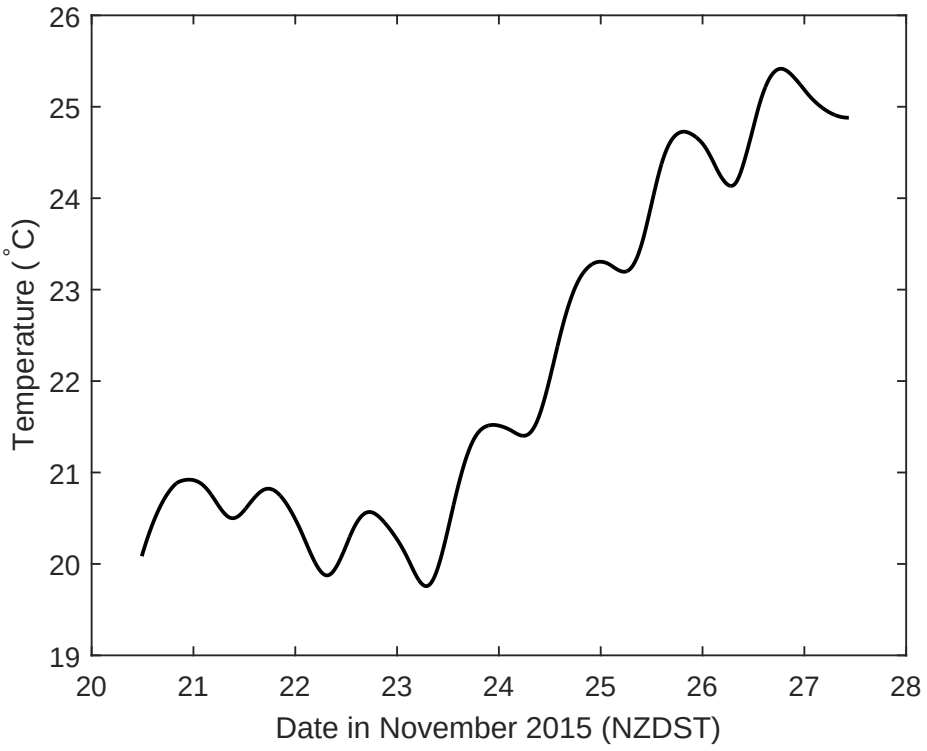

Figure. 6.1.: The variation in the wall temperature which PR-1 is mounted on for over 7 days in November 2015 (courtesy from Dr. R.B. Hurst from the School of Physical and Chemical Sciences, University of Canterbury).

mechanical disturbances can be compensated by mounting the laser on a stable base connected to bedrock or shielding the laser in an enclosure. On the other hand, an active stabilisation can be applied to control the laser perimeter via an automated servo-control system [136].

Figure 6.1 shows the wall (on which PR-1 is mounted) temperature variations for 7 days. By referring to the figure, the wall temperature excursion varies between 1 °C/day up to 2.7 °C/day. This implies that the wall[1] expands and contracts between 10 to 64 μm/day. In this chapter, we aim to implement an active perimeter control scheme against the temperature induced perimeter variations to stabilise the PR-1 laser frequency.

[1] Linear thermal expansion coefficient, α for concrete is 10×10^{-6}/°C. The change in length can be calculated by, $\delta\ell = L_0\alpha(t_1 - t_0)$, where $\delta\ell$ is the change in the object length, L_0 initial length of the object, t_0 is the initial temperature and t_1 is the final temperature (in °C).

6.2 A Self-Referenced Perimeter Stabilised Large Ring Laser Gyroscope

A ring laser gyroscope running in the phase-locked regime of operation exhibits a comparable gyroscopic performance to its operation in the single-mode regime [17], [91]. As the laser power is raised to provide enough gain for multiple longitudinal modes to co-exist, phase coupling between these modes results in stable laser operation; yielding a non-fluctuating Sagnac frequency.

The separation between these longitudinal modes (free spectral range) is governed by Equation 2.42 ($\nu_{fsr} = \frac{c}{P}$). Thus, detecting the ν_{fsr} signal provides a direct measurement of the laser perimeter, P. Small variations in the laser perimeter, δP shifts the free spectral range by,

$$\frac{\delta \nu_{fsr}}{\nu_{fsr}} = -\frac{\delta P}{P}, \tag{6.1}$$

or

$$\delta P = -\frac{\delta \nu_{fsr} c}{\nu_{fsr}^2}. \tag{6.2}$$

As a result, any changes in the ν_{fsr} give a direct indication of variations in the geometry of the laser cavity. Linear helium-neon laser frequency stabilisation by utilising the beat frequency arising between multiple longitudinal modes is well-known [137]–[139]. In this section, we present the experimental works performed to actively control the PR-1 laser perimeter by using the inter-longitudinal mode beat frequency, ν_{fsr} as a feedback signal.

6.2.1 Overview of the Experimental Setup

Figure 6.2 shows the experimental setup of the frequency stabilisation scheme for the PR-1 ring laser. The laser cavity length was held constant by two piezoelectric actuator stages (PZT) which were mounted on two diagonally opposite corners of the PR-1 cavity (on the top right corner and bottom left corner). These two PZTs were driven by voltage driver controllers (***piezosystem jena*** 12V40 voltage amplifier) that received control signals from a frequency servo unit. A Hamamatsu R3986 photomultiplier tube (PMT) was mounted on the lower left corner box of the PR-1 laser cavity to detect the counter-clockwise (CCW) laser beam. The signal detected by the PMT was filtered by a capacitor (connected in series) to allow the AC signal of the ν_{fsr} beat frequency between two longitudinal modes signal to be delivered into the input of a communication receiver (Yaesu VR-5000, 100 kHz- 2600 MHz reception bandwidth).

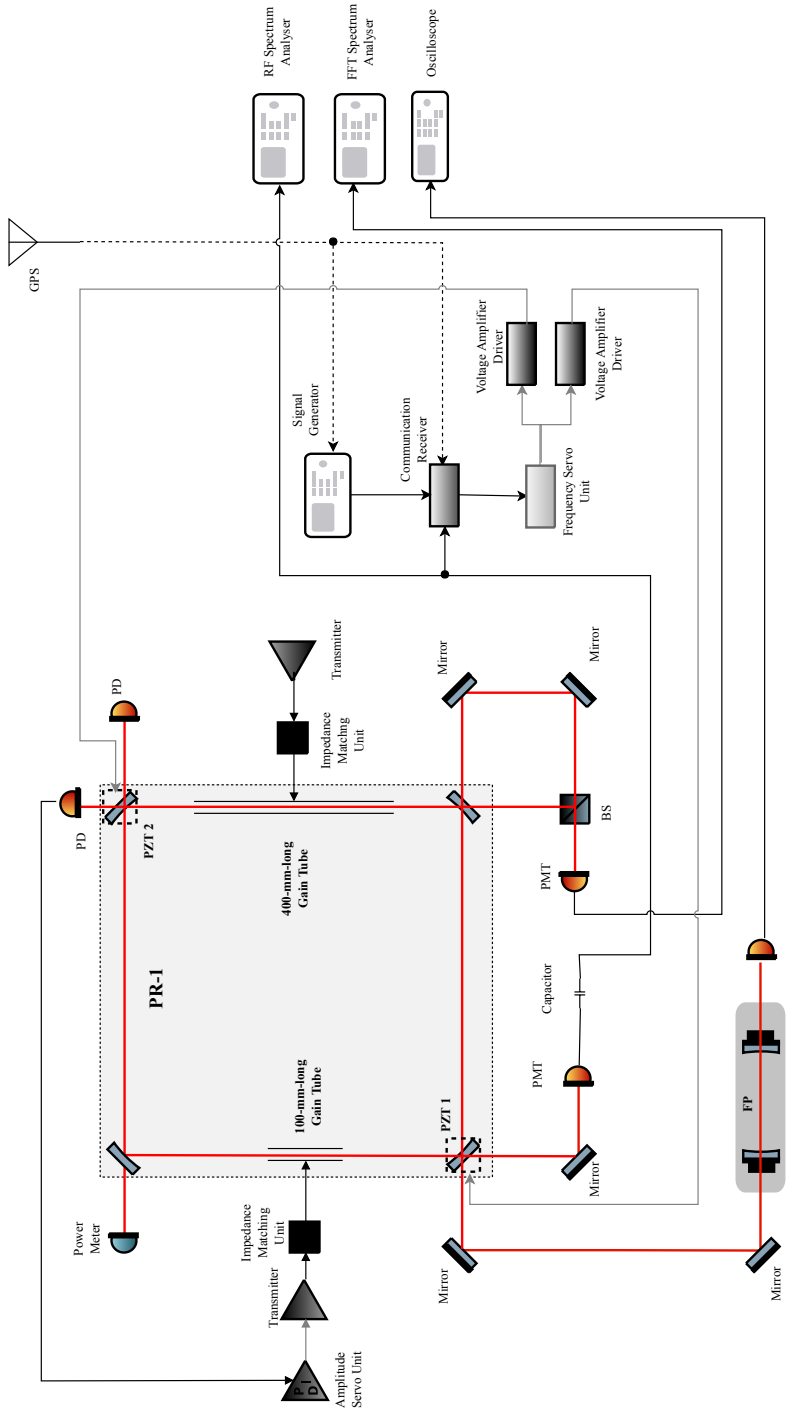

Figure. 6.2.: Experimental setup of the optical frequency stabilisation of the PR-1 ring cavity. PD: Photodiode; PMT: photomultipliertube; BS: beam splitter; FP: Fabry-Pérot interferometer.

A GPS-stabilised signal generator (Hewlett Packard 8684A) provided a reference signal, ν_{ref}, against the detected ν_{fsr} and this signal was injected into the second input of the communication receiver via a coaxial cable. The ν_{fsr} and ν_{ref} signals were heterodyned by the mixer and produced a beat signal, ν_{beat}. After that, the ν_{beat} was amplified via

an amplifier embedded within the communication receiver to be transferred to the frequency servo unit as a feedback signal.

The clockwise (CW) laser beam transmitted from the lower left corner of the laser cavity was fed into a Fabry-Pérot interferometer (Coherent, 33-6305-001) to monitor the longitudinal mode spectrum. At the same time, the beat frequency between the longitudinal modes was observed by connecting the PMT, which carries the ν_{fsr} information, to an RF spectrum analyser (HP ESA L-1500A). Simultaneously, the Sagnac frequency power spectrum was monitored closely by connecting the rotational signal detected by another PMT to an FFT spectrum analyser.

6.2.2 Free Spectral Range Detection

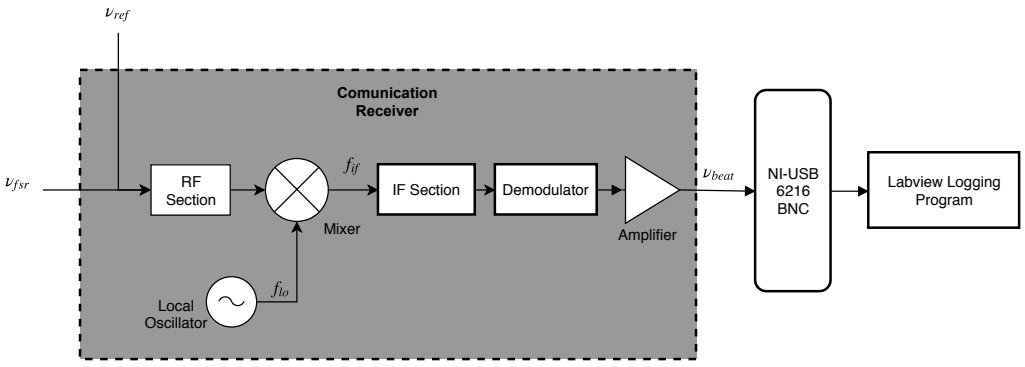

Figure. 6.3.: Simplified block diagram of the communication receiver (reproduced from [140]) and the experimental setup to measure ν_{beat} variations. The receiver consists of an RF section, mixers, a tunable local oscillator, an intermediate-frequency (IF) section, a demodulator and an amplifier.

A simplified block diagram of the experimental setup to detect variations in the ν_{fsr} signal is illustrated in Figure 6.3. As mentioned before, the GPS-stabilised RF signal generator will provide a reference frequency (ν_{ref}) against the ν_{fsr} frequency arising from the frequency beating between two longitudinal modes of the PR-1 laser (Figure 6.2). These two RF signals were connected to the Yaesu VR-5000 communication receiver via a BNC T-connector to the 'Antenna A' input on the rear side of the receiver.

Then, within the communication receiver, the ν_{fsr} and the ν_{ref} signals were passed through an RF section to be amplified. After passing through the RF section, the amplified ν_{ref} and the ν_{fsr} signals were heterodyned with a frequency provided by a tunable local oscillator to convert the carrier frequencies of these two RF signals to pre-determined (fixed) intermediate frequencies[2] (IF). Subsequently, the signals were received by an IF

[2] Intermediate frequencies are typically used in superheterodyne radio receivers, in which an incoming signal is shifted to an IF for amplification before final detection is done. At this mixer stage, the Yaesu communication receiver provides an IF of f_{if} = 10.7 MHz.

section. The IF section provides a series of mixer stages[3] and signal amplification. Finally, the RF signals were passed to a demodulator section as shown in Figure 6.3.

The ν_{fsr} signal can be represented as a sinusoidal electrical signal, $E_1(t)$ as,

$$E_1(t) = A\ \cos\ \omega_1 t, \tag{6.3}$$

where A is the amplitude of the signal and $\omega_1 = 2\pi\nu_{fsr}$. Likewise, the electrical signal for the reference frequency from the GPS-stabilised signal generator[4] can be represented as,

$$E_2(t) = B\ \cos\ \omega_2 t, \tag{6.4}$$

with B as the amplitude of the reference signal and $\omega_2 = 2\pi(\nu_{ref}) = 2\pi(\nu_{fsr} + f_{offset})$. These two signals were heterodyned in the demodulator section of the communication receiver, and a signal denoted as $x(t)$ is produced [140],

$$\begin{aligned} x(t) =& E_1(t)E_2(t) \\ =& A\ \cos\ \omega_1 t\ B\ \cos\ \omega_2 t \\ =& AB\Big[\frac{1}{2}\cos(\omega_1+\omega_2)t + \frac{1}{2}\cos(\omega_1-\omega_2)t\Big] \\ =& \frac{1}{2}AB\Big[\cos[2\pi(\nu_{fsr}+\nu_{fsr}+f_{offset})]t \\ &+ \cos[2\pi(\nu_{fsr}-\nu_{fsr}-f_{offset})]t\Big]. \end{aligned} \tag{6.5}$$

The demodulator section in the communication receiver consists of an envelope detector, which comprises a diode and a capacitor. This envelope detector provides signal passbands between 10 Hz to 10 kHz. As can be seen from Equation 6.5, the sum of the frequencies is situated outside of the passband of the envelope detector. Therefore, only the frequency difference between these two RF signals, i.e. the f_{offset} was allowed to be passed on to the amplification section as shown in Figure 6.3. As a result, only the amplification of the f_{offset} signal was detected at the output of the communication receiver [140].

The amplified signal, ν_{beat} ($\nu_{beat} = |\omega_1 - \omega_2| = f_{offset}$) was connected to the analog input of LabVIEW USB NI-6216 DAQ via a BNC cable and the data acquisition was realised by a LabVIEW logging program on the PC.

[3]The Yaesu VR-5000 communication provides 4 mixer stages, and this is to prevent image signal interference and also allows the receiver to tune over a wide frequency range 100 kHz to 2.6 GHz. The final mixer stage provides an f_{if} = 455 kHz.

[4]The Hewlett Packard 8684A RF signal generator is set to AM function with no modulation. ν_{ref} is set equivalent to the ν_{fsr} value, but with an offset frequency (f_{offset}) of within a few kHz higher than the ν_{fsr} frequency,

We measured the change in the free spectral range ($\delta\nu_{fsr}$) for several hours to investigate the rate of change in the PR-1 perimeter cavity over time. For this measurement, the laser was running with a gas fill of 0.2 mbar 50:50 neon with a total gas pressure of 6 mbar. We raised the RF input power until the laser exhibited phase-locked operation; where stable multiple longitudinal modes were observed on the FP spectrometer and the δf_s signal remained consistent. The laser power was maintained at 50 nW (to sustain the stable phase-locked operation) by the amplitude servo unit. We fixed the ν_{ref} at a frequency of 1500 Hz offset from the ν_{fsr} beat frequency. The sampling rate acquired by the LabVIEW logging program was set to 5 kHz, and the number of samples was fixed at 1000 to reproduce the detected ν_{beat} via the logging program.

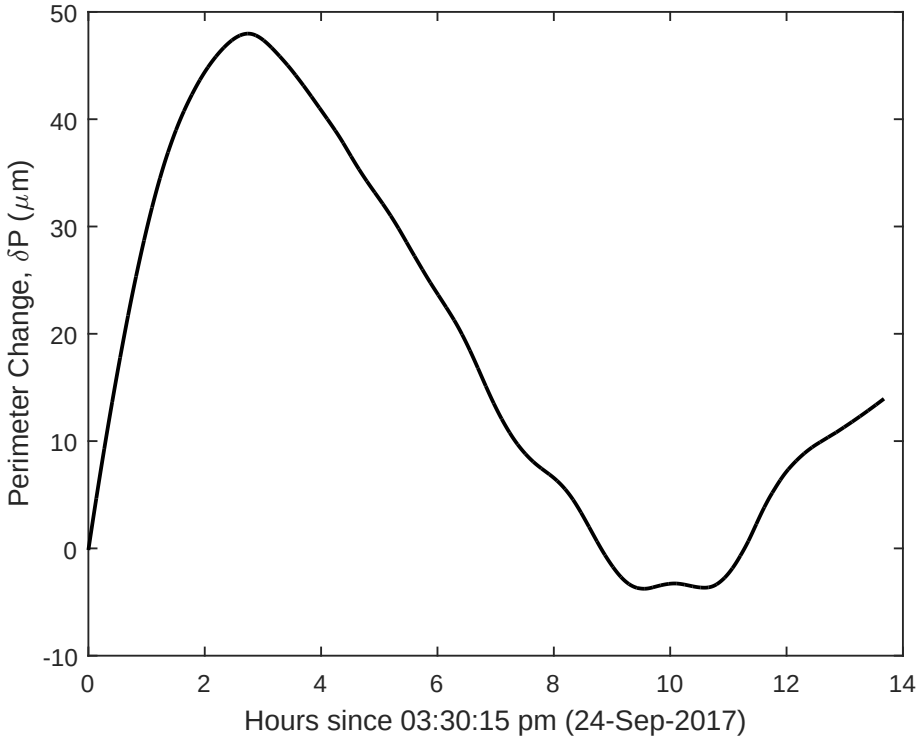

Figure. 6.4.: Variations in the PR-1 cavity perimeter for over 12 hours.

The beat frequency (ν_{beat}) was logged for over 12 hours and Figure 6.4 illustrates the changes in the PR-1 cavity perimeter, δP as a function of time; where δP is determined by Equation 6.2. As seen from the figure, the laser cavity was expanding by approximately 53 μm within the first 3 hours; attributed to the fact that the wall temperature[5] was rising. Then, the laser perimeter began to shrink slowly and continuously for the next 7 hours.

By fitting a lower order polynomial function through the data, the rate of the PR-1 perimeter change is between 2 to 5 nm/s. This is consistent with our observation on the Sagnac

[5]This measurement was logged at 03:30:15 pm (NZDST) on 24 September 2017. Therefore, the wall temperature was rising for the first three hours and started to drop at night.

frequency time series in the previous chapters, where mode hopping and mode splitting typically occur between 200 s to 300 s (632.8 nm /300 s ≈ 2 nm/s).

6.2.3 Piezoelectric Actuators Calibration

The drift in the PR-1 laser perimeter will be compensated by moving the two diagonally opposite mirrors through the movement of piezoelectric actuators (PZTs). The PZT is situated below the mirror chamber and a fine displacement of this actuator (when a high voltage is applied to the actuator) will move the corner box in a diagonal direction. The piezoelectric actuator is controlled by voltages ranging from - 10 V up to 150 V. The control voltages are driven by ***piezosystem jena*** 12V40 voltage amplifier and the technical data is tabulated in Table 6.1.

Parameter	Value
Supply Voltage	+12 V DC
Output Voltage (OUT)	-10 ... +150 V
Modulation Input (MOD)	0 ... +10 V
Monitor Voltage (MON)	-1 ... +10 V
Output Noise	< 0.3 V_{rms} at 500 Hz
Bandwidth	400 Hz

Table. 6.1.: Technical data for the 12V40 voltage amplifier.

The motion of the piezoelectric actuator is remotely controlled by connecting a modulation signal to the Modulation (MOD) input connector situated at the front panel. The control signal range is limited within 0 to 10 volts and the corresponding voltage output to the piezo actuators ranges from -10 to 150 V. The voltage value applied to the actuator can be monitored in real time by connecting the Monitor (MON) output connector to an oscilloscope. The signal detected from the Monitor (MON) output connector is the output voltage in 10:1 ratio with respect to the output voltage (OUT) that is connected to the actuator.

In this work, we employed 2 PZTs to actively control the PR-1 laser cavity perimeter. The characterisation of the 2 PZTs which was provided by ***piezosystem jena*** Inc. is listed in Table 6.2. As seen from the table, by applying -10 to 150 V across the piezo stacks, the maximum displacement achieved by PZT 1 and PZT 2 is 83 μm and 83.7 μm respectively.

Piezoelectric Actuator (PZT)	Total Displacement (μm)
1	83
2	83.7

Table. 6.2.: Total range of the piezoelectric actuators displacement as specified by ***piezosystem jena*** Inc.

For our laser perimeter stabilising scheme, we set the PZT driver (voltage amplifier) to operate below 4 V of voltage modulation to avoid continuous high voltage applied to the piezo stacks. The initial position of the PZT was fixed at 2 V so that the PZTs compensate for cavity shrinking and contracting equally. The total travel range for PZT 1 and PZT 2 will be 33.2 μm and 33.48 μm respectively. However, since both PZTs are travelling diagonally, theoretically (in terms of the laser perimeter change), both PZTs are expected to hold the laser cavity length within perimeter variations of 47.15 μm.

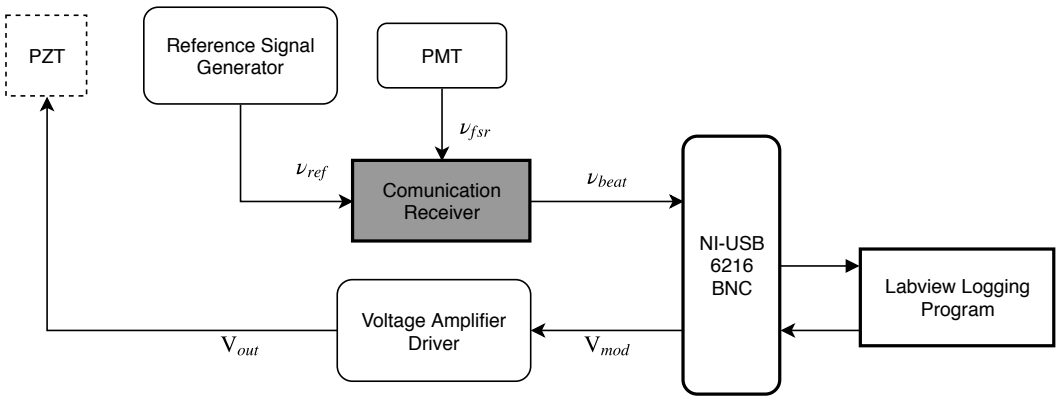

Figure. 6.5.: Block diagram of the experimental setup to measure ν_{beat} as a function of voltage modulation.

Figure 6.5 shows a block diagram to illustrate an experiment that was conducted to characterise the relationship between the voltage modulation to the PZT voltage amplifier and the laser perimeter variation, δP. The laser perimeter change will be extracted from the variation in ν_{beat} as described in the previous section. The voltage modulation input to the voltage amplifier was controlled from LabVIEW using the digital-to-analog output channel to provide voltages between 0 V to 4 V. The initial position of PZT 1 was fixed at the minimum by setting the input voltage modulation at 0 V. Then, the voltage modulation was increased in 0.1 V steps after every 5 s; and simultaneously, the ν_{beat} detected was recorded. The characteristics of the PZTs are slightly different as shown in Figure 6.6 where the total range of displacement (maximum voltage modulation = 4 V) for PZT 1 is 23.96 μm while the maximum range of travel for PZT 2 is 24.87 μm. Hence, the total range of laser cavity variation that can be compensated by the PZTs is 48.83 μm. By applying a linear function through the data obtained, we can calibrate the modulation voltage to be applied to PZT 1 and PZT 2, as a function of the perimeter displacement as 6.504 μm/V and 6.826 μm/V respectively.

From the piezo-actuator characteristic as specified in Table 6.2, the piezo-actuator response (displacement per voltage modulation) for PZT 1 and PZT 2 is 5.867 μm/V and 5.918 μm/V correspondingly; which implies a variation of approximately 1 μm/V from our measurement. Note that the calibration done here was influenced by the frequency pulling and frequency pushing in the active gain medium [47], [138]. Therefore, a discrepancy between the specified piezo-actuator response and the experimental value

is not unexpected. The PZT calibration is best done with a passive laser cavity so that the variation in the ν_{fsr} is free from the limitation imposed by the active gain medium [141].

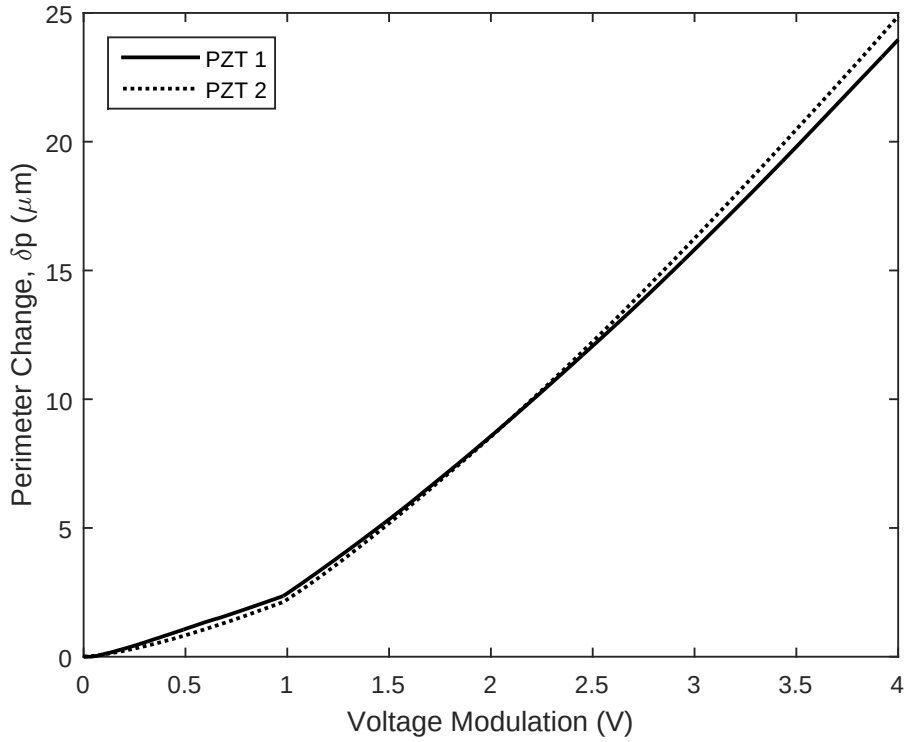

Figure. 6.6.: The modulation voltage to drive PZT 1 and PZT 2 as a function of the PR-1 laser perimeter change.

6.2.4 Frequency Servo Unit

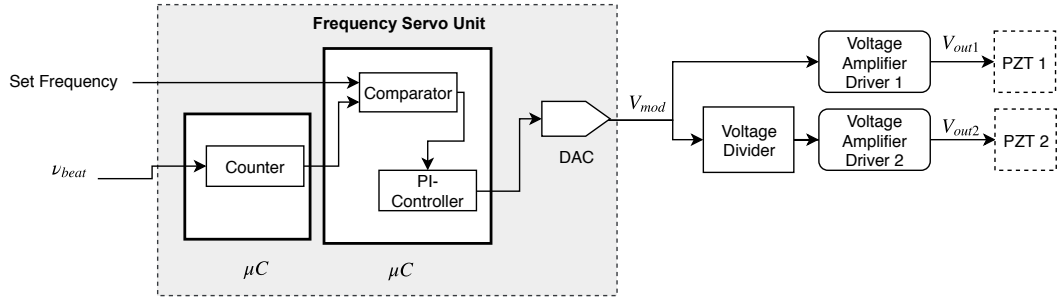

Figure. 6.7.: Block diagram of the frequency servo unit and the perimeter feedback system. μC: Micro-controller; DAC: digital-to-analog converter: frequency-to-voltage converter; PZT: piezoactuators.

Figure 6.7 shows the block diagram of the frequency servo unit and the feedback control mechanism. The frequency servo unit consists of a micro-controller which serves as a counter and another micro-controller with a proportional-integral-controller (PI-controller) function. The output of the second micro-controller is programmed to provide a fixed 2 V modulation voltage to set the initial position of both PZTs at mid-point.

As the heterodyned signal is connected to the input of the frequency servo unit, the ν_{beat} frequency is counted by the frequency counter with an integration time of 5 s. Then, the counted value is compared to a set value (set frequency) by a comparator function in the second micro-controller. The PI-controller output is proportional to the difference between the set frequency and the detected beat signal. Subsequently, the modulation voltage, V_{mod} is generated by converting the PI-controller output to 16-bit 0 to 4 V analog signal.

The output from the frequency servo unit (V_{mod}) is coupled to the modulation input connector located on the front panel of the voltage amplifier driver. Both voltage amplifier drivers generate a voltage output (V_{out}) corresponding to the modulation voltage and drive the PZTs to compensate for the laser perimeter drift. It is important to ensure the perimeter compensation introduced by the piezo actuators are equal to avoid asymmetry of the cavity as a result of the feedback regime. Therefore, a voltage divider was connected between the voltage modulation output to the second voltage amplifier so that the modulation voltage to drive PZT 2 (V_{out2}) is less than the voltage modulation to drive PZT 1 (V_{out1}) by a relationship: $V_{out2} = \frac{6.504}{6.826} V_{out1} \approx 0.953 V_{out1}$.

6.2.5 The Implementation of the Optical Frequency Feedback System

The procedure to implement the frequency feedback system was as follows. Firstly, we filled the laser cavity with a desired gas composition. Then, the laser was excited by applying RF power to the 100-mm-long gain tube. The laser power was tuned to a power regime where the laser was running on a phase-locked configuration (stable longitudinal modes configuration were seen on the FP spectrometer) and a ν_{fsr} beat frequency was observed on the RF spectrum analyser. It was essential to ensure a stable Sagnac frequency power spectrum was observed on the FFT spectrum analyser as well. The laser output was maintained at this power level via the amplitude servo unit.

Once stable phase-locked operation was established, the frequency servo unit was switched on, which positioned PZT 1 and PZT 2 at the middle point of their total displacement range respectively. Afterwards, the GPS-stabilised signal generator was set to a frequency within 1000 Hz to 2500 Hz above the detected ν_{fsr} beat frequency. Subsequently, the communication receiver was tuned to a frequency value close to ν_{fsr} and the resulted beat (ν_{beat} ≈1000 Hz to 2500 Hz) was observed on the frequency servo unit front display. Note that the amplitude of the ν_{beat} signal should be adjusted to (or maintained at) 1 V. The amplitude can be adjusted easily via the volume knob on the communication receiver. Finally, the desired ν_{beat} was set accordingly and followed by pressing the 'run' button on the frequency servo unit. The frequency servo unit will compensate any drift in the ν_{beat} by sending a feedback signal to the PZTs voltage controller.

For a cavity gas fill of 0.2 mbar of 50:50 neon and 6 mbar of total gas pressure, the laser reached a stable phase-locked regime at a laser output power of 50 nW. The ν_{fsr} beat frequency observed on the RF spectrum analyser was 93.557862 MHz; generated from the frequency beating between the main longitudinal mode and the second longitudinal mode at twice the free spectral range away from the main mode. The nominal frequency difference between the detected ν_{fsr} and the GPS-locked signal generator was set at 2000.7 Hz, and the ν_{beat} signal was logged via LabVIEW data acquisition. At the same time, the detected rotational signal, δf_s was acquired continuously.

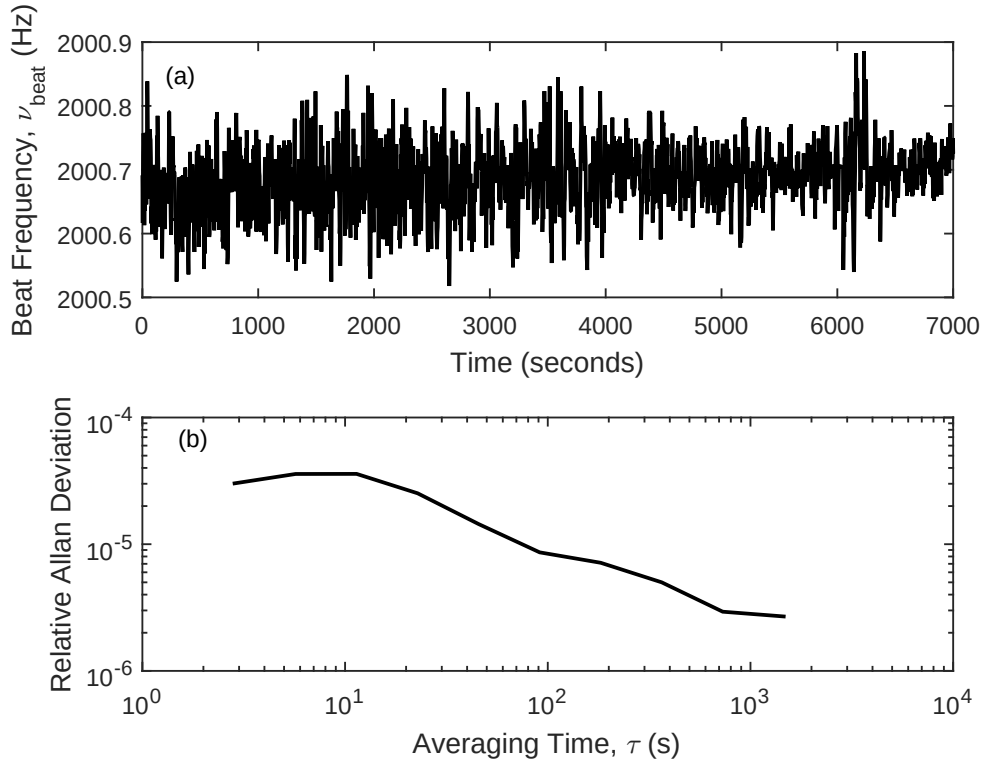

Figure. 6.8.: (a) The detected ν_{beat} signal for 7000 s; (b) the corresponding relative Allan deviation plot of the detected ν_{beat} signal normalised to the nominal ν_{beat}.

The frequency stabilisation scheme successfully locked the PR-1 laser cavity for almost 2 hours where the frequency servo unit successfully maintained the ν_{beat} frequency at 2000.7 Hz for 7000 s; as shown in Figure 6.8 (a). By referring to the figure, the heterodyned beat frequency variations stayed within 0.103 Hz for 7000 s; which implies that δP was held within 14 nm for more than an hour. The stability of the ν_{beat} signal was evaluated via an Allan deviation (ADEV) curve normalised to the nominal ν_{beat} as depicted in Figure 6.8 (b). The lowest variance was achieved at an averaging time of 1460 s with a stability of 2.7×10^{-6} relative to the nominal ν_{beat}.

Figure 6.9 (a) presents the δf_s signal logged corresponding to the period for which the laser cavity was locked to the ν_{beat} at 2000.7 Hz. From the figure, it is apparent that the Sagnac signal is free from mode hopping and mode splitting within the cavity stabilisation

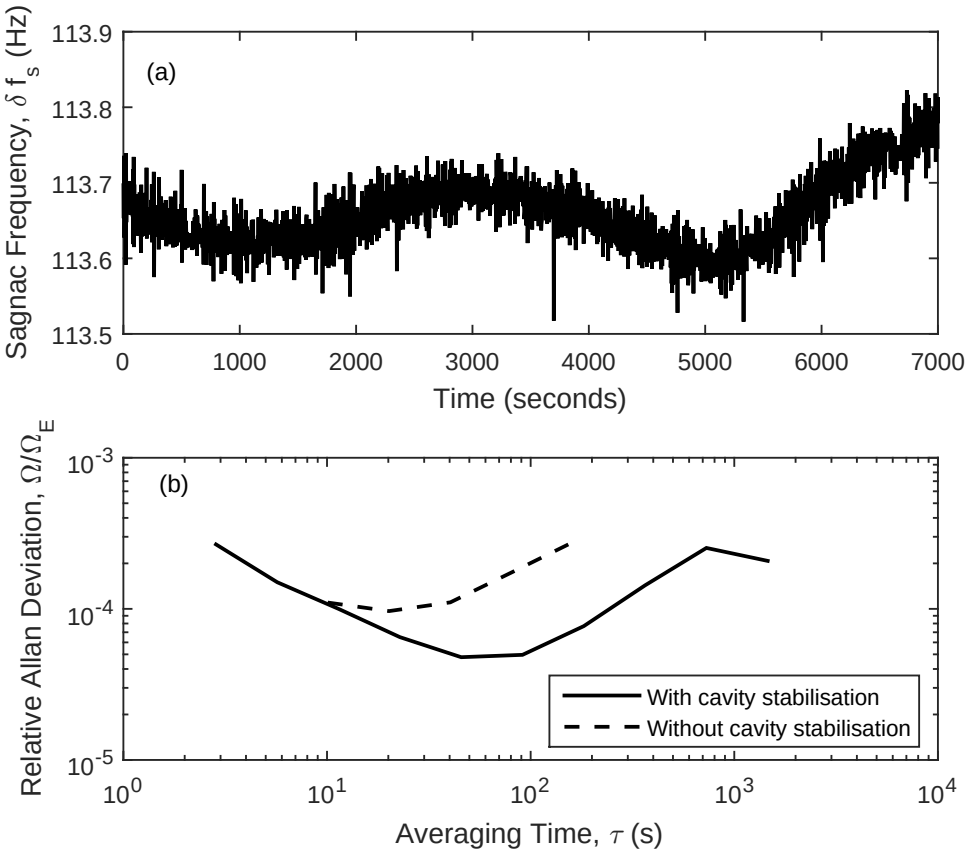

Figure. 6.9.: (a) The detected raw Sagnac frequency, δf_s after the implementation of the active frequency feedback system; for 7000 s; (b) relative Allan deviation of the Sagnac signal for the PR-1 ring laser with and without cavity stabilisation.

period. The laser cavity was only locked for more than one hour because the displacement of the piezo actuators went out of range. We note that there was about 30 mHz of modulation observed on the Sagnac signal time series. This slow modulation may be due to the nonlinear response of the PZTs movement.

Figure 6.9 (b) compares the ADEV curve normalised to the Earth rotation, Ω_E of the Sagnac frequency detected by the gyroscope with and without the frequency stabilisation. Without active control of the laser perimeter, the δf_s data set to be evaluated was limited between mode hops and mode splitting, typically between 200 s to 300 s. The lowest variance achieved by the laser without cavity stabilisation is $9.7 \times 10^{-5}\Omega_E$ at $\tau = 20$ s. On the other hand, by stabilising the ring laser perimeter, the detected Sagnac signal was free from mode hopping and mode splitting. Therefore, a more extended Sagnac signal data set can be analysed. As can be seen from the figure, the stabilisation of the laser cavity allows for a longer averaging time, where the knee of the ADEV curve occurs at a later time, i.e. at $\tau = 45$ s, with a minimum variance at $4.8 \times 10^{-5}\Omega_E$. To date, this is the best gyroscopic performance achieved by the PR-1 ring laser known to the author.

We repeated the experiment by operating the ring laser on the 611.8 nm laser wavelength. The experimental setup remained the same as depicted in Figure 6.2. We changed the supermirrors to the supermirror set that was described in Chapter 5 (Table 5.2). The laser cavity was filled with 0.2 mbar of 50:50 neon and a total gas pressure of 6 mbar. The laser output power was maintained at 2600 nW for stable phase-locked operation by connecting the amplitude servo unit to the second transmitter as we were utilising the 400-mm-long gain tube for this experiment.

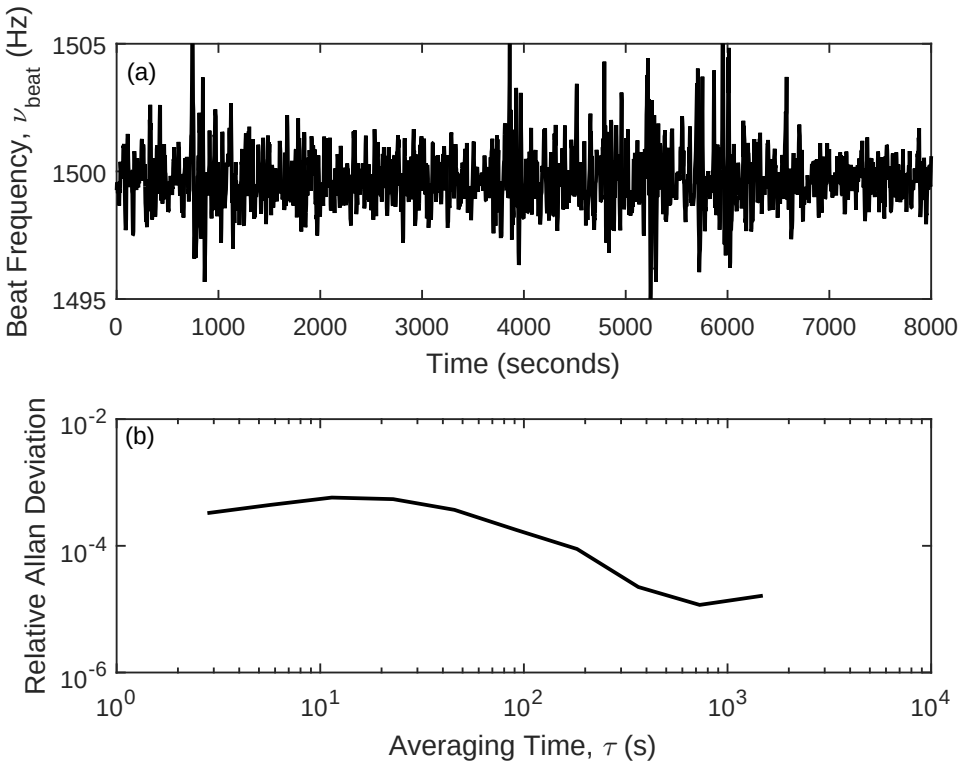

Figure. 6.10.: (a) The detected ν_{beat} signal over time; (b) the corresponding relative Allan deviation plot normalised to the nominal ν_{beat}.

Figure 6.10 (a) shows the PR-1 ring laser cavity locked to a ν_{beat} signal fixed at 1500 Hz by the frequency servo unit for 8000 s. The excursion of the ν_{beat} signal depicted in the figure varies within 1 Hz, signifying the perimeter feedback system maintained the laser cavity to within 140 nm. Figure 6.10 (b) portrays the ADEV curve of the detected ν_{beat} signal. The stability of the ν_{beat} signal reached a minimum variance of 1.2×10^{-5} relative to the nominal ν_{beat} frequency at τ = 730 s.

Figure 6.11 (a) and (b) are the detected raw δf_s signal for 8000 s after the cavity stabilisation feedback system was implemented and the corresponding relative ADEV curve of the δf_s data set. Similar to the observation in Figure 6.9 (a), mode-hopping and mode splitting are absent from the data set. Also, a slow modulation (25 mHz - 30 mHz) can be observed on the recorded Sagnac frequency over time. Similar to our observation in Figure 6.9 (a), the slow modulation may be correlated with the non-linearity of the PZT

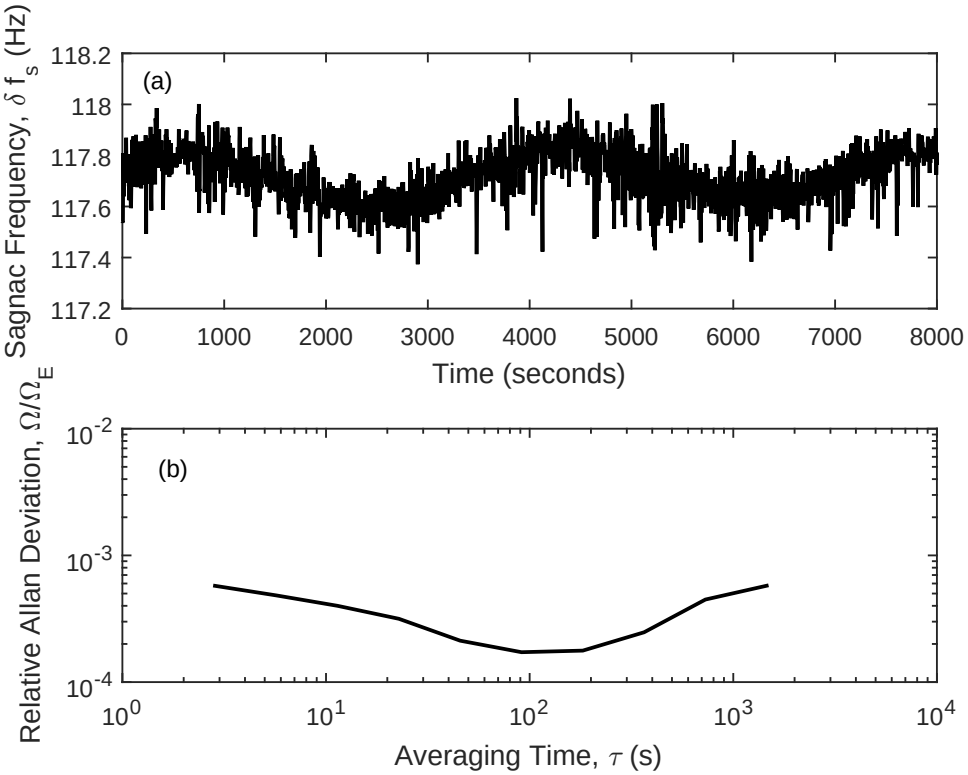

Figure. 6.11.: (a) The detected raw Sagnac frequency, δf_s after the implementation of the active frequency feedback system; for a period = 8000 s; (b) relative Allan deviation of the Sagnac signal for the PR-1 ring laser with and without cavity stabilisation with an operating wavelength of 611.8 nm.

response. The gyroscopic performance of the laser on the 611.8 nm operating wavelength achieved a minimum variance of $\Omega/\Omega_E = 1.8 \times 10^{-4}$ at τ = 180 s. The stability of the laser improved to some extent; where without the perimeter feedback system, the laser achieved a minimum variance of 3.3×10^{-4} relative to the Earth rotation (Table 5.5).

The main setback for this perimeter stabilisation system is the laser perimeter was only locked for a short time period (approximately 2 hours). The main reason for this setback was the PZT displacement had gone out of range. Further improvement of the stabilisation system is possible by modifying the frequency servo unit to reset to the initial υ_{mod} value (to set the PZTs back to the midpoint position) when the PZTs reached their maximum displacement range. We note that another heterolithic ring laser gyroscope, denoted as G-Pisa, was actively stabilised and achieved a stability of 2×10^{-5} [58]. The 1.82 m^2 heterolithic ring laser perimeter remained locked for days. This is possibly because G-Pisa is located in a laboratory which is inherently more stable than our laboratory in the West Rutherford building.

6.3 A Stabilised He-Ne Laser as a Frequency Reference for Perimeter Stabilisation

The advantage of the self-referenced feedback system described in the previous section is that it can be implemented for a ring laser with different operating wavelengths (besides 632.8 nm). However, to enforce the feedback scheme, the laser is required to run in the phase-locked regime. An alternative method of stabilising the PR-1 perimeter is by comparing the optical frequency to another stabilised laser.

Let us assume the optical frequencies of the stabilised reference laser and the laser gyroscope are ν_1 and ν_2 respectively. Their optical fields, $E_1(\nu_1)$ and $E_2(\nu_2)$ can be written as [81], [82], [142],

$$E_1(\nu_1) = A_1 \cos(2\pi\nu_1)\, t \tag{6.6}$$

and

$$E_2(\nu_2) = A_2 \cos(2\pi\nu_2)\, t, \tag{6.7}$$

correspondingly, where A_1 and A_2 represent the amplitudes of the two laser beams. As these two laser beams are superimposed; the resultant combined signal which is detected at the photodetector will generate a photo-current output, i_p (assuming E_1 and E_2 have the same polarisation) [142],

$$\begin{aligned} i_p \approx I(t) =& E^2(t) \\ =& [E_1(\nu_1) + E_2(\nu_2)]^2 \\ =& [A_1 \cos(2\pi\nu_2)\, t + A_1 \cos(2\pi\nu_2)\, t]^2 \\ =& A_1^2 \cos^2(2\pi\nu_1)\, t + A_2^2 \cos^2(2\pi\nu_2)\, t \\ &+ 2\ A_1 A_2 \cos(2\pi\nu_1)\, t\ \cos(2\pi\nu_2)\, t \end{aligned} \tag{6.8}$$

Using the trigonometric identity: $2\cos A \cos B = \cos(A+B) + \cos(A-B)$, the above equation can be re-written as,

$$\begin{aligned} I(t) =& A_1^2 \cos^2(2\pi\nu_1)\, t + A_2^2 \cos^2(2\pi\nu_2)\, t \\ &+ A_1 A_2 \cos[2\pi(\nu_1+\nu_2)]\, t + A_1 A_2 \cos[2\pi(\nu_1-\nu_2)]\, t. \end{aligned} \tag{6.9}$$

The first, second and third terms from Equation 6.9 involve of frequencies (10^{14}) way above the photodetector time response[6]. Therefore, the photodetector output is proportional to the time average of Equation 6.9 over the response time of the detector. Only the frequency value from the fourth term falls inside the cut-off frequency of the photodetector. Thus, the i_p output from the photodiode is [142],

$$i_p = \frac{1}{2} A_1^2 + \frac{1}{2} A_2^2 + A_1 A_2 \cos[2\pi(\nu_1 - \nu_2)\, t], \tag{6.10}$$

[6] The typical time response for a Hamamatsu photomultiplier tube is 2 ns.

with a resultant beat frequency, $\Delta\nu = \nu_1 - \nu_2$. The frequency difference lies within the radio frequency (RF) spectrum. Thus, we can utilise $\Delta\nu$ as the feedback signal to actively control the ring laser perimeter. In this section, we described our preliminary efforts to develop a feedback scheme to stabilise the PR-1 laser frequency by locking the laser perimeter to the RF beating between the PR-1 laser and a stabilised helium-neon laser.

6.3.1 Characterising a Stabilised He-Ne Laser Using a Frequency Comb

The reference laser we employed in this work is SIOS Meßtechnik GmBH Stabilised He-Ne Laser, SL-03 Series (SIOS laser). The SIOS laser is stabilised by employing a dual-longitudinal-mode stabilisation scheme which can be operated either with a frequency stabilised or amplitude stabilised mode of operation. The laser was purchased in 2010 and the SIOS factory test certificate dated on 03/11/2010 specified that the nominal frequency of this SIOS laser is 473612547.1 MHz with a maximum frequency drift of ±5 MHz. The stability of the SIOS laser was determined by comparing the frequency against an iodine-cell-stabilised He-Ne laser (China2 J_2-Cell-Stabilised He-Ne Laser). The maximum frequency stability of the SIOS laser is reached after 30 minutes of warm-up time, and in practice, the maximum frequency stability of the SIOS laser is expected to be $\pm 2 \times 10^{-8}$. The technical data of the SIOS laser is depicted in Table 6.3.

Technical Data	
Nominal (vacuum) wavelength	632.9909539 nm
Output power	≥ 0.8 mW
Nominal frequency	473612547.1 MHz
Mode/polarisation	single, linearly polarised, longitudinal mode
Beam diameter (TEM_{00})	0.55 mm
Beam divergence (TEM_{00})	1.5 mrad
Maximum frequency drift	± 5 MHz
Maximum frequency stability	over 1 minute: $\pm 1\times10^{-9}$
	over 1 hour: $\pm 2\times10^{-9}$
	over 24 hour: $\pm 1\times10^{-8}$

Table. 6.3.: SIOS stabilised He-Ne laser, SL 03 Series technical data.

The absolute frequency as well as the frequency stability of the SIOS laser were characterised against a femtosecond (fs) fibre laser frequency comb, FC 1500 Optical Frequency Synthesizer manufactured by Menlo Systems GmbH, Germany. This frequency comb[7] (FC) was utilised in the G-ring laser frequency locking scheme in ref. [18].

To understand the operating principle of a frequency comb, firstly, consider a single pulse generated from a mode-locked laser, circulating in a laser cavity with length, L. This pulse

[7] An FC is generally a train of optical pulses generated from a mode-locked laser; which appears as discrete and regularly spaced sharp and narrow lines in the frequency spectrum [143].

will have a power spectrum that is the Fourier transform of its envelope function, $a(t)$. This envelope is centred at the optical frequency of the pulse's continuous carrier wave with a frequency, ω_c. The frequency width of the spectrum will be inversely proportional to the temporal width of the envelope [143].

For a train of identical pulses which are separated by a fixed time interval, the frequency spectrum can be obtained by a Fourier series expansion that generates a comb of evenly spaced frequencies. The spacing between each comb is inversely proportional to the time between pulses, which is also known as the repetition rate (f_r) of the mode-locked laser, and each pulse with ω_c is the integer (n) repetition of f_r. Therefore, the optical frequency of an individual comb, ν_n is [143],

$$\nu_n = n f_r. \tag{6.11}$$

However, the propagation of a single pulse through a dispersive material (the laser cavity) will introduce a phase shift, ϕ_{ce} between the peak of the pulse envelope and the nearest peak of the carrier wave. There will be a phase increment of $\Delta\phi_{ce}$ between pulses at a time separation of $T = \frac{1}{f_r}$. The pulse-to-pulse phase change for the train of pulses occurs because the phase (v_p) and group (v_g) velocities inside the cavity are different, where $\Delta\phi_{ce} = (\frac{1}{v_g} - \frac{1}{v_p})L\omega_c$. In the frequency domain, this shift is determined by $(1/2\pi)\Delta\phi_{ce}/T$ [143].

As a result, the envelope function will be denoted as $a(t) = a(t-T)$, and the electric field of the envelope function is written, in terms of a Fourier series as [143],

$$E(t) = a(t)e^{-i\omega_c t} = \sum_n a_n e^{-i(\omega_c + n\omega_r)t}, \tag{6.12}$$

where a_n are Fourier component of $a(t)$. This equation represents a comb of laser frequencies with spacing $\omega_r = 2\pi f_r$ that is shifted as a whole from the harmonics of ω_r. Now, since ω_c is not necessarily the integer repetition of f_r, we can re-number every shifted comb line by [143],

$$\nu_n = n f_r + f_o, \tag{6.13}$$

where n is the index of the comb lines and f_o is the carrier envelope offset frequency due to the pulse-to-pulse phase shift where [143],

$$f_o = (1/2\pi) f_r \Delta\phi_{ce}. \tag{6.14}$$

The laser repetition rate, f_r can be detected by using a fast photodiode. By contrast, the measurement of the carrier envelope offset frequency, f_o is determined by 'self-referencing' approach. In an octave-spanning optical spectrum, a single comb line, with

index n can be frequency doubled (typically through a second harmonic crystal). This frequency doubled comb line will have approximately the same frequency as the comb line on the high-frequency side of the spectrum with an index of $2n$. The beat frequency resulted from heterodyning these two comb lines will yield the offset frequency, f_o, where [143],

$$f_o = 2\nu_n - \nu_{2n} = 2(nf_r + f_o) - (2nf_r + f_o). \tag{6.15}$$

The absolute frequency of a continuous wave (cw) laser can be determined if the optical frequency of the laser lies close to a comb line with an index n in the low-frequency portion of the frequency comb spectrum. At the same time, the second harmonic of the laser will also lie close to the comb line with an index of $2n$.

When a cw laser with an optical frequency of ν_{cw} is heterodyned with a comb line with an index n, a beat frequency, f_{beat1} is generated,

$$f_{beat1} = \nu_{cw} - (nf_r + f_o). \tag{6.16}$$

Similarly, by heterodyning the second harmonic of the cw laser optical frequency, ν_{cw} with the comb line with an index at $2n$ will generate a beat frequency, f_{beat2},

$$f_{beat2} = 2\nu_{cw} - (2nf_r + f_o). \tag{6.17}$$

Experimental Details

Figure 6.12 is the photo of the experimental setup of the characterisation of the SIOS laser against the Menlo FC 1500. On the left-hand side of the figure is the opto-mechanical setup of the Menlo FC 1500 along with the mounted SIOS laser. The optomechanical setup of the FC 1500 consists of an fs fibre laser (M-Comb), an amplifier for the generation of the carrier envelope offset beat (P250-XPS-WG-PM EDFA), an amplifier (P250) for the HMP port 633 nm that provides an output radiation of around 1266 nm for the second harmonic generation and broadening of the spectrum in the visible range (SHG 633 Frequency Doubling Module), and a fully fibre-coupled beat detection unit (BDU-FF).

On the right-hand side of Figure 6.12 is a photo of the electronic rack for operating the Menlo FC 1500. The electronic setup of the Menlo FC 1500 is basically divided into three main categories: the control electronics, the locking electronics and the monitoring system. The control electronics comprise an amplifier control unit (AC-1550) that controls the current and the temperature of several laser diodes; an fs laser pump power controller unit (TC-1550) and a direct digital synthesizer (DDS120 synthesizer). Meanwhile, the lock-

ing electronics include an electronic unit to lock the repetition rate, f_r (SYNCRO-RRE), and another electronic locking unit for the carrier envelope offset beat, f_o (SYNCRO-CEO). Finally, the signal monitoring system consists of 2 RF spectrum analysers (Hameg, HM5510, 1 GHz), an oscilloscope (Agilent Technologies DSO-X-2004A, 70 MHz) and a computer to control the electronic systems and for data acquisition. All generators and counters were referenced to a hydrogen maser (10 MHz, EFOS 18). Note that the HeNe 633 nm transfer laser and SYNCRO-LLE were not utilised in this experiment.

The schematic diagram of the experimental setup is shown in Figure 6.13. The M-Comb module consists of an Erbium-doped fibre (EDF) ring resonator that generates mode-locked pulses; with a semiconductor laser as the pumping mechanism. A light pulse that propagates in the fibre ring is amplified by the Erbium-doped fibre and the semiconductor laser supplies the energy required for amplification. The laser pump power is controlled from the TC-1550 controller unit which contains a laser diode controller along with an automated micro-controller [144].

The mode-locked pulses generated by the fs laser are equally spaced by f_r and this f_r signal is detected by an internal fast diode (InGaAs photodetector). The f_r signal detected by the fast photodiode is high-pass filtered at 1000 MHz to suppress lower harmonic signals. Then, this high-pass-filtered f_r signal is mixed with a 980 MHz RF reference from a DRO (a very clean fixed frequency generator), yielding a 20 MHz intermediate frequency; which is counted by a counter (FXM50 counter). This intermediate frequency is then fed into the SYNCRO-RRE unit [144].

The SYNCRO-RRE unit consists of a phase detector, a PID circuit and a high voltage (HV) amplifier (HVA150). The intermediate frequency signal is mixed down to 20 MHz by the frequency synthesizer (DDS120) to convert the signal into a DC signal. After that, the generated DC signal is sent to a PID circuit to lock the laser cavity through an intra-cavity piezo. As a result, the repetition rate is 'locked' [144].

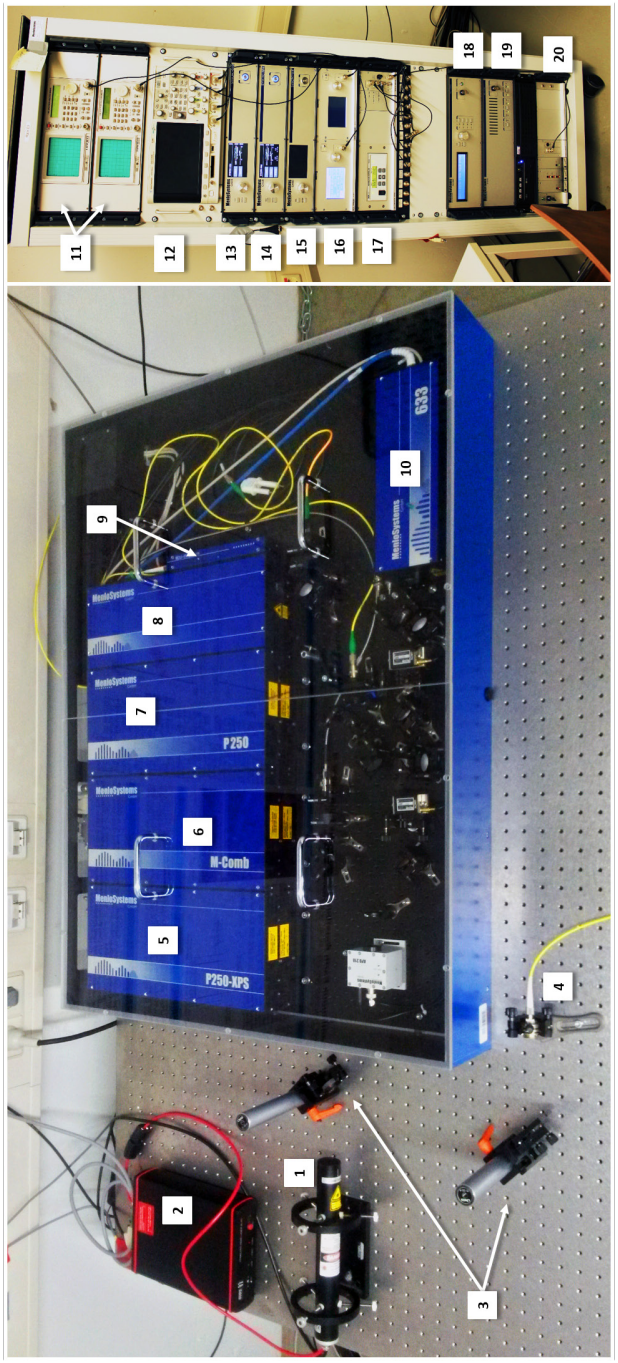

Figure. 6.12.: Photo of the experimental setup to measure the absolute frequency of SIOS laser. Left: SIOS laser with the opto-mechanical setup of FC 1500 Frequency Synthesizer. Right: the electronics system of FC1500 Frequency Synthesizer. 1. SIOS laser; 2. SIOS laser power supply; 3. dielectric mirrors; 4. laser beam coupler (Schäfter+Kirchhoff 60SMS-1-0-A11-02) and a single mode fibre; 5. Amplifiers and Offset frequency generation (P250-XPS-WG-PM EDFA); 6. Femtosecond fibre laser (M-Comb); 7. P250-PM EDFA for HMP port 633 nm (HMP: High Power Measurement Port 633 nm); 8. SHG 633 Frequency Doubling Module; 9. Fully fibre Beat detection unit (BDU-FF); 10. He-Ne 633 nm transfer laser (unused); 11. Hameg 1 GHz spectrum analyser (HM5510); 12. digital oscilloscope (Agilent Technologies DSO-X-2004A 70 MHz); 13. SYNCRO-CEO; 14. SYNCRO-RRE; 15. SYNCRO-LLE (not used); 16. DDS120 Synthesizer; 17. Thorlabs TC200 Temperature Controller; 18. AC-1550 unit; 19. TC-1550 unit; 20. high voltage amplifier and power supply.

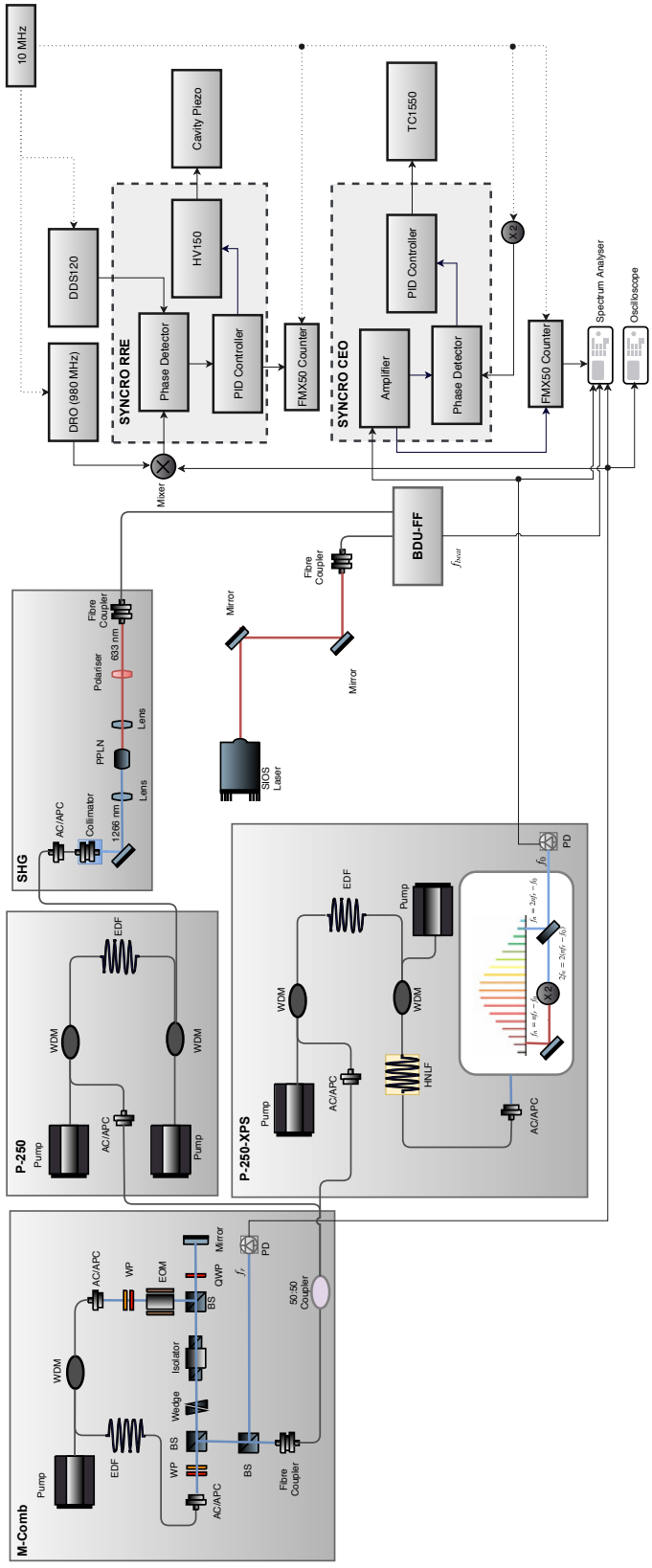

Figure. 6.13.: Schematic diagram of the experimental setup to characterise the frequency stability and to measure absolute frequency of the SIOS laser. EDF: Erbium doped fibre; WDM: wavelength division multiplexer; WP: wave plates; QWP: quater wave plates; BS: beam splitter; AC/APC: fibre optic connector; EOM: electro optic modulator; PD: photodiode; HNLF: highly nonlinear fibre; PPLN: periodically-poled Lithium Niobate.

The repetition rate, f_r is calculated from the FXM50 counter value ($f_{counter}$ = intermediate frequency) by using the equation [144],

$$f_r = \frac{f_{counter}}{4} + 245 \text{ MHz}. \tag{6.18}$$

The P250 XPS-WG-PM EDFA unit generated the carrier envelope offset frequency, f_o. This unit consists of a high power Erbium-fibre laser amplifier (EDFA) and a highly nonlinear fibre (HNLF). The AC-1550 control unit controlled the laser pump in the EDFA setup. The fs laser output signal was connected to the EDFA through the wavelength division multiplier (WDM) to generate a spectral broadening of the 1.56 μm input spectrum. This spectrum is tunable between 1 μm to 2.1 μm through the nonlinear effect generated by the HNLF. The amplified pulses and broadened spectrum were divided into two portions: a short wavelength portion (approximately 1050 nm) and a long wavelength portion (approximately 2100 nm). The short wavelength portion was frequency doubled by the second harmonic effect [144].

By comparing the non-frequency doubled wavelength portion to the frequency doubled wavelength portion, a beat note is generated and this beat note is also known as the carrier envelope offset frequency, f_o. This offset frequency is detected by a fast photodetector (FPD510-INT) and monitored via the RF spectrum analyser. At the same time, the f_o is counted by the FXM50 counter. Note that the signal-to-noise ratio (SNR) of the f_o should be at least 32 dB to ensure accurate measurements with the frequency counter [144].

The f_o signal is stabilised by tuning it to 20 MHz by using the DDS120. This tuned f_o is then sent to the SYNCRO-CEO unit; to be counted and fed into a phase detector. It is then referenced to a 20 MHz signal generated by the hydrogen maser and through frequency doubling. The phase detector output is fed into a PID circuit to lock the f_o by sending a feedback signal to the fs laser pump power controller (TC-1550).

Another output of the femtosecond laser is fed into P250-PM EDFA unit. The laser output was amplified by a second EDFA setup, and the amplified signal was adjusted to 1266 nm by controlling the fibre amplifier pump power through the AC-1550 controller unit. Increasing pump power will shift the output to a shorter wavelength. This amplified FC signal at 1266 nm is then converted to a second harmonic at 633 nm in the SHG 633 Frequency Doubling Module by using two aspheric focusing lenses and a periodically-poled Lithium Niobate crystal (PPLN). The FC signal output at 633 nm is then fed into a single mode fibre to be connected to the Beat Detection Unit (BDU-FF).

The SIOS laser was mounted on an optical table, and the output power was measured to be 0.5 mW. The laser beam was coupled into a single mode fibre with the aid of two

dielectric mirrors and Schäfter+Kirchhoff laser beam coupler (60SMS-1-0-A11-02). The laser output from the fibre was optimised and measured to be 100 μW (20% efficiency). The fibre was then fed in the BDU unit. This BDU unit will combine the SIOS laser with the amplified 633 nm FC signal and the beat signal can be observed on the RF spectrum analyser. The polarisation of the FC laser was optimised by adjusting the half and quarter wave plates.

In order to determine the absolute frequency of the SIOS laser, Equation 6.3.1 is re-written as follows,

$$f_{SIOS} = n \cdot f_r \pm f_o \pm f_{beat}, \tag{6.19}$$

where f_{SIOS} is the SIOS laser frequency, f_r is the repetition rate of the frequency comb, f_o is the carrier envelope frequency offset, and f_{beat} is the measured beat note between the SIOS laser and the nearest adjacent comb mode with the mode number, n. Since we measured the beat frequency after the SHG 633, Equation 6.19 is modified to multiply the f_o by a factor of two:

$$f_{SIOS} = n \cdot f_r \pm 2f_o \pm f_{beat}. \tag{6.20}$$

Note that, f_r remains unchanged because the dominant process in the SHG process is the sum frequency generation. For instance, let us consider two adjacent comb modes with mode numbers of n and $n+1$. The frequencies of these two modes will be [144],

$$f_n = n \cdot f_r + f_o, \tag{6.21}$$

and

$$f_{n+1} = (n+1) \cdot f_r + f_o, \tag{6.22}$$

respectively. The double frequencies of these modes are,

$$2f_n = 2n \cdot f_r + 2f_o, \tag{6.23}$$

and

$$2f_{n+1} = 2(n+1) \cdot f_r + f_o = 2n \cdot 2f_r + 2f_o, \tag{6.24}$$

correspondingly. Then, the frequency difference between these two modes after the frequency doubling is,

$$2f_{n+1} - 2f_n = 2f_r, \tag{6.25}$$

which is equal to two times the repetition rate. The value of n can be calculated if the cw laser frequency is known with an accuracy to within a few MHz, where,

$$n = \frac{c}{\lambda \cdot f_r}. \tag{6.26}$$

The signs in Equation 6.20 depend on the actual measurement conditions and can be determined by changing f_o and f_r while monitoring the changes in f_{beat}. As we increase the f_r, the mode spacing of the frequency comb will increase as well. On the other hand, the comb modes remain constant when f_o is changed, but all of the comb modes will move in a frequency space depending on the sign of f_o [145].

After we detected the f_{beat} on the RF spectrum analyser, f_r was varied slightly by using the output voltage at the SYNCRO-RRE to determine whether the beat is falling in case A or case B where [144]:

- Case A: If the f_{beat} is decreasing when the f_r is increased, then, the sign of the f_{beat} is **positive**.

- Case B: If the f_{beat} is increasing when the f_r is increased, then, the sign of the f_{beat} is **negative**.

After determining which case the detected f_{beat} fell into, the correct sign of f_o was determined by, firstly, lock the f_r. Then, the value of f_o was either increased or decreased, followed by observing the changes in f_{beat}. For case A, if f_{beat} decreases when f_o is increased, then the sign of f_o is positive. But, if f_{beat} increases when f_o was increased, then the sign of f_o is negative. The reverse is true in case B [144].

Parameters	Mean (Hz)	Standard Deviation (Hz)
f_r	248657788.76	0.054061687
f_o	- 20000000.00	0.597165662
f_{beat}	+ 56110071.37	3583268.744

Table. 6.4.: Measurement taken to determine absolute frequency of SIOS laser. By using the nominal SIOS frequency as denoted in Table 6.3, n = 1904676.

From Equation 6.26, the value of n is calculated to be 1904676. Therefore, by using the relevant value as tabulated in Table 6.4 in Equation 6.19, the absolute optical frequency of the SIOS laser is f_{SIOS} = (473612539 ± 9) MHz.

We repeated the measurement by assuming the number of n is unknown. For the second measurement, the measurement of f_{beat} will include an uncertainty Δ, and Equation 6.19 is changed into,

$$f_{SIOS} = n \cdot f_r \pm f_o \pm f_{beat} + \Delta. \tag{6.27}$$

Two different measurements at two different values of f_r were performed. By defining n_1, n_2, and f_{r1}, f_{r2} as the mode numbers and the repetition rate of the two measurements respectively [144], we can write,

$$n_1 f_{r1} + f_{o1} + f_{beat1} + \Delta_1 = n_2 f_{r2} + f_{o2} + f_{beat2} + \Delta_2. \tag{6.28}$$

If we defined m as,

$$m = n_1 - n_2, \tag{6.29}$$

one can solve for n_1 by,

$$n_1 = \frac{m \cdot f_{r2} + f_{o2} + f_{beat2} - f_{o1} - f_{beat1}}{f_{r1} - f_{r2}} \pm \frac{\sqrt{\Delta_1^2 + \Delta_2^2}}{f_{r1} - f_{r2}}. \tag{6.30}$$

Note that, if we measure two repetition rates with a relatively large difference, the second term from the Equation 6.30 becomes negligible. Equation 6.28 can be re-written as,

$$n_1 = \frac{n_2 f_{r2}}{f_{r1}} + \frac{f_{o2} + f_{beat2} - f_{o1} - f_{beat1}}{f_{r1}}. \tag{6.31}$$

Parameters	Measurement 1 (Hz)	Measurement 2 (Hz)
f_r	248657789.75	251037003.50
f_o	- 40000000.00	40000000.00
f_{beat}	+ 62400000.00 Hz	+ 55800000.00
Δ	3500000.00 Hz	3500000.00

Table. 6.5.: Measurement taken to determine the absolute frequency of the SIOS laser.

From the measurement as depicted in Table 6.5, n_1 = 1904676, n_2 = 1886624, the absolute frequency SIOS laser is determined to be 473612547 MHz with an uncertainty of ± 5 MHz.

Figure 6.14 shows the time series of the beat frequency between the frequency comb and the SIOS laser. The SIOS laser can resolve stability up to $\pm 2 \times 10^{-9}$ at 1 hour of integration time as shown in the Allan deviation plot in Figure 6.15. This implies that the stability of the SIOS laser is sufficient to serve as a stable reference laser for stabilising the PR-1 optical frequency.

6.3.2 Heterodyning a Stabilised He-Ne Laser with the PR-1 Ring Laser

The aim of this section is to investigate the frequency difference between the SIOS laser and the PR-1 laser. Before proceeding with the experimental work, firstly, we estimated the beat frequency between the SIOS laser and the PR-1 laser so that it will be convenient to locate the beat signal on the monitoring device.

Three deductions were performed based on the ^{20}Ne line [146], UG-1 optical frequency measurement with ^{22}Ne at a total gas pressure of 8 mbar and UG-1 optical frequency measurement with natural neon at a total pressure of 10 mbar as references:

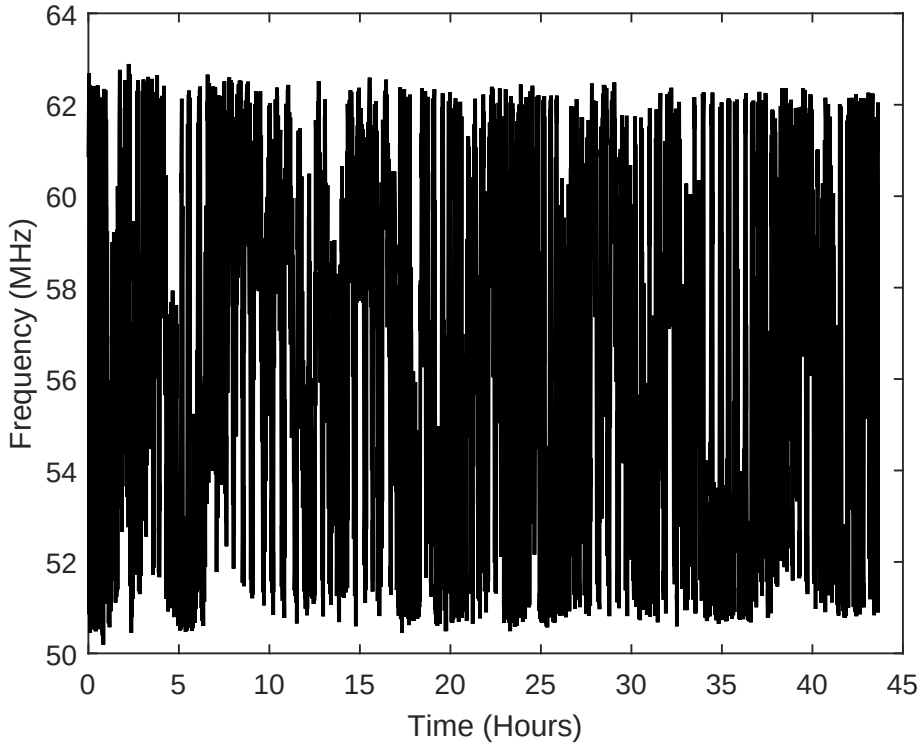

Figure. 6.14.: Time series of the f_{beat} between the SIOS laser and Menlo FC 1500 for more than 40 hours.

- **Deduction 1**: The frequency of the ^{20}Ne line corresponding to 'j' line in the iodine spectrum is 473612194 MHz with gas pressure estimation of 3 torr (approximately 4 mbar) [146]. Therefore, if PR-1 is running with natural neon at 12 mbar of total gas pressure, the optical frequency can be estimated by adding 87.5 MHz (10% of ^{22}Ne) and a pressure shift of 120 MHz. As a result, the estimated PR-1 optical frequency is 473612404 MHz.

- **Deduction 2**: UG-1 measurement with ^{22}Ne gas fill: The optical frequency of UG-1 is coincided with the 'h' line = 4736123137 MHz with 8 mbar of ^{22}Ne gas pressure. Hence, the optical frequency PR-1 ring laser with a total gas pressure of 12 mbar, we subtracted 805.5 MHz for the 90% isotope shift introduced by the ^{20}Ne isotope; and minus another 60 MHz for the pressure shift, PR-1 optical frequency is 473612392 MHz.

- **Deduction 3**: The optical frequency of the UG-1 ring laser relative to 'g' line with natural neon gas fill at 10 mbar is 473612300 MHz. Thus, the PR-1 laser frequency with 12 mbar of natural neon is estimated by subtracting 30 MHz (pressure shift) which resulted in an optical frequency of 473612330 MHz.

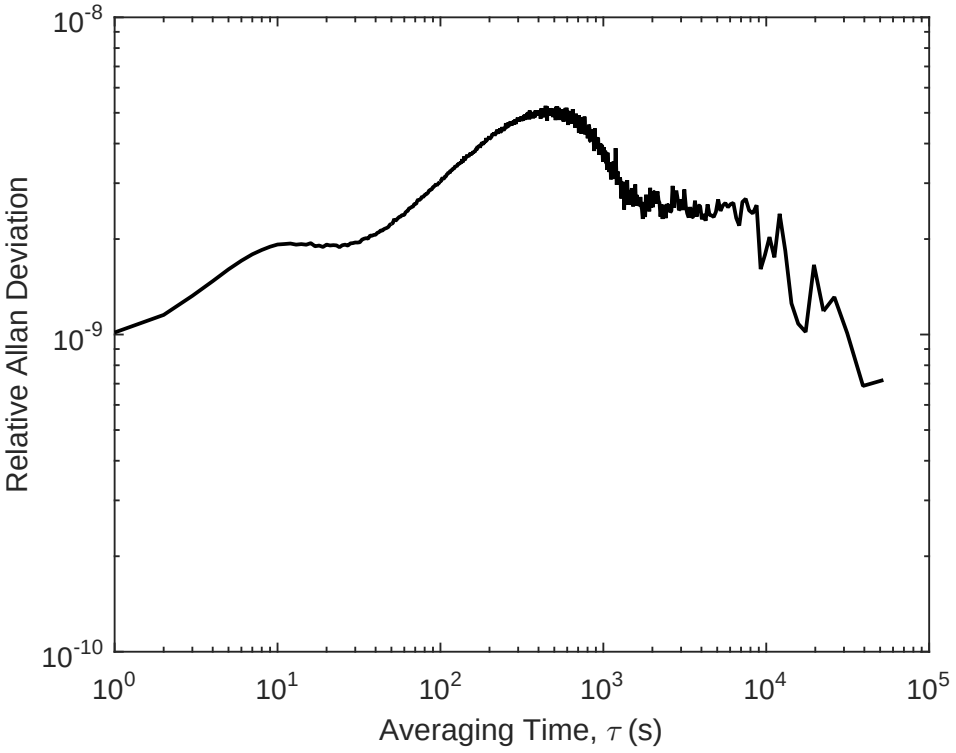

Figure. 6.15.: Stability of the f_{beat} between the SIOS laser and Menlo FC 1500.

Total Pressure	Natural Neon (MHz)			50:50 Neon (MHz)		
(mbar)	Deduction 1	Deduction 2	Deduction 3	Deduction 1	Deduction 2	Deduction 3
6	473612314	473612302	473612240	473612672	473612660	473612688
8	473612344	4736122350	473612270	473612702	473612690	473612718
10	473612374	473612362	473612300	473612732	473612720	473612748
12	473612404	473612392	473612330	473612762	473612750	473612779

Table. 6.6.: Estimation of PR-1 optical frequency.

Table 6.6 lists the estimated optical frequency for PR-1 at various gas mixtures while Table 6.7 tabulates the predicted frequency difference between PR-1 and SIOS laser. The negative sign in Table 6.7 indicates that the PR-1 optical frequency is higher than the SIOS laser optical frequency. From the table, the beat frequency we anticipated lies between 100 to 300 MHz.

Total Pressure	Natural Neon (MHz)			50:50 Neon (MHz)		
(mbar)	Deduction 1	Deduction 2	Deduction 3	Deduction 1	Deduction 2	Deduction 3
6	233	245	307	-125	-113	-142
8	203	215	277	-155	-143	-172
10	173	185	247	-185	-173	-202
12	143	155	217	-215	-203	-232

Table. 6.7.: Predicted beat frequency between the PR-1 laser and the SIOS laser (f_{SIOS} = 473612547 MHz).

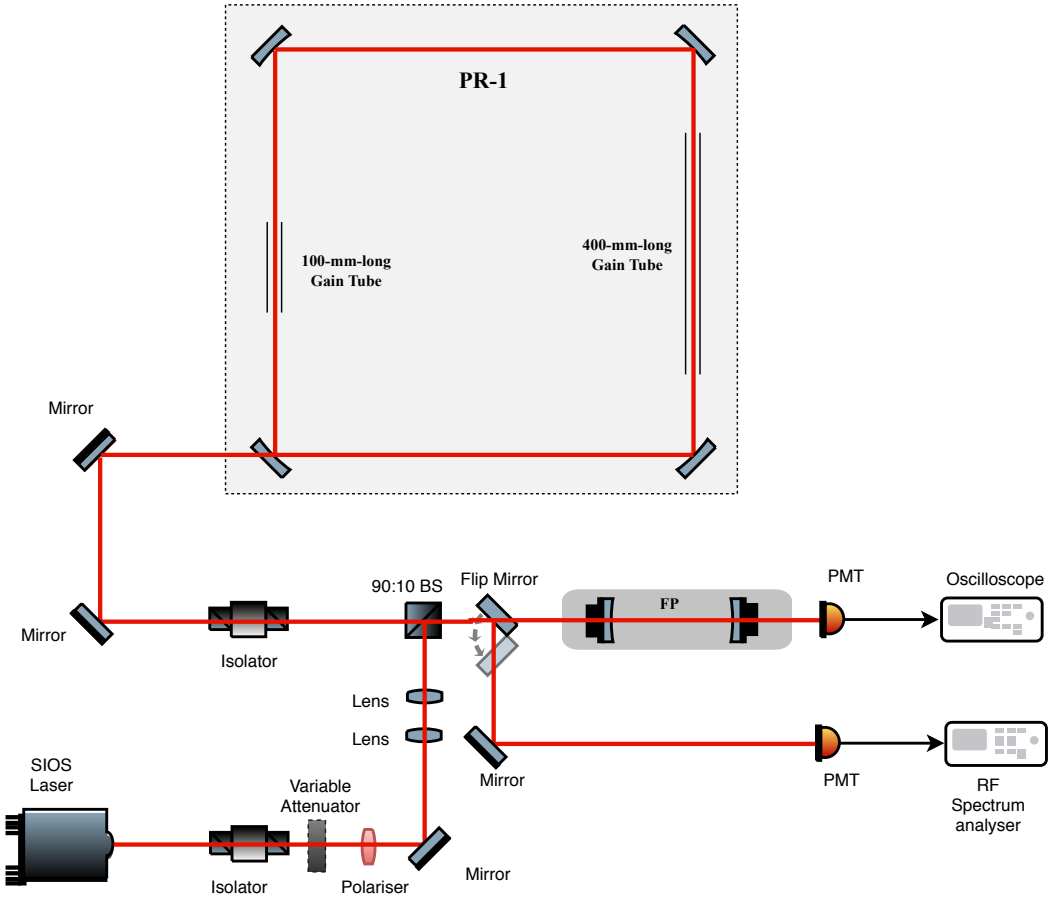

Figure. 6.16.: Experimental setup to measure the beat frequency from heterodyning the SIOS laser with the PR-1 laser. BS: beam splitter; PMT: Hamamatsu photomultiplier tube.

Experimental Details

Figure 6.16 shows the experimental setup measure the beat frequency between the SIOS laser and the PR-1 laser. The clock-wise (CW) laser beam and the SIOS laser were directed through Faraday rotation isolators. Optical isolation of the lasers was necessary because the light reflected from various surfaces of the optical setup caused the laser frequency to jitter.

The amplitude of the beat signal depends on the mode matching alignment and relative polarisation of the two laser beams [147]. The SIOS laser beam diameter (from the specification) is 0.55 mm with 1.5 mrad of divergence, where as the PR-1 laser beam spot size at the beam splitter (at a distance of 1.5 m away from the location of the CW beam exited through the PR-1 corner box) is 3.7 mm in-plane and 3.6 mm out-of-plane. Thus, two convex lenses with focal lengths of f_1 = 35 mm and f_2 = 21 mm were inserted to match the SIOS laser beam diameter to the PR-1 laser beam. Also, a polariser was placed

in front of the SIOS laser to ensure the polarisation of the SIOS laser beam propagated in the same direction as the PR-1 laser beam.

If we denoted A_1 and A_2 from Equation 6.10 as the electric field amplitudes of the SIOS laser beam and the PR-1's CW beam respectively, the third term from the equation will be the alternating component (AC current) consists the frequency difference between the SIOS laser and the PR-1's CW beam. This alternating current, $i_{peak\ ac}$ is represented as [81], [142],

$$i_{peak\ ac} = \left[\frac{2A_1A_2}{A_1^2 + A_2^2}\right] i_{dc}. \tag{6.32}$$

If the amplitude of the SIOS laser is much higher than PR-1 laser, where $A_1 \gg A_2$,

$$i_{ac}^2 = 2\left(\frac{A_2}{A_1}\right)^2 i_{dc}^2 = 2\left(\frac{P_2}{P_1}\right) i_{dc}^2, \tag{6.33}$$

where P_1 and P_2 are the laser powers correspond to A_1 and A_2.

The first two terms of Equation 6.10 represent the zero frequency component, i.e. the DC current, i_{dc} of the resulted i_p. Since $A_1 \gg A_2$, i_{dc} is [81], [142],

$$i_{dc} = e\eta_{qe}\frac{P_1}{h\nu}, \tag{6.34}$$

where, η_{qe} is the detector quantum efficiency and e is the electric charge. This DC current exhibits shot noise[8], i_N,

$$i_N = 2ei_{dc}B = 2e(e\eta_{qe}\frac{P_1}{h\nu})B, \tag{6.35}$$

where B is the bandwidth of the detector. By making P_1 sufficiently high, the shot noise dominates and the signal to noise ratio of the detection system is thus limited by [81], [142],

$$\begin{aligned}\frac{S}{N} = \frac{i_{ac}^2}{i_N^2} &= \frac{2\left(\frac{P_2}{P_1}\right) i_{dc}^2}{2e(e\eta_{qe}\frac{P_1}{h\nu})B} \\ &= \frac{2\left(\frac{P_2}{P_1}\right)(e\eta_{qe}\frac{P_1}{h\nu})^2}{2e(e\eta_{qe}\frac{P_1}{h\nu})B} \\ &= \frac{P_2\eta_{qe}}{h\nu B}.\end{aligned} \tag{6.36}$$

From Equation 6.32, increasing the SIOS laser power should improve the intensity of the detected beat signal as the PR-1 laser output is relatively low. However, a further increase in the SIOS laser power would not increase the signal-to-noise ratio because the power of the beat signal and the shot noise power spectral density are equally increased. Hence,

[8] Arises from the probabilistic nature of the generation of the electrical charge within the detector [81]. The detector emits electrical charges at an average rate proportional to the DC current. As each emission is statistically independent, shot noise is generated in the current.

the PR-1 CW beam was superimposed with the SIOS laser by using a 90:10 beam splitter so that most of the PR-1 laser output power is detected by the detector (Hamamatsu photomultiplier tube (PMT)). The resulting high loss of the SIOS laser power received by the PMT can be compensated by increasing the SIOS laser power. For this reason, it was essential to place a variable attenuator in front of the SIOS laser to vary the optical powers of the SIOS laser. The combined beam was directed to an FP to observed the laser mode structures on the oscilloscope. A flip mirror was placed in front of the FP so that the signal can be directed to the PMT to monitor the beat signal on an RF spectrum analyser.

At a total gas pressure of 12 mbar (0.2 mbar of natural neon), the highest power for the PR-1 laser to operate with single mode operation was 122 nW (power measured after the isolator). The SIOS laser power output was varied to obtain the optimum signal to noise ratio of the beat signal. As can be seen from Figure 6.17, the peak of the SIOS laser spectrum is approximately 214 MHz away from the peak of the PR-1 laser spectrum. The detected beat signal was 213.4 MHz as depicted in Figure 6.18. As seen from the figure, the power of the detected beat signal was approximately -70 dBm (0.1 nW). The beat frequency excursion was between 20 to 30 MHz. Despite our best attempt, we could not obtain a stronger beat signal.

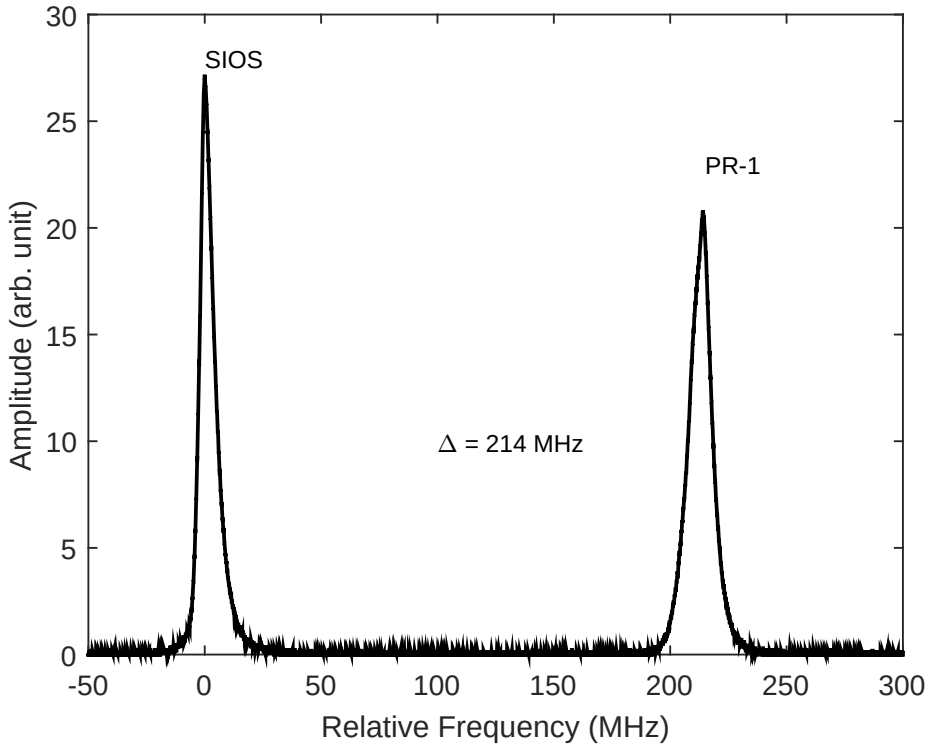

Figure. 6.17.: The mode spectrum of the SIOS laser and the PR-1 laser. The frequency difference between the two laser peaks was approximately 214 MHz.

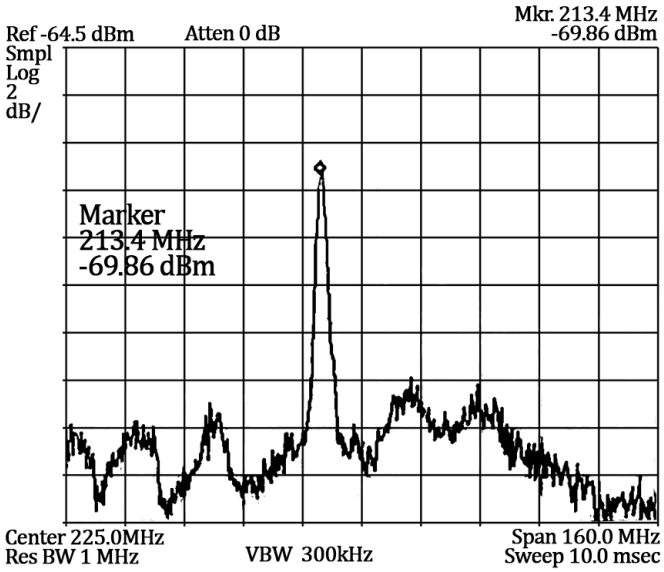

Figure. 6.18.: Snapshot of the spectrum of the beat signal between the PR-1 laser and the SIOS laser as seen on the RF spectrum analyser. The PR-1 laser cavity was filled with 12 mbar of total gas pressure.

Our strategy for tracking the beat signal for the frequency feedback system was by using a frequency tracker (Wettzell Tracker), developed by Manuel Popp (Leibniz University of Hanover). This tracker unit consists of a pre-amplifier circuit that provides input signal amplification within a frequency range of 10 to 240 MHz. There are 4 mini circuit gain blocks with two filters which form the gain pass filter for this frequency range. For the tracking unit, the input signal (beat signal) is down-mixed by a voltage controlled oscillator (VCO). This VCO is phase-locked with a 20 MHz quartz reference. It can be tuned via a frequency divider with a voltage controller. An electronic circuit (phase locked loop (PLL)) locks the output frequency of the VCO with a desired input frequency by comparing the phase of the input frequency (via a phase detector) to the output frequency of the VCO simultaneously. Hence, the output frequency of the VCO is continuously adjusted until it matches the input frequency.

The Wettzell Tracker detects a minimum signal of -25 dBm and the VCO frequency range is between 75 to 145 MHz. Our on-going efforts include the modification of the frequency range of the tracker unit and improving the bandwidth along with the gain of the pre-amplifier circuit. Note that the frequency difference between SIOS and PR-1 (between 100 to 300 MHz) is rather close to the frequency of the carrier frequency of RF transmitter (80 MHz). Ideally, in order to utilise the frequency difference between the SIOS laser and the PR-1 laser as a feedback signal, the transmitter has to be at a frequency far away from 80 MHz. This is to prevent the feedback control locking on to the carrier frequency of the RF transmitter instead of to the detected beat signal (the signal to noise ratio of the RF transmitter carrier frequency is very high in comparison to the detected beat signal between the two lasers).

Unfortunately, due to time constraints, the author was unable to continue the experiment. The continuation of this work is therefore carried on by another PhD student.

6.4 Discussion and Conclusion

Controlling the PR-1 perimeter against the temperature variations via a servo-controlled system has improved the laser stability tremendously. The PR-1 rotational signal is free from mode hopping and mode splitting and allowing for longer data acquisition. The beauty of the self-referenced feedback system is it can be implemented without an external reference cavity. Therefore, for a frequency up-scaled ring laser, i.e. performing gyroscopic activities with an operating wavelength of 611.8 nm or 543.4 nm, the same feedback system can be implemented easily by running the laser on a phase-locked operation, and using the beat signal arising from the adjacent stable longitudinal modes as a feedback signal.

There are still a few improvements that should be done to enhance the self-referenced perimeter stabilising scheme. For example, it is notable that the non-linear response of the two piezo actuators introduced slow modulations on the detected Sagnac frequency data series over time (see Figure 6.9 and 6.11). Other than that, the PR-1 cavity was locked to the ν_{fsr} beat frequency for a short time (2 hours) due to the limitation from the piezo actuators travel range. Future work is planned to eliminate or minimise the effect introduced by the non-linear response of the PZT stages and to modify the current frequency servo unit. Furthermore, to improve the optical frequency stability of the PR-1 laser, passive stabilisation methods can be used. The laser can be mounted on a more stable concrete base and relocated to a controlled environment such as a temperature-and-pressure-stabilised laboratory.

The self-referenced stabilisation is less sensitive than the stabilisation scheme based on the optical beat frequency, as the latter scheme works depending on the optical frequency difference. Due to the high-Q of our ring laser, the laser output power while running on single-mode operation is low. This introduces a challenge in obtaining a strong beat signal between the stabilised helium-neon laser (the SIOS laser) and the PR-1 laser[9]. As an alternative measure, we note that the frequency difference between the PR-1 laser and the SIOS laser can be measured by measuring the peak-to-peak distance between these two laser spectra as scanned by the FP interferometer. Then, a LabVIEW program can be implemented to detect the position of the laser peaks and providing a feedback signal to a servo control unit for stabilising the PR-1 laser perimeter [47], [58], [148].

[9] Although the strongest beat signal obtained in this experiment was -70 dBm, this signal still can be amplified significantly using a series of amplifier circuits.

In conclusion, we have developed a simple frequency stabilisation feedback system for a 2.56 m^2 ring laser gyroscope by utilising the beat frequency between adjacent longitudinal laser modes. By implementing the self-referenced frequency stabilising scheme, the PR-1 laser achieved a stability of $4.8 \times 10^{-5} \Omega_E$. We also demonstrated the first actively-stabilised ring laser gyroscope with an operating wavelength at 611.8 nm; where the laser exhibited a frequency stability of 1.8×10^{-4} relative to the Earth rotation.

7 Concluding Remarks and Future Research

Ring lasers remain the only measurement device with direct reference to the Earth rotation axis. As such, they are viable as a complementary tools to the VLBI technique for the precise monitoring of Earth rotation. Precise Length of Day (LoD) measurements by ring lasers can provide corrections for biases (due to data latency) which potentially exist in VLBI measurements [6]. This would be a significant contribution towards the maintenance of the geodetic reference frames. The resolution required for such an application is 10^{-9} with respect to the Earth's rotation rate, along with a similar stability over several months [13]. Currently, the G ring laser achieves a laser sensitivity of 3×10^{-9} relative to Earth rotation over an hour of integration time; which means ring lasers are very close to achieving precise monitoring of LoD variations [18].

With the prospective of achieving comparable LoD measurements to a VLBI network, there is a growing interest in the measurement of absolute Earth rotation via ring laser interferometers [149]. Measuring the absolute rotation rate of the Earth will open the possibility to detection of general relativistic precessions such as the Lense-Thirring effect (appears as an offset between Earth rotation measured by terrestrial interferometry and the VLBI system). The key to achieving absolute Earth rotation measurement via ring lasers would be by means of rigorous removal of systematic errors as the magnitude of the Lense-Thirring effect is approximately 10 orders of magnitude smaller than the Earth's rotation rate [150].

Since the first demonstration of Earth rotation sensing by the Canterbury-I (C-I) ring laser, we have continued on a steady path of increasing the sensor resolution by up-scaling the laser geometrically. However, as we have seen from experience with Ultra Gross Ring-2 (UG-2), the gyroscopic performance of an ever-larger gyroscope is eventually detrimentally affected by the geometric instabilities arising from the compulsory heterolithic cavity design [15]. Hereupon, a trade-off between enhancing the resolution and stability of the interferometers becomes crucial. Today, the development of large ring laser technology has matured to a point where tiny geophysical signals such as the Chandler and annual wobbles of the rotating Earth are now routinely measurable [6]. The major factors that enable ring lasers to operate at this level of performance; other than increasing the resolution of the interferometer; are through improvement in cavity

stabilisation and elimination of perturbations (e.g. backscattering errors) that limit the laser performance [18], [60], [151].

In this thesis, we aim to contribute towards the development of laser gyroscopes but from an entirely new perspective. We have investigated the performance of ring lasers operating on different wavelengths because in addition to its dimension, the scale factor of the gyroscope depends on the laser wavelength.

To this end, firstly, we revisited the seminal experiment by Macek and Davis by operating the PR-1 ring laser on the $2s_2 \rightarrow 2p_4$ neon transition at 1152.3 nm. Following that, we have utilised a novel approach to increase the scale factor of ring laser gyroscopes by operating PR-1 at wavelengths shorter than 632.8 nm ($3s_2 \rightarrow 2p_4$): 543.4 nm ($3s_2 \rightarrow 2p_{10}$) and 611.8 nm ($3s_2 \rightarrow 2p_6$). Table 7.1 summarises relevant PR-1's gyroscopic characteristics while it was operated at different laser wavelengths. Note that the tabulated parameters are corresponding to the laser rotation sensing performance while running in the single-mode operating regime. The gyroscopic performance of our 2.56 m^2 test cavity at 632.8 nm served as a reference for comparison with its performance at other neon transitions.

Operating Wavelength, λ (nm)	543.4	611.8	632.8	1152.3
Optical frequency, ν_0 (THz)	552	490	474	260
Detected Sagnac frequency, δf_s (Hz)	132.8	117.2	113.0	60.2
Ring-down time, τ_{decay} (μs)	112	40	120	33
Quality factor, Q	3.9×10^{11}	1.2×10^{11}	3.6×10^{11}	5.4×10^{10}
Total loss, L (ppm)	190.5	533	177.8	646.5
Finesse, F	3.3×10^4	1.2×10^4	3.5×10^4	9.7×10^3
Neon partial pressure, p_{ne} (mbar)	0.2	0.2	0.2	0.2
Total pressure, p (mbar)	0.8	3.5	10	6
Gain tube diameter, d (mm)	3	4	4	4
Gain tube length, ℓ (mm)	400	580	100	100
Beam spot diameter, D (mm)	2.5	2.7	2.7	3.7
Laser power, P_i (nW)	6	1000	75	4
Resolution, Ω_s (rad/s/$\sqrt{\text{Hz}}$)	8.4×10^{-10}	2.7×10^{-10}	2.4×10^{-10}	1.6×10^{-8}
Lock-in threshold, f_L (μHz)	1.2	0.94	0.42	0.94
Relative Allan deviation, Ω/Ω_E	2.6×10^{-4}	1.6×10^{-4}	9×10^{-5}	1×10^{-4}

Table. 7.1.: Comparison of PR-1's gyroscopic characteristics (single-mode operation) at four different operating wavelengths.

For PR-1 operation on the 1152.3 nm neon transition, we employed GaAs/AlGaAs crystalline coated supermirrors to form our laser cavity as opposed to the conventional ion beam sputtered (IBS) mirrors. This state-of-the-art mirror technology offers the advantage of minimising thermally induced mechanical fluctuations in the mirror coatings. By referring to the table, this infrared laser gyroscope performed well as a rotation sensor. A sensor resolution of 1.6×10^{-8} rad/s/$\sqrt{\text{Hz}}$ is achieved. The frequency lock in threshold (f_L) is measured to be 0.94 μHz; which is only slightly inferior to the laser performance at 632.8 nm (which yields an f_L of 0.42 μHz). However, the possible advantage of employing

the crystalline coating mirrors in a large laser gyroscope is yet to be fully determined since in this study the gyroscopic performance was mainly limited by the small coating area of the mirror substrates. Despite that, operating a ring laser on a longer laser wavelength may decrease the amplitude of the scattering of the intra-cavity laser beams into the counter-propagating beam path. The possibility of minimising the perturbations on the laser rotation signal provides a reasonable motivation to continue pursuing the feasibility of running an infrared ring laser gyroscope.

For rotation sensing operation at 543.4 nm, the laser cavity Q is high, at 3.9×10^{11} which compares well with the laser cavity Q at 632.8 nm, where a Q of 3.6×10^{11} is measured. There is a 10% reduction in the beam diameters on the mirrors in comparison to 632.8 nm, a likely reason to the increase in the cavity Q. The performance of PR-1 at 611.8 nm is very promising, despite the higher cavity loss ($Q = 1.2 \times 10^{11}$) as the IBS-mirrors were not optimised at this wavelength. The sensor resolution achieved at 543.4 nm ($\Omega_s = 8.4 \times 10^{-10}$ rad/s/$\sqrt{\text{Hz}}$) and 611.8 nm ($\Omega_s = 2.7 \times 10^{-10}$ rad/s/$\sqrt{\text{Hz}}$) compares well with the resolution achieved while PR-1 is operated at 632.8 nm ($\Omega_s = 2.4 \times 10^{-10}$ rad/s/$\sqrt{\text{Hz}}$). These preliminary results provide compelling evidence that improving the performance of ring laser gyroscopes via the 'frequency up-scaling' approach is highly desirable, especially now that the geometric-up-scaling approach has reached a point where it offers no further advantages.

Lastly, as PR-1 is a wall-mounted heterolithic laser, we stabilised the laser optical frequency by actively control the laser perimeter with two piezo-actuators. Exploiting the fact that PR-1 performed well as a gyroscope while running in the phase-locked regime (comparable to single-mode operation), the beat frequency generated by the adjacent stable longitudinal modes (ν_{fsr}) was employed as the feedback signal. The stability of the PR-1 cavity improved significantly with the implementation of the self-referenced perimeter stabilisation scheme. PR-1 successfully yields a laser stability of $4.8 \times 10^{-5}\Omega_E$. We utilised the same approach to characterise PR-1 gyroscopic performance at 611.8 nm, and the achieved laser stability was $1.8 \times 10^{-4}\Omega_E$. Since no external reference is needed to realise this cavity feedback scheme, it is convenient to be implemented in a frequency up-scaled laser gyroscope, where the operating wavelength differs from 632.8 nm.

The next step to obtain better performance of a frequency up-scaled ring laser gyroscope would be the optimisation of the gain excitation system. The long gas discharge for operation at 543.4 nm was unstable due to inefficiencies in the RF excitation mechanism (refer to Section 5.5). Improved impedance matching unit design and electrode geometry are crucial to ensure sufficient gain is provided to sustain the laser action and obtain a stable laser output. A few shorter gain tubes instead of one single long gain section may be required to avoid the instabilities associated with the long plasma discharge.

Other than that, the optimum pressure for PR-1 operation at 543.4 nm (and 611.8 nm) is noticeably low (due to the low laser gain). In order to run a ring laser at 543.4 nm with operating pressures above 2 mbar (to attain higher output power), multiple gain tubes and an RF input power of more than 50 W may be necessary to provide more gain to excite the over-pressured helium-neon laser gyroscope. In future work, a hydrogen getter should be installed to prohibit contamination by hydrogen out-gassing from the stainless steel for long-term rotation sensing performance.

Very long-term rotation sensing (over several months) without any gaps in the data series would be a substantial push towards an accurate measurement of LoD by large ring laser gyroscopes. In this context, further investigation to explore other laser frequency stabilisation techniques need to be explored, especially for heterolithic ring lasers, where their mechanical stability is usually a few orders of magnitude lower to those demonstrated by monolithic devices. Although monolithic ring structures such as G and C-II have the advantage regarding higher mechanical stability, active control of these monolithic cavities remains critical in order to enhance their gyroscopic performance. This is proven by the improvement in the stability of the G laser by a factor of 60 through a cavity stabilisation using a frequency comb line as stable reference [18].

One of the more straightforward techniques would be to lock the ring laser optical frequency to a highly-stabilised frequency standard as a reference. Highly stable frequency references can be frequency stabilised linear helium-neon lasers, hydrogen masers or atomic clocks. The Pound-Drever-Hall technique is another desirable method that may be suitable for our high Q ring laser cavities. This stabilisation technique utilises phase modulation of the laser to produce feedback signals, thus being insensitive to laser intensity fluctuations [152]. It is worth noting that the structure of the C-II ring laser cavity has diagonal boreholes which suggest that they could be used as high Q linear cavities to stabilise the scale factor of the gyroscope. This concept has been demonstrated in ref. [38] where two diagonal cavities (1.32 m in length) were constructed from the features of a square ring cavity diagonal resonators. The high Q linear cavities were locked to the same reference laser, providing a length stabilisation at the level of 1×10^{-11} for 100 s of integration time.

Furthermore, extreme laser frequency stability can be achieved by mounting the device in an underground laboratory, isolated from the environmental perturbations [4], [37]. In the case where the available laboratory space limits the size of the laser, frequency up-scaling could be utilised. Our proof of principle experiments using the 543.4 nm neon transition demonstrate that this is viable.

With regards to high-accuracy absolute measurement of Earth rotation, it has been estimated that a large cavity with a side length of more than 10 m might provide sufficient resolution to detect the general-relativistic Lense–Thirring precession [149]. Moreover, by

building a larger device, backscatter errors, one of the main systematic error contributions in Earth rotation rate measurements by large ring lasers, will decrease significantly [15].

The PR-1 laser demonstrated multi-wavelength operation at 611.8 nm, 604.6 nm and 593.9 nm (Section 5.2.4). These transitions originated from the same neon upper level, $3s_2$ and it is known that the simultaneous operation of these neon transitions can provide a stable laser output [70]. This is a promising approach to operation of a multi-wavelength large ring laser gyroscope. Gyroscopic operation with multiple laser transitions will offer advantages such as laser perimeter control and at the same time allows for high-resolution rotation sensing measurements. The relatively high gain neon transition at 611.8 nm may be utilised for the cavity control feedback system to maintain the stability of the laser perimeter. Then, the shorter wavelength neon transition at 593.9 nm could be employed to upscale the ring laser, and provide precise rotation sensing operation. This concept can be further implemented by applying next-generation supermirrors with multiple stop-bands, particularly at 632.8 nm and 543.4 nm, to exploit the high gain available at 632.8 nm and at the same time, achieving high-resolution rotation sensing at 543.4 nm. Research is currently underway to investigate the optimum condition for these neon transitions to run in the phase-locked regime simultaneously (to avoid mode-competition) which will yield stable rotational signals.

Another notable advantage of a multi-oscillator ring laser gyroscope is that it provides a calibration of corrections for systematic errors which are introduced by the refractive index and the dispersion within the gain medium. These residual systematic biases lead to null-shift errors in the rotational signal. The rotation rate as measured at either wavelength should result in the same value at any given time. Therefore, by acquiring and comparing the Sagnac signal time series from both laser wavelengths at the same time; these null-shift errors can be checked and removed simultaneously; thus resulting in an absolute rotation measurement.

Alternatively, the systematic errors caused by the gain medium in large gyroscopes could be avoided by exploring the plausibility of operating a passive large ring laser. Ezekiel and Balsamo first proposed this concept in 1977 [153]. Recently, Korth et al. reported an externally injected passive ring laser gyroscope achieving a rotation sensitivity of 10^{-7} rad/s/$\sqrt{\text{Hz}}$ [154]. They employed a 1064 nm Nd:YAG laser as the continuous wave source. The laser was split into two beams, and one of the laser beams was locked to the counter-clockwise mode of a 0.75 m × 0.75 m ring cavity. The other laser beam was dithered by an acousto-optic modulator (AOM); so that the optical frequency is higher than the counter-rotating beam by one cavity free spectral range (FSR); prior to being locked to the clockwise mode of the ring cavity. The performance of the passive ring laser gyroscope was limited by the mechanical stability of the ring cavity. It would be interesting to implement the same technique on a monolithic laser structure such as C-II and compare its performance to that of active ring laser interferometers.

Appendix I: The Vacuum System and Gas Fill Procedures

A

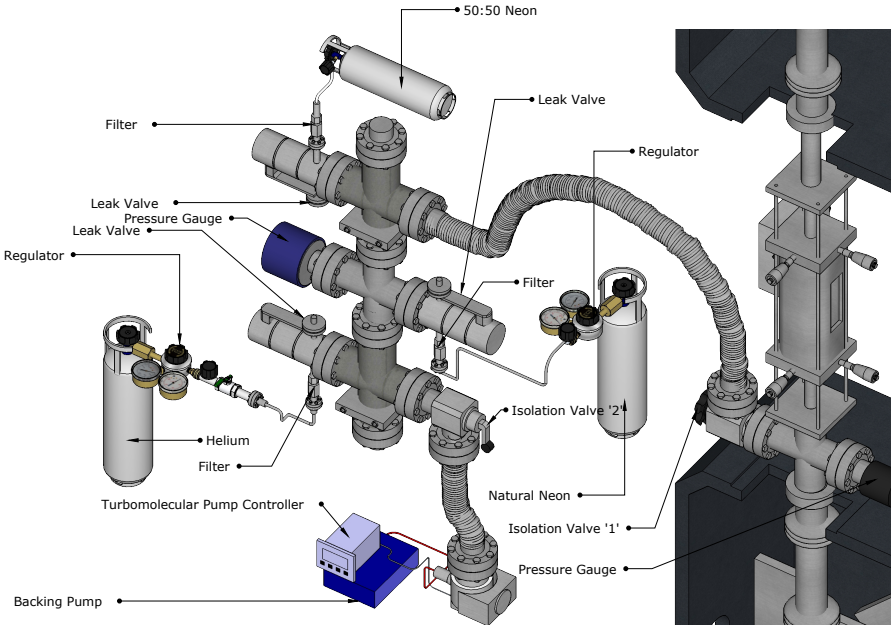

Figure. A.1.: Schematic diagram of the vacuum system.

Figure A.1 illustrates the details of the vacuum system for PR-1. The PR-1 laser cavity is isolated from the vacuum system by Isolation Valve '1'. All three gas cylinders are installed with high-pressure regulators[1] and are isolated by variable leak valves. Filters are installed between the gas cylinders and the variable valves to avoid any contamination from the gas cylinders leaking into the laser cavity. The pressure gauge at the vacuum system (denoted as Pressure Gauge '2'[2]) monitors the gas pressure in the vacuum system while another pressure gauge (Pressure Gauge '1'[3]) is attached to the ring cavity to monitor the gas pressure inside the PR-1 cavity.

Prior to refilling the laser cavity with a new gas mix, the gas inside the vacuum system has to be evacuated first to ensure there are no impurities from the vacuum system which

[1] A control valve that reduces the high pressure from the gas cylinder to a low pressure (or vacuum) system

[2] This gauge reading was calibrated in 'torr'.

[3] The unit of this pressure gauge reading was calibrated in 'mbar' and the pressure unit throughout this study will be in 'mbar'.

flow into the PR-1 cavity. Isolation Valve '1' should be closed tightly before turning on the vacuum pump. Once the vacuum pump is turned on, Isolation Valve '2' is opened to evacuate gases from the vacuum system to the atmosphere. When the pressure reading from Pressure Gauge '2' has reached 0.004 torr, the turbomolecular pump is switched on. At this point, the variable leak valve attached to the gas line between the helium gas cylinder is opened to evacuate any gas along the system. Once all the helium gas along the gas line is fully evacuated, the variable leak valves along both of the neon gas cylinders are opened to pump out any residual neon gas along the system. After that, Isolation Valve '1' is opened slowly to avoid a sudden flow of gas from the PR-1 cavity to the atmosphere. The pressure reading from Pressure Gauge '1' will start to drop to indicate the gas inside the cavity is evacuated slowly to the atmosphere. Once both of the pressure gauge readings are at zero, all valves are closed except for Isolation Valve '1'. The vacuum system and the PR-1 cavity are now under vacuum.

Once vacuum is established, the laser cavity is filled with neon gas by loosening the neon (either natural or 50:50 neon) cylinder's stop valve to allow a small quantity of neon gas to flow out and fill the gas line. Then, the stop valve is closed followed by opening the leak valve to fill the cavity with the desired neon pressure. Once the required neon pressure is reached, the leak valve is tightened. The same procedure is applied to fill the cavity with helium gas. The helium cylinder's stop valve is loosened first to allow helium gas to fill the gas line between the cylinder and the leak valve. After that, the helium cylinder's stop valve is tightened, and the helium leak valve is opened to allow helium gas to flow into the cavity. When the desired total pressure is achieved (by checking the Pressure Gauge '1' reading), the leak valve is closed and the PR-1 ring cavity is secluded from the vacuum system by closing the Isolation Valve '1' tightly. Finally, all the gas from the vacuum system is pumped out as a precautionary measure.

A.1 Portable Vacuum System

In Section 5.2.2, vacuum was established by turning on the turbo-molecular pump followed by the opening of the pneumatic valve. This pneumatic valve was held open with a pressure established by the nitrogen gas from the nitrogen cylinder. At the same time, the leak valves throughout the gas lines were unfastened to evacuate residual gas in the system. Once vacuum has been achieved, these leak valves were fastened tightly and subsequently the pneumatic valve was closed. Then, to fill the gain tube with a fixed gas pressure, the cylinder valve (either helium, natural neon or 50:50 neon) was opened and gas allowed to fill the line between the pressure regulator and the leak valve. After that, the gas cylinder valve was firmly closed and the leak valve was opened to allow gas flow into the system. These steps were repeated until the desired pressure had been achieved.

B

Appendix II: Procedures for Changing and Cleaning of the Supermirrors

The procedures to install and change the supermirrors in PR-1 is an important task in this research. Before removing the supermirrors from the ring, the laser cavity is pumped up to atmospheric pressure[1] by slowly leaking in helium gas into the cavity. After the cavity has reached the atmospheric pressure, the supermirror and its mirror holder are removed from the corner box and placed in a sealed container to be transported to the clean room. It is essential to remove the supermirrors located at the top corners first to avoid dust dropping down on the clean supermirrors in the lower corners if the bottom supermirrors are being cleaned first.

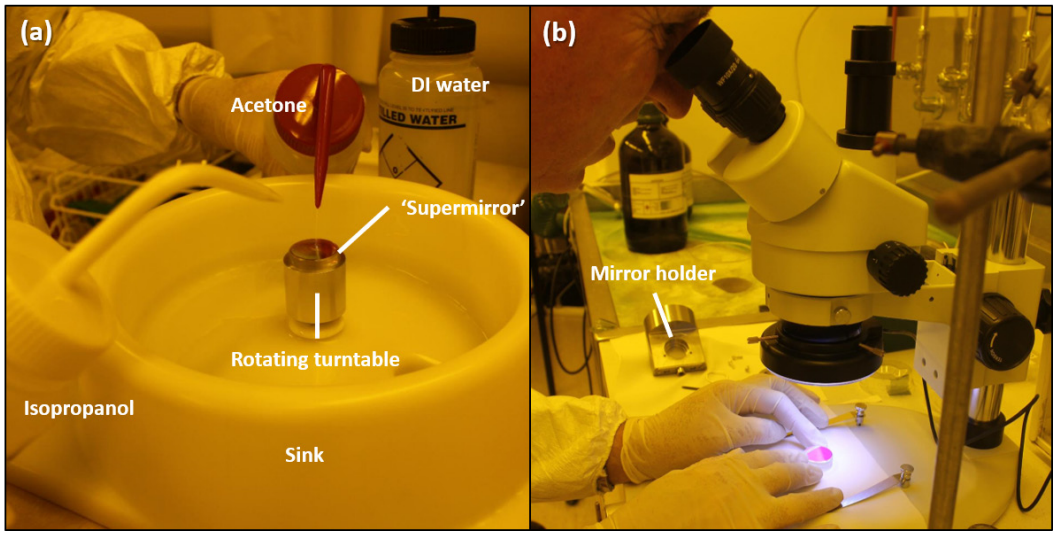

Figure. B.1.: (a) The supermirror surface is rinsed with acetone, isopropanol and de-ionised water; (b) the supermirror's centre surface is examined under a microscope.

In the clean room, the table top and sink are wiped thoroughly to eliminate unwanted contamination. Then, the supermirror is removed from the sealed container and mounted onto the turntable. After that, the turntable is rotated from low speed up to a maximum speed of 10000 rpm. At the same time, de-ionised (DI) water, acetone ($(CH_3)_2CO$) and isopropanol (CH_3H_8O) are sprayed alternately to the rotating supermirror to dissolve and to remove particles from the surface of the mirror (Figure B.1 (a)). A cotton swab is

[1] 1 atm = 1013.25 bar.

applied to remove stubborn particles if necessary. Pure nitrogen gas is blown onto the surface of the supermirror to remove excess moisture before being examined under a low magnification optical microscope. A low power helium-neon laser illuminates the centre of the supermirror to inspect the scattering on the surface as shown in Figure B.1. Minimum scattering from the centre surface indicates the supermirror is clean. Then, the supermirror is transported back to the ring cavity by placing it in a sealed container to minimise airborne particles contamination.

C

Appendix III: Mode Structure of the G Ring Laser Gyroscope

The G ring laser is known to run in the phase-locked regime of operation to establish self-reference perimeter stabilising scheme [18], [150]. The beat frequency between the main mode and the adjacent longitudinal modes, ν_{fsr} is measured using an RF spectrum analyser. ν_{fsr} is mixed with a signal generated from a reference signal generator which locked to a hydrogen maser. The laser longitudinal mode configuration, however, has never been observed. This section aims to observe the G ring laser mode structure through a Fabry-Pérot interferometer (FP) and to investigate the single-mode and phase-locked regime of operations for the G ring laser gyroscope.

The experimental setup is shown in Figure C.1. The counter-clockwise (CCW) beam from the south-west corner of the G ring was fed into an FP (Coherent 33-6305-001) with the aid of 3 fold mirrors and the signal from the FP was detected by a photomultiplier tube (PMT). Then, this signal was connected to an oscilloscope (Tektronix TDS 3014C Digital Phosphor Oscilloscope 100 MHz). The free spectral range (FSR) of the FP is 300 MHz while the G laser FSR is 18.734380691 MHz [150]. This implies that the FP can resolve up to 16 modes of the G ring laser. The clockwise (CW) and CCW beams were combined at the north-west corner of the G ring, and another PMT detected this combined beam. The combined signal consisted of two beat signals, i.e. the Sagnac frequency, δf_s = 348.5 Hz and the ν_{fsr}. Hence, the PMT signal was connected to an oscilloscope and an RF spectrum to monitor the δf_s signal and ν_{fsr} signal respectively.

At the time of the experiment, the gas composition inside the G ring cavity was 0.100 mbar of ^{20}Ne, 0.098 mbar of ^{22}Ne, and 9.682 mbar of ^{4}He [150]. As the laser power was raised slowly from 0 mV to a maximum of 1800 mV of RF input, the CCW along with the CW beam powers were measured using Thorlabs S130C power sensor and Thorlabs PM100D power meter. Simultaneously, the laser mode structure (scanned by the FP spectrum analyser) was observed via the oscilloscope. When multiple longitudinal modes began to appear on the oscilloscope, the δf_s signal and the ν_{fsr} beat signal were examined. G is denoted to be operated in phase-locked regime if a stable δf_s signal along with stable multiple longitudinal modes configuration is observed at the same time. The location of the adjacent modes from the main longitudinal mode scanned by the FP was determined by the ν_{fsr} signal on the RF spectrum analyser. On the other hand, if the laser modes and the δf_s signal are unstable, the G laser is noted as free-running.

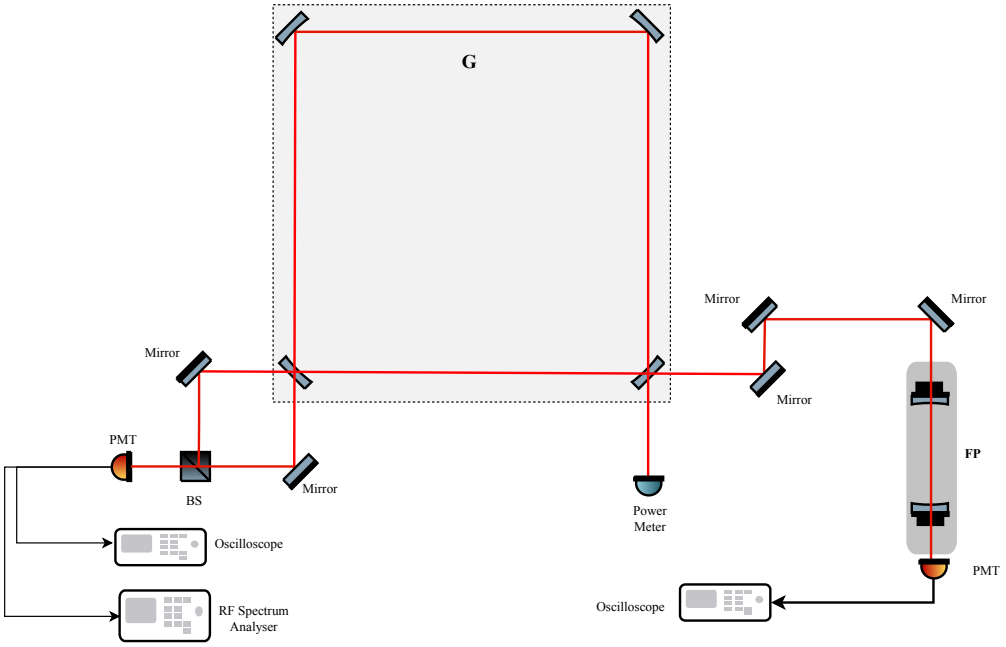

Figure. C.1.: Experimental setup to observed the mode structure of the G laser at a gas fill of approximately 0.2 mbar of 50:50 neon and a 9.88 mbar of total gas pressure.

Figure C.2 shows the CW and CCW output power as a function of the RF input power. The G ring laser was running on a single longitudinal mode within the region labelled as (i). In the region labelled as (ii), the G laser was running on 'stable' multiple longitudinal modes, while the region labelled as (iii) is where 'unstable' multiple mode configurations were observed. As seen from the figure, the CW beam output power is consistently about 5% higher than the CCW beam. Also, it is notable that there is a gap (region (iii)) before the laser established the phase-locked operating regime.

From Figure C.2, the G laser maintained single-mode operation for RF inputs below 550 mV. An example of a single longitudinal mode structure scanned by the FP spectrum analyser at CW beam power of 5.6 nW is displayed in Figure C.3. As the CW beam power was raised above 28.5 nW, the laser mode configurations observed began to establish chaotic behaviour. The δf_s signal was unstable in this operating regime. The laser remained running on this 'unstable' multi-mode configuration within a narrow gap labelled as (iii) in Figure C.2, between RF input of 550 mV to 600 mV.

Then, the laser began to settle into 'stable' multiple modes configuration as we increased the laser power above 30.2 nW (region (ii) between RF = 600 mV until 1100 mV in Figure C.2). Figure C.4 shows an example of the G laser mode scanned by the FP while running in phase-locked regime of operation at a laser power of 36 nW. Two longitudinal modes, denoted as 'b', located approximately 112 MHz from the main longitudinal mode, 'a' were observed. A beat frequency at 112.4 MHz was detected on the RF spectrum analyser to indicate 'b' is approximately 6 times FSR away from the main mode, 'a'.

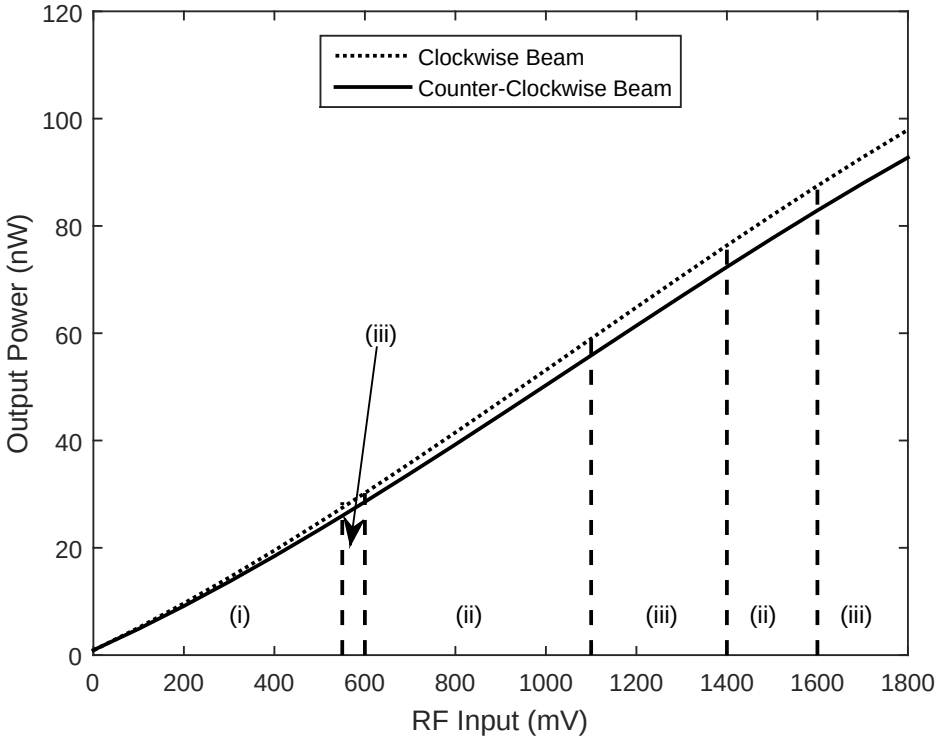

Figure. C.2.: CW and CCW output powers as a function of RF input (in mV). Region: (i) indicates the laser is running on a single longitudinal mode; (ii) is where the laser is running in phase-locked regime; and (iii) is where the laser is free running.

Another pair of longitudinal modes began to appear as the RF input was increased beyond 1000 mV,. Figure C.5 shows the longitudinal modes, labelled as 'c', as observed on the oscilloscope. Although 'c' appeared to be located approximately 75 MHz from 'a', 'c' is actually located at 12 times FSR away from the main mode 'a'; confirmed by the detection of a ν_{fsr} (generated from the beating between 'c' and the main mode) at 224.8 MHz on the RF spectrum analyser.

G began to enter the free-running operating regime again (region (iii) in Figure C.2) when the laser power was raised above CW beam power of 59 nW (RF = 1100 mV). Figure C.6 shows the chaotic laser mode configurations observed at CW beam power of 70.6 nW (RF = 1300 mV). The peaks at 'b' and 'c' disappeared and one longitudinal mode; located about 8 times FSR (ν_{fsr} = 150 MHz) away from the main mode began to become prominent. As seen in Figure C.6, this mode was only persisted for about 2 to 4 seconds. The amplitude of the mode at 8 times FSR decreases at time = 5 s and its amplitude is approximately equal to that of adjacent longitudinal modes at time = 6 s. Then, the mode began to become dominant again after time = 12 s.

The G laser established another phase-locked regime of operation denoted as region (ii) between CW beam power of 76 nW to 87 nW in Figure C.2. Figure C.7 shows an example

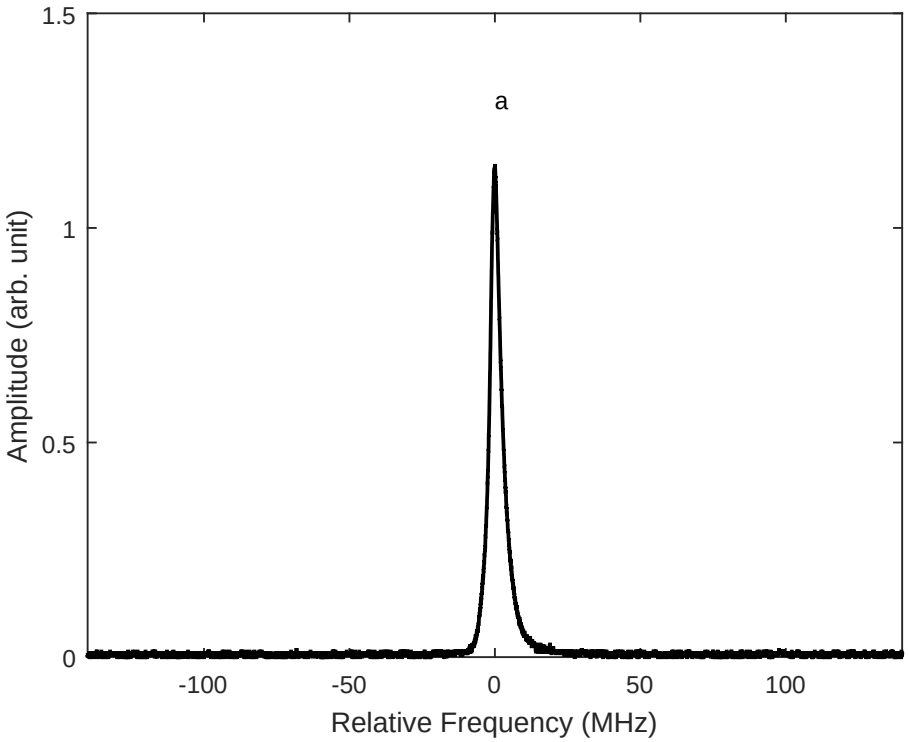

Figure. C.3.: Laser mode structure observed at a laser beam power of 5.6 nW where the peak labelled as 'a' is the main longitudinal mode.

of the 'stable' multiple longitudinal modes structure scanned by the FP at CW beam power of 82.5 nW. As shown in the figure, peaks labelled as 'b' are the wrapped around of laser modes located at 168.75 MHz away from 'a' while peaks labelled as 'c' are the wrap around of laser modes situated about at 14 free spectral range from the main longitudinal mode, 'a'. The location of these cavity modes were confirmed by the ν_{fsr} frequencies observed at 168.75 MHz and 262.5 MHz on the RF spectrum analyser.

No stable δf_s was observed as laser power increased beyond RF = 1600 mV. The G laser was essentially free running above CW beam power of 88 nW.

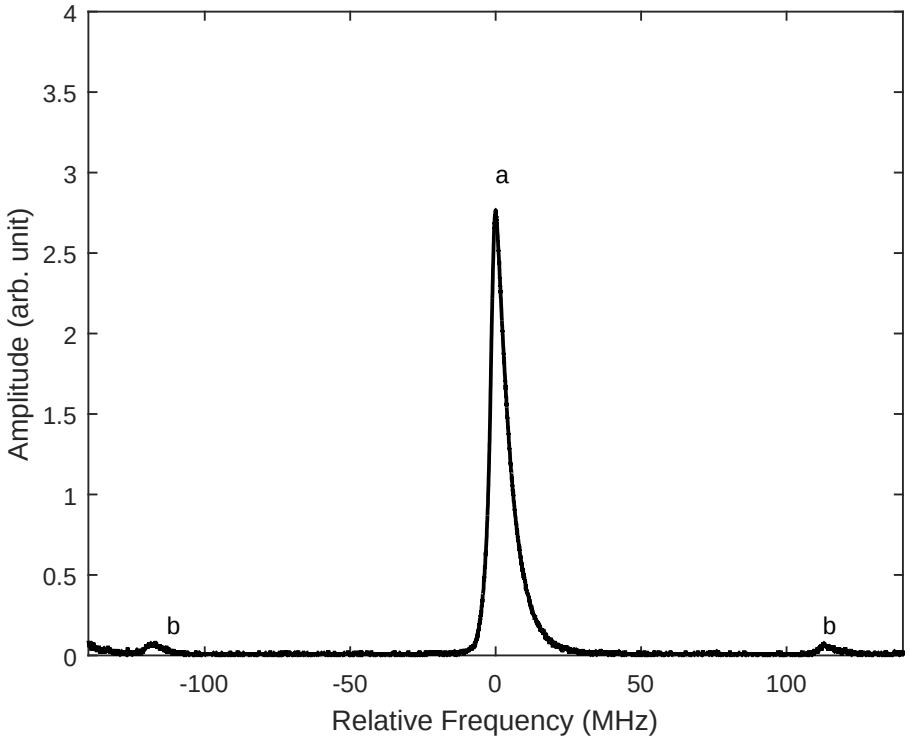

Figure. C.4.: G laser spectrum scanned by the FP at CW beam output power of 36 nW. The main mode is labelled as 'a' and 2 modes labelled as 'b' are approximately 112.4 MHz (6 FSR) apart from the main mode.

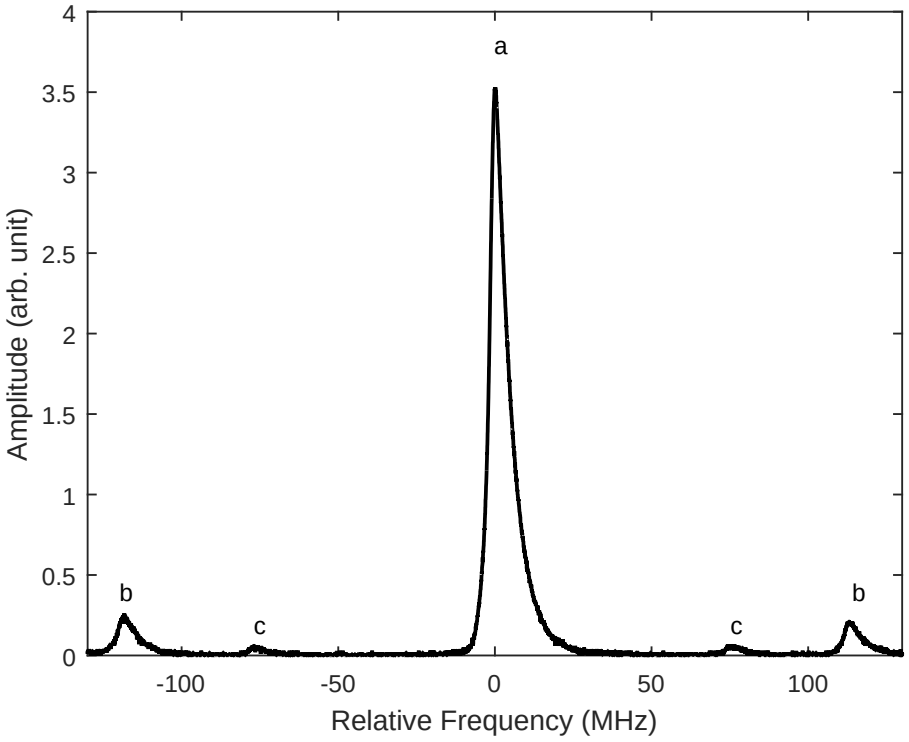

Figure. C.5.: G laser spectrum scanned by the FP at CW beam output power of 47 nW. The main mode is labelled as 'a' and 2 modes labelled as 'b' are approximately 112.4 MHz (6 FSR) apart from the main mode and peak labelled as 'c' is 12 times FSR (peak 'c') away from the main mode.

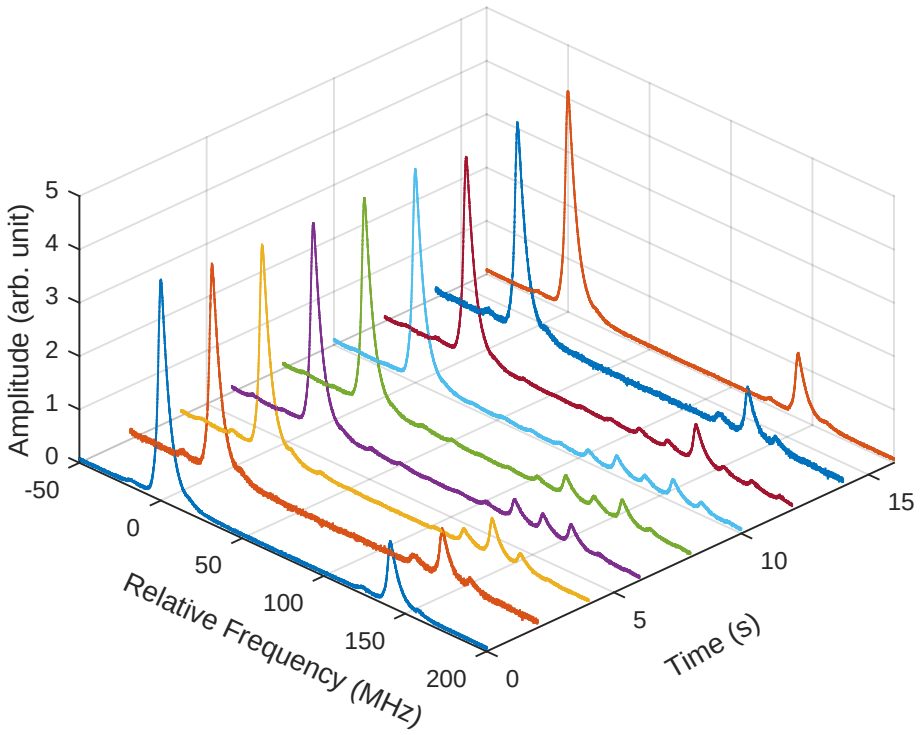

Figure. C.6.: G laser spectrum scanned by the FP at CW beam output power of 70.6 nW as a function of time when the laser is free running.

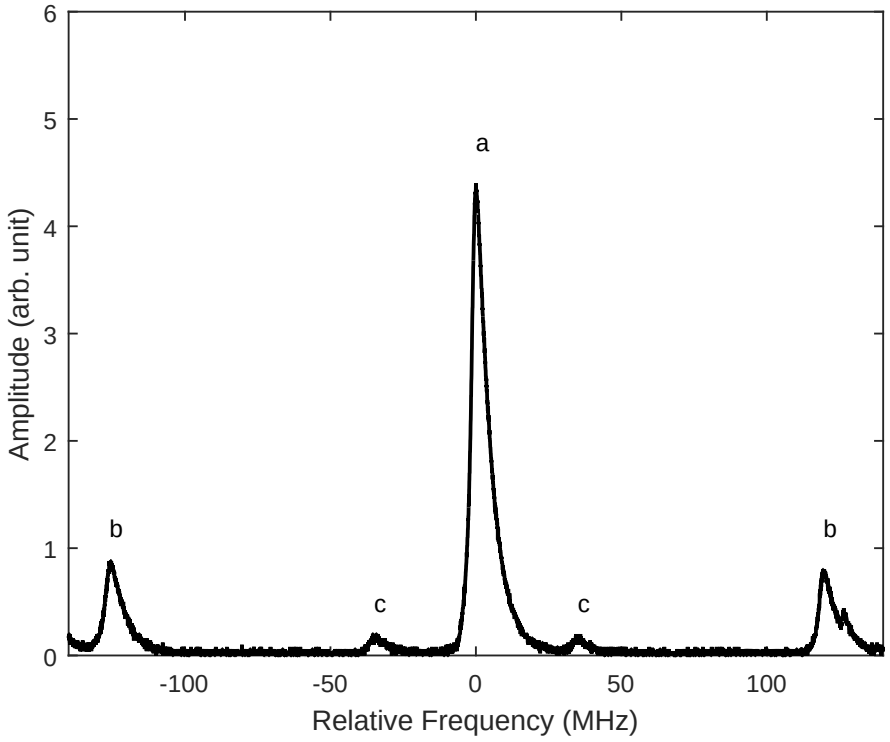

Figure. C.7.: G laser spectrum scanned by the FP at CW beam output power of 82.5 nW. The peak labelled as 'b' is corresponding to a cavity mode located at 9 FSR from 'a' while the peak labelled as 'c' is the wrapped around of a mode situated at 14 FSR from 'a'.

Publications

Published Articles in Peer Reviewed Scholarly Journals:

- **C. L. Anyi**, R. J. Thirkettle, D. Zou, D. Follman, G.D. Cole, K. U. Schreiber, and J.-P R. Wells, "The Macek and Davis experiment revisited: A large ring laser interferometer operating on the $2s_2 \rightarrow 2p_4$ transition of neon", *Applied Optics*, vol. 58, no. 2, pp. 302-307, 2019.

In Submission:

- **C. L. Anyi**, R. J. Thirkettle, , G. J. MacDonald, K. U. Schreiber, and J.-P R. Wells, "Gyroscopic operation on the $3s_2 \rightarrow 2p_{10}$ 543.3 nm transition of neon in a 2.56 m^2 ring cavity", *Optic Letters*, 2019.

In Preparation:

- D. Zou, **C. L. Anyi**, R. J. Thirkettle, K. U. Schreiber, and J.-P R. Wells, "Initial gyroscopic operation of a multi-wavelength large ring laser", 2019.

Abstracts and Conference Proceedings:

- **C. L. Anyi**, J.-P. R. Wells, R. J. Thirkettle, R. B. Hurst, and K. U. Schreiber, "A large helium-neon ring laser gyroscope operating at 543 nm", *in Conference on Lasers and Electro-Optics/Pacific Rim 2018*, Hong Kong, China, July 29 – August 3, 2018, Optical Society of America, 2018, pp. Tu3F.4.

- **C. Anyi**, J.-P. R. Wells, R. J. Thirkettle, R. B. Hurst, and K. U. Schreiber, "Initial development of frequency stabilization of a 2.56 m_2 ring laser gyroscope", Poster presented at: The 3rd Australia New Zealand Conference on Optics (ANZCOP) 2017, Queenstown, New Zealand, 4-7 December 2017.

- **C. Anyi**, R.J. Thirkettle, K.U. Schreiber, R.B. Hurst, and J.-P.R. Wells, "The performance of large He-Ne gyroscopes operating at 612 nm", Poster presented at: 10th Annual Dodd-Walls Symposium, Dunedin, New Zealand, 23-27 January 2017.

- **C. L. Anyi**, "Experiments with ring laser gyroscope", Seminar talk presented at: DWC Seminar Series, University of Auckland, New Zealand, 13 October 2017.

- **C. Anyi**, J.-P R. Wells, R. J. Thirkettle, R. B. Hurst, K. U. Schreiber, and M. F. Reid,"A Ring Laser Gyroscope Unlocking the Earth Rotation at 1.1523 μm", Poster presented at: 9th Annual Dodd-Walls Symposium, Queenstown, New Zealand, 27 June–1 July 2016.

Internal Presentations:

- **C. Anyi**, J.-P. R. Wells, R. J. Thirkettle, R. B. Hurst, and K. U. Schreiber, "Frequency Stabilization of a Ring Laser Gyroscope", 34th Physics and Astronomy Research Presentation Workshop, University of Canterbury, New Zealand, 7 September 2017.

- **C. Anyi**, J.-P. R. Wells, R. J. Thirkettle, R. B. Hurst, and K. U. Schreiber, "Ring laser gyroscope Unlocking the Earth rotation at 1.1523 μm and 543 nm", 33rd Annual Physics and Astronomy Conference, University of Canterbury, New Zealand, 2 September 2016

- **C. Anyi**, "Ring laser gyroscopes operating at wavelengths of 543 nm and 1.15 micron", Department of Physics and Astronomy, 32nd Annual Department Conference, University of Canterbury, New Zealand, 19 August 2015.

Bibliography

[1] P. Brosche and H. Schuh, "Tides and Earth rotation", *Surveys in Geophysics*, vol. 19, no. 5, pp. 417–430, 1998.

[2] F. Seitz and H. Schuh, "Earth rotation", in *Sciences of Geodesy - I: Advances and Future Directions*, G. Xu, Ed. Berlin, Heidelberg: Springer Berlin Heidelberg, 2010, pp. 185–227.

[3] H. Schuh and D. Behrend, "VLBI: A fascinating technique for geodesy and astrometry", *Journal of Geodynamics*, vol. 61, pp. 68–80, 2012.

[4] K. U. Schreiber, T. Klügel, A. Velikoseltsev, W. Schlüter, G. E. Stedman, and J.-P. R. Wells, "The large ring laser G for continuous Earth rotation monitoring", *Pure and Applied Geophysics*, vol. 166, no. 8-9, pp. 1485–1498, 2009.

[5] K. U. Schreiber, A. Velikoseltsev, M. Rothacher, T. Klügel, G. E. Stedman, and D. L. Wiltshire, "Direct measurement of diurnal polar motion by ring laser gyroscopes", *Journal of Geophysical Research: Solid Earth*, vol. 109, no. B6, 2004.

[6] K. U. Schreiber, T. Klügel, J.-P. R. Wells, R. B. Hurst, and A. Gebauer, "How to detect the Chandler and the annual wobble of the Earth with a large ring laser gyroscope", *Physical Review Letters*, vol. 107, no. 17, p. 173 904, 2011.

[7] G. Sagnac, "L'éther lumineux démontré par l'effet du vent relatif d'éther dans un interféromètre en rotation uniforme", *Comptes Rendus*, vol. 157, pp. 708–710, 1913.

[8] A. A. Michelson and H. G. Gale, "The effect of the Earth's rotation on the velocity of light, II", *The Astrophysical Journal*, vol. 61, p. 140, 1925.

[9] W. M. Macek and D. T. M. Davis Jr, "Rotation rate sensing with travelling-wave ring lasers", *Applied Physics Letters*, vol. 2, no. 3, pp. 67–68, 1963.

[10] G. E. Stedman, "Ring-laser tests of fundamental physics and geophysics", *Reports on Progress in Physics*, vol. 60, no. 6, p. 615, 1997.

[11] G. E. Stedman, H. R. Bilger, L. Ziyuan, M. P. Poulton, C. H. Rowe, I. Vetharaniam, and P. V. Wells, "Canterbury ring laser and tests for nonreciprocal phenomena", *Australian Journal of Physics*, vol. 46, no. 1, pp. 87–102, 1993.

[12] B. Höling, G. Leuchs, H. Ruder, and M. Schneider, "An argon ion ring laser as a gyroscope", *Applied Physics B*, vol. 55, no. 1, pp. 46–50, 1992.

[13] C. H. Rowe, K. U. Schreiber, S. J. Cooper, B. T. King, M. Poulton, and G. E. Stedman, "Design and operation of a very large ring laser gyroscope", *Applied Optics*, vol. 38, no. 12, pp. 2516–2523, 1999.

[14]R. W. Dunn, D. E. Shabalin, R. J. Thirkettle, G. J. MacDonald, G. E. Stedman, and K. U. Schreiber, "Design and initial operation of a 367 m^2 rectangular ring laser", *Applied Optics*, vol. 41, no. 9, pp. 1685–1688, 2002.

[15]R. B. Hurst, G. E. Stedman, K. U. Schreiber, R. J. Thirkettle, R. D. Graham, N. Rabeendran, and J.-P. R. Wells, "Experiments with an 834 m^2 ring laser interferometer", *Journal of Applied Physics*, vol. 105, no. 11, p. 3115, 2009.

[16]R. Graham, "New concepts for operating ring laser gyroscopes", PhD thesis, Department of Physics and Astronomy, University of Canterbury, 2010.

[17]K. U. Schreiber and J.-P. R. Wells, "Invited review article: Large ring lasers for rotation sensing", *Review of Scientific Instruments*, vol. 84, no. 4, p. 041 101, 2013.

[18]K. U. Schreiber, A. Gebauer, and J.-P. R. Wells, "Closed-loop locking of an optical frequency comb to a large ring laser", *Optics Letters*, vol. 38, no. 18, pp. 3574–3577, 2013.

[19]T. Nilsson, J. Böhm, H. Schuh, K. U. Schreiber, A. Gebauer, and T. Klügel, "Combining VLBI and ring laser observations for determination of high frequency Earth rotation variation", *Journal of Geodynamics*, vol. 62, pp. 69–73, 2012.

[20]K. U. Schreiber, G. E. Stedman, H. Igel, and A. Flaws, "Ring laser gyroscopes as rotation sensors for seismic wave studies", *Source Asymmetry, Structural Media and Rotation Effects*, p. 377, 2006.

[21]K. U. Schreiber, J. N. Hautmann, A. Velikoseltsev, J. Wassermann, H. Igel, J. Otero, F. Vernon, and J.-P. R. Wells, "Ring laser measurements of ground rotations for seismology", *Bulletin of the Seismological Society of America*, vol. 99, no. 2B, pp. 1190–1198, 2009.

[22]K. U. Schreiber, H. Igel, J. Wassermann, C.-J. Lin, A. Gebauer, and J.-P. R. Wells, "ROMY-the first large 3D ring laser structure for seismology and geodesy", in *EGU General Assembly Conference Abstracts*, vol. 18, 2016, p. 4967.

[23]G. E. Stedman, K. U. Schreiber, and H. R. Bilger, "On the detectability of the Lense–Thirring field from rotating laboratory masses using ring laser gyroscope interferometers", *Classical and Quantum Gravity*, vol. 20, no. 13, p. 2527, 2003, ISSN: 0264-9381.

[24]A. Velikoseltsev, K. U. Schreiber, T. Klügel, S. Voigt, and R. Graham, "Sagnac interferometry for the determination of rotations in geodesy and seismology", *Gyroscopy and Navigation*, vol. 1, no. 4, pp. 291–296, 2010.

[25]J. M. Bardeen and J. A. Petterson, "The Lense-Thirring effect and accretion disks around kerr black holes", *The Astrophysical Journal*, vol. 195, p. L65, 1975.

[26]C. W. F. Everitt, D. B. DeBra, B. W. Parkinson, J. P. Turneaure, J. W. Conklin, M. I. Heifetz, G. M. Keiser, A. S. Silbergleit, T. Holmes, J. Kolodziejczak, *et al.*, "Gravity probe B: Final results of a space experiment to test general relativity", *Physical Review Letters*, vol. 106, no. 22, p. 221 101, 2011.

[27]N. Beverini, M. Allegrini, A. Beghi, J. Belfi, B. Bouhadef, M. Calamai, G. Carelli, D. Cuccato, A. Di Virgilio, and E. Maccioni, "Measuring general relativity effects in a terrestrial lab by means of laser gyroscopes", *Laser Physics*, vol. 24, no. 7, p. 074 005, 2014.

[28]J. Belfi, F. Bosi, A. Di Virgilio, R. Santagata, A. Ortolan, N. Beverini, G. Carelli, E. Maccioni, and D. Cuccato, "Experimental activity toward GINGER (Gyroscopes IN GEneral RElativity)", in *Laser Optics, 2014 International Conference*, IEEE, 2014, p. 1.

[29]A. Di Virgilio, M. Allegrini, J. Belfi, N. Beverini, F. Bosi, G. Carelli, E. Maccioni, M. Pizzocaro, A. Porzio, U. Schreiber, *et al.*, "Performances of 'g-pisa': A middle size gyrolaser", *Classical and Quantum Gravity*, vol. 27, no. 8, p. 084 033, 2010.

[30]J. Belfi, N. Beverini, F. Bosi, G. Carelli, D. A. Virgilio, D. Kolker, E. Maccioni, A. Ortolan, R. Passaquieti, and F. Stefani, "Performance of "G-Pisa" ring laser gyro at the Virgo site", *Journal of Seismology*, vol. 16, no. 4, pp. 757–766, 2012, ISSN: 1383-4649.

[31]J. Belfi, N. Beverini, F. Bosi, G. Carelli, D. Cuccato, G. De Luca, A. Di Virgilio, A. Gebauer, E. Maccioni, A. Ortolan, *et al.*, "First results of GINGERino, a deep underground ringlaser", *arXiv preprint arXiv:1601.02874*, 2016.

[32]R. Santagata, A. Beghi, J. Belfi, N. Beverini, D. Cuccato, A. Di Virgilio, A. Ortolan, A. Porzio, and S. Solimeno, "Optimisation of the geometrical stability in square ring laser gyroscopes", *Classical and Quantum Gravity*, vol. 32, no. 5, p. 055 013, 2015.

[33]N. Rabeendran, "A study of ring laser gyroscopes", Master's thesis, Department of Physics and Astronomy, University of Canterbury, 2008.

[34]R. W. Dunn, "Design of a triangular active ring laser 13 m on a side", *Applied Optics*, vol. 37, no. 27, pp. 6405–6409, 1998.

[35]K. U. Schreiber, H. Igel, A. Cochard, A. Velikoseltsev, A. Flaws, B. Schuberth, W. Drewitz, and F. Müller, "The GEOsensor project: Rotations—A new observable for seismology", in *Observation of the Earth System from Space*. Springer, 2006, pp. 427–443.

[36]R. W. Dunn, H. H. Mahdi, and H. J. Al-Shukri, "Design of a relatively inexpensive ring laser seismic detector", *Bulletin of the Seismological Society of America*, vol. 99, no. 2B, pp. 1437–1442, 2009.

[37]J. Belfi, N. Beverini, G. Carelli, A. Di Virgilio, U. Giacomelli, E. Maccioni, A. Simonelli, F. Stefani, and G. Terreni, "Analysis of 90 day operation of the GINGERINO gyroscope", *Applied Optics*, vol. 57, no. 20, pp. 5844–5851, 2018.

[38]J. Belfi, N. Beverini, D. Cuccato, A. Di Virgilio, E. Maccioni, A. Ortolan, and R. Santagata, "Interferometric length metrology for the dimensional control of ultra-stable ring laser gyroscopes", *Classical and Quantum Gravity*, vol. 31, no. 22, p. 225 003, 2014, ISSN: 0264-9381.

[39]R. B. Hurst, J.-P. R. Wells, and G. E. Stedman, "An elementary proof of the geometrical dependence of the Sagnac effect", *Journal of Optics A: Pure and Applied Optics*, vol. 9, no. 10, p. 838, 2007, ISSN: 1464-4258.

[40]A. Javan, W. R. Bennett Jr, and D. R. Herriott, "Population inversion and continuous optical maser oscillation in a gas discharge containing a He-Ne mixture", *Physical Review Letters*, vol. 6, no. 3, p. 106, 1961.

[41]W. R. Bennett, "Gaseous optical masers", *Applied Optics*, vol. 1, no. 101, pp. 24–61, 1962.

[42]J. Hecht, "Helium neon lasers flourish in face of diode-laser competition", *Laser focus world*, vol. 28, no. 11, pp. 99–108, 1992.

[43]M. Csele, *Fundamentals of Light Sources and Lasers*. John Wiley & Sons, 2011.

[44]A. D. White and J. D. Rigden, "The effect of super-radiance at 3.39 μ on the visible transitions in the He-Ne maser", *Applied Physics Letters*, vol. 2, no. 11, pp. 211–212, 1963.

[45]B. S. Gray, I. D. Latimer, and S. P. Spoor, "Gain measurements at 543 nm in helium neon laser discharges", *Journal of Physics D: Applied Physics*, vol. 29, no. 1, p. 50, 1996.

[46]D. Perry, "CW laser oscillation at 5433 Å in neon", *IEEE Journal of Quantum Electronics*, vol. 7, no. 2, pp. 102–102, 1971.

[47]K. U. Schreiber, C. H. Rowe, D. N. Wright, S. J. Cooper, and G. E. Stedman, "Precision stabilisation of the optical frequency in a large ring laser gyroscope", *Applied Optics*, vol. 37, no. 36, pp. 8371–8381, 1998.

[48]R. Balhorn, H. Kunzmann, and F. Lebowsky, "Frequency stabilisation of internal-mirror helium–neon lasers", *Applied Optics*, vol. 11, no. 4, pp. 742–744, 1972.

[49]F. Aronowitz, "Fundamentals of the ring laser gyro", in *Optical Gyros and their Application*, RTO AGARDograph, 1999, ch. 3.

[50]E. J. Post, "Sagnac effect", *Reviews of Modern Physics*, vol. 39, no. 2, p. 475, 1967.

[51]W. W. Chow, J. Gea-Banacloche, L. M. Pedrotti, V. E. Sanders, W. Schleich, and M. O. Scully, "The ring laser gyro", *Reviews of Modern Physics*, vol. 57, no. 1, p. 61, 1985.

[52]S. F. Jacobs and R. Zanoni, "Laser ring gyro of arbitrary shape and rotation axis", *American Journal of Physics*, vol. 50, no. 7, pp. 659–660, 1982.

[53]P. Langevin and P. Langevin, "Theorie de l'experience de sagnac", *CR Acad. Sc (Paris)*, vol. 173, p. 821, 1921.

[54]G. B. Malykin and V. I. Pozdnyakova, *Ring interferometry*. Walter de Gruyter, 2013, vol. 13.

[55]G. Pascoli, "The sagnac effect and its interpretation by paul langevin", *Comptes Rendus Physique*, vol. 18, no. 9-10, pp. 563–569, 2017.

[56]F. Aronowitz, "The laser gyro. (Laser gyro operational principles, discussing passive Sagnac and active ring laser interferometers, readout, errors due to null shift, lock-in and mode pulling, etc)", *Laser Applications*, vol. 1, pp. 133–200, 1971.

[57]A. Velikoseltsev, "The development of a sensor model for large ring lasers and their application in seismic studies", PhD thesis, Technische Universität München, 2005.

[58]J. Belfi, N. Beverini, F. Bosi, G. Carelli, A. Di Virgilio, E. Maccioni, A. Ortolan, and F. Stefani, "A 1.82 m^2 ring laser gyroscope for nano-rotational motion sensing", *Applied Physics B*, vol. 106, no. 2, pp. 271–281, 2012.

[59]T. Podgorski and F. Aronowitz, "Langmuir flow effects in the laser gyro", *IEEE Journal of Quantum Electronics*, vol. 4, no. 1, pp. 11–18, 1968.

[60]R. B. Hurst, N. Rabeendran, K. U. Schreiber, and J.-P. R. Wells, "Correction of backscatter-induced systematic errors in ring laser gyroscopes", *Applied Optics*, vol. 53, no. 31, pp. 7610–7618, 2014.

[61]C. E. Moore and J. E. Mack, "Atomic energy levels, as derived from the analyses of optical spectra", *Physics Today*, vol. 5, p. 23, 1952.

[62]W. R. Bennett, P. J. Kindlmann, and G. N. Mercer, "Measurement of excited state relaxation rates", *Applied Optics*, vol. 4, no. 101, pp. 34–57, 1965.

[63]A. V. Eletskii and B. M. Smirnov, "Physical processes in gas lasers", *Journal of Soviet Laser Research*, vol. 7, no. 3, pp. 207–323, 1986.

[64] L. J. Radziemski, “Spectroscopic notation for the energy levels of helium and neon”, *Optics News*, vol. 15, no. 1, pp. 15–16, 1989.

[65] H. Haberland, W. Konz, and P. Oesterlin, “Interaction potentials and energy transfer cross sections for collisions of metastable helium and neon. II. He (2^1S)+ Ne”, *Journal of Physics B: Atomic and Molecular Physics*, vol. 15, no. 17, p. 2969, 1982.

[66] A. D. White and J. D. Rigden, “Continuous gas maser operation in visible”, *Proceedings of the Institute of Radio Engineers*, vol. 50, no. 7, p. 1697, 1962.

[67] A. L. Bloom, W. E. Bell, and R. C. Rempel, “Laser operation at 3.39 μ in a helium-neon mixture”, *Applied Optics*, vol. 2, no. 3, pp. 317–318, 1963.

[68] K. U. Schreiber, Personal Communication, 2018.

[69] A. L. Bloom, “Observation of new visible gas laser transitions by removal of dominance”, *Applied Physics Letters*, vol. 2, no. 5, pp. 101–102, 1963.

[70] P. Franke, A. Feitisch, F. Riehle, K. Zhao, and J. Helmcke, “Simultaneous cw laser emission including a Raman line of a He–Ne laser at six wavelengths in the visible range”, *Applied Optics*, vol. 28, no. 17, pp. 3702–3707, 1989.

[71] C. K. N. Patel, “Optical power output in He-Ne and pure Ne maser”, *Journal of Applied Physics*, vol. 33, no. 11, pp. 3194–3195, 1962.

[72] W. R. Bennett and J. W. Knutson, “Simultaneous laser oscillation on the neon doublet at 1.1523 μ”, *Proceedings of the IEEE*, vol. 52, no. 7, pp. 861–862, 1964.

[73] H. G. Heard and J. Peterson, “Super-radiant yellow and orange laser transitions in pure neon”, *Proceedings of the IEEE*, vol. 52, no. 10, pp. 1258–1258, 1964.

[74] E. F. Labuda and E. I. Gordon, “Microwave determination of average electron energy and density in He–Ne discharges”, *Journal of Applied Physics*, vol. 35, no. 5, pp. 1647–1648, 1964.

[75] E. I. Gordon and A. D. White, “Similarity laws for the effects of pressure and discharge diameter of gain of He-Ne lasers”, *Applied Physics Letters*, vol. 3, no. 11, pp. 199–201, 1963.

[76] W. R. Bennett, “Inversion mechanisms in gas lasers”, *Applied Optics*, vol. 4, no. 101, pp. 3–22, 1965.

[77] A. D. White and E. I. Gordon, “Excitation mechanisms and current dependence of population inversion in He-Ne lasers”, *Applied Physics Letters*, vol. 3, no. 11, pp. 197–199, 1963.

[78] K. D. Mielenz and K. F. Nefflen, “Gas mixtures and pressures for optimum output power of RF-excited helium–neon gas lasers at 632.8 nm”, *Applied Optics*, vol. 4, no. 5, pp. 565–567, 1965.

[79] B. T. King, “Ring laser dynamics”, PhD thesis, Department of Physics and Astronomy, University of Canterbury, 1999.

[80] C. P. Wyss, D. N. Wright, B. T. King, D. P. McLeod, S. J. Cooper, and G. E. Stedman, “Collision broadening and quantum noise in a very large laser gyroscope”, *Optics Communications*, vol. 174, no. 1-4, pp. 181–189, 2000.

[81] J. T. Verdeyen, *Laser Electronics*. Englewood Cliffs, NJ, Prentice Hall, 1989.

[82] C. C. Davies, *Lasers and Electro-Optics: Fundamentals and Engineering*. Cambridge University Press, 2014.

[83]J. W. Knutson Jr and W. R. Bennett Jr, "Line broadening of the $3s_2$-$2p_n$ laser transitions of neon", *Physical Review A*, vol. 13, no. 1, p. 318, 1976.

[84]W. R. Bennett Jr, "The physics of gas lasers", *NASA STI/Recon Technical Report A*, vol. 78, 1977.

[85]B. V. Rybakov and A. I. Yakushev, "Investigation of the collisional broadening of the $2s_2$–$2p_4$ neon transition line", *Soviet Journal of Quantum Electronics*, vol. 4, no. 2, p. 217, 1974.

[86]R. H. Cordover, T. S. Jaseja, and A. Javan, "Isotope shift measurement for 6328 Å He–Ne laser transition", *Applied Physics Letters*, vol. 7, no. 12, pp. 322–324, 1965.

[87]A. Szöke and A. Javan, "Isotope shift and saturation behaviour of the 1.15- μ transition of Ne", *Physical Review Letters*, vol. 10, no. 12, p. 521, 1963.

[88]D. C. Gerstenberger, A. Drobshoff, and S. C. Sheng, "Isotope shift of the 543.3 nm laser transition of neon", *IEEE Journal of Quantum Electronics*, vol. 24, no. 3, pp. 501–502, 1988.

[89]R. B. Hurst, R. W. Dunn, K. U. Schreiber, R. J. Thirkettle, and G. K. MacDonald, "Mode behavior in ultralarge ring lasers", *Applied Optics*, vol. 43, no. 11, pp. 2337–2346, 2004.

[90]D. G. C. Jones, M. D. Sayers, and L. Allen, "Mode self-locking in gas lasers", *Journal of Physics A: General Physics*, vol. 2, no. 1, p. 95, 1968.

[91]J. Holdaway, R. B. Hurst, R. Graham, N. Rabeendran, K. U. Schreiber, and J.-P. R. Wells, "Self-locked operation of large He–Ne ring laser gyroscopes", *Metrologia*, vol. 49, no. 3, p. 209, 2012.

[92]A. L. Schawlow and C. H. Townes, "Infrared and optical masers", *Physical Review*, vol. 112, no. 6, p. 1940, 1958.

[93]G. E. Stedman, R. B. Hurst, and K. U. Schreiber, "On the potential of large ring lasers", *Optics Communications*, vol. 279, no. 1, pp. 124–129, 2007.

[94]M. A. Lombardi, "Fundamentals of time and frequency", in *The Mechatronics Handbook*, CRC Press, 2002.

[95]D. W. Allan, "Time and frequency (time-domain) characterisation, estimation, and prediction of precision clocks and oscillators", *IEEE Transactions on Ultrasonics, Ferroelectrics, and Frequency Control*, vol. 34, no. 6, pp. 647–654, 1987.

[96]L. C. Ng and D. J. Pines, "Characterisation of ring laser gyro performance using the Allan variance method", *Journal of Guidance, Control, and Dynamics*, vol. 20, no. 1, pp. 211–214, 1997.

[97]K. U. Schreiber, R. J. Thirkettle, R. B. Hurst, D. Follman, G. D. Cole, M. Aspelmeyer, and J.-P. R. Wells, "Sensing Earth's rotation with a helium–neon ring laser operating at 1.15 μm", *Optics Letters*, vol. 40, no. 8, pp. 1705–1708, 2015.

[98]D. Kuizenga and A. Siegman, "FM and AM mode locking of the homogeneous laser- Part I: Theory", *IEEE Journal of Quantum Electronics*, vol. 6, no. 11, pp. 694–708, 1970.

[99]R. W. Dunn, "Multimode ring laser lock-in", *Applied Optics*, vol. 28, no. 13, pp. 2584–2587, 1989.

[100]G. D. Cole, W. Zhang, M. J. Martin, J. Ye, and M. Aspelmeyer, "Tenfold reduction of brownian noise in high-reflectivity optical coatings", *Nature Photonics*, vol. 7, no. 8, pp. 644–650, 2013.

[101] D. MacKenzie, "From the luminiferous ether to the Boeing 757: A history of the laser gyroscope", *Technology and Culture*, vol. 34, no. 3, pp. 475–515, 1993.

[102] D. T. Wei and A. W. Louderback, *Method for fabricating multi-layer optical films*, US Patent 4,142,958, 1979.

[103] E. Hecht, *Optics*. Pearson Education, Inc., 2002, pp. 86–90.

[104] G. Harry, T. P. Bodiya, and R. DeSalvo, *Optical coatings and thermal noise in precision measurement*. Cambridge University Press, 2012.

[105] Y. Y. Jiang, A. D. Ludlow, N. D. Lemke, R. W. Fox, J. A. Sherman, L.-S. Ma, and C. W. Oates, "Making optical atomic clocks more stable with 10^{-16}-level laser stabilisation", *Nature Photonics*, vol. 5, no. 3, p. 158, 2011.

[106] B. P. Abbott, R. Abbott, R. Adhikari, P. Ajith, B. Allen, G. Allen, R. Amin, S. B. Anderson, W. G. Anderson, M. A. Arain, *et al.*, "LIGO: The laser interferometer gravitational-wave observatory", *Reports on Progress in Physics*, vol. 72, no. 7, p. 076 901, 2009.

[107] S. D. Penn, P. H. Sneddon, H. Armandula, J. C. Betzwieser, G. Cagnoli, J. Camp, D. Crooks, M. M. Fejer, A. M. Gretarsson, G. M. Harry, *et al.*, "Mechanical loss in tantala/silica dielectric mirror coatings", *Classical and Quantum Gravity*, vol. 20, no. 13, p. 2917, 2003.

[108] R. Nawrodt, S. Rowan, J. Hough, M. Punturo, F. Ricci, and J.-Y. Vinet, "Challenges in thermal noise for 3rd generation of gravitational wave detectors", *General Relativity and Gravitation*, vol. 43, no. 2, pp. 593–622, 2011.

[109] G. M. Harry, A. M. Gretarsson, P. R. Saulson, S. E. Kittelberger, S. D. Penn, W. J. Startin, S. Rowan, M. M. Fejer, D. Crooks, G. Cagnoli, *et al.*, "Thermal noise in interferometric gravitational wave detectors due to dielectric optical coatings", *Classical and Quantum Gravity*, vol. 19, no. 5, p. 897, 2002.

[110] K. Numata, A. Kemery, and J. Camp, "Thermal-noise limit in the frequency stabilisation of lasers with rigid cavities", *Physical Review Letters*, vol. 93, no. 25, p. 250 602, 2004.

[111] M. Aspelmeyer, P. Meystre, and K. Schwab, "Quantum optomechanics", *Physics Today*, vol. 65, no. 7, pp. 29–35, 2012.

[112] A. L. Bloom, *Gas Lasers*. Wiley, 1968.

[113] C. R. Jones, F. E. Niles, and W. W. Robertson, "Temperature dependence of the excitation transfer rate constants for He (2^3S_1)+ Ne→ He + Ne $(2s)$ and He (2^1S_0)+ Ne → He+ Ne $(3s)$", *Journal of Applied Physics*, vol. 40, no. 10, pp. 3967–3969, 1969.

[114] D. P. McLeod, "Seismic effects in ring lasers and transverse mode selection in helium-neon lasers", PhD thesis, Department of Physics and Astronomy, University of Canterbury, 2000.

[115] W. R. C. Rowley and P. Gill, *Helium-neon lasers*, US Patent 4,987,574, 1991.

[116] K. Seta and S. Iwasaki, "Frequency stabilisation of a HeNe laser using a thin film heater coated on the laser tube", *Optics Communications*, vol. 55, no. 5, pp. 367–369, 1985.

[117] G. D. Cole, W. Zhang, B. J. Bjork, D. Follman, P. Heu, C. Deutsch, L. Sonderhouse, J. Robinson, C. Franz, A. Alexandrovski, *et al.*, "High-performance near-and mid-infrared crystalline coatings", *Optica*, vol. 3, no. 6, pp. 647–656, 2016.

[118] H. Conrads and M. Schmidt, "Plasma generation and plasma sources", *Plasma Sources Science and Technology*, vol. 9, no. 4, p. 441, 2000.

[119]A. Bogaerts, E. Neyts, R. Gijbels, and J. van der Mullen, "Gas discharge plasmas and their applications", *Spectrochimica Acta Part B: Atomic Spectroscopy*, vol. 57, no. 4, pp. 609–658, 2002.

[120]M. A. Lieberman and A. J. Lichtenberg, *Principles of Plasma Discharges and Materials Processing*. John Wiley & Sons, 2005.

[121]Y. P. Raizer, M. N. Shneider, and N. A. Yatsenko, *Radio-Frequency Capacitive Discharges*. CRC Press, 1995.

[122]W. J. Goedheer, "Lecture notes on radio-frequency discharges, dc potentials, ion and electron energy distributions", *Plasma Sources Science and Technology*, vol. 9, no. 4, p. 507, 2000.

[123]R. Ludwig, *RF Circuit Design: Theory & Applications*. Pearson Education India, 2000.

[124]G. Grammer, "Simplified design of impedance-matching networks", *QST*, pp. 29–42, 1957.

[125]P. H. Smith, "Transmission line calculator", *Electronics*, vol. 12, no. 1, pp. 29–31, 1939.

[126]C. Coleman, *An Introduction to Radio Frequency Engineering*. Cambridge University Press, 2004.

[127]American Radio Relay League. Headquarters Staff and D. DeMaw, *The Radio Amateur's Handbook 1980*. American Radio Relay League, Incorporated, 1979.

[128]H. Wittenberg, "Gas tube design", in *Electron Tube Design*, RCA's Electron Tube, 1962, pp. 792–817.

[129]N. S. J. Braithwaite, "Introduction to gas discharges", *Plasma Sources Science and Technology*, vol. 9, no. 4, p. 517, 2000.

[130]Research Electro-Optics Inc., Personal Communication, 2015.

[131]A. E. Siegman, *Lasers*. University Science Books, McGraw-Hill, 1986.

[132]C. I. Eom, T. B. Eom, and M. S. Chung, "Frequency stabilisation of a 612 nm He-Ne laser in a transverse magnetic field", *Applied Physics Letters*, vol. 57, no. 8, pp. 739–740, 1990.

[133]R. H. Morris, J. B. Ferguson, and J. S. Warniak, "Frequency stabilisation of internal mirror He-Ne lasers in a transverse magnetic field", *Applied Optics*, vol. 14, no. 12, pp. 2808–2808, 1975.

[134]F. El-Diasty, M. A. Sobee, H. Hussein, and R. Sayed, "Study of mode structure of a 612 nm He-Ne laser in a transverse magnetic field", *Mapan*, vol. 25, no. 2, pp. 73–77, 2010.

[135]J. Ferguson and R. Morris, "Single-mode collapse in 6328-Å He-Ne lasers", *Applied Optics*, vol. 17, no. 18, pp. 2924–2929, 1978.

[136]A. J. Wallard, "The frequency stabilisation of gas lasers", *Journal of Physics E: Scientific Instruments*, vol. 6, no. 9, p. 793, 1973.

[137]H. S. Suh, T. H. Yoon, M. S. Chung, and O. S. Choi, "Frequency and power stabilisation of a three longitudinal mode He-Ne laser using secondary beat frequency", *Applied Physics Letters*, vol. 63, no. 15, pp. 2027–2029, 1993.

[138]S. Yokoyama, T. Araki, and N. Suzuki, "Intermode beat stabilised laser with frequency pulling", *Applied Optics*, vol. 33, no. 3, pp. 358–363, 1994.

[139] J. D. Ellis, K.-N. Joo, E. S. Buice, and J. W. Spronck, "Frequency stabilised three mode HeNe laser using nonlinear optical phenomena", *Optics Express*, vol. 18, no. 2, pp. 1373–1379, 2010.

[140] S. Haykin, *Communication Systems*. John Wiley & Sons, 2008.

[141] D. N. Wright, "Optimisation of ring-laser gyroscopes", PhD thesis, Department of Physics and Astronomy, University of Canterbury, 2001.

[142] S. Jacobs, "Optical heterodyne (coherent) detection", *American Journal of Physics*, vol. 56, no. 3, pp. 235–245, 1988.

[143] J. Ye and S. T. Cundiff, *Femtosecond Optical Frequency Comb: Principle, Operation and Applications*. Springer Science & Business Media, 2005.

[144] MenloSystems, *FC1500-250-WG User Manual*, Menlo Systems GmbH, Munich, Germany, 2016.

[145] N. R. Newbury and B. R. Washburn, "Theory of the frequency comb output from a femtosecond fibre laser", *IEEE Journal of Quantum Electronics*, vol. 41, no. 11, pp. 1388–1402, 2005.

[146] G. R. Hanes and C. E. Dahlstrom, "Iodine hyperfine structure observed in saturated absorption at 633 nm", *Applied Physics Letters*, vol. 14, no. 11, pp. 362–364, 1969.

[147] C. E. Webb and J. D. Jones, *Handbook of Laser Technology and Applications: Laser design and laser systems*. CRC Press, 2004, vol. 2.

[148] A. Rossi, V. Biancalana, B. Mai, and L. Tomassetti, "Long-term drift laser frequency stabilisation using purely optical reference", *Review of Scientific Instruments*, vol. 73, no. 7, pp. 2544–2548, 2002.

[149] F. Bosi, G. Cella, A. Di Virgilio, A. Ortolan, A. Porzio, S. Solimeno, M. Cerdonio, J. Zendri, M. Allegrini, J. Belfi, *et al.*, "Measuring gravitomagnetic effects by a multi-ring-laser gyroscope", *Physical Review D*, vol. 84, no. 12, p. 122 002, 2011.

[150] R. B. Hurst, M. Mayerbacher, A. Gebauer, K. U. Schreiber, and J.-P. R. Wells, "High-accuracy absolute rotation rate measurements with a large ring laser gyro: Establishing the scale factor", *Applied Optics*, vol. 56, no. 4, pp. 1124–1130, 2017.

[151] K. U. Schreiber, A. Gebauer, and J.-P. R. Wells, "Long-term frequency stabilisation of a 16 m^2 ring laser gyroscope", *Optics Letters*, vol. 37, no. 11, pp. 1925–1927, 2012.

[152] Y. A. Blagodarov, Y. P. Buravin, L. N. Orlov, A. I. Ryabov, and G. N. Toropkin, "Temperature effects in a helium-neon laser", *Journal of Applied Spectroscopy*, vol. 15, no. 6, pp. 1576–1578, 1971.

[153] S. Ezekiel and S. R. Balsamo, "Passive ring resonator laser gyroscope", *Applied Physics Letters*, vol. 30, no. 9, pp. 478–480, 1977.

[154] W. Z. Korth, A. Heptonstall, E. D. Hall, K. Arai, E. K. Gustafson, and R. X. Adhikari, "Passive, free-space heterodyne laser gyroscope", *Classical and Quantum Gravity*, vol. 33, no. 3, p. 035 004, 2016.